

1a. REPORT SECURITY CLASSIFICATION
Unclassified

2a. SECURITY CLASSIFICATION AUTHORITY

2b. DECLASSIFICATION/DOWNGRADING SCHEDULE

4. PERFORMING ORGANIZATION REPORT NUMBER

Approved for public release;
distribution is unlimited

5. MONITORING ORGANIZATION REPORT NUMBER(S)

AFOSR-TR- 92 0508

6a. NAME OF PERFORMING ORGANIZATION

University of Maryland

6b. OFFICE SYMBOL
(If applicable)

7a. NAME OF MONITORING ORGANIZATION

AFOSR/NA

6c. ADDRESS (City, State, and ZIP Code)

College Park, MD 20742

7b. ADDRESS (City, State, and ZIP Code)

Bolling AFB
Washington, DC 20332-64488a. NAME OF FUNDING/SPONSORING
ORGANIZATION
AFOSR8b. OFFICE SYMBOL
(If applicable)
NA

9. PROCUREMENT INSTRUMENT IDENTIFICATION NUMBER

AFOSR-88-0280

8c. ADDRESS (City, State, and ZIP Code)

Bolling Air Force Base
Washington, DC 20332-6448

10. SOURCE OF FUNDING NUMBERS

PROGRAM
ELEMENT NO.
61102FPROJECT
NO.
2302TASK
NO.
C2WORK UNIT
ACCESSION NO.

11. TITLE (Include Security Classification)

Mechanisms of Fracture and Fragmentation by Explosive Loading

12. PERSONAL AUTHOR(S)

R.D. Dick, W.L. Fourney, X.J. Wang, C. Young, III, and Y. Wei

13a. TYPE OF REPORT

Final

13b. TIME COVERED

From 8/1/88 to 7/31/91

14. DATE OF REPORT (Year, Month, Day)

1992, April 21

15. PAGE COUNT

186

16. SUPPLEMENTARY NOTATION

17. COSATI CODES

FIELD

GROUP

SUB-GROUP

18. SUBJECT TERMS (Continue on reverse if necessary and identify by block number)

Fracture, Fragmentation, Explosive Loading

19. ABSTRACT (Continue on reverse if necessary and identify by block number)

The research reported here involved a study to answer some fundamental questions on the mechanisms of rock fracture and fragmentation by explosive loading. The program was experimental and dealt with the dynamic event as a three dimensional problem. Specifically, small scale models were used to obtain dynamic behavior of the model materials by measuring strain, stress, and particle velocity during the explosive event. Dynamic photoelastic methods were used to obtain data on the fracture patterns, propagation speeds, and sequences involved in the process. The effects of small flaws, large joints and discontinuities, and explosive source geometry were studied. The findings are: (1) At early times, shock wave effects promote fracture initiation, coalescence, and branching in the matrix material. At later times,

20. DISTRIBUTION/AVAILABILITY OF ABSTRACT

☒ UNCLASSIFIED/UNLIMITED ☐ SAME AS RPT. ☐ DTIC USERS

21. ABSTRACT SECURITY CLASSIFICATION

Unclassified

22a. NAME OF RESPONSIBLE INDIVIDUAL

Spencer T Wu

22b. TELEPHONE (Include Area Code)

(202) 767-6962

22c. OFFICE SYMBOL

AFOSR/NA

19. the explosive gas pressure causes the cracks to extend and fragments to form. Finally at very late times, the gas pressure causes the fragments to move outward forming the crater. (2) Radial fractures initiate and propagate immediately from the explosive borehole; (3) spall fractures form after the P-wave reflects from the free surface and are essential for continued generation of circumferential cracks to produce fragmentation. (4) Joints and flaws in the material have a significant effect on the extent of fracturing and the fragmentation process. (5) There is no clear relationship between the measured field parameters (strain, stress, and velocity) and the observed fracture and fragmentation; (6) Spherical charges produced larger craters in rock-like models than cylindrical charges; and (7) Results from finite element calculations of the process agree reasonably well with experimental the results.

**MECHANISMS OF FRACTURE AND FRAGMENTATION
BY EXPLOSIVE LOADING**

By

Richard D. Dick
William L. Fourney
Xiang Jun Wang
Chapman Young, III
Youzhi Wei

Department of Mechanical Engineering
University of Maryland
College Park, MD 20742

21 April, 1992

Prepared for
Dr. Spencer T. Wu
Air Force Office of Scientific Research
Bolling Air Force Base
Washington, DC 20332-6448



Accession For	
NTIS GR&I	<input checked="" type="checkbox"/>
DTIC TAB	<input type="checkbox"/>
Unannounced	<input type="checkbox"/>
Justification	
By	
Distribution/	
Availability Codes	
Dist	Avail and/or Special
A-1	

92 6 18 100

92-15621



**MECHANISMS OF FRACTURE AND FRAGMENTATION
BY EXPLOSIVE LOADING**

By

Richard D. Dick

William L. Fourney

Xiang Jun Wang

Youzhi Wei

Department of Mechanical Engineering

University of Maryland

College Park, MD 20742

21 April, 1992

Prepared for

Dr. Spencer T. Wu

Air Force Office of Scientific Research

Bolling Air Force Base

Washington, DC 20332-64

MECHANISMS OF FRACTURE AND FRAGMENTATION BY EXPLOSIVE LOADING

TABLE OF CONTENTS

- I. INTRODUCTION
- II. FRACTURE AND FRAGMENTATION MODEL TESTING
- III. FRAGMENTATION MECHANISM IN CRATER BLASTING
- IV. COMPUTATIONAL INVESTIGATION
- V. OPTIMIZING CRATER VOLUME
- VI. EFFECTS OF JOINTS
- VII. SUMMARY

APPENDIX

TESTS CONDUCTED

CHAPTER I. INTRODUCTION.

The goal of this research project was to answer fundamental questions on the mechanisms of rock and concrete breakage by explosive loading. The program was experimental in nature and dealt with the dynamic event as a three-dimensional problem. Objectives include classifying the role of flaws, joints, and discontinuities in the fragmentation process; relating the explosive source geometry to damage and breakage; and determining the local physical parameters that correlate best with fracture and fragmentation.

When explosives are used to break rock, the technique is to drill holes into the rock mass and to place explosives into the holes. When the explosive detonates the relatively small mass of chemical explosive is transformed into gas in a small volume and very high pressures. This process is accompanied by the generation of very large shock pressures - in the hundred kilobar range - and large increases in temperature. The resulting breakage that is caused by the explosive detonation is not well understood from the standpoint of what actually causes the resulting breakage.

The breakage could be due to one of two causes. The very large pressures which are generated in the borehole by the explosive detonation result in a very intense series of shock waves being sent out into the rock mass. These waves are of various types (P Wave, Shear Wave) and travel very rapidly through the media or along the free surfaces of the rock mass (Rayleigh Wave). This wave propagation event occurs very quickly after detonation and only lasts from a few hundreds of microsecond to a few hundred milliseconds.

The same pressure that caused the shock waves to form as it interacted with the borehole wall still needs to be relieved. This pressure relief occurs as a result of borehole expansion and by gases entering into and expanding fractures which were inherent to the rock mass or which were caused by the intense loading by the shock waves. This gas pressure phase of breakage occurs much slower than the shock wave phase and typically lasts for hundreds of milliseconds up to many seconds after detonation occurs.

Very little is known about what causes the rock to break. Nearly all rock material is very much stronger in compression than in tension. Rock is a non-isotropic, inhomogeneous material with bedding and joint sets which complicates understanding the process. Early theories of rock breakage due to explosive loading attributed the breakage to the intense shock wave. The resulting breakage was based upon the premise that the stresses in the shock wave upon reflection from a free boundary change from compression to tension.

(1.2)

These very high tensile stresses exceed the tensile strength of the material and spalling near the free boundary takes place.

Later more researchers felt that the pressure loading of the fracture network had more to do with the breakage than the shock wave loading. Some felt that the very high gas pressures tended to load the rock located in the area between the top of the borehole and the bottom of the borehole much like a beam in bending until the tensile stresses in the "bent beam" exceeded the tensile strength of the rock and fracture occurred.

Experimentally, the situation is very complicated and not easy to investigate. The loading takes place in a very rapid fashion, the material is very complicated with regard to its response to load, even in a static fashion, the material is opaque, and any instrumentation that is used to assess the stress/strain state alters significantly the behavior of the material.

Under funding from the National Science Foundation studies were conducted by the University of Maryland and Martin Marietta Laboratories into fracture and fragmentation of rock like materials by explosive loading. This work was fruitful and progress was made into understanding more about the fracture process when explosives are utilized. There were two main deficiencies to the results that were obtained in that program. First, most of the testing that was conducted under that study was done in two dimensional models made from transparent birefringent materials. These materials were used since the main tool used in the investigation was dynamic photoelasticity. This permitted the observation of fracture initiation and at the same time permitted a determination of the state of stress in the model. Due to the restrictions in using the dynamic polariscope information is lacking both from the standpoint of a three dimensional state of stress and from the standpoint of having results obtained for true rock like materials. The second deficiency was the inability to obtain information on the dynamic event in regions very close to the borehole. When the explosive was detonated in these thin models the borehole region was very quickly hidden by the smoke and debris created in the detonation process. This was true even though the explosive used (PETN) was one of the cleaner explosives.

The results obtained in that study were helpful in understanding more fully the process of fracture and fragmentation due to explosive loading. In particular it was found that the shock wave does play an important role in fragmentation. In a material such as rock where there are inherent flaws present the outward traveling shock wave was found to initiate fractures as it passed over the flaws. The tensile circumferential stress component in the outward traveling wave was found to initiate and propagate radial cracks around the borehole. Upon reflection from a free boundary, the stress (shock) waves were found to initiate

(1.3)

cracks from flaws that were of a critical size. Whether a flaw was of a critical size or not of course depends upon the level of stress in the propagating wave and since the maximum tensile value of stress occurred very near the boundary some spalling failure was observed. The inward traveling waves were found to interact with the outward traveling radial cracks and to affect these cracks so that they propagated in a circumferential direction. At the same time these cracks branched and multiplied in number. This circumferential cracking was found to benefit the fragmentation process greatly. After the inward propagating stress waves passed over the now circumferential cracks the cracks would turn and travel again in the radial direction.

Testing conducted in models which contained large flaws (which were meant to represent joints and bedding planes) also showed that the shock (stress) waves were important in the fragmentation event. In particular, it was found that the joint or bedding plane was the source for multiple initiations as the waves passed over them. It appeared that the bedding plane (or joint) even though tightly bonded appeared as a crack to the outward traveling waves. It was observed that any shear component of stress in the outwardly traveling wave loaded the joint in a Mode II fashion and multiple cracks initiated which made an angle of 80 to 90 degrees to the interface. This cracking contributed greatly to the fragmentation process.

Although the research described above answered some questions with regard to the fragmentation process much mystery still remains. In particular, the research demonstrated (in brittle transparent flawed materials) that the stress waves play an important role in the fragmentation process. This role was viewed as a preconditioning of the rock mass such that the later gas pressurization phase will be more effective. It should not be assumed from the work described above that shock waves are the dominant mechanisms of fragmentation, but only that they are an important part of the process and should not be neglected in the design of any blasting.

In the present study which was funded by AFOSR the approach was somewhat different from the NSF study. The present study involved testing three dimensional models and the testing was conducted in materials similar to rock. Several different materials were used to simulate rock including rockite, Hydrocal, cement, and Hydrostone. In those tests, which did involve two dimensional models, much better techniques were developed permitting a better view of the fragmentation process. That is to say, methods were developed that permitted the gases and debris from the detonation to not interfere with the observation of the fragmentation event. Many different instrumentation techniques were used to measure the parameters felt to be important in the fragmentation event - including stress gages, strain gages, and

(1.4)

velocity gages. As a result it is felt that much more understanding of the fracture and fragmentation event currently exists as a result of the research conducted under this funding.

The objectives of the current study were: 1) Identify mechanisms of fracture and fragmentation, 2) Determine the effect of explosive source geometry upon fragmentation results, 3) Determine the effects of joints/interfaces on fragmentation results, 4) Measure in-situ response parameters such as particle velocity, strain, stress, etc. which occur due to explosive loading, and 5) Measure surface displacements which occur due to explosive loading.

The results of the testing conducted to investigate these objectives will be described in the following sections. In the following chapter the testing conducted to study the fracture and fragmentation will be described. In Chapter 3 the fragmentation mechanism identified in crater blasting will be described. The results of a computational study that substantiates the mechanism is described in Chapter 4. Chapter 5 presents the results of testing conducted to investigate the possibility of optimizing the results of crater blasting. Chapter 6 present the results of testing conducted to evaluate the effects of joints on the outgoing stress waves. Finally, Chapter 7 presents a summary of the program results. A description of all of the tests conducted during the program are given in the Appendix.

CHAPTER 2. FRACTURE AND FRAGMENTATION MODEL TESTING.

A. Introduction.

Tests were conducted in two types of materials, namely transparent polymeric materials and materials which were rock-like in behavior. Three dimensional models from these materials were instrumented and dynamically loaded using small explosive charges. The purpose was to measure dynamic parameters such as stress, strain, and particle velocity within the models. The results from these measurements were then related to the observed fracture patterns and the fragmentation to determine a fragmentation mechanism. The measurements were used to identify the most important parameters in fragmentation process. The transparent model materials included PMMA (Plexiglas), Homolite 100, and Epon 815. The rock-like materials were Rockite, cement, and gypsum.

In addition to the fracture and fragmentation test series, a large number of tests were conducted to study the effect of joints and discontinuities on the fragmentation mechanism. The effect of small flaws on fragmentation is discussed in this chapter. The details of the joint tests are reported in Chapter 6.

B. Fragmentation Tests in Transparent Models.

The initial fragmentation tests were conducted in PMMA models whose boundaries were sufficiently distant to be considered three dimensional. Typically these models were 230 mm by 230 mm by 150 mm thick, so the stress wave round trip time from the charge location to the side and bottom boundaries and return was about 100 microseconds. By that time the shape and size of the fracture zone and the crater were basically defined. Layers of PMMA were bonded together to construct models 125 and 150 mm thick because the thickest PMMA commercially available was 100 mm. Layering was also needed to allow placement of transducers at interior locations to measure strain, stress, and particle velocity. However, difficulties arose because of the bonding agents and of the effects the bonding surface (discontinuity) had on wave propagation.

Bonding agents such as chloroform, acrylic cements, and cyanoacrylate cements (super glue) failed to produce an interface material that behaved like the PMMA. The chloroform and acrylic cements which require evaporation curing failed to cure in the interior of the large models. Epoxy and cyanoacrylate have an impedance (material initial density times wave speed) sufficiently different from PMMA that the dynamic response did not match at the interface. The epoxy glue also had a low dynamic strength and hence the bond failed during the dynamic event. During explosive loading the discontinuity from the bond layer controlled the fracture and fragmentation of the PMMA models. These difficulties along with difficulties encountered with bonding the gages to the PMMA with adequate strength caused the abandonment of PMMA as a model material for fragmentation and for measurements of strain and

(2.2)

stress after five tests.

For the PMMA model tests PETN explosive charges of 250 mg and 500 mg mass were placed at the bottom of a 6 mm diameter borehole. These spherically shaped charges were typically 50 to 60 mm from the free surface. A few tests had stem material in the borehole behind the explosive which consisted of a combination of fine sand next to the charge and clay at the collar. The other tests had no stemming. Figure 2.1 shows a diagram of a typical test and details of the test geometry are presented in Table 1 (Tests CG1 through CRT7). The tests were conducted using spherically shaped PETN explosive charges. The explosive was compacted to a density of about 1300 kg/m^3 . The PETN was obtained by slicing detonator cord and extracting the powder which was then placed in a mold and compacted. This procedure was duplicated for each test and produced a consistent explosive density, weight, and size. In the early PMMA tests the charge was initiated by inserting the end of a 1.5-mm diameter coaxial cable at the center of the explosive. A 5 to 10 mg lead azide booster explosive was contained in a pocket at the end of the cable to ensure the initiation of the PETN. Detonation was started by applying a high voltage spark from the detonator box between the inner and outer conductors at the open end of the cable. This initiates the lead azide which in turn initiates the PETN. With this scheme the average initiation time is approximately two microseconds. The process is very reliable and inexpensive to accomplish. Because the inherent electrical noise generated by the high voltage discharge interfered with the recording of the signals, a length of non-electric detonating tube was placed between the coaxial cable and the explosive. This provided a 25- to 50-microsecond delay between the spark and explosive initiation and allowed the initiation electrical noise to decay to zero before the signal arrived on the oscilloscope trace. This method was very successful in mitigating the noise problems and was used for the remaining tests.

Instrumentation for the PMMA models consisted of strain gages placed at the bond interface and on the free surface. These gages were oriented in the circumferential and radial directions to measure strain produced by the stress waves emanating from the detonation of the explosive. Slant distances to the gages ranged from 25 to 107 mm from the charge center and strains were about 2000 microstrain for both the circumferential and radial directions, except for Test CRT7. Table 2 is a list of the measured strain values. Compared to strains measure in the Epon 815 models, these values seem low. There are two possible reasons for these low amplitudes. 1) Strain gages in the interior locations of the PMMA models were bonded to the surface between the layers. The strength at this interface was weak and hence, the gages likely debonded during the passage of the stress wave. 2) Several of the gages were attached to the free surface to measure the surface strain, but in almost every instance the reflection of the stress wave at the

Table 1. Test and crater data for PMMA, Homolite,
Epon 815, and rock-like materials.

Test id	DOB (mm)	Hole diam (mm)	Charge weight (mg)	Charge length (mm)	Crater radius (mm)	Crater depth (mm)	Crater volume (mm ³)	Groove above bottom (mm)	Num major cracks	P-wave speed (m/s)
CG1PC	28.58	6.4	600	19.05	30		20000	0		
CG2PC	28.58	6.4	600	19.05	38		195000	12.7		
CG3PC	28.58	6.4	600	19.05	39		31000	25.4		
CG4PC	28.58	6.4	600	19.05	41		32000	19.1		
CG5PC	28.58	6.4	600	19.05	49		50000	6.4		
CG6PC	28.58	6.4	600	19.05	56		80000	12.7		
CG7PC	28.58	6.4	600	19.05	23		14000	12.7		
CG8PC	28.58	6.4	600	19.05	44		70000	12.7		
CG9PC	28.58	6.4	600	19.05	40		39000	12.7		
CG10PC	28.58	6.4	600	19.05	35		34000	12.7		
CRT1PS	55.69	9.8	500	9.78	23				1	2546
CRT2PS	55.69	9.8	500	9.78	0	0	0		6	2467
CRT3PS	54.6	7.6	250	7.6	23		47000		6	2479
CRT4PS	54.6	7.6	250	7.6	0	0	0		0	
CRT5PS	54.6	7.6	250	7.6	0	0	0		5	
CRT6PS	76.2	7.6	250	7.6	0	0	0		3	
CRT7PS	76.2	7.6	500	7.6	0	0	0		3	
CRT8ES	50.8	7.9	350	7.9	64		250000		11	2381
CRT9ES	63.5	7.9	350	7.9	127		890000		5	
CRT10ES	63.5	7.9	350	7.9	102		485000			
CRT11ES	61	7.9	350	7.9	104	50				
CRT12EC	45	4	350	20	50	35				
CRT13ES	60	7.9	350	7.9	104	56			5	2325
CRT15ES	50	7.9	350	7.9	124	56	753600		7	
RT1C	38.1	6.4	1000	25.4	67	32	155000		7	
RT2S	57.2	11.5	950	11.4	51	48	460000		7	3240
RT3S	57.2	11.5	1000	11.4	95	57			14	
RT4S	57.2	11.5	1000	11.4	86	57			10	
RT5S	57.2	9.5	500	9.5	0	0			8	
RT6S	57.2	11.5	1000	11.5						3210
RT7C	38.1	6.4	1000	25.4	74	57			15	
RT8C	38.1	6.4	1000	25.4	77	50			14	
RT9S	57.2	11.5	1000	11.5	63	32			14	
RT10S	57.2	11.5	1000	11.5	63	57			11	
RT11S	57.2	11.5	1000	11.5	73	57			7	
RT12S	57.2	11.5	1000	11.5	89	57			8	
RT13S	57.2	11.5	1000	11.5	105	57			9	
JT1ES	50.8		350							
JT2ES	50.8		350							
JT3ES	50.8		350							
CS1ES	25	7.9	350		66	25				
CS2ES	25	7.9	350		75	25				
PJ1H		6.4	200							
PJ2H		5.1	200							
PJ3H		5.1	200							
PJ4H		5.1	200							
PJ5H		5.1	200							
PJ6H		5.1	200							
PJ7H		5.1	200							
PJ8H		5.1	200							
CZ1H		6.4	250							
CZ2H		7.5	350							

CZ3H	8.7	500
IC1H	4.8	150
IC2H	5.1	250
IC3H	5.1	250
IC4H	5.1	220
IC5H	5.1	220
IC6H	5.1	220
IS1P	7.8	220
IS2P	5.1	380
IS3P	5.1	260
IS4P	7.6	600
IS5P	7.6	174
IS6P	7.6	400
MT1P		300
MT2P		200
MT3P		350
MT4P		350
MT5P		350
WD1P		300
WD2P		300
WD3P		300
WD4P		300

Table 1 (cont). Test identification key.

CG Series - Circumferentially Grooved Borehole Test
CS Series - Cranz-Schardin Camera Usage Test
CT Series - Crater Test
CZ Series - Two-Dimensional Photoelastic Test
IC Series - Isoclinic Test
IS Series - Isochromatic Test
JT Series - Joint Test
MT Series - Moire' Test
PT Series - Jointed Plate Test
RT Series - Rock-like Test
WD Series - w-displacement Test
C - Cylindrical Charge Geometry
E - Epon 815 Epoxy Model Material
H - Homolite Model Material
N - Nylon Model Material
P - PMMA Model Material
S - Spherical Charge Geometry

CRT10/6ir	50				6100
CRT12/1ir	20	350			38880
CRT12/2it	20		8.3	19440	
CRT12/3ir	35				15840
CRT12/4it	35		14.9	9360	
CRT13/1ir	25	350			20000
CRT13/2it	25		11.1	12500	
CRT13/3ir	50				6250
CRT13/4it	50			3000	
CRT13/5ir	50				6100
CRT13/6it	50		16.7	5100	
CRT15/1ir	25	350			18000
CRT15/2it	25		34.4	13300	
CRT15/3ir	40				8100
CRT15/4it	40		39.3	6200	

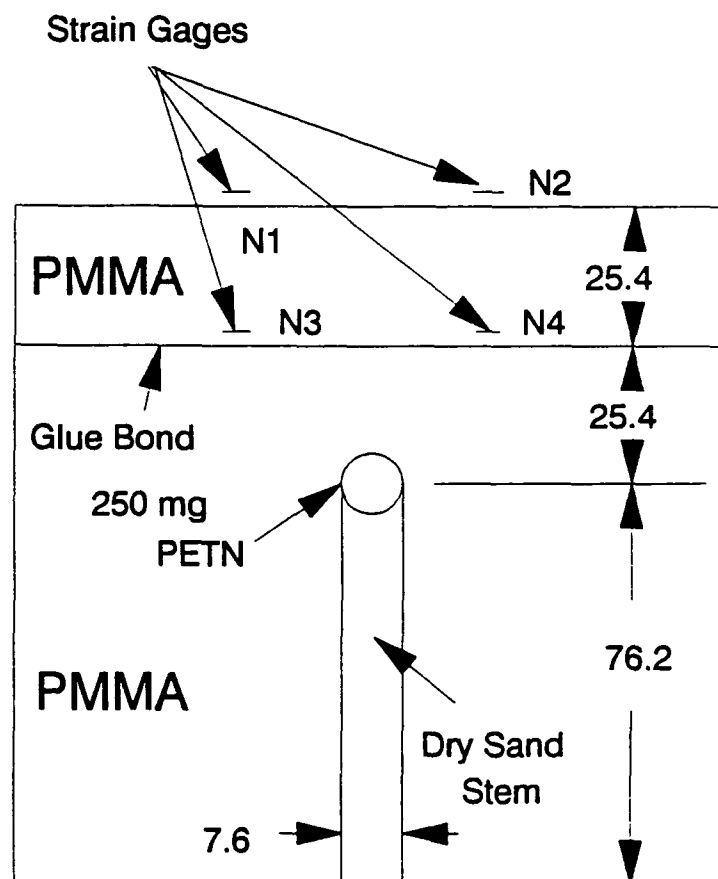


Figure 2.1. Diagram of a typical model test using PMMA.

(2.3)

surface caused these gages to debond. This debonding probably occurred before the peak strain was reached. Test CRT7 is the one exception to these low strain values in the PMMA models for reasons not understood.

Strain gage signals from a typical fracture and fragmentation test in PMMA are shown in Fig. 2.2 where both radial and circumferential strain signals are presented. Figures 2.3 and 2.4 are plots of the measured peak circumferential and radial strains from all the PMMA model tests as a function of slant distance from the charge. The results for Test CRT7 are not included in these figures. The surface strain measurements (radial and circumferential) are consistently 1000 -2000 microstrain (0.1% - 0.2 % strain), but the interior strains vary widely, 2000 - 14,000 microstrain. The method of gage attachment may be the reason for the inconsistent interior values. On the surface the strain gages detach very soon after arrival of the stress wave at the free surface. The data are too sparse to fit a mathematical expression for either strain measurement direction. There is no obvious connection between the strain measurements and the fragmentation results for the PMMA model tests.

Only one PMMA model test formed a crater (CRT3P) to the surface, but one to six major fractures formed in all but one test. In a few PMMA model tests a crater started to form but the cracks that would have eventually defined the crater arrested at the bond interface. This observation demonstrates the strong influence of the bond interfaces, in this case a horizontal surface, had on the fracture and fragmentation results. Based on the shape of the fragments from Test CRT3P the observation was made that radial cracks form and propagate first as a consequence of the explosive loading. Circumferential cracks appear to form at a later time than the radial cracks. There was good agreement in terms of amplitude and signal structure between the radial and circumferential strain records for identical Tests CRT3P and CRT4P, even though the levels seem low compared to the Epon 815 strain measurements. This result indicates reproducible explosive loading conditions that carried through all the other test series of this research project. The Average measured P-wave speed in PMMA from the strain signals was 2475 m/s over the interval 35 to 60 mm.

The remaining three-dimensional transparent models were constructed from Epon 815 castable epoxy. This material was chosen because of it's ease in mixing and casting, it's transparent property, and strength. Large model sizes were cast to increase boundary distances from the explosive charges. The curing process is exothermic and hence a considerable amount of heat was generated in the large models. This required continuous cooling during the 24 hour curing time. The finished models were transparent with a light brownish-yellow color. The models were usually constructed in two or three pours to reduce the heat generated to preserve the transparent condition. (High heat causes the Epon to turn a dark

CRATER TEST 4,5

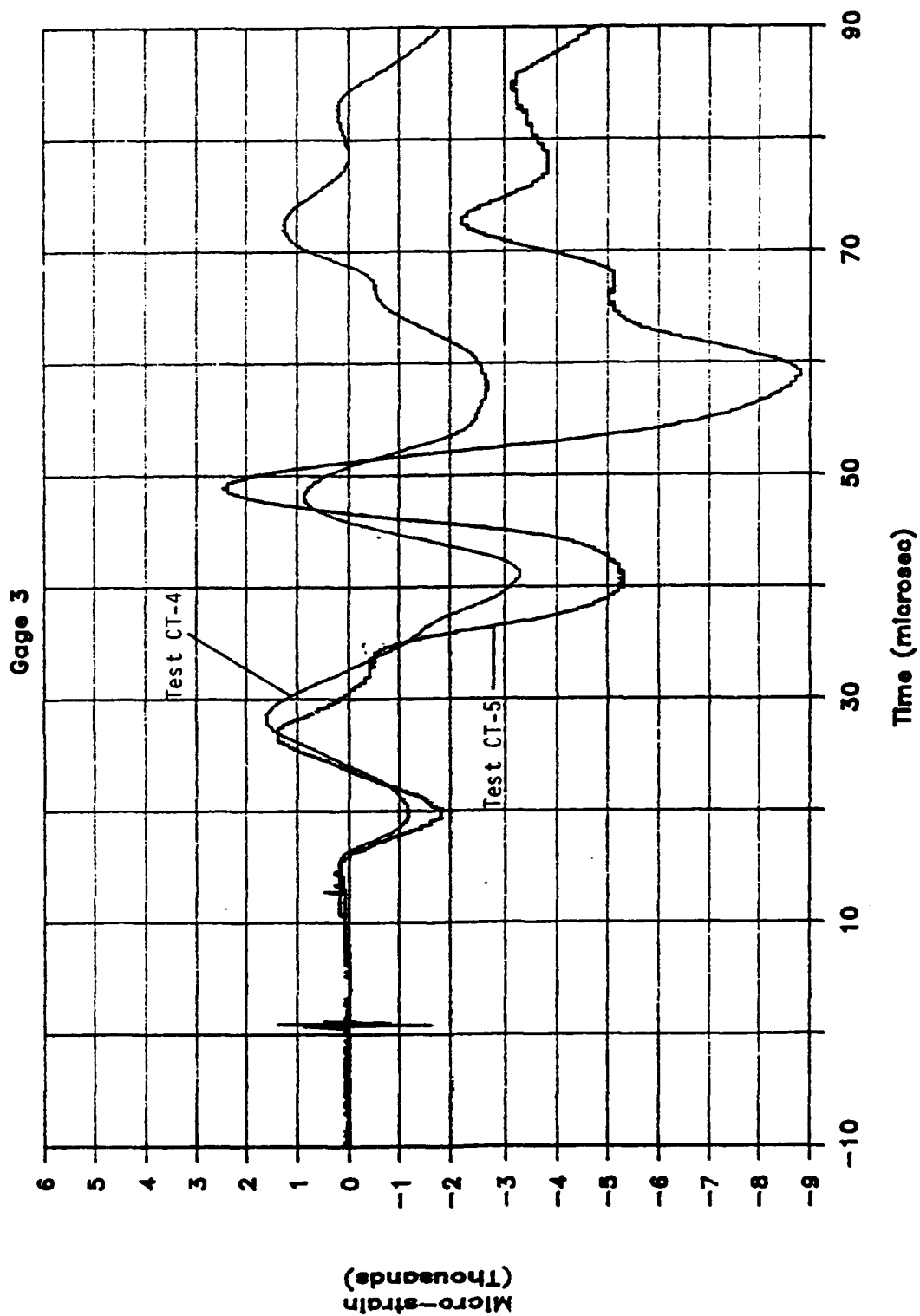


Figure 2.2a. Gage 3 radial strain signals from PMMA Tests CRT4 and CRT5.

CRATER TEST 4,5

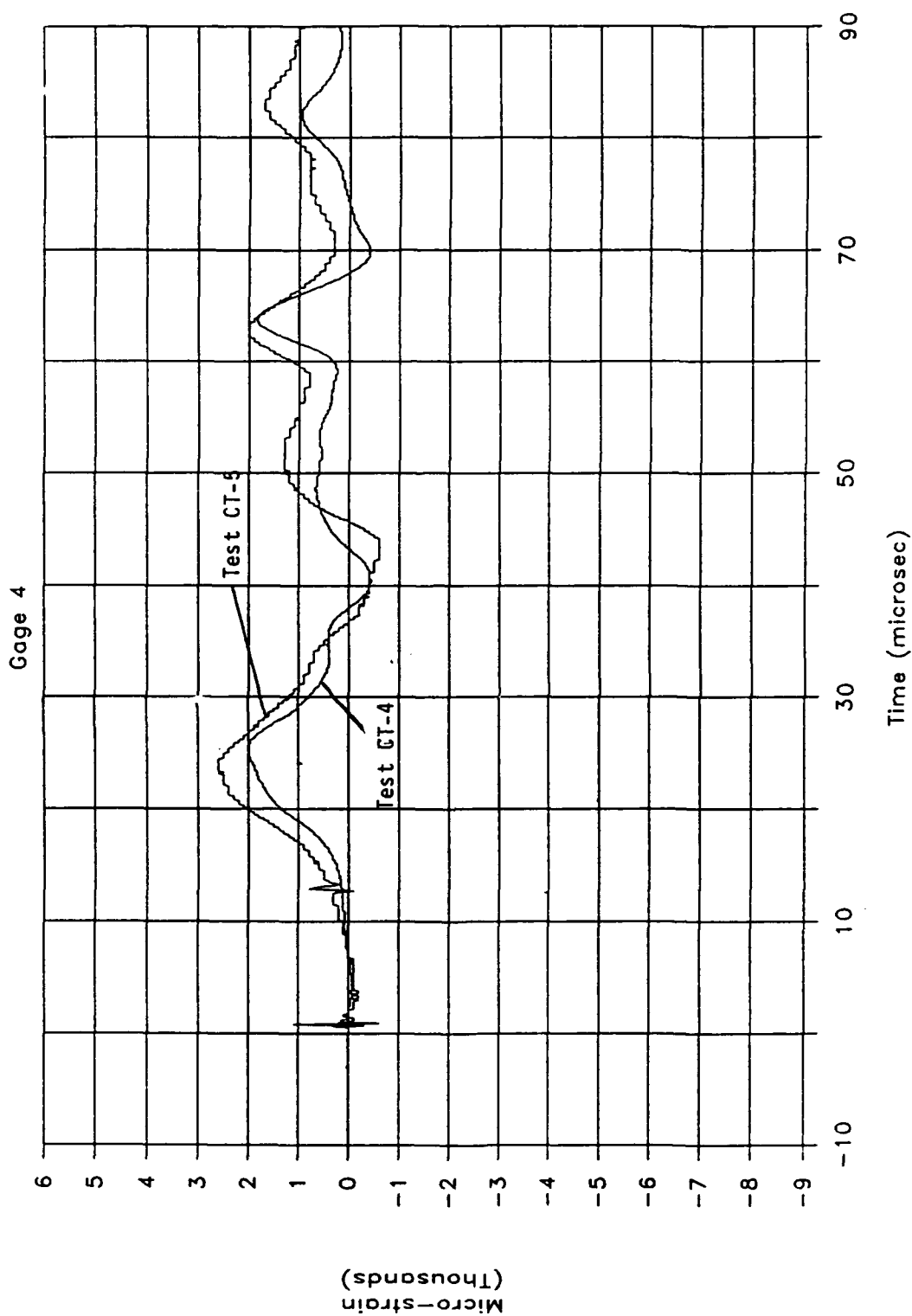


Figure 2.2b. Gage 4 tangential strain signals from PMMA Tests CRT4 and CRT5.

(2.4)

brown). As a result a strong and sometimes visible interface was formed in some models between pours. Casting these models provided the opportunity to embed gages to measure stress, strain, and particle velocity at known locations relative to the explosive. The models were nominally 300-mm square by 250-mm thick and for some 300-mm diameter by 125 or 150-mm thick. Strain gages were the primary transducer and were oriented to measure strain in the radial and circumferential directions. Carbon or manganin pressure gages were embedded in the Epon models to measure stress in the radial direction near the explosive. In one Epon model tests (Test CRT13), electromagnetic gages were included to measure the particle velocity in the radial direction. Figure 2.5 is a diagram of a typical test showing the gage locations in Epon 815 model. Table 1 also defines the geometry for these tests (Tests CRT8 through CRT15).

The explosive charge used in the Epon 815 models was placed in a 7.9-mm diameter borehole drilled from the bottom. The borehole did not extend to the free surface, meaning the explosive was perfectly stemmed. However, the explosive was stemmed to the bottom surface with clay and fine sand. A spherically shaped charge with a mass of 350 mg was used for most of the Epon model tests. The explosive initiation system was the same as the later PMMA model tests and typically the center of the explosive was located 57 mm from the free surface and an equal distance from the either side.

The effects of small flaws and joints of various strengths on the fracture and fragmentation pattern in Epon 815 transparent models were studied in several three dimensional tests. This was accomplished by introducing small mica flakes and horizontal and vertical joints at the time the Epon 815 models were cast. In some tests the Cranz-Schardin framing camera was used to view the sequence of crack formation and propagation. Also each model was examined after each test to inspect the crack initiation site and propagation path.

The mica flaws which simulated small flaws were nominally 3 mm by 3 mm by 0.1 mm thick and were cast into place in the epoxy models. They were oriented to produce a flat surface and an edge-on alignment to the outwardly propagating stress wave. However, because of the difficulty maintaining the position of the mica pieces as the model cured, some flakes changed position slightly. The mica represents a small discontinuity that has a shock impedance four to five time larger than the Epon material. This should produce reflected tensile waves strong enough to form cracks, but the small size of the mica flakes mitigated some of the effects of the tensile stresses.

As it turned out the embedded stress and strain gages themselves provided site for cracks to initiate in the Epon. The gages were larger than the mica flakes, but the impedance was

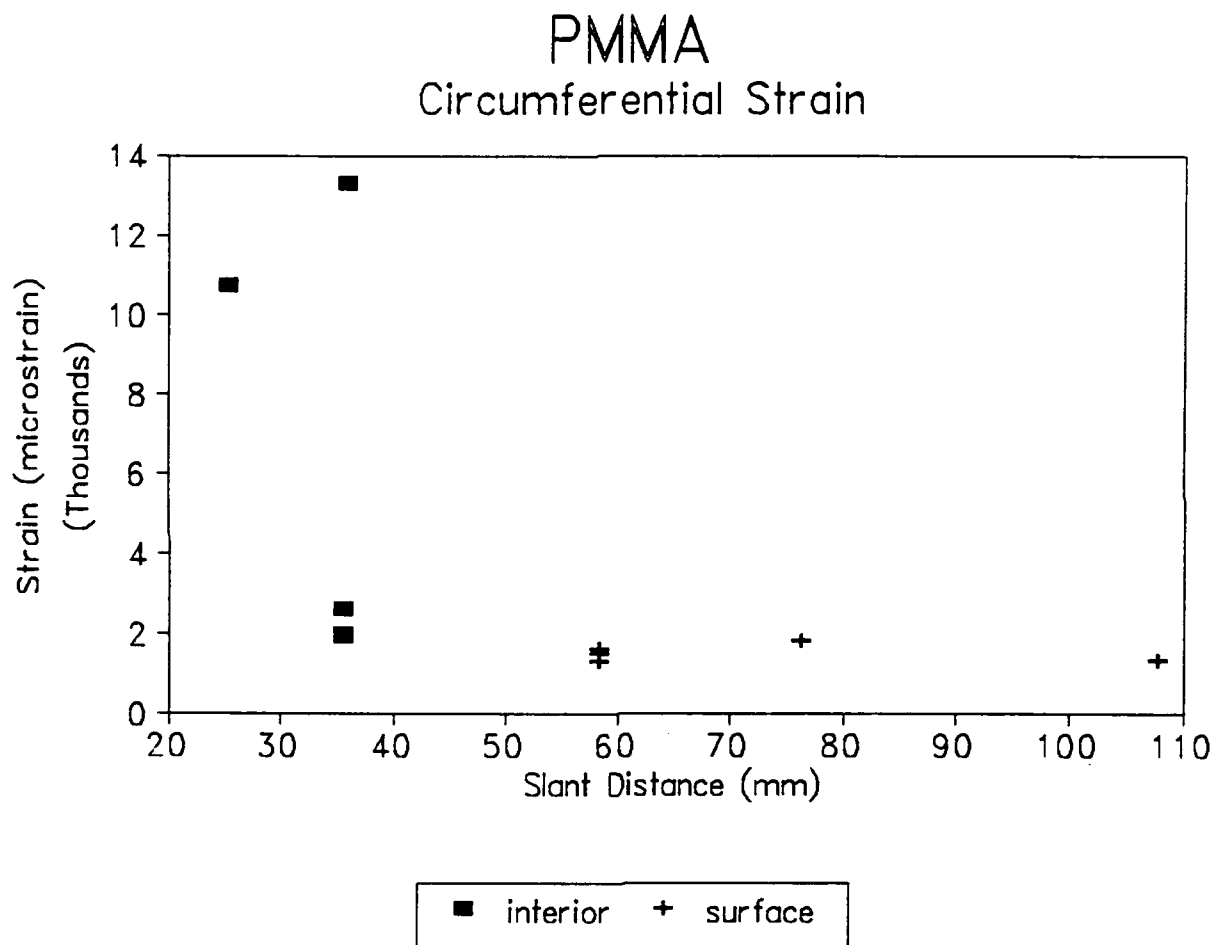


Figure 2.3. Peak circumferential strains for the PMMA model tests.

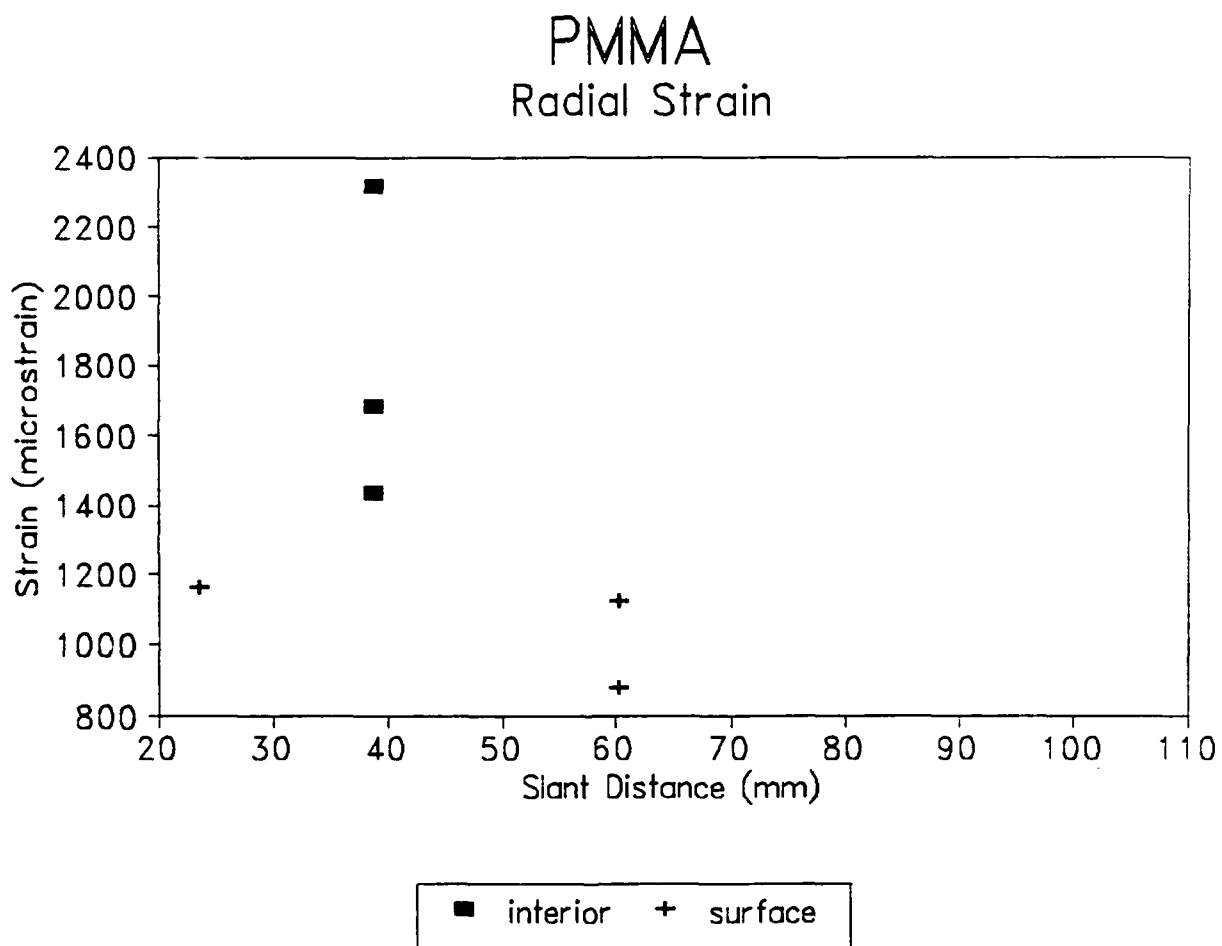


Figure 2.4. Peak radial strains for the PMMA model tests.

(2.5)

probably similar to the epoxy. Several thick one-dimensional models were constructed to investigate the crack initiation and propagation process using the Cranz-Schardin camera. As with the mica flakes, the gages were oriented to produce profiles that were flat, edge-on and end-on to the radially propagating stress wave. The strain signals were recorded as the P- and S-waves traversed the gages. Figure 2.5 is a diagram of the model test with Epon 815.

By examining the dynamic photographs taken during the test and correlating the strain signals as a function of time after detonation to the fracture patterns, the cracks formed after a delay of approximately 20 microseconds as the stress wave passed over the flaws. These cracks and the growth of the crack are easily observed in the photographs. Also, a post-mortem examination of the fragments clearly shows imprints of the gages and mica flakes along with some extension of the crack around the flaws.

The strain data for the Epon 815 model tests are plotted in Figures 2.6 and 2.7, where both normal and log-log plots are presented. Both circumferential and radial strain curves indicate decreasing strain with increasing slant distance (straight line distance from the center of the explosive to the gage center) according to a power law form. The strains are reduced by a factor four (20000 to 5000 microstrain) as the distance increases by a factor of two (20 mm to 40 mm). There is more scatter for the circumferential strain data than for the radial strain data. A typical set of signal records from several gages for Test CRT9 is shown in Figure 2.8. The signal records contain several peaks and the first signal peak is considered the initial strain level from the P-wave. Later peaks result from reflections from the free surface, sides, and the bottom boundaries and are affected by crack initiation at the strain gage site.

A log-log plot of the measured peak circumferential and radial strains from the Epon 815 tests indicates the data is well represented by a line. Hence, the peak strains are fit by an equation of the form

$$S = A / d^n$$

where A and n are fitted constants, S = strain in microstrain, and d = slant distance in mm. A least squares fit of the circumferential strain data produced the strain equation given by

$$S = 3748000 / d^{1.76}.$$

Similarly a least squares fit to the radial strain data produced an equation given by

$$S = 5514000 / d^{1.73}.$$

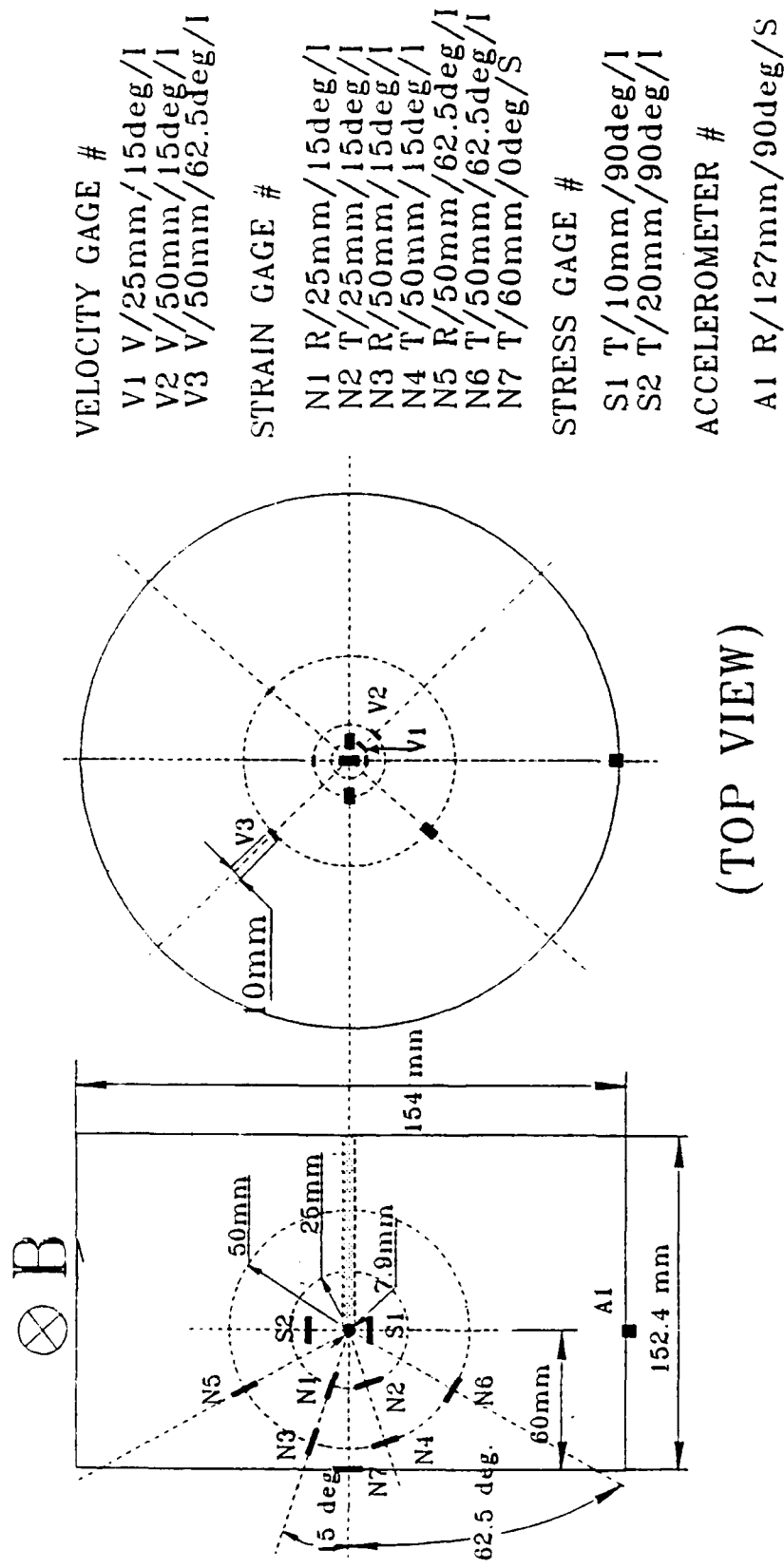


Figure 2.5. Diagram of a typical model test using Epon 815 epoxy.

EPON 815

Circumferential Strain

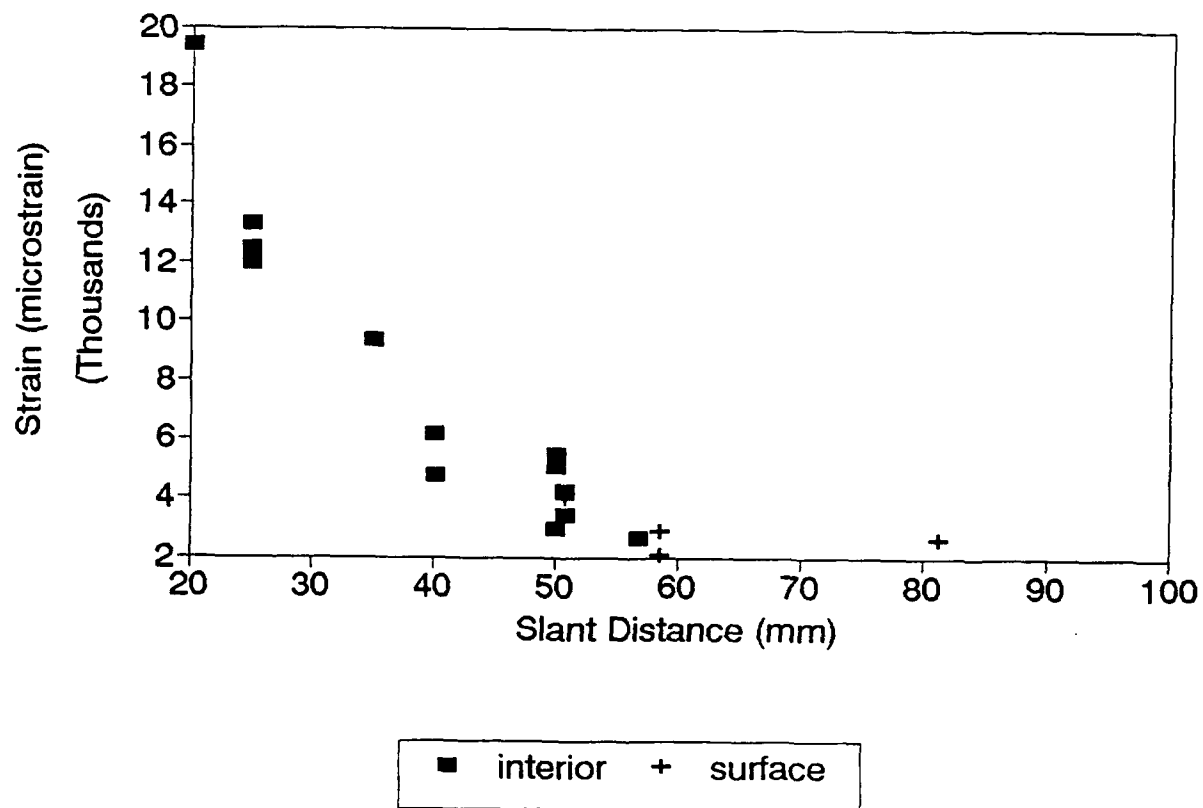


Figure 2.6a. Peak circumferential strains for the Epon model tests.

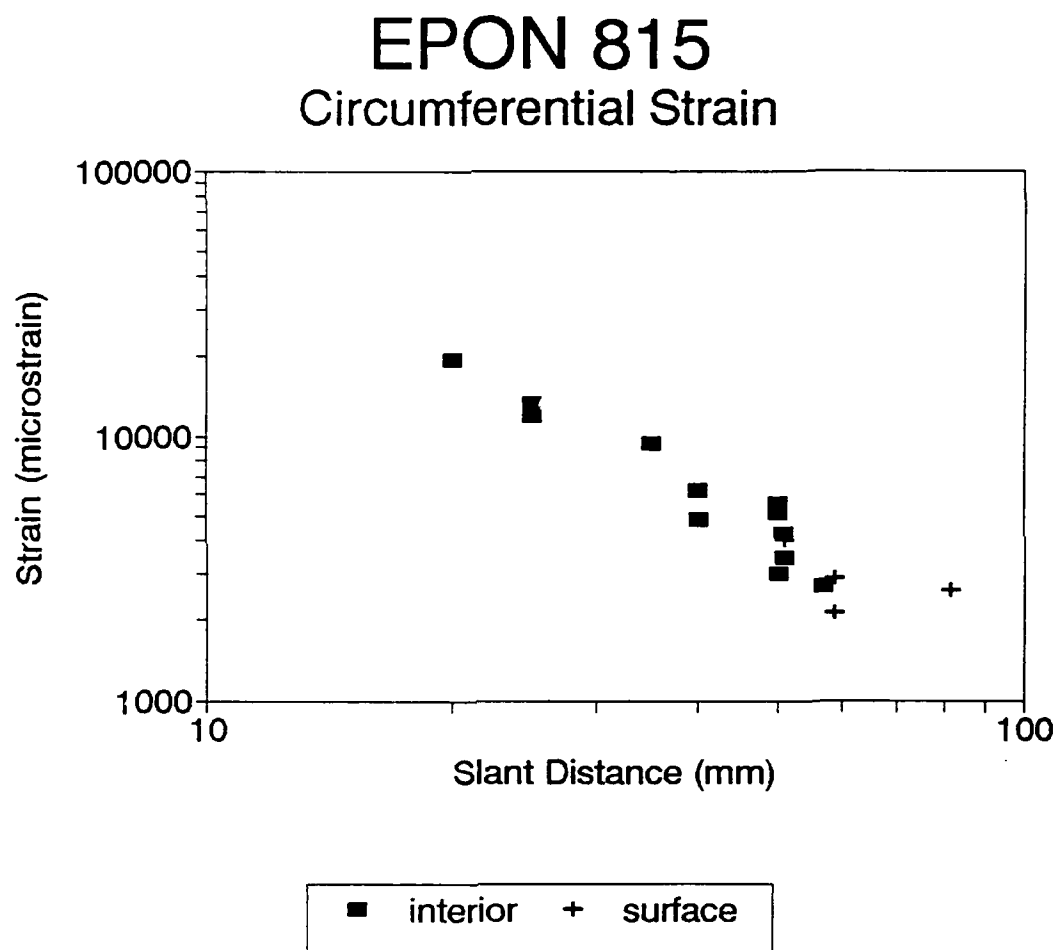


Figure 2.6b. Log-log plot of the strain data in Figure 2.6a.

EPON 815

Radial Strain

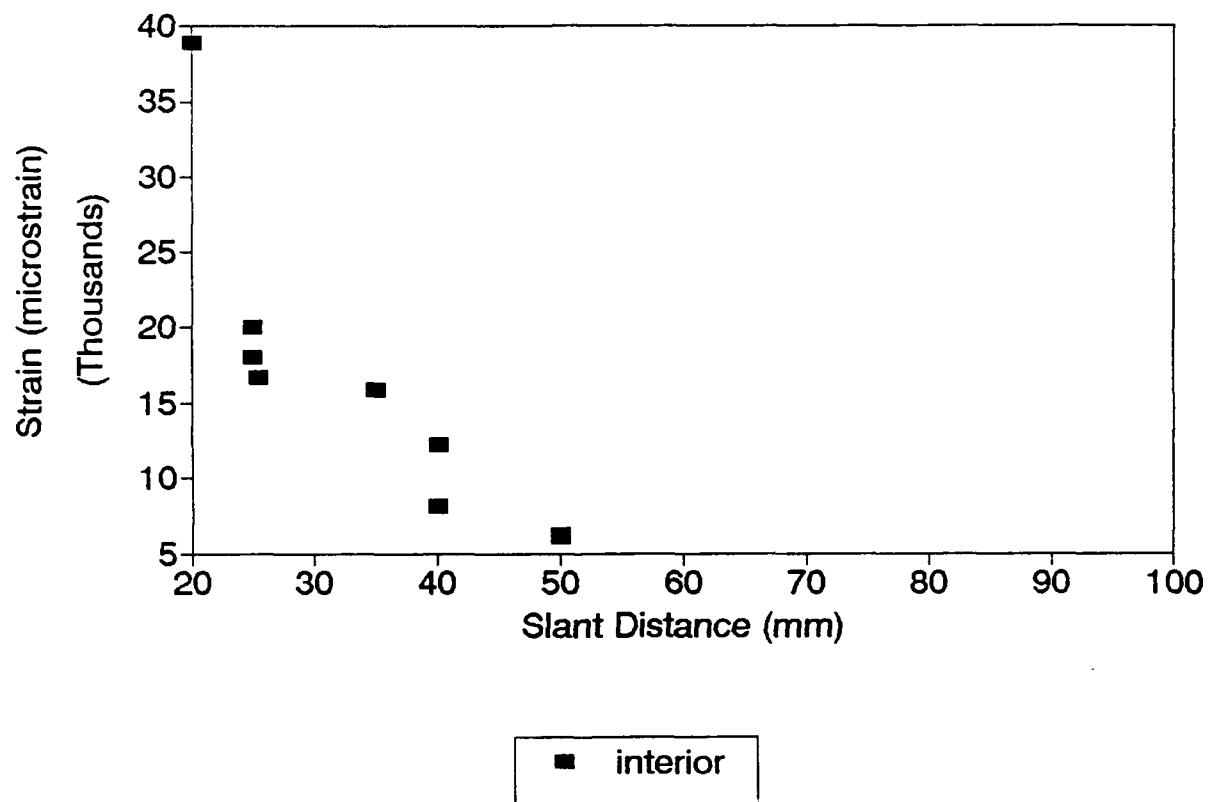


Figure 2.7a. Peak radial strains for the Epon model tests.

EPON 815

Radial Strain

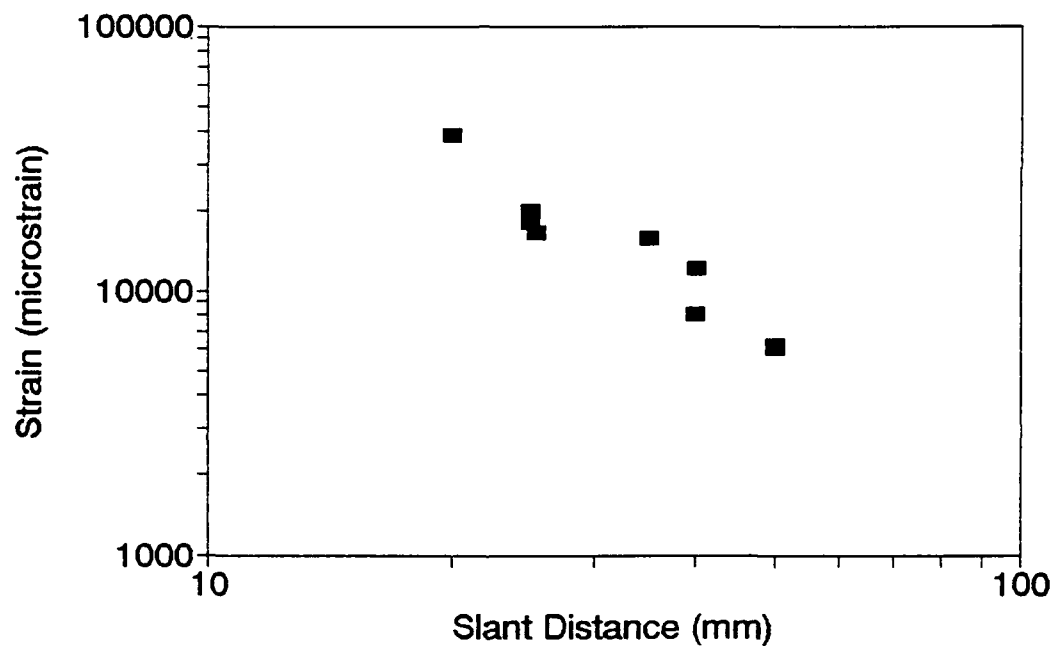


Figure 2.7b. Log-log plot of the strain data in Figure 2.7a.

CRATER TEST 9, MAY 25, 89

10"×10"×6", pt charge, 350mg, stemming

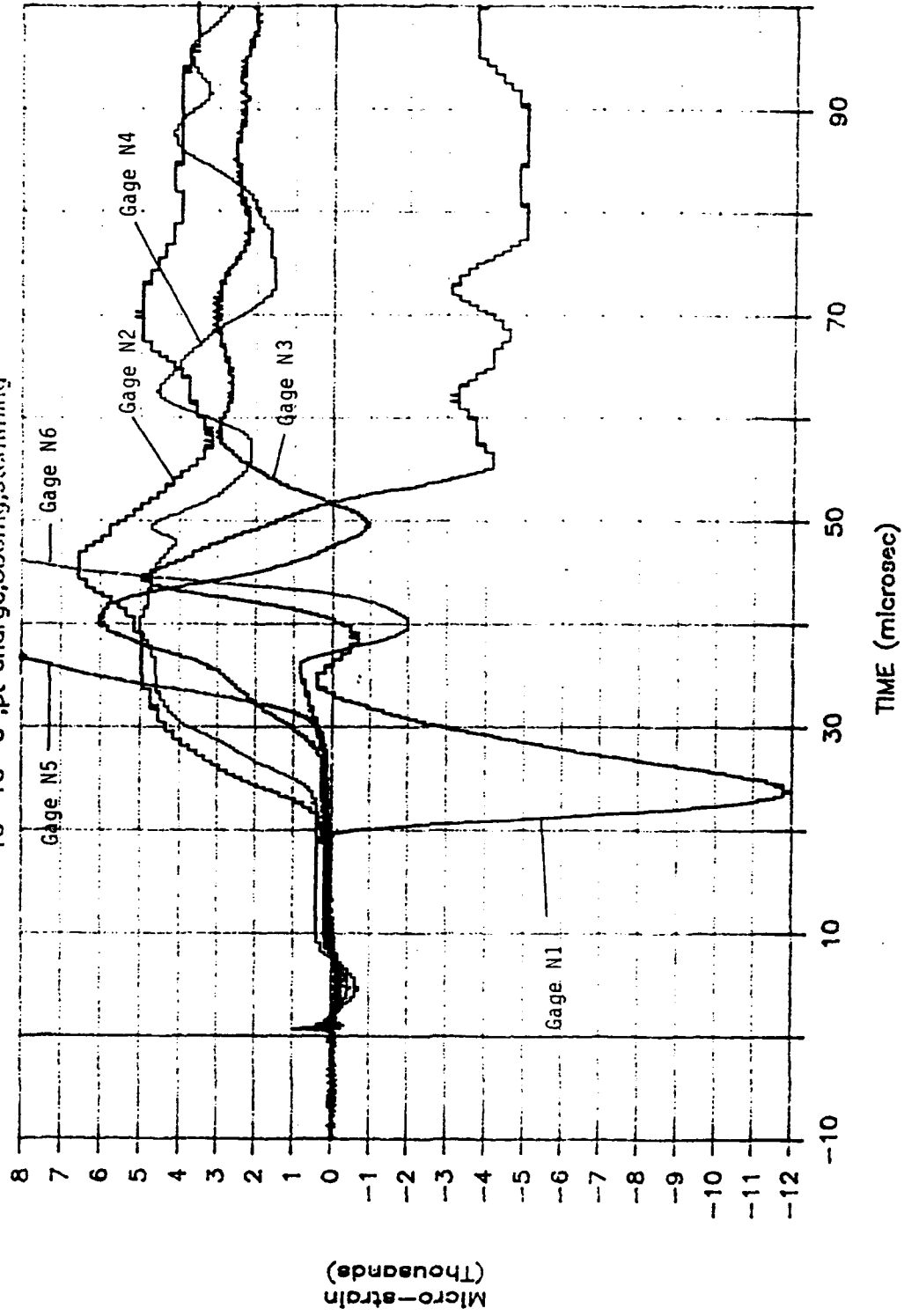


Figure 2.8. Composite of the strain records from Test CRT9.

(2.6)

These data include both interior and surface strain values. The circumferential and radial strains attenuate in a comparable fashion as indicated by the values for the exponent but less than the expected value of $n = 2$.

The velocity gage records for Test CRT13 were integrated to calculate the displacement (both radial and circumferential) and the strain magnitudes to compare with the strain gage measurement results. Figures 2.9a and 2.9b are plots of the radial and circumferential strains versus time from the integrated velocity gage signals. At 25 mm slant distance the measured peak radial strain from the strain gage was 20,000 microstrain and 14,000 microstrain from the velocity gage record. The corresponding peak circumferential strains were 12,500 and 9000 microstrain from the strain gage and the electromagnetic gage, respectively. The average peak radial strain at a 50 mm slant distance was 6200 microstrain as measured from the strain gage and 6500 microstrain from the electromagnetic gage. The average peak circumferential strain at 50 mm slant distance was 4000 microstrain from the strain gage and 2000 microstrain from the velocity gage. It is reassuring to know that the measurement of the explosively produced strains in the radial and circumferential directions by two very different methods is in good agreement.

The arrival times of the later signals have significance, but the strain values are probably inaccurate. This conclusion is based on the results from the model tests conducted in the Cranz-Schardin camera. The photographs from these special Epon models containing embedded strain gages and mica revealed that fractures were initiated from the site of every strain gage and flake approximately 15 to 20 microseconds after the passage of the P-wave. The fractures arrested after propagating a few millimeters, however by then the strain gage had separated, at least partially, from the Epon matrix material. Post-test observations of the model also revealed the presence of fractures from the gage and small flaw sites. As a consequence, the strain levels after the initial peak are considered inaccurate.

A few tests were instrumented with pressure gages to measure stress near the explosive. Carbon or manganin piezoresistive pressure gages were placed from 8 to 25 mm from the explosive center to measure the compressional wave amplitude. These measurements were difficult to accomplish because the gage and/or gage leads broke during the transit of the shock wave. The response of the manganin gage is small at low pressures and hence, measurements in the 2000 MPa range are not reliable. On the other hand the carbon gage is sensitive at low stress amplitudes and these data are credible. Since the gages were close-in the diverging wave at those ranges produced unwanted and unknown strain effects on the gage and compromised the measurements. However, some stress levels were measured that seem reasonable (the carbon gage results). Table 3 is a list of these measurements. The

Table 3. Stress gage measurements.

Test id/gage	PETN (mg)	Gage	Material	Range (mm)	Signal time (musec)	Stress (MPa)
CRT9/1	350	manganin	Epon	12.7		2000
CRT9/2		manganin	Epon	25.4	26.3	1500
CRT12/1	350	carbon	Epon	8	3.7	1750
CRT12/2		carbon	Epon	15	5.7	1000
CRT15/5	350	manganin	Epon	25	31.3	330
RT11/1	1000	carbon	cement	12.7		
RT11/2		50 ohm		12.7		
RT12/1	1000	carbon	cement	12.7		
RT12/2		carbon		19.5		
RT12/3		carbon		25.4		
RT12/4		carbon		38.1		
RT13/1	1000	carbon	cement	12.7		
RT13/2		carbon		25.4		

AFOSR - Mechanisms of Fragmentation

Crater Test 13 - Epoxy Resin

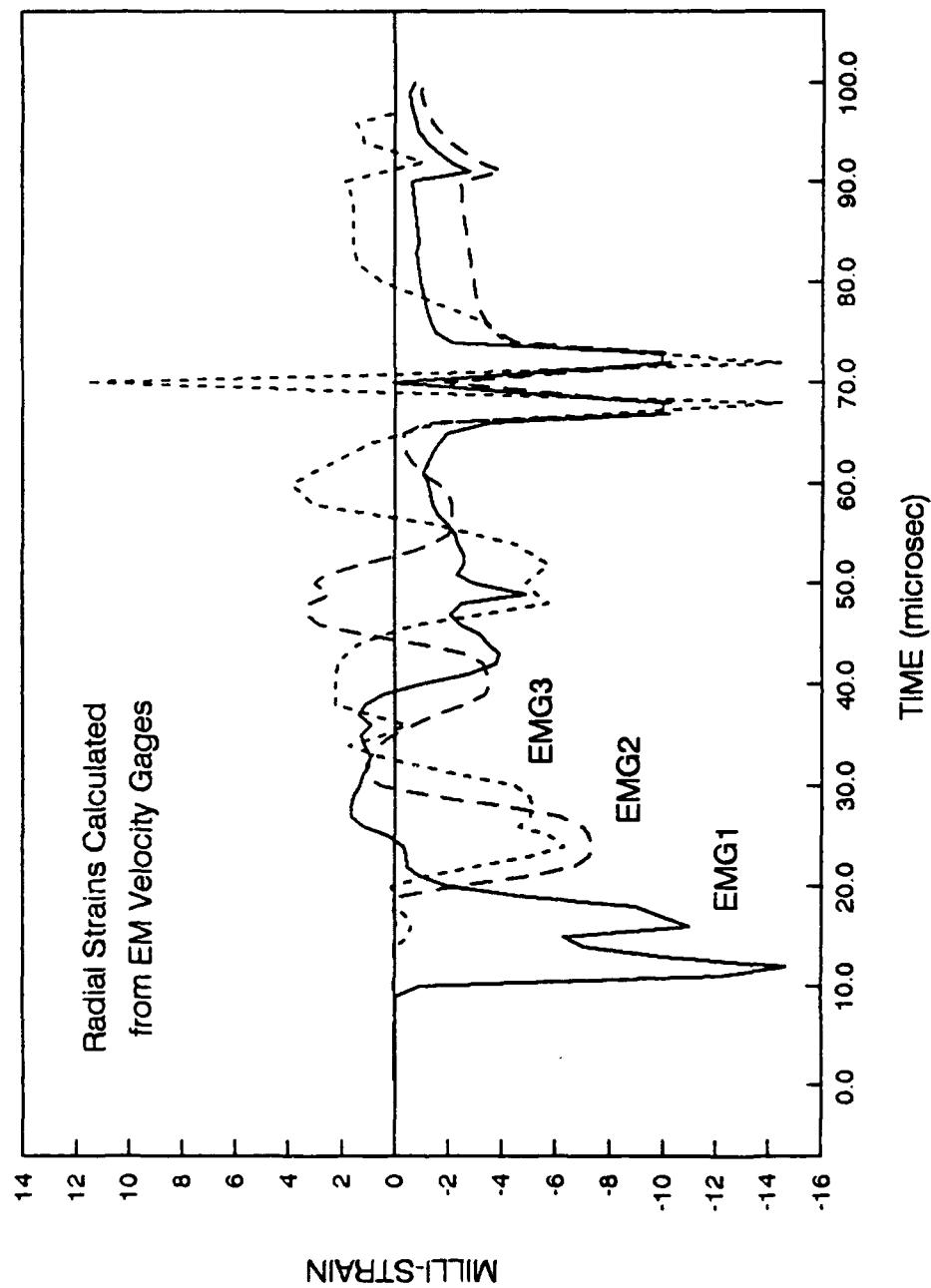


Figure 2.9a. Radial strains calculated from the electromagnetic gages from Test CRT13.

AFOSR - Mechanisms of Fragmentation
Crater Test 13 - Epoxy Resin - Tangential Strains

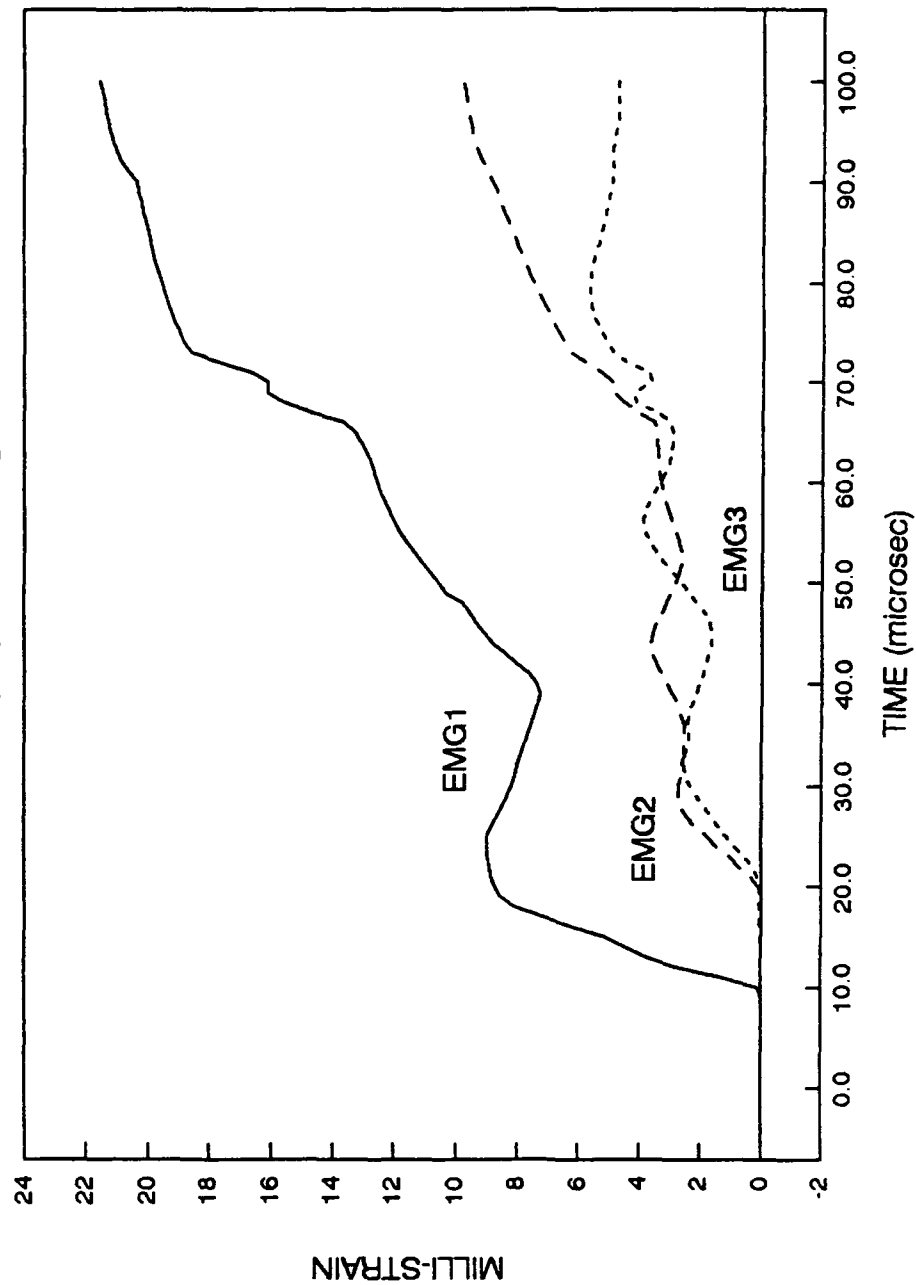


Figure 2.9b. Circumferential strains calculated from the electromagnetic gages from Test CRT13.

(2.7)

configuration of all tests were very similar and as a result particle velocity measurements from Test CRT13 and the P-wave velocity measurements provided sufficient data to compute the stress amplitude from the Hugoniot "jump conditions" to compare with the stress measurement. The equation has the form

$$P = \rho_0 U_s U_p = 147 \text{ MPa}$$

where $\rho_0 = 1200 \text{ kg/m}^3$ (initial density), $U_s = 3500 \text{ m/s}$ (shock velocity), and $U_p = 36 \text{ m/s}$ (particle velocity) from Test CRT13 at the 25 mm location. The measured stresses from the carbon gages in Epon 815 Test CRT12 were 1750 MPa at 8 mm and 1000 MPa at 15 mm. A crude extrapolation of these data to 25 mm indicates a stress of about 200 MPa which is in reasonable agreement with 147 MPa from the Hugoniot calculation. The other stress measurements in Table 3 are, however, in poor agreement with this comparison.

Two tests were conducted to determine the attenuation of the P- and S-waves as function of range and to measure the crack propagation velocity. A bonus was realized from the test in that the velocity of formation of the crater was also measured. These Epon 815 models were 254 by 254 mm and 50.8 mm thick and contained a 350 mg PETN charge at the center. The Cranz-Schardin framing camera was then used to produce high speed photographs of the propagating stress waves and fractures by photoelastic means. These were the same set of tests used to investigate the ability of an embedded strain gage to act as flaw site from which cracks originated. The high speed photographs showed the P- and S-waves propagating from the detonating explosive, the initiation and propagation of radial cracks, and the changing fringe pattern. The P-wave, identified as a concentration of fringe patterns on the photograph, is formed by the shock loading of the model material from the detonated explosive. Since the S-wave is slower it is observed at a later time on the photographs. The P-wave velocity was measured and was found to decrease from 3360 m/s to 2440 m/s or about 33% over a range of 150 mm while the S-wave velocity was found to decrease from 2450 m/s to 1800 m/s, also about 33%, over a range of only 20 mm. Fracture propagation measured over a distance of 50 mm had an average velocity of 500 m/s or about 15 - 20% of the P-wave speed and about 25% of the S-wave speed. From the high speed photographs of the Epon 815 model tests the radial cracks appeared to initiate first and to start to propagate a few microseconds after detonation. The cracks that eventually outlined the crater was visible early in the photographs and from this data the progress of the crater was measured. The crater was observed to form about 11 microseconds after explosive detonation and to initially propagate at a speed of 1800 m/s. 200 microsecond later in the process the speed decreased to about 350 m/s. By this time the fracture surface defining the crater had reached the free surface.

There was little reproducibility in the crater and fragmentation results from the CRT-series of transparent model tests. The same pattern was observed in terms of the number of major fractures formed. Table 1 lists crater parameters determined for this series of tests. There are several reasons for the inconsistency. (1) The explosive was buried too deeply to produce good crater data in most of the tests. (2) Fractures terminated at interfaces and joints. (3) Model size was too small causing the radial fractures to cleave the model before a crater had developed completely.

C. Fragmentation in Cement Models.

The second major series of fracture and fragmentation tests were conducted in models that simulated geologic materials in terms of porosity, strength, density, natural flaws, and micro-structure. Electromagnetic velocity gages were emplaced to measure the particle velocity in the radial and vertical directions in these three dimensional models. The materials used were Rockite grout, cement, super cement, Hydrostone, and Hydrocal. The latter two materials were used to study the effects of joints in large models and the results are discussed in Chapter 6.

A Rockite grout (Hartline Products, Cleveland, Ohio) was selected as the starting material because of its high strength and rapid curing rate. The specimens were cast from low-water Rockite mix, from a low water Rockite plus sand mix, and from a Rockite-sand mix which was dry compacted prior to immersion in water for curing. All specimens were constructed in a cylindrical shape 254-mm diameter by 152-mm or 178-mm thick.

The mixture for the first two models was a low-water mix composed of 14 kg of Rockite and 4 kg of water. The mix was poured into a mold on a vibrating table to float the bubbles to the surface to reduce the porosity (about 30 %). In one model velocity gages in the form of complete copper wire loops were cast in the Rockite to measure the particle velocity in the radial direction. In the other model test, 25-mm long copper wire lengths were cast in place to measure the particle velocity along the Z-axis (vertical direction). Figures 2.10a and 2.10b are diagrams of these test configurations. These are typical arrangements for the other geologic simulant tests as well.

The third and fourth specimens were made from a Rockite-sand mix to reduce the porosity further and were compacted differently. For one model, 7.0 kg of the grout was dry mixed with 7.0 kg each of 10-20 quartz sand and 3.0 kg of water was added to make a viscous paste. The mix was poured into the mold and vibrated. The other model was made by dry compacting the Rockite-sand mix in a 150,000 lbf load machine to reduce the porosity. The mix proportions were 7.0 kg of Rockite and 7.0 kg of quartz sand.

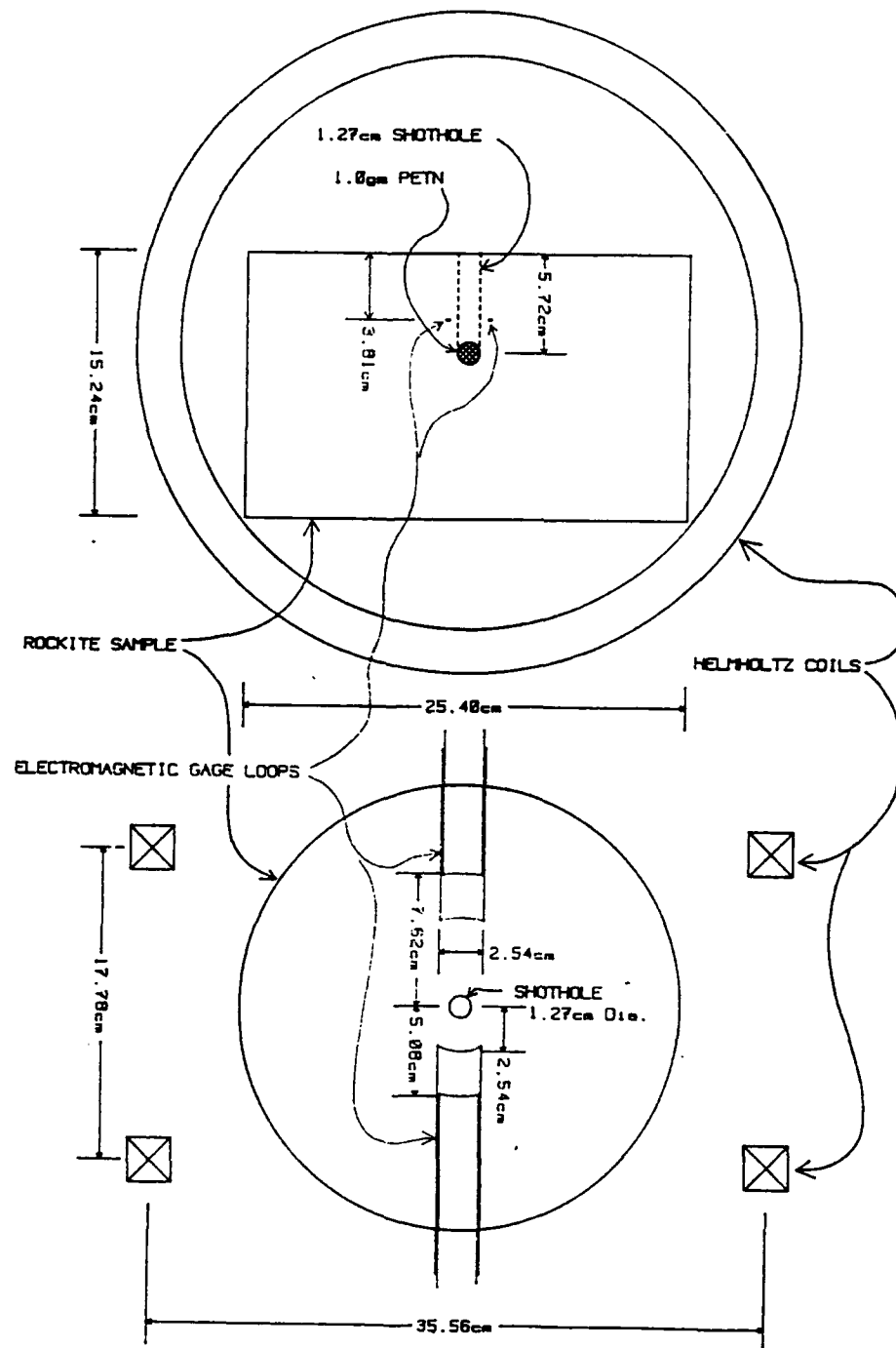


Figure 2.10a. Diagram of a typical cement model showing the vertical velocity measurement setup and the spherical charge location.

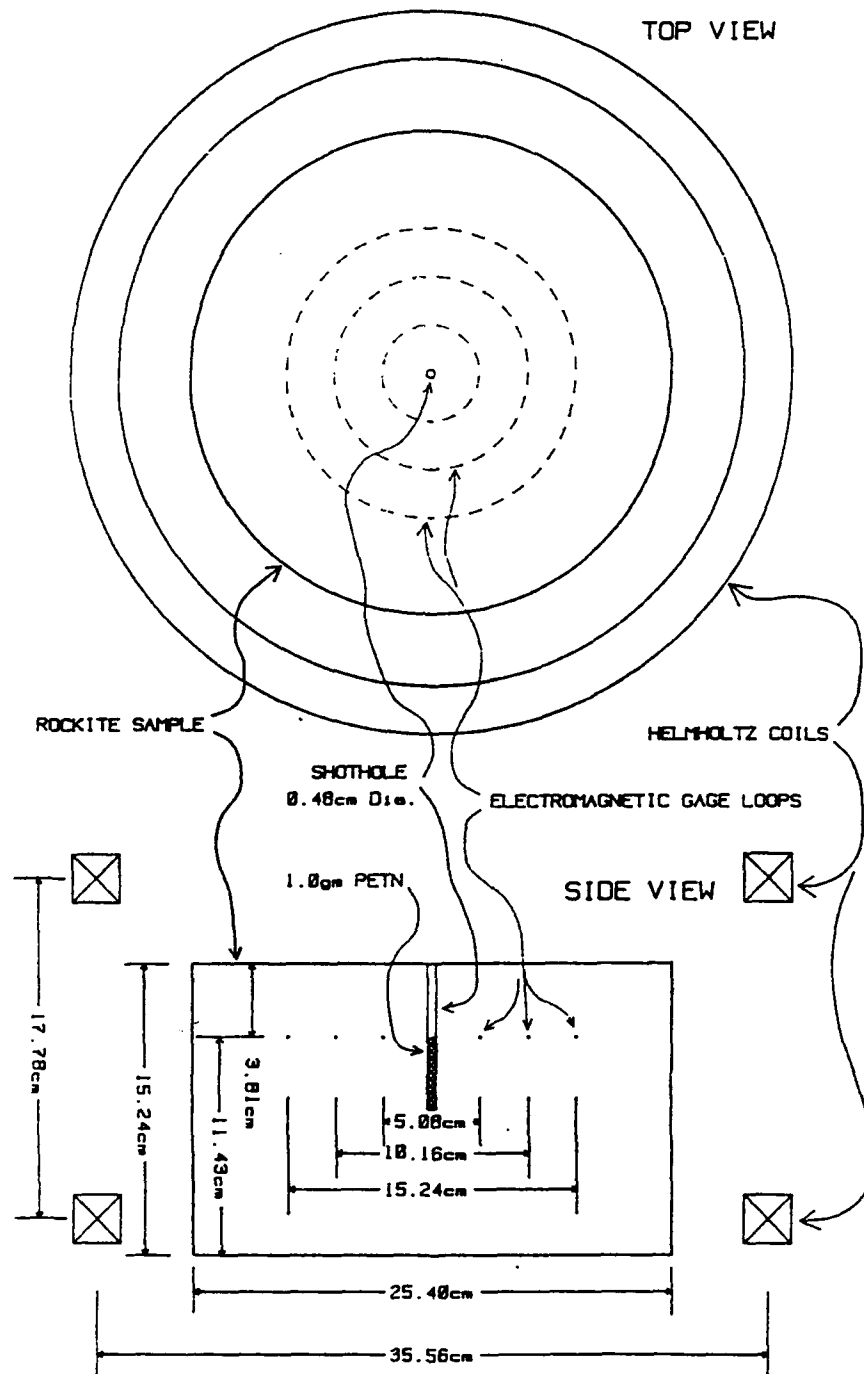


Figure 2.10b. Diagram of a typical cement model showing the radial velocity measurement setup and the cylindrical charge location.

(2.9)

Approximately 2.0 kg of the mix was spread into a cylindrical mold and compacted by 60,000 lbf of force applied to an aluminum and plywood disk sized to fit inside the mold. Nearly all compaction of the dry mix occurred at a load of 20,000 lbf load. Less than five percent additional compaction was obtained by increasing the load to 60,000 lbf. After the first layer was compacted, the next layer was spread and compacted and the process was repeated until the model was completed. The compacted specimen was immersed in water for wetting by diffusion and curing. At the levels where electromagnetic gage loops were installed, the gage loops were oriented on the top surface of the compacted layer before the next layer was spread and compacted.

The fifth and sixth models were constructed from a mixture of fine limestone and Portland cement. In this mix the limestone was thought to provide a better impedance match to the cement phase and the grains to have a more rock-like failure mechanism. In both models velocity gages were cast at known locations to measure vertical velocity.

Finally, super-concrete, a high strength and low porosity cement based grout model, was constructed using the pozzolon technique. Previous work [2.1] indicated a concrete with compression strength three to four times greater than conventional concretes and porosities near 15 % were attainable using these mixing techniques. Conventional Portland cements have high porosity from the natural cement particle size and this porosity is increased by removal of water during the curing process. The pozzolon cement mixture consisted of silica fume (micron size amorphous silicon dioxide in powder form) to fill the void volume, super plasticizer (a surfactant wetting agent) to reduce the amount of water, crushed limestone, and Portland cement. The crushed limestone is a product called Barngrit which is used in the agriculture industry as an anti-skid material in a barnyard. The mold containing the cement mix was placed on a vibrating table to force the entrapped bubbles out before the cement hardened. These cured models had a density near 2000 kg/m³, high strength, and 10 - 20 % pore volume. The total of seven models were cast using these methods. All models were 254-mm diameter by 152-mm high except one model which was 305-mm square by 152-mm high. This last model was used to study the effect of model shape on the fracture pattern and crater size in contrast to the tests results from models with cylindrical geometry. The recipe for the mix is in Table 4.

Radial and vertical velocity measuring wires loops were placed in a "sauna" tube mold at known locations and orientation relative to the explosive charge before the cement mixture was poured in the mold. After the cement had set a 12-mm diameter borehole was drilled from the bottom of the model for the 1000 mg explosive charge. The explosive was perfectly stemmed as was for

Table 4. Super cement recipe.

<u>Material</u>	<u>Amount by Weight (g)</u>
Barngrip	1000
Portland Cement I	400
Silica Fume	120
Rheobuild	6
Water	200

(2.10)

the transparent models. Sand and clay was used to stem the borehole from the charge to the end of the borehole at the bottom of the model away from the free surface defined by the test. To study source geometry effects, both cylindrical and spherical charge geometries were placed in the models. Explosive initiation was similar to the method used for the transparent model tests. Each model was placed in a magnetic field arising from a Helmholtz coil and oriented to measure either radial or vertical velocity.

Table 5 documents the results of the particle velocity measurements from all of the rock simulant tests and one test conducted in a transparent model. The data encompasses the slant distance from the explosive center to the gage location, angle between the cylindrical axis and the gage, measured velocity, and resultant velocity. The resultant velocity, V_r , was calculated from

$$V_r = V_m / \cos \theta$$

where V_m = measured velocity and θ = gage angle relative to the vertical axis.

Normal and log-log plots of the measured radial particle velocity as a function of slant distance are shown in Figures 2.11a and 2.11b and normal and log-log plots of the resultant radial particle velocity are shown in Figures 2.12a 2.12b. These data include the velocities obtained in Rockite, cement, and super cement. All the tests were conducted using 1000 mg of PETN except for one. As can be seen from the figures, the radial particle velocity decays as the slant distance increases. The calculated resultant velocity has more scatter than the measured velocity as observed from the plots. A log-log plot of the measured velocity data was done to determine the fit to a power law form. The equation representing the measured radial velocity data is given by

$$V_m = 7210 / d^{1.71}$$

where d = slant distance in mm. The equation representing the resultant radial velocity data is given by

$$V_r = 1870 / d^{1.26}$$

The attenuation as a function of distance specified by the exponent is less than the expected value of two.

Normal and log-log plots of the measured vertical particle velocity as a function of slant distance are shown in Figures 2.13a and 2.13b and normal and log-log plots of the resultant vertical particle velocity are shown in Figures 2.14a and 2.14b. The data have considerable scatter foreboth the measured and the

Table 5. Radial and vertical velocity gage results in Rockite, cement, and Epon 815.

Test id/gage	Model/ PETN	Charge geom	Slant dist (mm)	Angle from vert (deg)	Meas peak vert vel (m/s)	Result peak vert vel (m/s)	Meas peak rad vel (m/s)	Result peak rad vel (m/s)
RT1/1	Rockite/	cyl	25.4	90			34	34
RT1/2	950mg		50.8	90			9	9
RT1/3			76.2	90			5	5
RT2/1	Rockite/	Sph	31.8	53.1	10.5	17.5		
RT2/2a	1000mg		54.3	69.4	2.2	6.3		
RT2/2b			54.3	69.4	2.2	6.3		
RT2/3			78.6	75.9	0.8	3.3		
RT3/1	Rockite	Sph	37.2	43.1	13.3	18.2		
RT3/2	mix/		49.3	31	10.7	12.5		
RT3/3	1000mg		57.5	61.9	3	6.4		
RT3/4			66	50.3	0.2	0.3		
RT4/1	Rockite	Sph	37.2	43.1	11	15.1		
RT4/2	mix/		49.3	31	9	10.5		
RT4/3	1000mg		57.6	61.9	4.2	8.9		
RT4/4			66	50.3	2	3.1		
RT5/1	Cement	Sph	37.2	43.1	8.9	12.2		
RT5/2	large		49.3	31	6	7		
RT5/3	limest/		57.6	61.9	2	4.2		
RT5/4	500mg		66	50.3	1.9	3		
RT5/5			80.9	70.4	1	3		
RT5/6			87.1	61	0.8	1.7		
RT6/1	Cement	Sph	37.2	43.1	11.2	15.3		
RT6/2	small		49.3	31	9.9	11.6		
RT6/3	limest/		57.6	61.9	4.1	8.7		
RT6/4	1000mg		66	50.3	7.2	11.3		
RT6/5			80.9	70.4	1.3	3.9		
RT6/6			87.1	61	2.3	4.7		
RT7/1	Super	Cyl	25.4	90			35	35
RT7/2	cement/		31.8	41.6			25	37.7
RT7/3	1000mg		45.9	56.3			12	14.4
RT7/4			54.3	25.6			9	20.8
RT7/5			63.6	36.9			8	13.3
RT7/6			85.2	26.6			5	11.2
RT8/1	Super	Cyl	25.4	90				
RT8/2	cement/		31.8	36.9	12	15		
RT8/3	1000mg		45.9	56.3	4.5	8.1		
RT8/4			54.3	20.6	4	4.3		
RT8/5			63.6	36.9	2.3	2.9		
RT8/6			85.2	26.2	1.5	1.7		
RT9/1	Super	Sph	25.4	90				
RT9/2	cement/		31.8	36.9	9.5	11.9		
RT9/3	1000mg		45.9	56.3	9	16.2		
RT9/4			54.3	20.6				
RT9/5			63.6	36.9	4	5		
RT9/6			85.2	26.6	1.5	1.7		
RT10/1	Super	Sph	25.4	90			30	30
RT10/2	cement/		31.8	36.9			12	20
RT10/3	1000mg		45.9	56.3			5	6
RT10/4			54.3	20.6			5	14.2
RT10/5			63.6	36.9			5	8.3

RT10/6			85.2	26.6			3	6.7
RT11/1	Super	Sph	45.8	123.7				
RT11/2	cement/		31.7	143.1				
RT11/2'			31.7	143.1				
RT11/3	1000		25.4	90				
RT11/4			31.7	53.1				
RT11/5			45.8	33.7				
RT11/5'			45.8	33.7				
RT12/1	Super	Sph	31.8	53.1				
RT12/2	cement/		31.8	143.1				
RT12/3	1000		45.8	33.7	11.2	13.5		
RT12/4			45.8	123.7	9.9	11.9		
RT13/1	Super	Sph	31.8	53.1				
RT13/2	cement/		54	69.4	2.2	6.3		
RT13/3	1000		45.8	33.7	7.1	8.5		
RT13/4			45.8	53.1	9.7	16.2		
RT13/5			31.8	143.1				
CRT13/1	Epon/350	Sph	25	15	35	36.2		
CRT13/2			50	15	17.5	18.1		
CRT13/3			50	62.5	7	15.2		

Rockite/Cement Radial Velocity

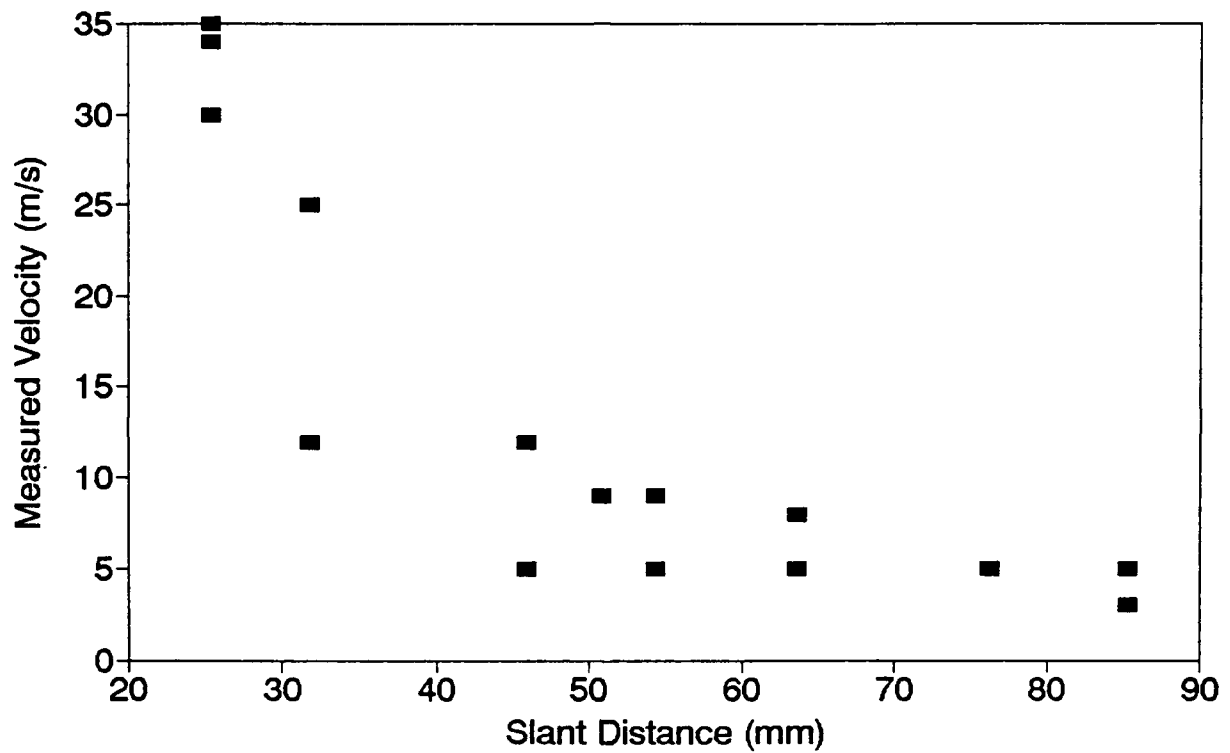


Figure 2.11a. Measured peak radial velocity from all the rock simulant model tests.

Rockite/Cement Radial Velocity

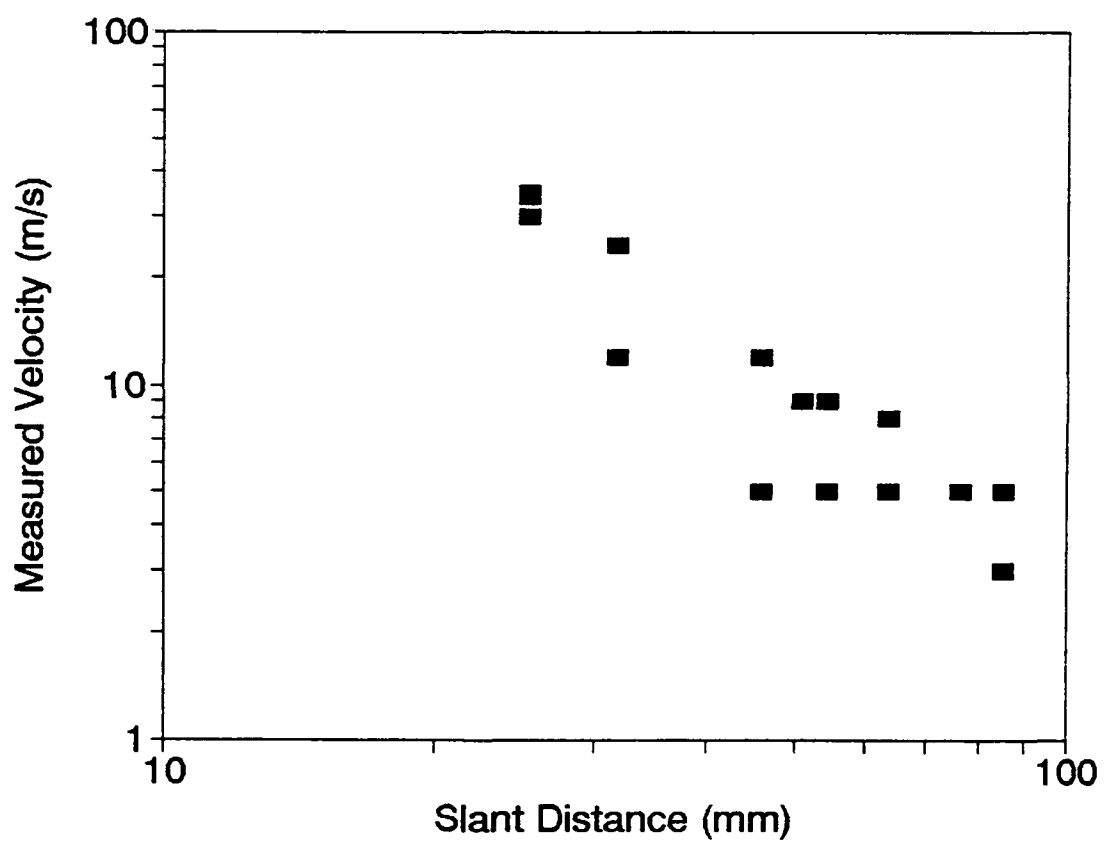


Figure 2.11b. Log-log plot of the velocity data in Figure 2.10a.

Rockite/Cement Radial Velocity

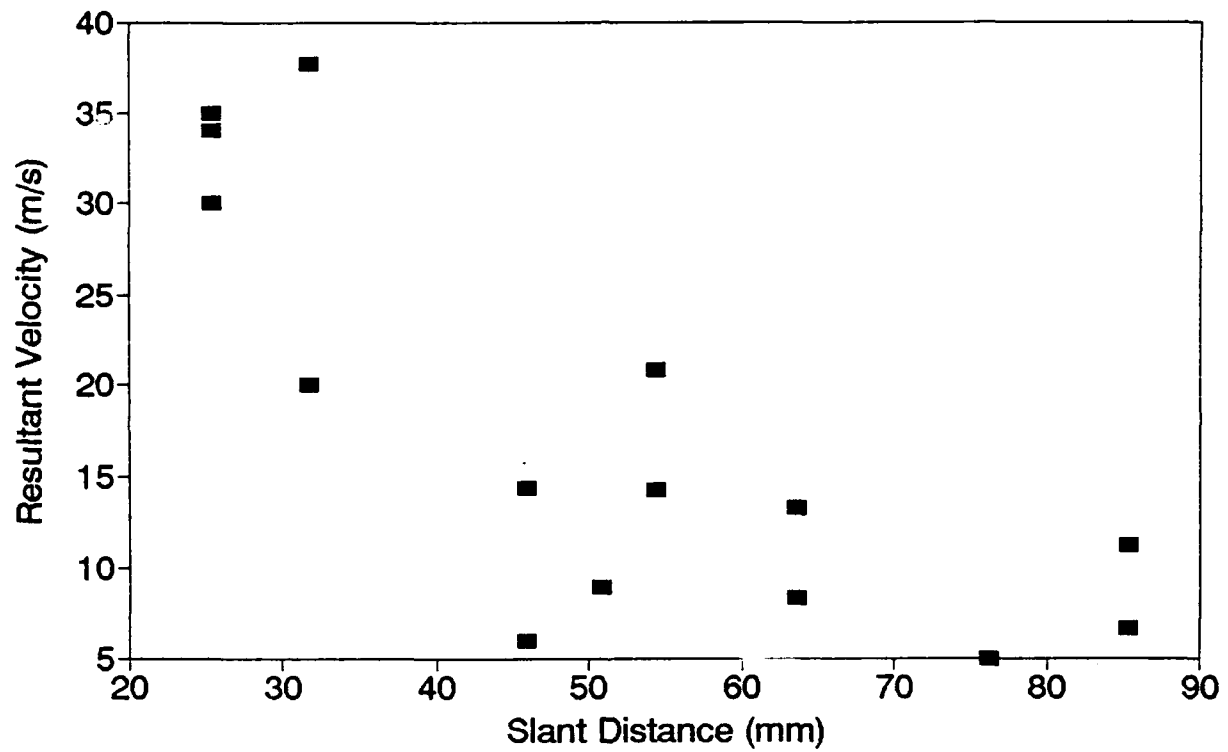


Figure 2.12a. Resultant peak radial velocity plot.

Rockite/Cement

Vertical Velocity

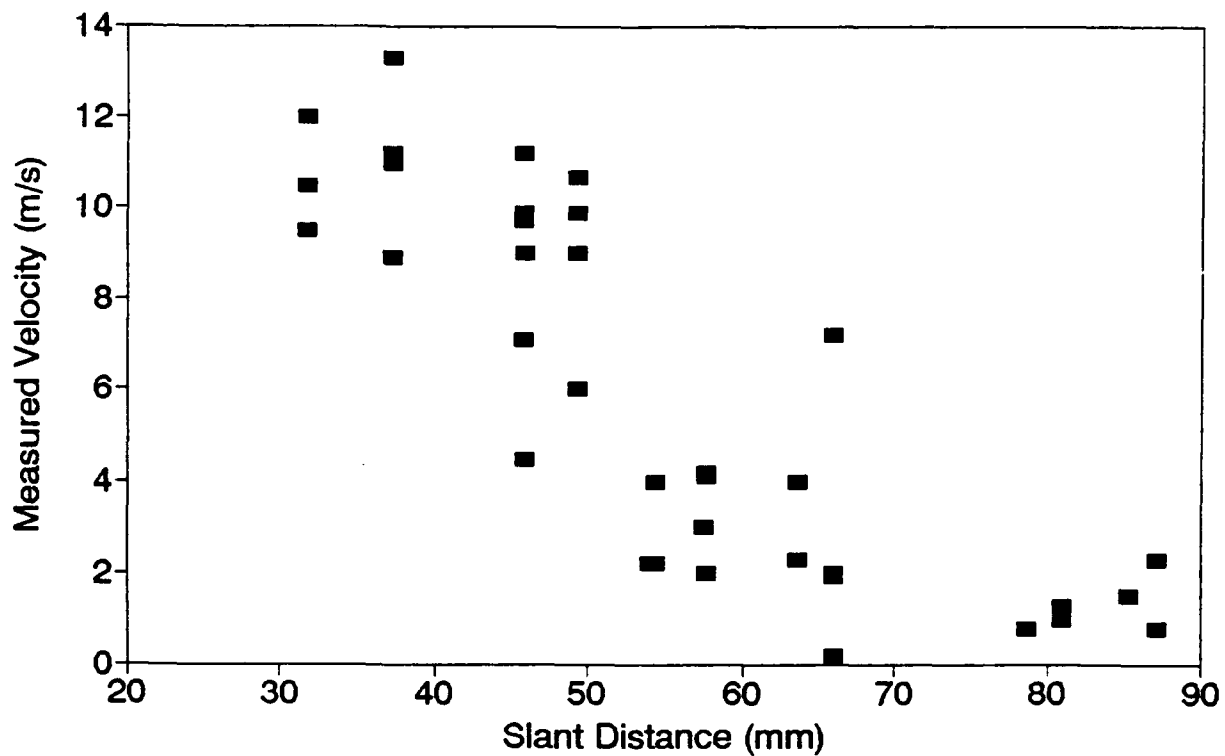


Figure 2.13a. Measured vertical velocity from all the rock simulant model tests.

Rockite/Cement Vertical Velocity

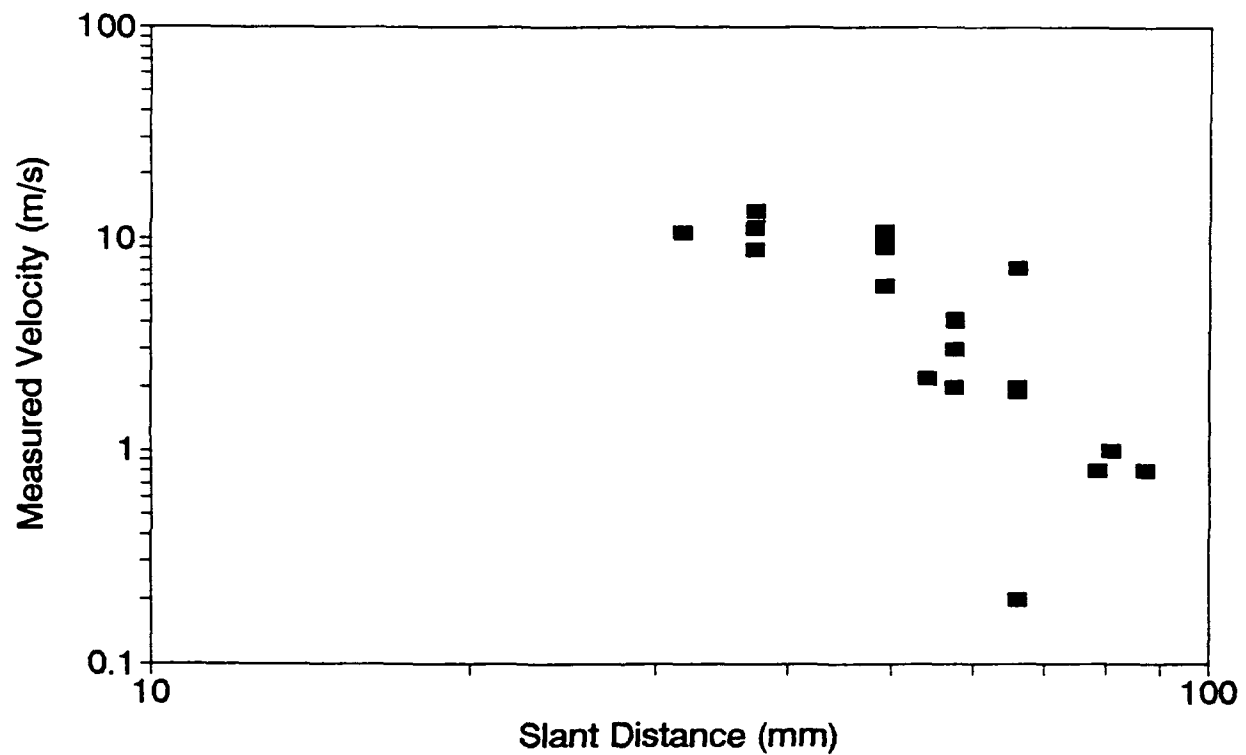


Figure 2.13b. Log-log plot of the velocity data in Figure 2.12a.

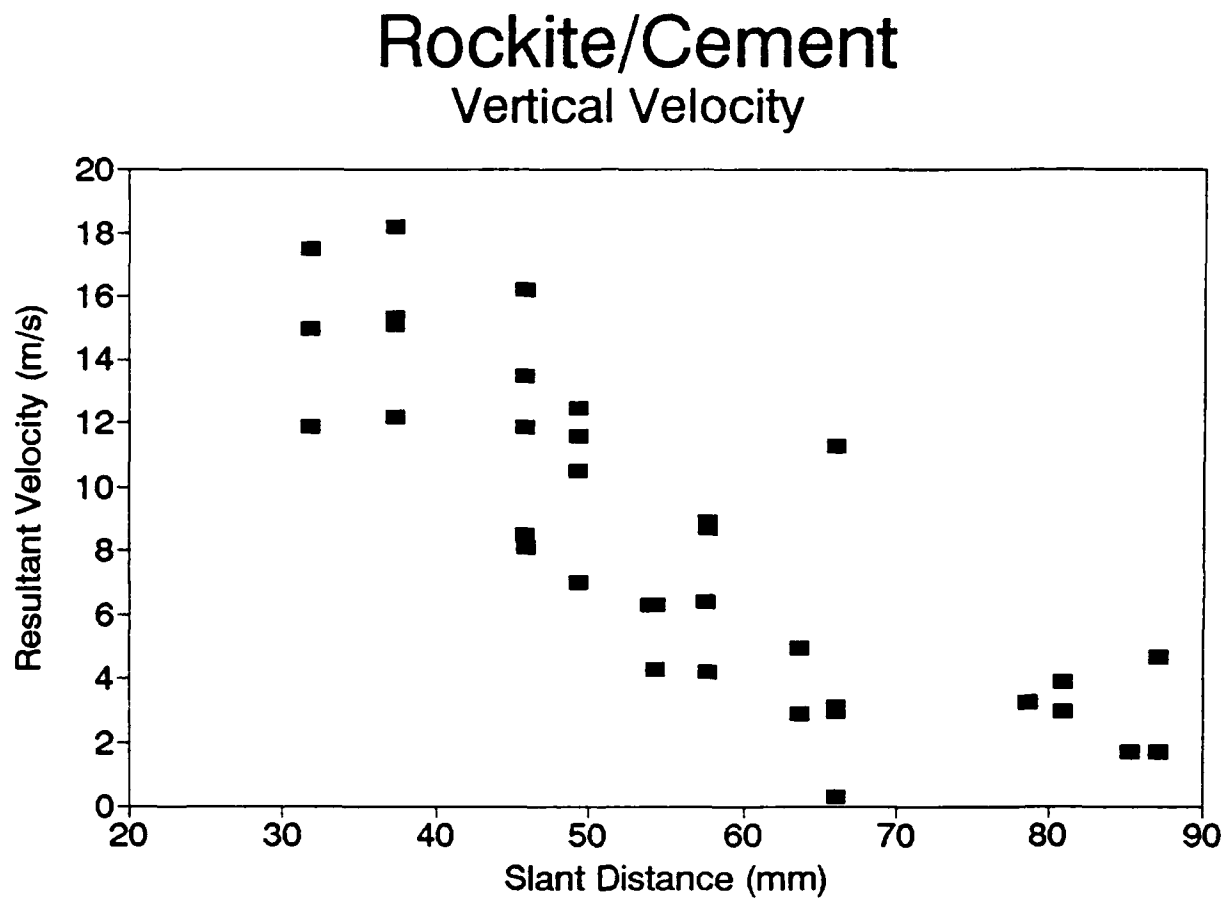


Figure 2.14a. Resultant peak vertical velocity plot.

Rockite/Cement

Vertical Velocity

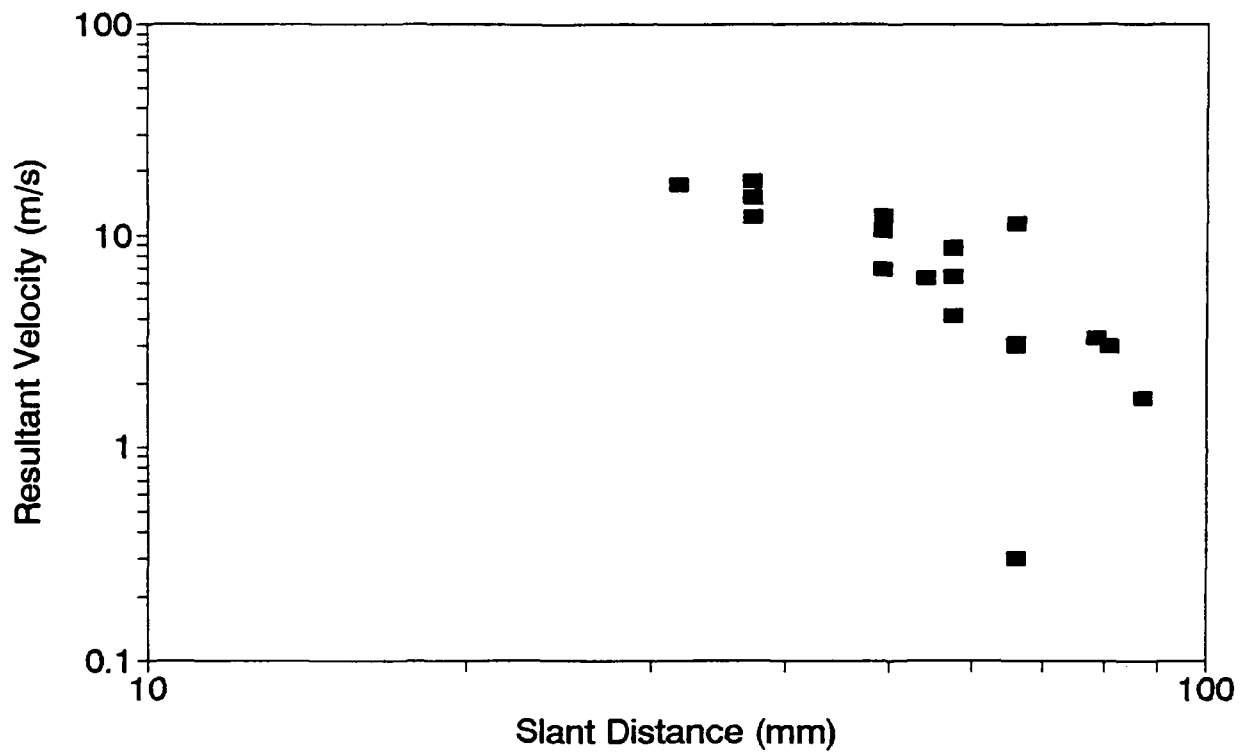


Figure 2.14b. Log-log plot of the velocity data in Figure 2.13a.

(2.11)

calculated resultant vertical velocities. A log-log plot was prepared to determine the exponent of the power law form and the coefficient. The equation describing the measured vertical velocity data is given by

$$V_{vm} = 230100 / d^{2.74}.$$

The equation representing the resultant vertical velocity is given by

$$V_{vr} = 54800 / d^{2.26}.$$

The attenuation in this case is greater than the expected value of two. The exponents for the radial and vertical velocity measurements are not in good agreement.

The measured radial and vertical velocity data are plotted together in Figure 2.15 and the resultant velocity data are plotted in Figure 2.16. A linear least squares fit to the data produced equations describing the velocity as a function of slant distance and are given by

$$V_m = 76500 / d^{2.43}$$

$$V_r = 18400 / d^{1.95}$$

where V_m = measured velocity (m/s), V_r = resultant velocity (m/s), and d = slant distance (mm). The attenuation exponent for the measured velocity fit is 20% larger than the expected value of two, the exponent is nearly two for the fit to the resultant velocity data. However, the correlation coefficients for the two fits are only about 0.6, indicating considerable scatter of the data.

Typical velocity gage records from several different tests are shown in Figure 2.17a through 2.17d. Close-in radial velocity gage records are presented in Figures 2.17a and 2.17b to illustrate the similarity in amplitudes and features from a test (Test RT7) with a cylindrical charge and a test (Test RT10) with a spherical charge. The explosive depth-of-burial was the same for both tests. This result is typical and suggests the velocity field is not sensitive to charge geometry, at least for the model geometries, sizes, and materials used in this study. Figures 2.17c and 2.17d are signal records from Test RT12 (spherical charge) illustrating the correspondence between vertical particle velocity gage response at comparable locations above and below the charge. There is a factor of two difference in amplitude during the release phase of the wave propagation sequence. The minimum velocity from the two records, however, occurs at the same time, namely about 130 μ s.

Rockite/Cement Vertical/Radial Velocity

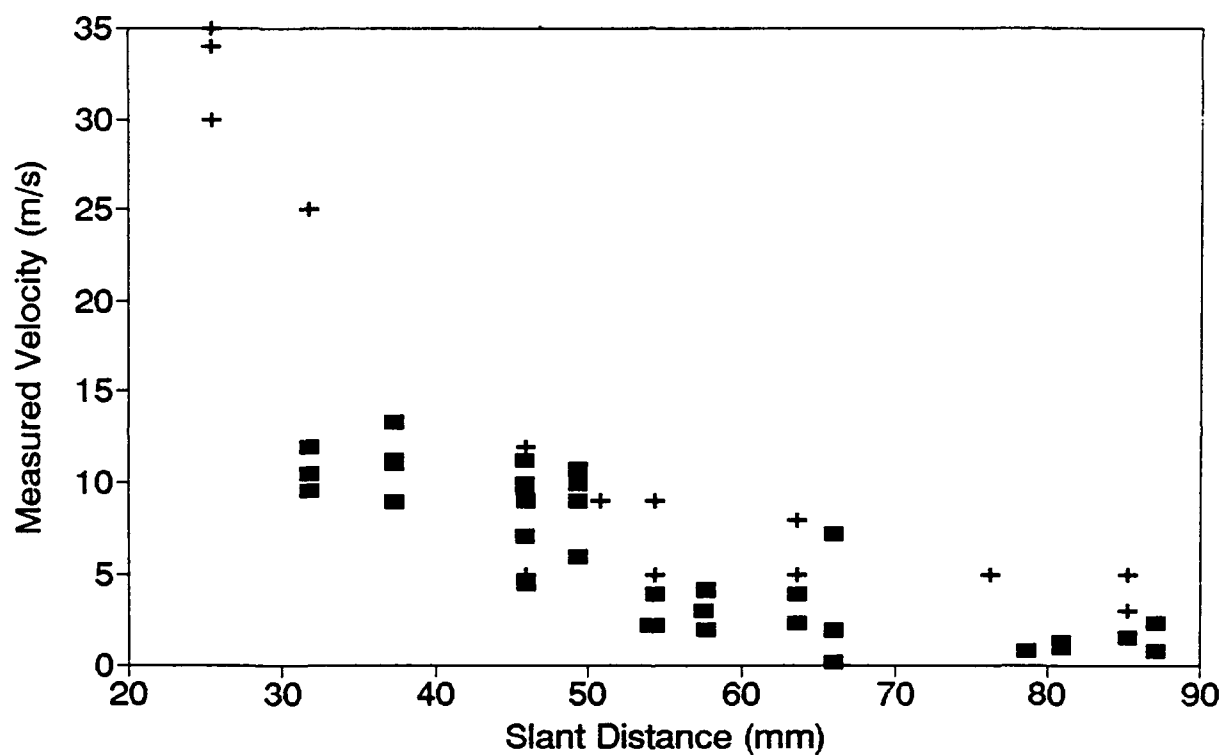


Figure 2.15. Combined measured peak radial and vertical velocities from all the rock simulant tests.

Rockite/Cement Vertical/Radial Velocity

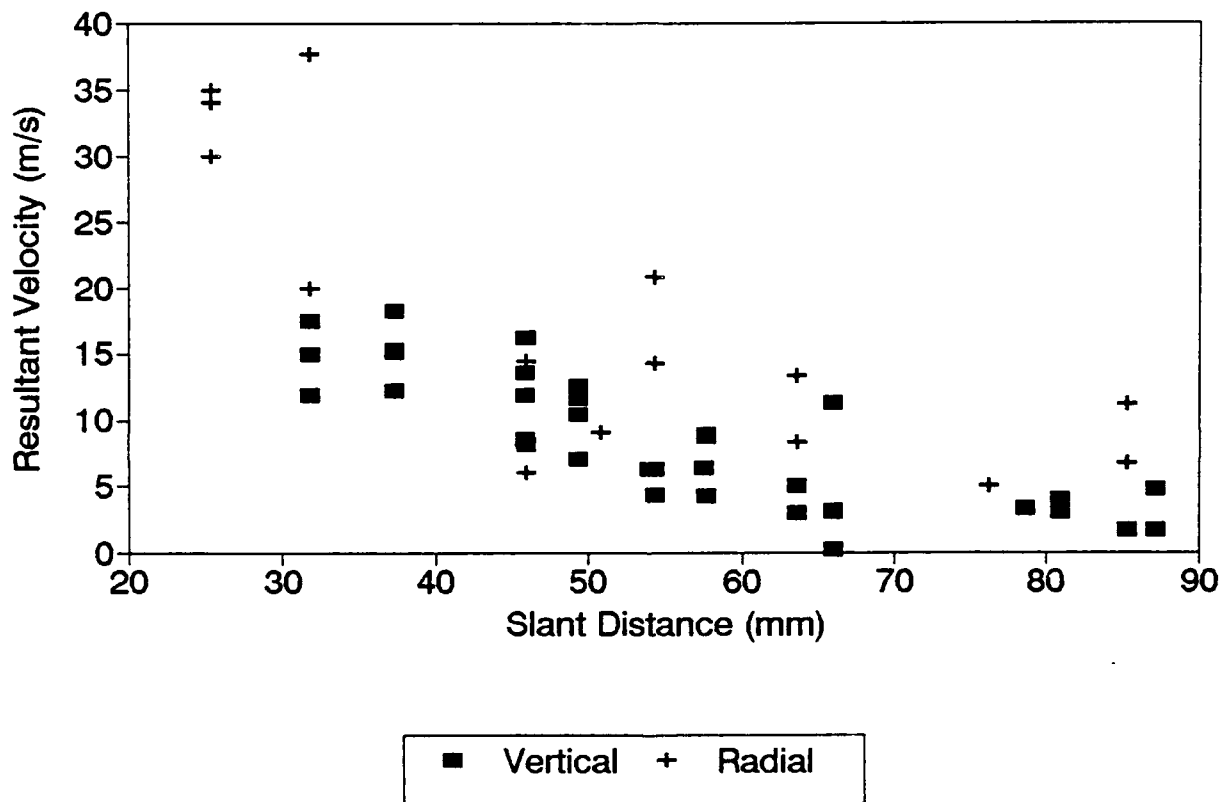


Figure 2.16. Combined resultant peak radial and vertical velocities from all the rock simulant tests.

RT7 --- G1 --- RADIAL VELOCITY --- CONCRETE MODEL

1.0g PETN --- CYLINDRICAL

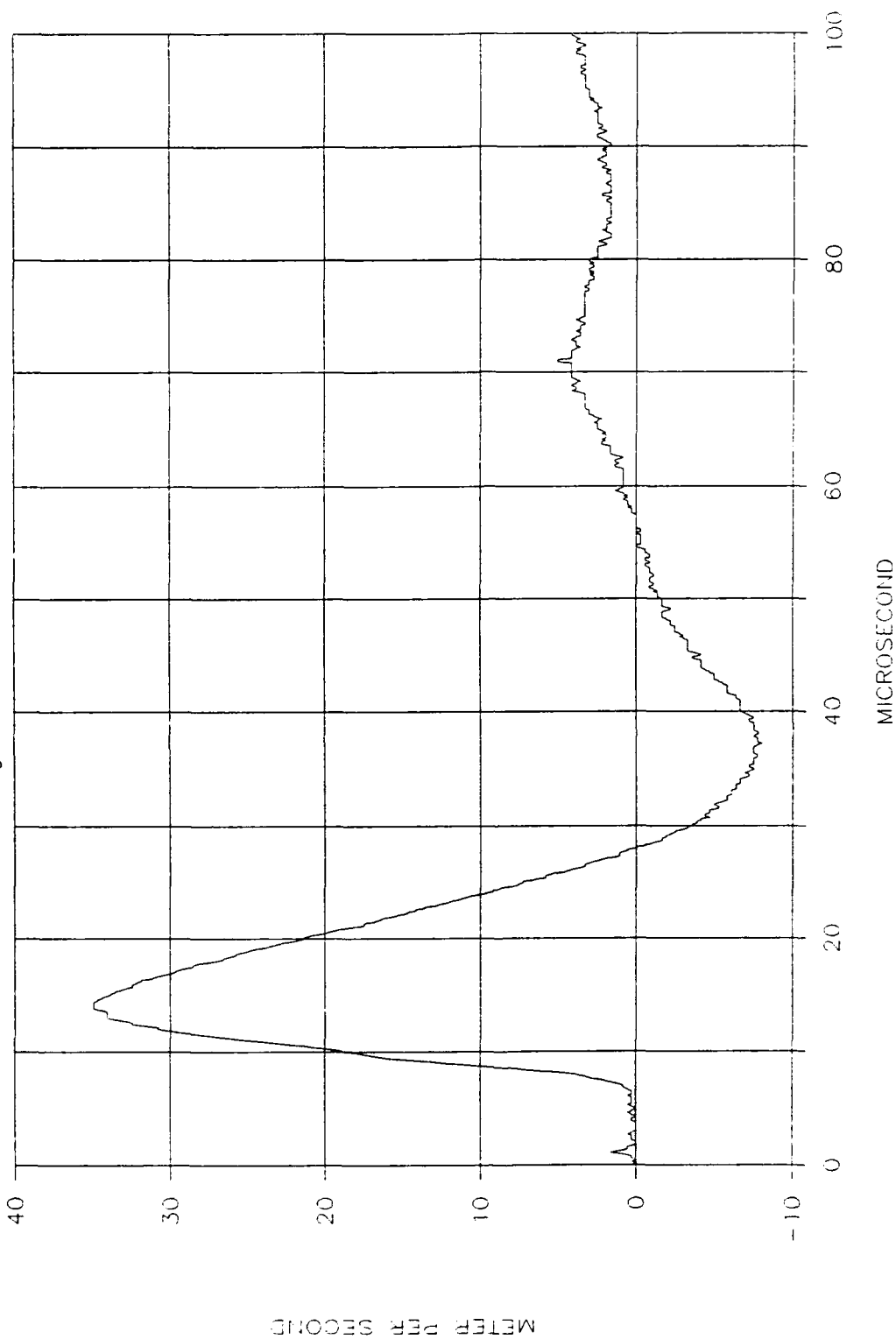


Figure 2.17a. Test RT7 (cylindrical charge) gage 1 radial velocity signal.

RT10--G1--RADIAL VELOCITY--CONCRETE MODEL

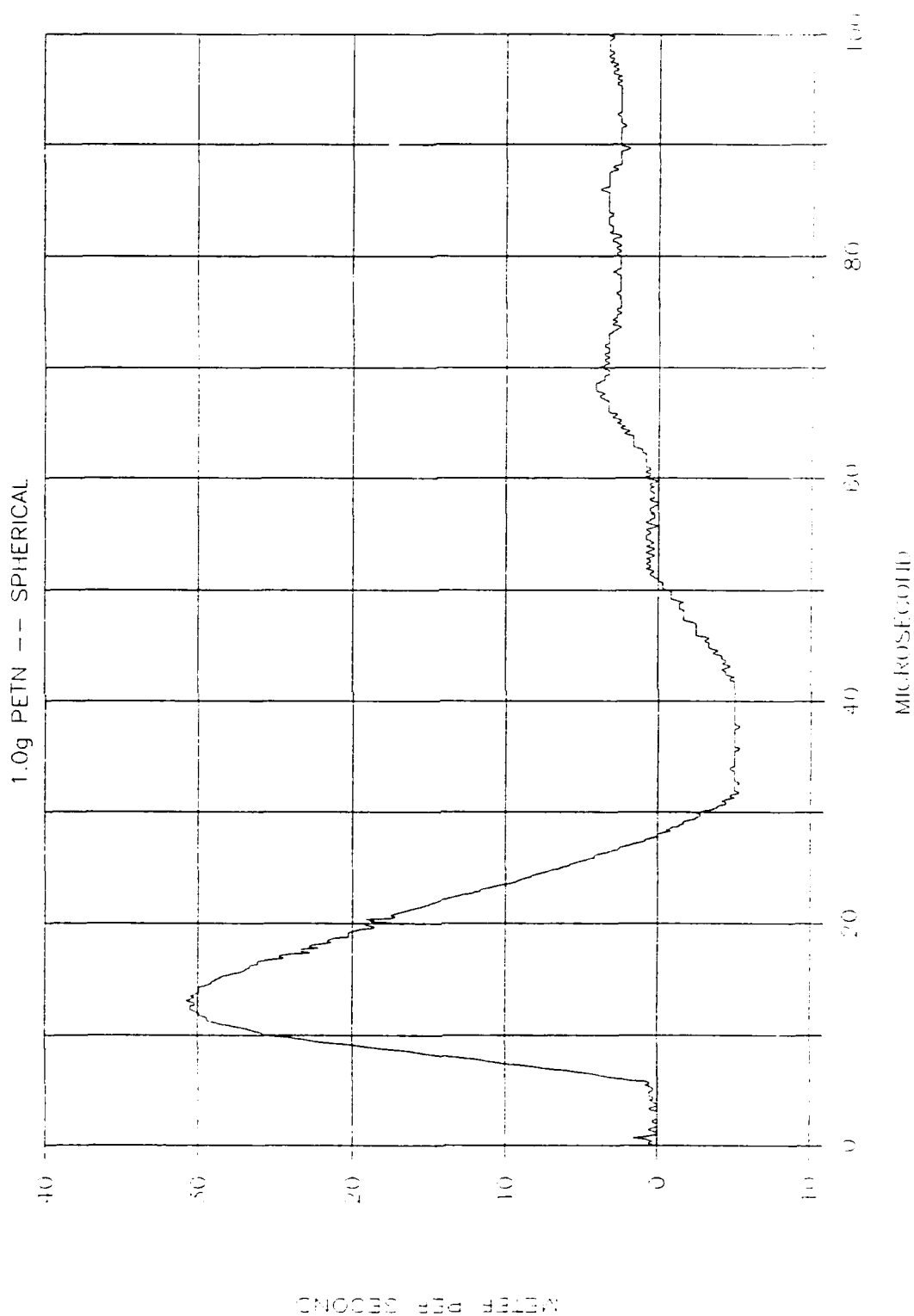


Figure 2.17b. Test RT10 (spherical charge) gage 1 radial velocity signal.

RT12 PARTICLE VELOCITY GAGE G3

0.75in. ABOVE, 1in. OFF CHARGE CENTER

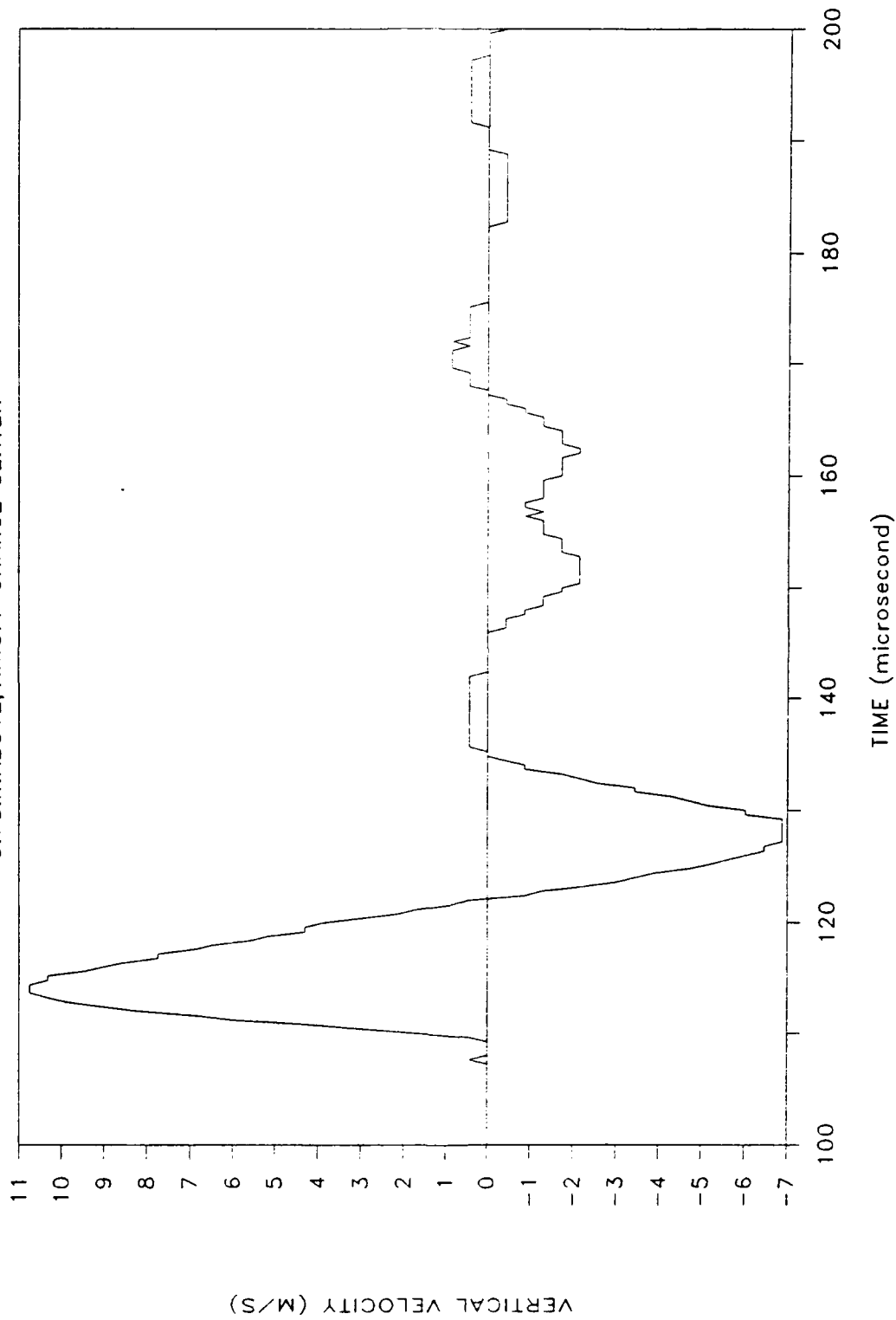


Figure 2.17c. Signal from Test RT12 (spherical charge) vertical velocity gage 3 above the charge center.

RT12 PARTICLE VELOCITY GAGE G4

0.75in.BELOW,1in.OFF CHARGE CENTER

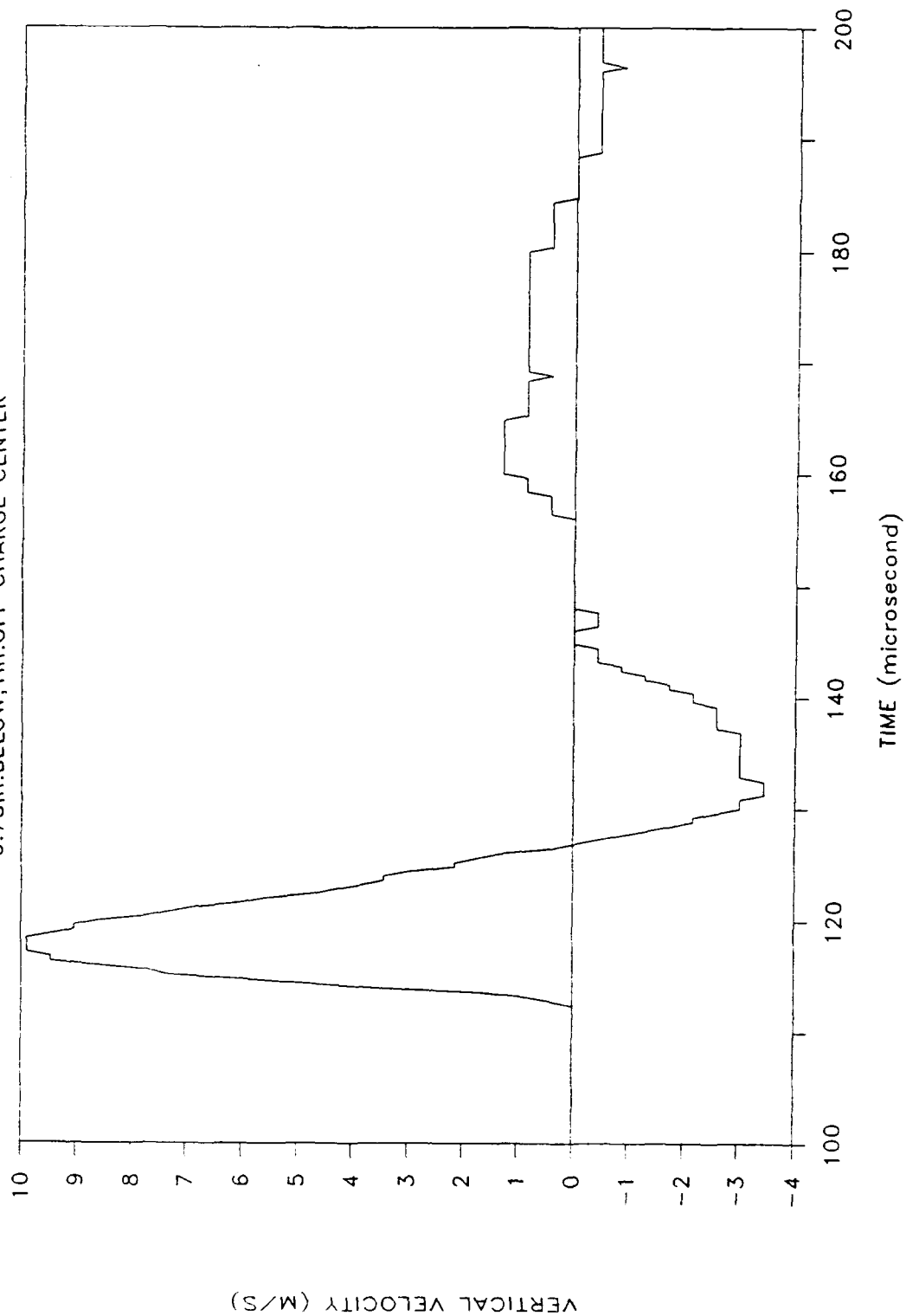


Figure 2.17d. Signal from Test RT12 with velocity gage 4 below the charge center the same distance as Figure 2.16c.

The velocity gage records were integrated to calculate displacement versus time and then vertical and radial displacement were plotted together as a hodograph or a displacement trajectory. In this manner the displacements at several locations resulting from the detonation of spherical and cylindrical charge geometries were compared. Figure 2.18a shows the trajectories for Tests RT7 (radial velocity) and RT8 (vertical velocity) both of which had cylindrical explosive charges. Figure 2.18b shows the trajectories for Tests RT9 (vertical velocity) and RT10 (radial velocity) both of which had spherical explosive charges. The depth-of-burial was the same for each test. A comparison of the two hodographs indicate there is little difference in direction and magnitude of displacement trajectories for the two source geometries.

D. Summary.

The principal conclusions from the model tests are listed below.

1. Radial fractures initiate immediately after the detonation of the spherical and cylindrical charges in the borehole. This conclusion is based on the results from the tests performed using the Cranz-Schardin framing camera.

2. Small flaws such as mica flakes and strain gages embedded in the epoxy models act as crack initiation sites. These cracks initiated approximately 20 μ s after the passage of the P-wave across the flaw. This observation is based on the results from the tests performed using the Cranz-Schardin framing camera.

3. Joints control the crater shape and size. The greater the impedance mismatch between the matrix material and the joint/discontinuity material, the greater the influence the joint has on the fracture and fragmentation patterns. Subtle discontinuities/flaws sometimes act as sites for cracks and hence, influence the crater definition. This observation is from Cranz-Schardin photographs and from post-test observations.

4. The presence of boundaries have some influence on the size and shape of the fragmentation volume. To a degree the shape of the model (rectangular versus cylindrical) seems to influence the fracture pattern and the size of the crater. The craters formed in the rectangular and cylindrical models were similar. The major difference was the number of fractures formed.

5. The crater volumes were slightly larger for spherical charges than for cylindrical charges in Epon 815. For Rockite models spherical charges produced much larger crater volumes than cylindrical charges at the same depth-of-burial. These observations were based on the results from Tests RT1C and RT2S (Tests RK-1C and RK-2S in Chapter V).

6. The fragmentation and crater formation occur in stages

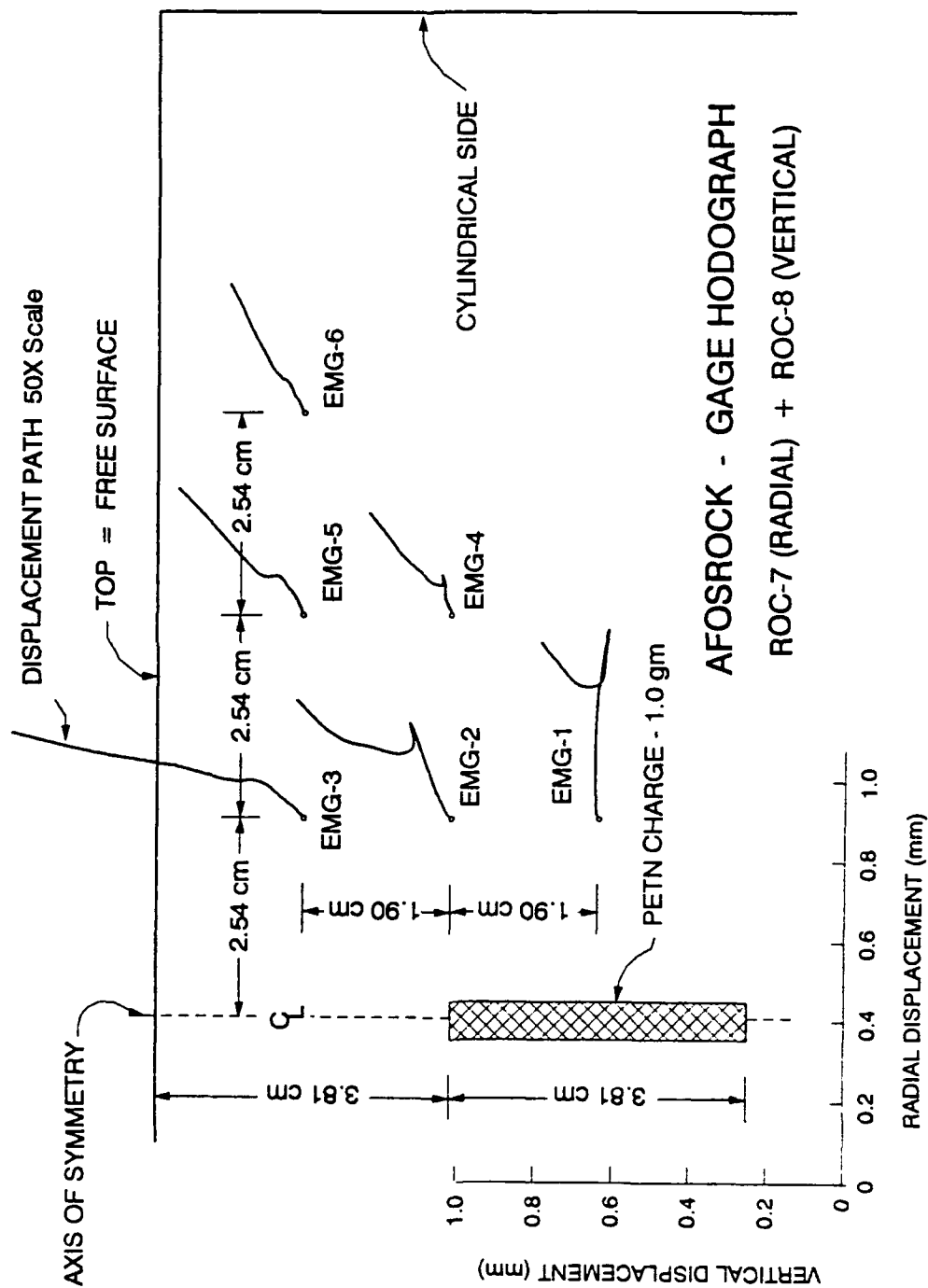


Figure 2.18a. Gage hodograph for Tests RT7 and RT8.

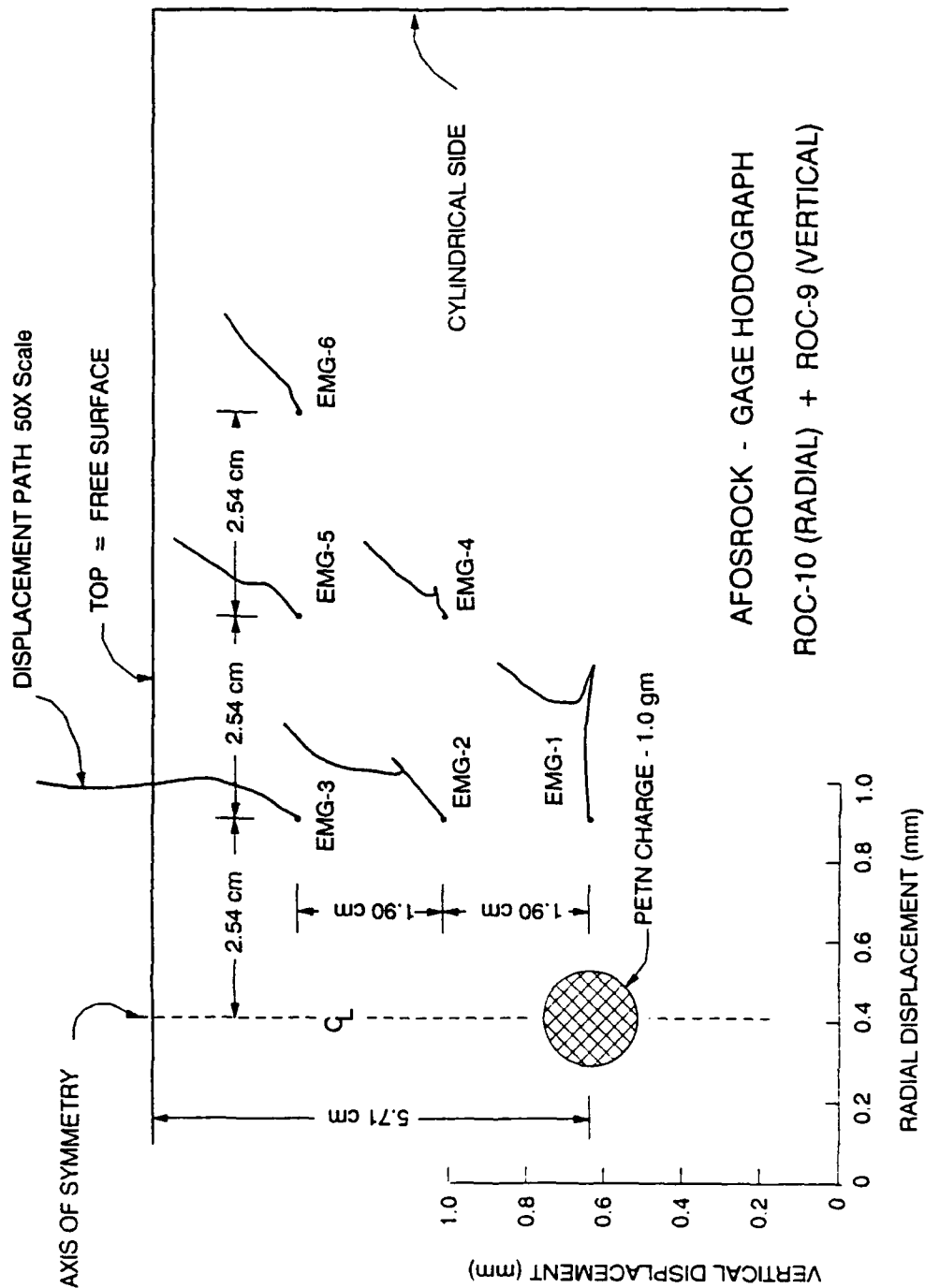


Figure 2.18b. Gage hodo-graph for Tests RT9 and RT10.

(2.13)

as a function of time. That is, a crater within a crater will be a crater in the sequence because spall fractures are the first "circumferential" cracks to form after the P-wave reflects from the initial free surface and then from the subsequent spall surfaces. This observation is based on post-test observations from Tests RT3S to RT13S and from Cranz-Schardin framing camera photographs of the two dimensional transparent model tests.

7. Deeply buried charges produce incomplete fragmentation and poorly formed craters. Many fractures are produced which absorb much of the explosive/stress wave energy.

8. The crater size and shape is sensitive to joints, porosity, depth-of-burial, and charge weight.

9. There is not a clear correlation between fracture and fragmentation and the measurements of strain, stress, particle velocity, and material strength (epoxy versus cement).

E. References.

2.1. Wolsiefer, J., 1984, "Ultra High-Strength Field Placeable Concrete with Silica Fume Admixtures," Concrete International, April.

CHAPTER III. FRAGMENTATION MECHANISM IN CRATER BLASTING

The main objective of the research conducted under this program was to investigate fracture and fragmentation of brittle geologic materials due to explosive charges being detonated near a free surface. When an explosive is detonated a chemical reaction occurs very rapidly and a relatively small quantity of explosive is converted into gas at very high pressure. As a result of this reaction the material in which the explosive is placed is subjected to extremely high pressures - in the hundred kilobar range. This reaction results in two types of loading being applied to the material - a shock wave loading that quickly travels out into the material surrounding the borehole and a longer duration gas pressurization loading. There is not at this time a good understanding of the mechanism by which these loads fracture and fragment the brittle material. Our aim in conducting the research program being described was to perform experiments which would lead to a better understanding of these mechanisms.

We had earlier [3.1] conducted tests in a similar vein at Maryland. These tests were funded by the National Science Foundation and used two dimensional models to investigate the role of flaws and imperfections on fragmentation. The model material used in that series of tests was Homolite 100 and the effects of the presence of both small and large flaws were investigated. For the most part the small flaws were simulated by routing small flaws into one surface of the thin plate models. These models were tested in a dynamic polariscope which permitted observation of both flaw initiation and the stresses (due to stress wave propagation) in the model. These tests included an investigation of fracture initiation by the outgoing stress waves as well as an examination of the effects of the reflected stress waves.

In a separate series of two dimensional tests the effects of stress wave propagation past embedded large flaws were investigated. These large flaws were intended to simulate joints and bedding planes in a geologic media. The large flaws were simulated by bonding together strips of Homolite 100 with edges which had been routed smooth. These models were viewed in a dynamic polariscope in order to permit visual observation of the initiation and propagation of fractures from the simulated joints and bedding planes.

While these earlier tests were very informative they had several drawbacks from an applications standpoint. Probably the most limiting feature was that all tests conducted were two dimensional in nature. Although they were followed by a series of full scale testing by Martin Marietta [3.2] there was no direct verification of the results obtained in the laboratory by either a larger scale test series or ones which included three dimensional testing. (The testing done by Martin Marietta used high speed photography to investigate the effects of different delay sequences

(3.2)

on fragmentation in quarrying applications but did not contain any instrumentation to give stress levels, accelerations, or other basic material response parameters). While the results obtained in the laboratory tests series seemed to help explain the results obtained in the quarry there was no direct verification. The current series of tests employed many different types of diagnostic instrumentation such as stress gages, strain gages, accelerometers, velocity gages, photoelasticity, and moire' interferometry. The current series of tests also employed the use of many three dimensional models and used a wider variety of materials in the construction of models. These materials were both transparent and opaque and included PMMA, Epoxy, Cement, Rockite, Hydrostone, and Hydrocal. The latter three materials being fast setting gypsum products which were felt to respond to explosive loading in a somewhat similar fashion to the geologic materials of interest.

The experimental technique in the earlier test program was primarily photoelasticity which provided only shear stresses (or differences in principal stresses) except on model boundaries where one of the two principal stress components is zero. In this current series of tests we wanted to use a variety of instrumentation in an effort to determine which of the many material response parameters could best be used to predict fragmentation. The results obtained from the testing described in detail in Chapter 2 were used to formulate a mechanisms for fragmentation due to an explosive load located near to a single free face (i.e. a cratering shot).

Figure 3.1 depicts the propagation sequence of a dilatational wave which is produced from a highly dynamic load being applied at a point on the interior of a two dimensional body. The location of the point source is shown a distance "h" from the nearest free face -this being the geometry of interest, i.e. a cratering geometry. The leading edge of the P-wave travels outward with a velocity of:

$$V_p = \sqrt{E/(\rho(1-\nu^2))} \quad (1)$$

where ν is poisson's ratio, E is Young's Modulus, and ρ is the material density.

At time $t=h/V_p$ the wave front reaches the free boundary and begins to reflect back into the media. At points where there is non-normal incidence of the outgoing P-wave, both a dilatational (P) wave and a distortional (shear or S) wave occurs. The creation of both types of waves is due to the stress free boundary condition that must be met at the free face. Fig 3.1 shows the development of the P wave up to the time that the reflected P-wave (PP-Wave)

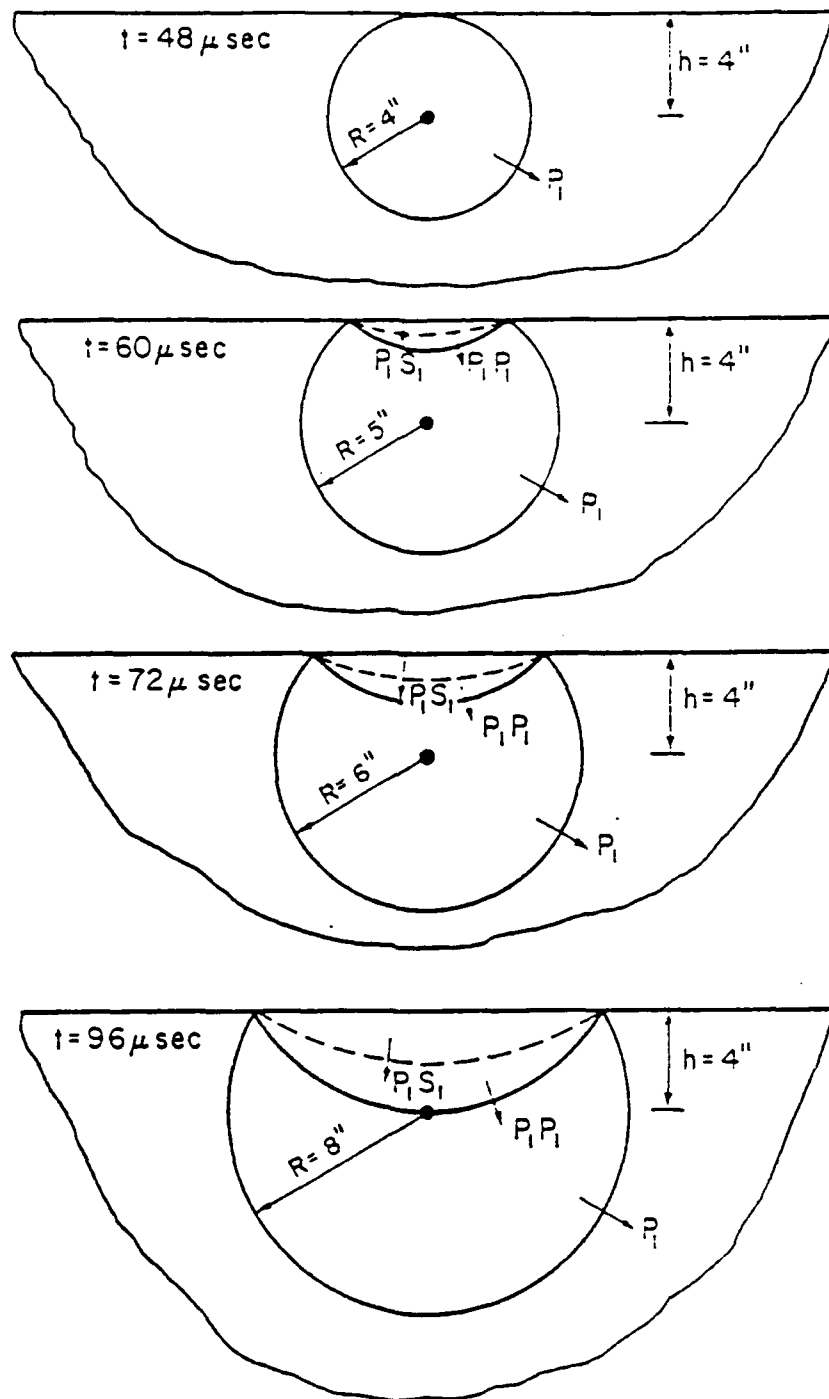


Figure 3.1. Stress Wave Fronts in a Half Plane with an Internal Point Source.

(3.3)

reaches the point source (borehole). Due to fracturing that occurs at the borehole a distortional (shear) wave is also created at the explosive source and this travels at a slower velocity given by:

$$V_s = \sqrt{(E/(2\rho(1+\nu)))} \quad (2)$$

When this S-wave strikes the boundary it also creates two wave types at points of non-normal incidence - a shear wave (SS-Wave) and a P wave (SP-Wave). These reflected waves travel back over the load site in much the same fashion as the P wave does (shown in Figure 3.1).

Typical high speed photographs taken of the dynamic event by a multiple spark gap camera [3.3] are shown in Figure 3.2. In this figure the model has been photographed at approximately 200,000 frames per second while being viewed under polarized lighting conditions. The fringes shown are lines of constant shear stress (difference in the principal stress). From the fringe patterns obtained and the theory of elasticity it is possible to determine the state of stress (or strain) in the outgoing P wave. The strain in the tangential direction ϵ_θ is obtained from the equation:

$$\epsilon_\theta = -((1+\nu)/E)((f_\sigma)_d/h) \int (N/r)dr \quad (3)$$

where $(f_\sigma)_d$ is the dynamic stress fringe value, N is the fringe order, and r is the radial position. Once ϵ_θ is known the radial strain, ϵ_r , can be found from:

$$\epsilon_r = \epsilon_\theta - ((1+\nu)/E)(N/h)(f_\sigma)_d \quad (4)$$

From these strains - both stresses and displacements can be obtained from the stress displacement relationships and the stress strain relationships. Figure 3.3 shows for a given test the fringe order as a function of position obtained at various times throughout the dynamic event. Basically, each of the curves represents information obtained in one photograph from the multiple spark gap camera.

Figure 3.4 shows the results obtained for the tangential stress as a function of position from the borehole (and time after detonation). Figure 3.5 gives the results obtained for the radial stress as a function of position from the borehole.

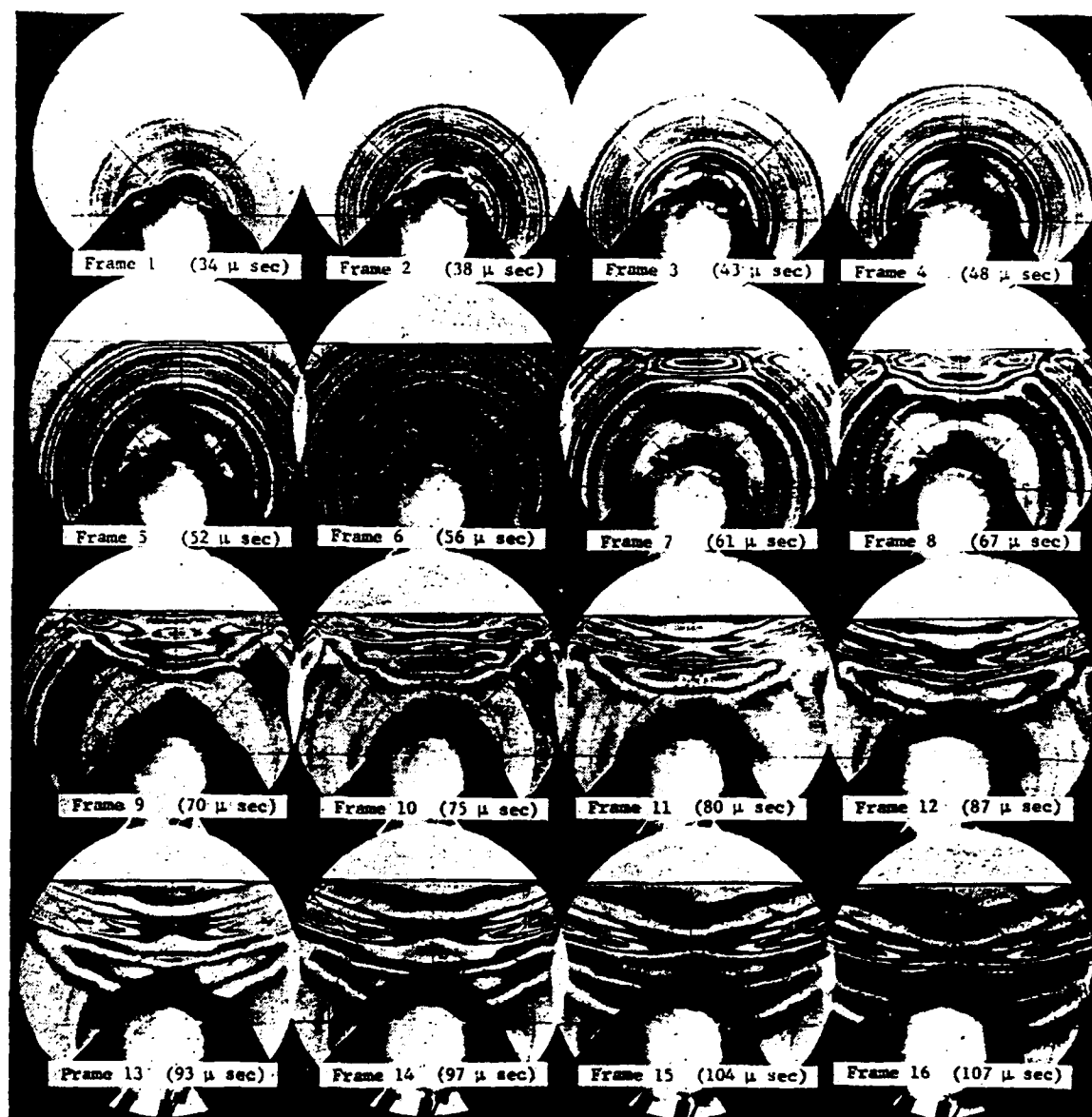


Figure 3.2. Typical Fringe Patterns from a Dynamic Point Source.
From Dally and Riley.

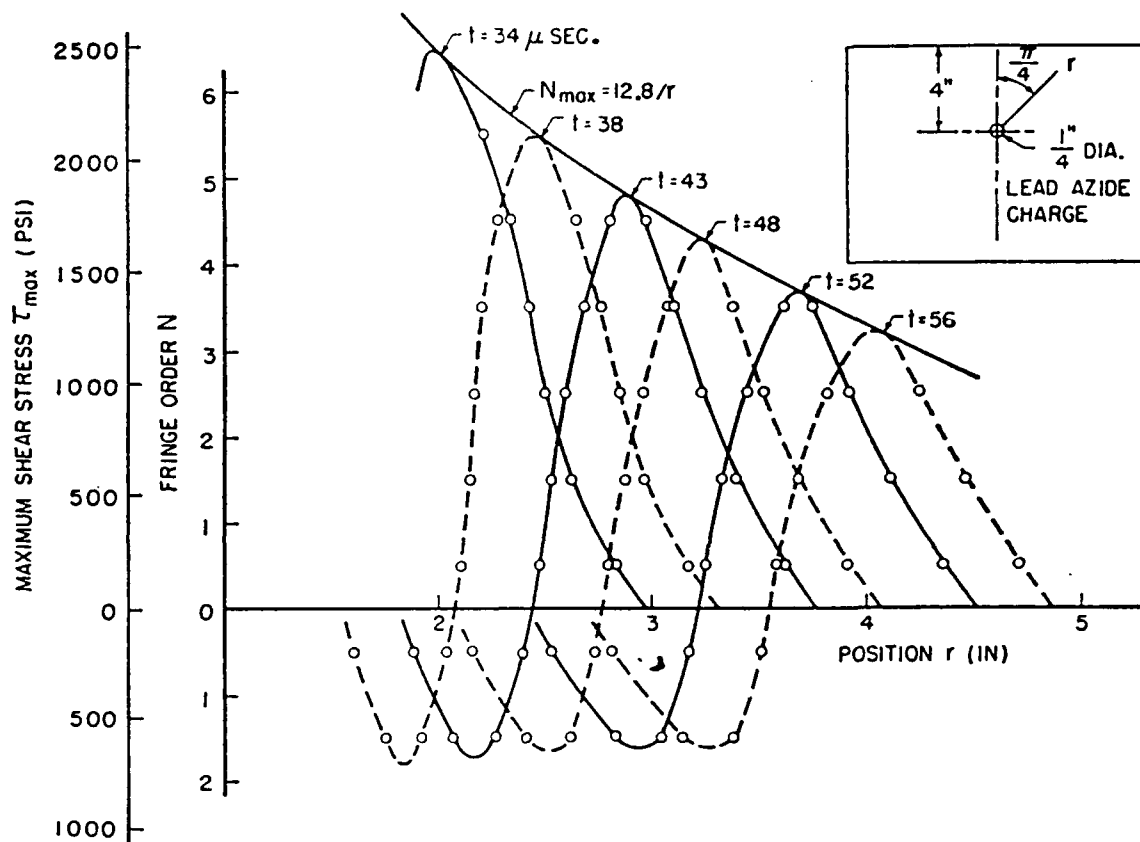


Figure 3.3. Fringe Order and Maximum Shear Stress as a Function of Position of Position at Several Times After Detonation of the Lead Azide Charge. From Dally and Riley.

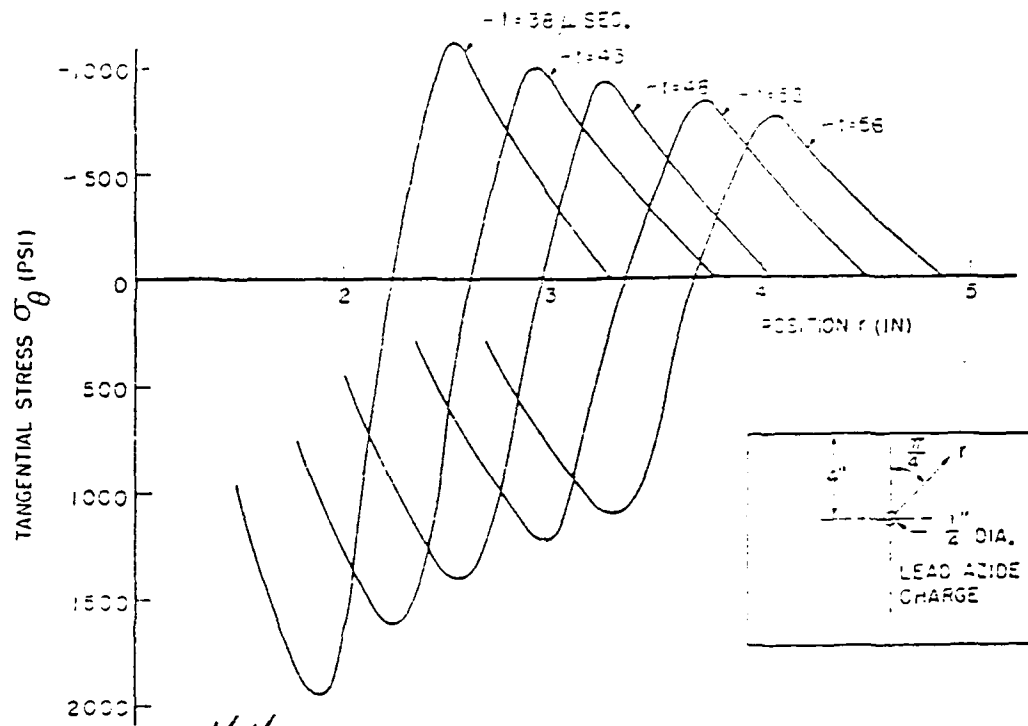


Figure 3.4. Tangential Stress as a Function of Position at Several Times after Detonation of the Lead Azide Charge. From Dally and Riley.

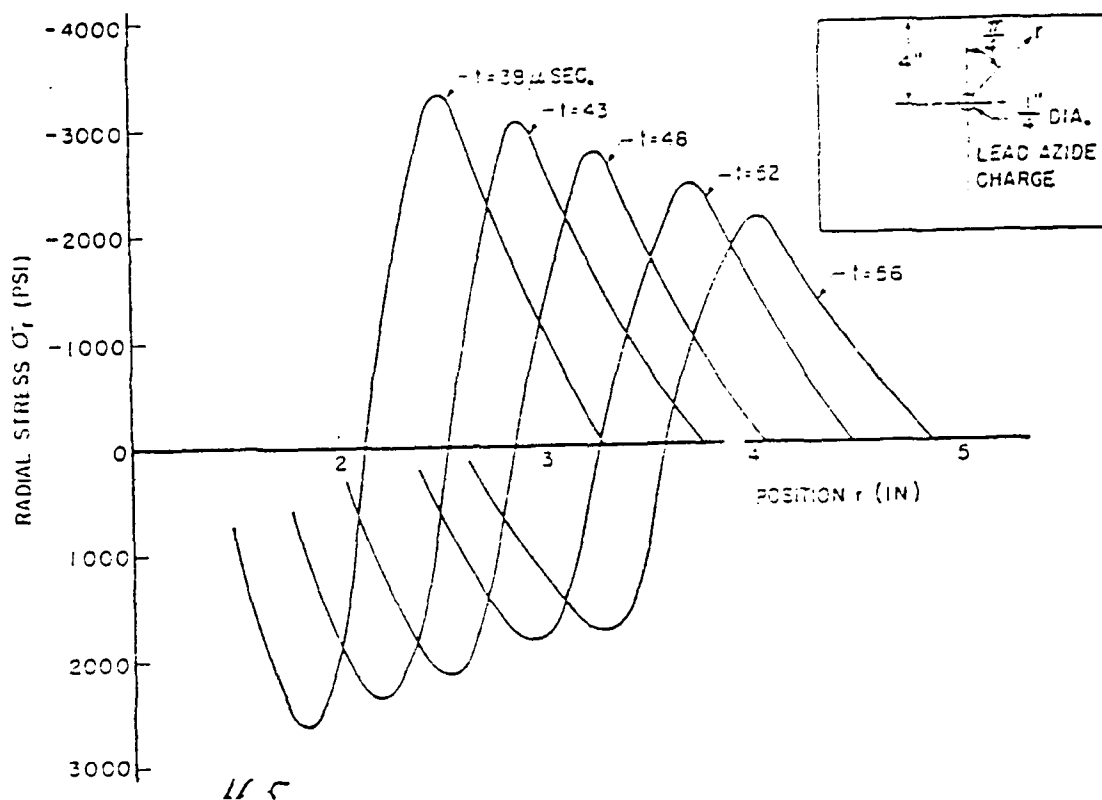


Figure 3.5. Radial Stress as a Function of Position at Several Times after Detonation of the Lead Azide Charge. From Dally and Riley.

(3.4)

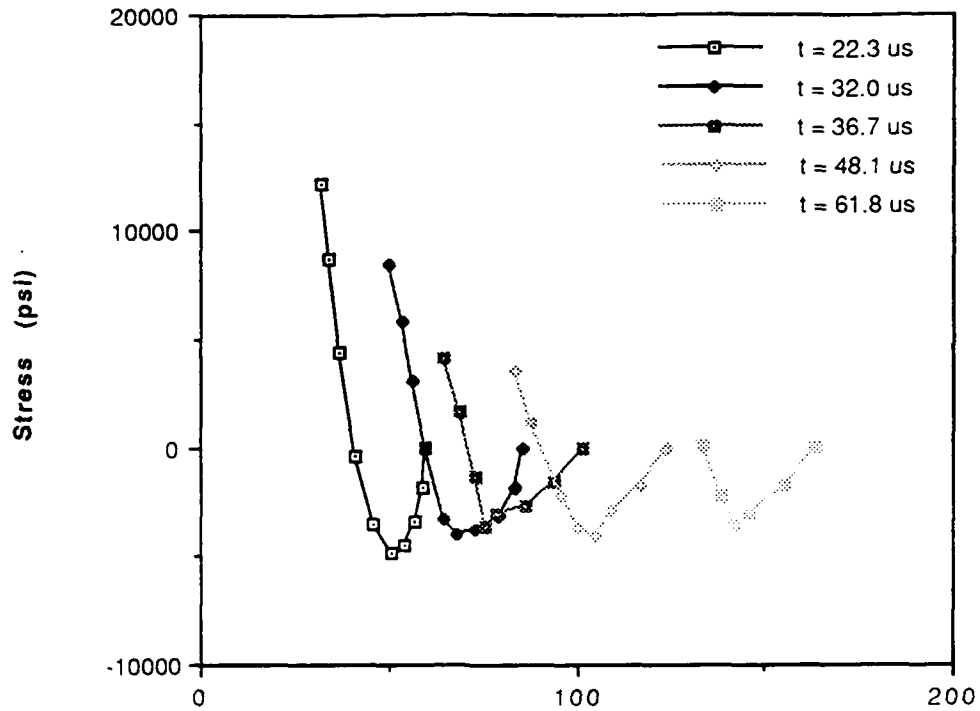
Notice from Figure 3.3 that the maximum fringe order decreases as the distance from the borehole (or time) increases. This decrease is due both to material damping and geometric dispersion. As the stress wave travels from the source some amplitude is lost due to hysteresis losses in the material. This is the material damping. As the wave front travels from the source the front must cover more and more area and therefore the amplitude decreases due to geometric dispersion. Most of the decrease in amplitude seen in Figure 3.3 is due to geometric dispersion. In a three dimensional medium the geometric dispersion would be even greater than the amount seen here in two dimensions.

A close examination of the two curves showing the tangential and radial stresses at 38 microseconds after detonation in Figures 3.4 and 3.5 shows that in the leading edge of the P wave that a bi-axial compressive stress state exists. That is, both the radial and the tangential stresses are compressive. The radial stress is about three times larger than the tangential stress with the maximum radial value being about 3000 psi in compression. In the trailing part of the outgoing P wave both stress components are tensile with the radial maximum being about half again as large as the tangential value. Here the maximum radial value is about 2800 psi.

The curves presented in Figures 3.3 through 3.5 are for a relatively small charge. As the charge size is increased the compression stress (wave) sent out into the medium is increased. If the compressive stresses in the leading edge of the outgoing wave are sufficiently large (larger than the compressive strength of the material) then crushing of the material will occur - in both the tangential and the radial directions. Early theories for fragmentation mechanisms assigned all of the fragmentation to the reflection of the compressive (outgoing wave) into a tensile inward traveling wave. To maximize fragmentation then it would be desirable to have the outgoing compressive pulse be as large as possible. If, however, crushing occurs whenever the compressive pulse reaches the compressive strength of the material it appears that as charge size is increased that stress (or fringe order) will reach a peak and not increase further. At the same time the size of the crushed zone around the borehole should continue to increase as charge size increases.

A series of tests were conducted to investigate this possibility. Six tests were conducted in PMMA (plexiglas) with charge sizes increasing from 220 mg to 600 mg. The borehole diameter ranged from 5 mm for the smallest charge to 7.6 mm for the largest charge. All charges were fully coupled to the borehole wall. The multiple spark gap camera was used to record the fringe patterns for all tests and the size of the crushed zone was also measured after each test. Figure 3.6 shows typical curves for tangential and radial stresses obtained in Test 2 which used a 380 mg charge of PETN in a 5 mm diameter

Tangential Stress vs. Distance Isochromatic Fringe Test #2



Radial Stress vs. Distance Isochromatic Fringe Test #2

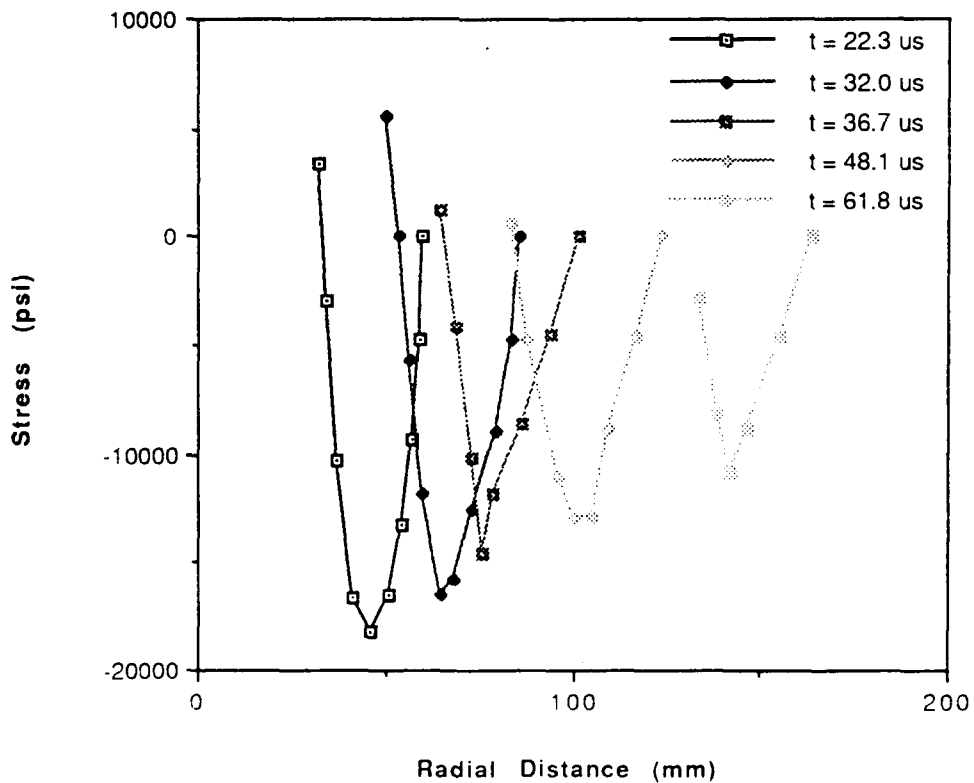


Figure 3.6. Tangential and Radial Stresses obtained in Test 2 which utilized 380 milligrams of PETN as the Explosive Charge.

(3.5)

borehole. As can be seen from the figure the radial stresses are once again larger by a factor of three or more than are the tangential stress values. In this case the tensile tail is not so predominate and the reason for this will be discussed in detail in a section to follow. The PMMA material was chosen for this series of tests since the fringe constant for it is much lower than other photoelastic materials which meant that the charge size could be increased greatly without resulting in large increases in fringe order. If the fringe order increases too much the fringes become so closely spaced that they cannot be counted.

Figure 3.7 shows the decay of the fringe order number as a function of distance from the borehole for the PMMA material. The data for all six tests fits well a straight line when the natural log of fringe order is plotted against natural log of propagation distance with a negative slope of 0.805. The scatter in the data shown is not bad considering the variation in charge size and borehole diameter for the six tests. The amplitude decay curve for the fringe order is therefore given by:

$$N = 111.72/r^{0.805} \quad (5)$$

As indicated earlier this decay is the result of both material damping and geometric dispersion. Figure 3.8 shows the fringe order as a function of charge size for various different distances from the borehole. With the exception of Figure 3.8a which shows fringe order after only 75 mm of travel the increase in fringe order with charge size is almost non-existent. At 75 mm for a 300 % increase in charge size the fringe order increases by 33 %. At 100 mm the increase is only 10 % (Figure 3.8b). This very slight increase in fringe order indicates that the increase in energy when additional charge is used is not very effective in increasing the magnitude of the outgoing stress wave. Figure 3.9 shows the results of the crushed zone measurements made on the models after the tests were concluded. Figure 3.9a shows the crushed zone diameter as a function of charge size for the PMMA models. The upper three points marked L- show the results for the models which used boreholes of diameter 7.62 mm and the three lower points marked S- are for the models with a 5.07 mm diameter borehole. As can be seen from the figure the crushed zone size is very nearly constant with charge size. The fact that the smaller diameter boreholes resulted in a larger crushed zone are contrary to what would be expected. Figure 3.9b shows similar results for the Homolite models. Once again the smaller boreholes resulted in a smaller diameter for the crushed zone. In Figure 3.9c the volume of the crushed zone is shown as a function of the charge size for

Fringe Order vs. Distance from Borehole Wall

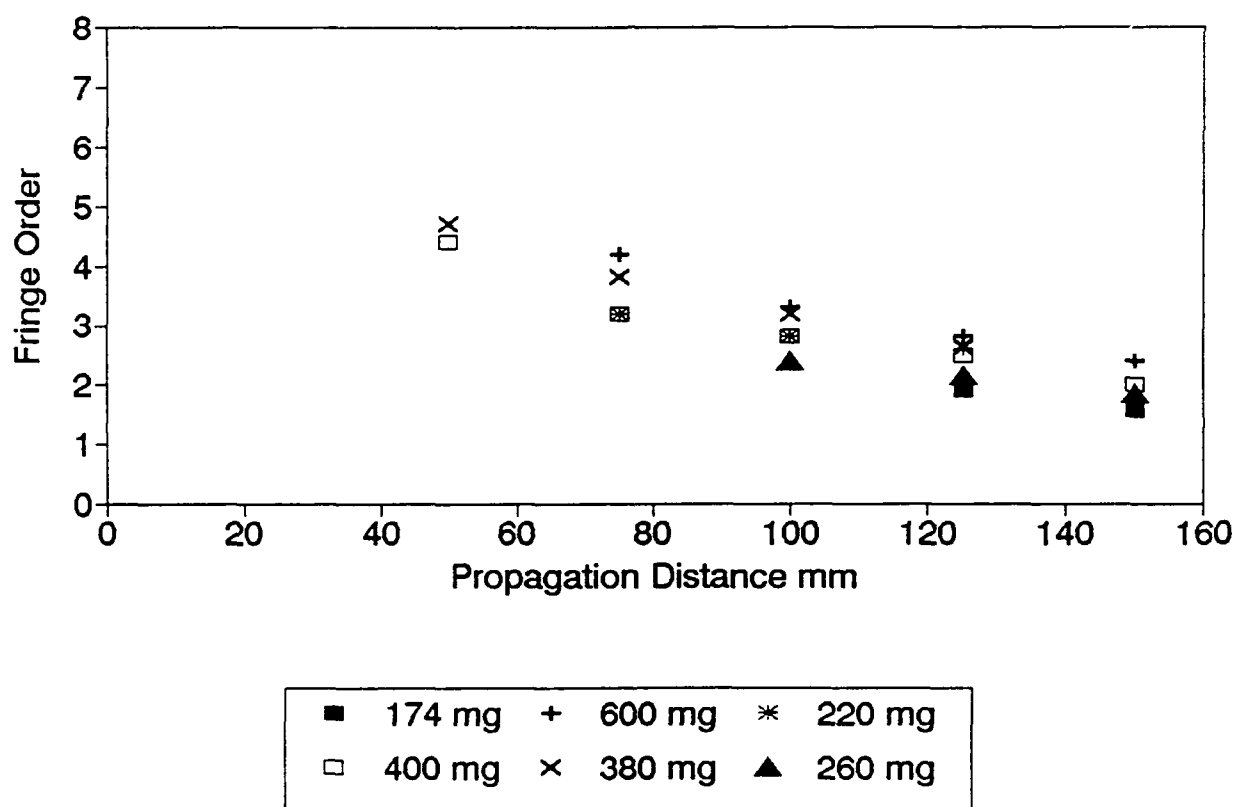


Figure 3.7. Fringe Order as a Function of Distance from the Borehole for Various Charge Sizes.

Fringe Order vs. Charge Size

After 75 mm of Travel

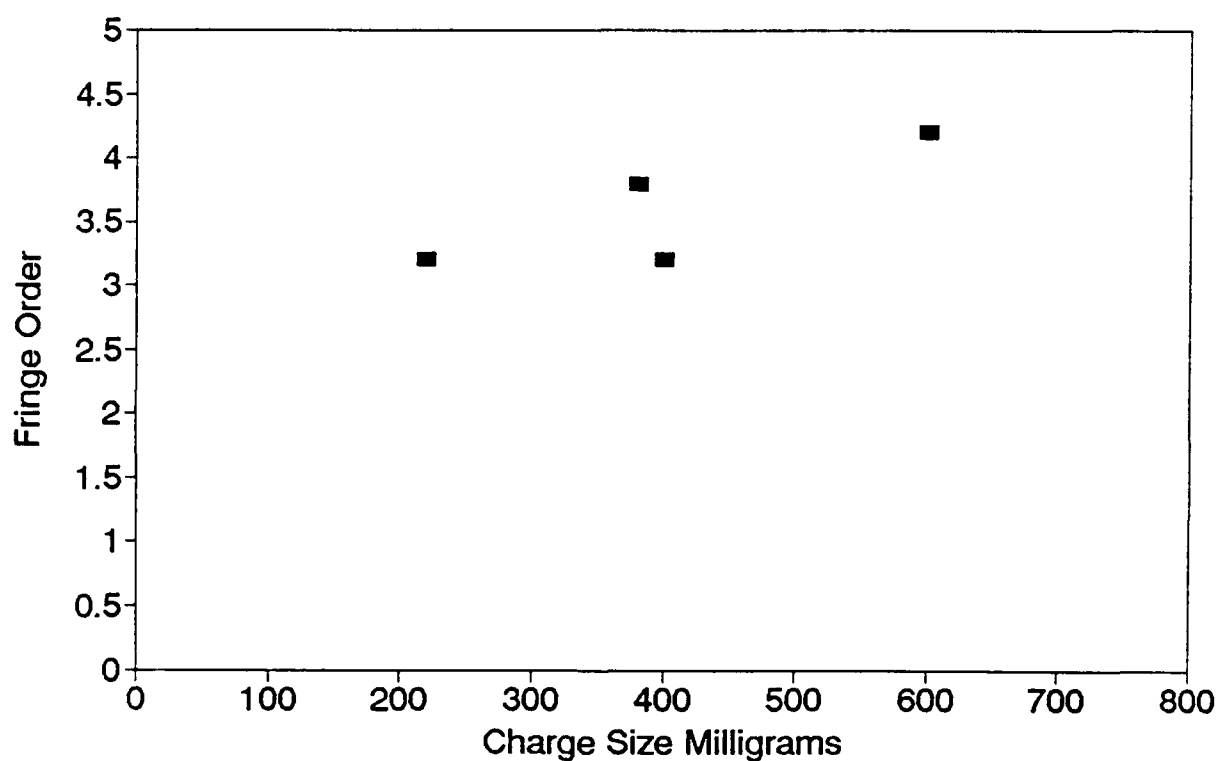


Figure 3.8a. Fringe Order as a Function of Charge Size after 75 mm of Propagation from the Borehole.

Fringe Order vs. Charge Size

After 100 mm of Travel

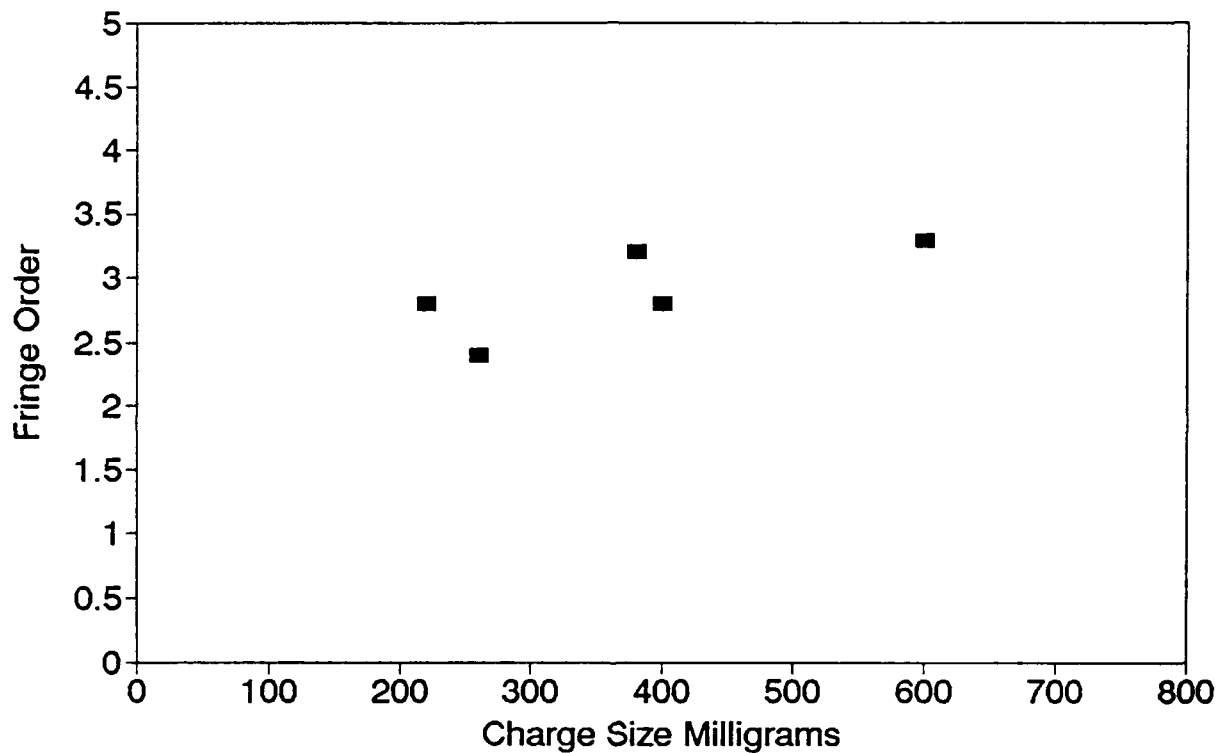


Figure 3.8b. Fringe Order as a Function of Charge Size after 100 mm of Propagation from the Borehole.

Fringe Order vs. Charge Size

After 125 mm of Travel

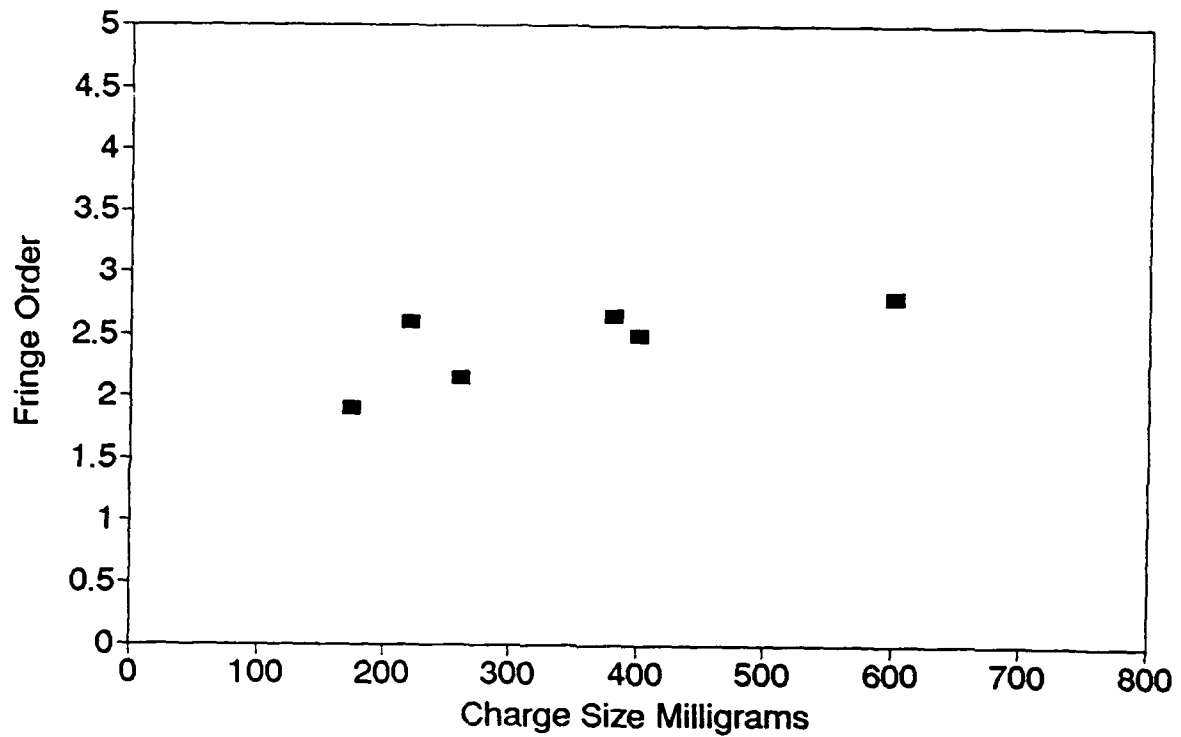


Figure 3.8c. Fringe Order as a Function of Charge Size after 125 mm of Propagation from the Borehole.

Fringe Order vs. Charge Size

After 150 mm of Travel

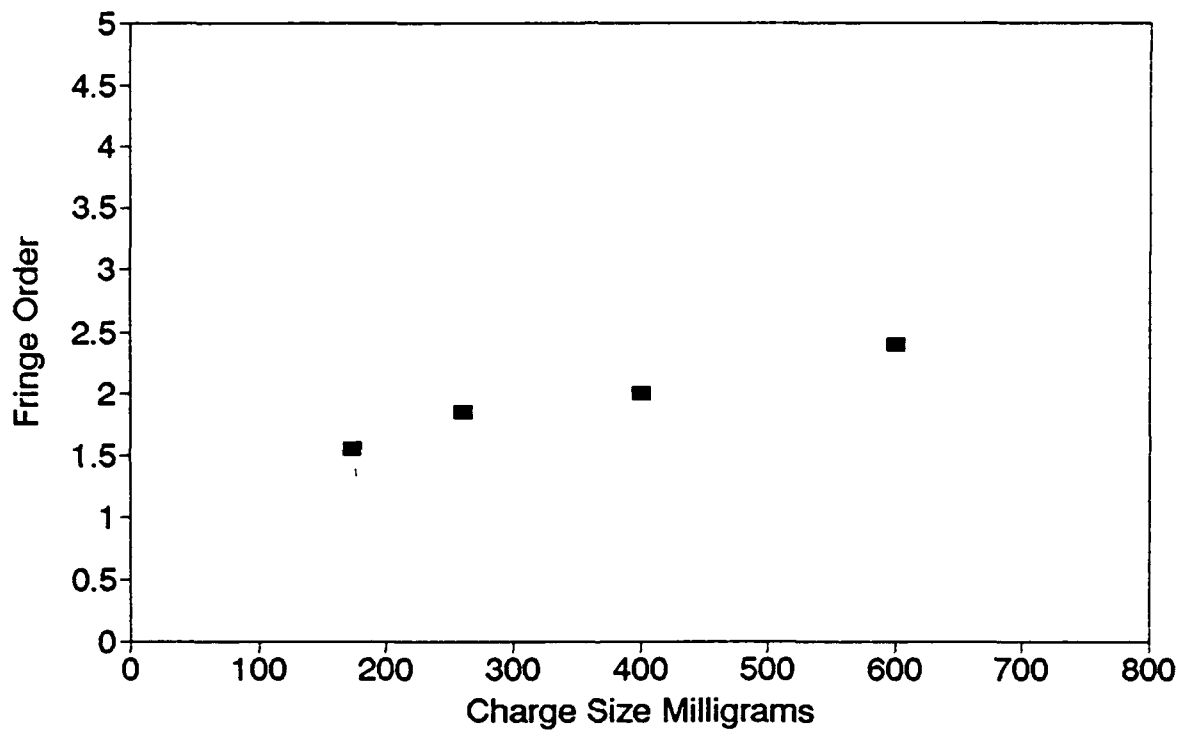


Figure 3.8d. Fringe Order as a Function of Charge Size after 150 mm of Propagation from the Borehole.

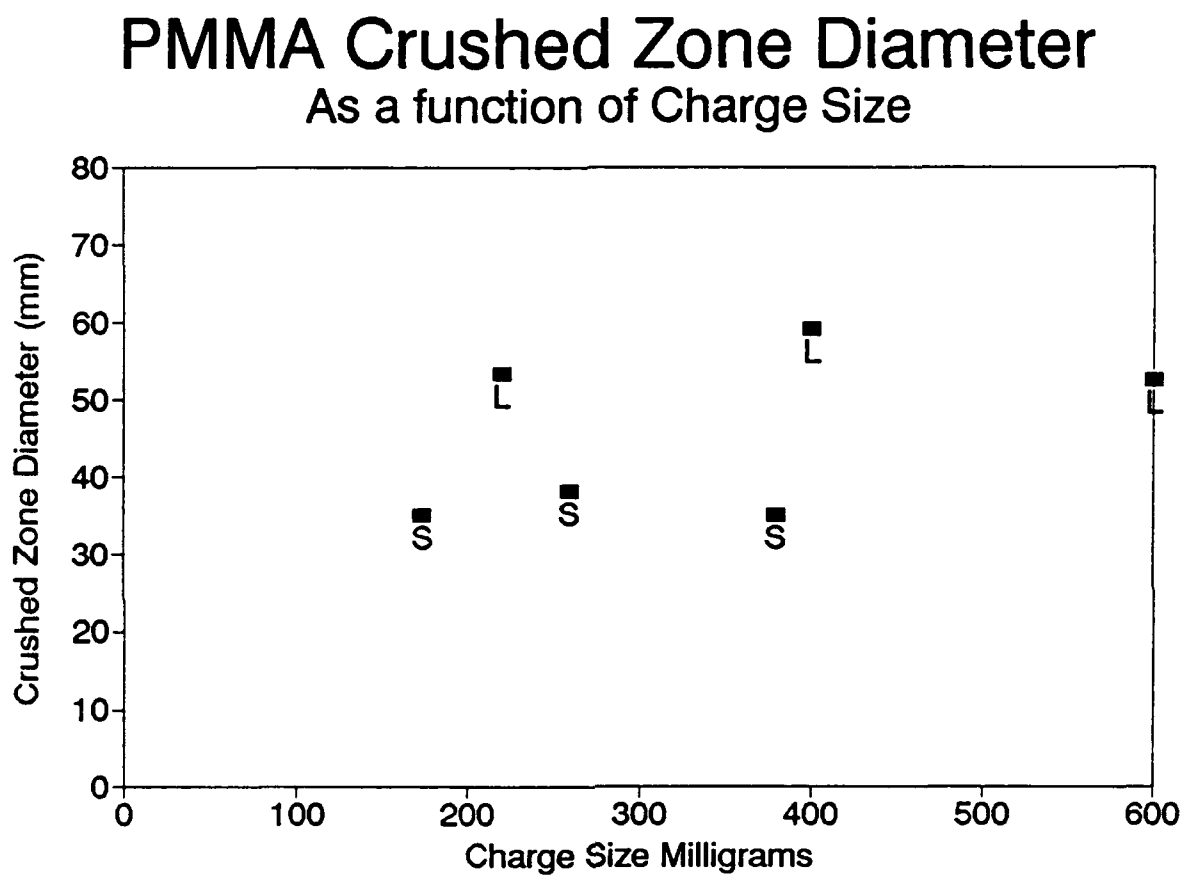


Figure 3.9a. Crushed Zone Diameter as a Function of Charge Size - PMMA.

Homolite Crushed Zone Diameter As a function of Charge Size

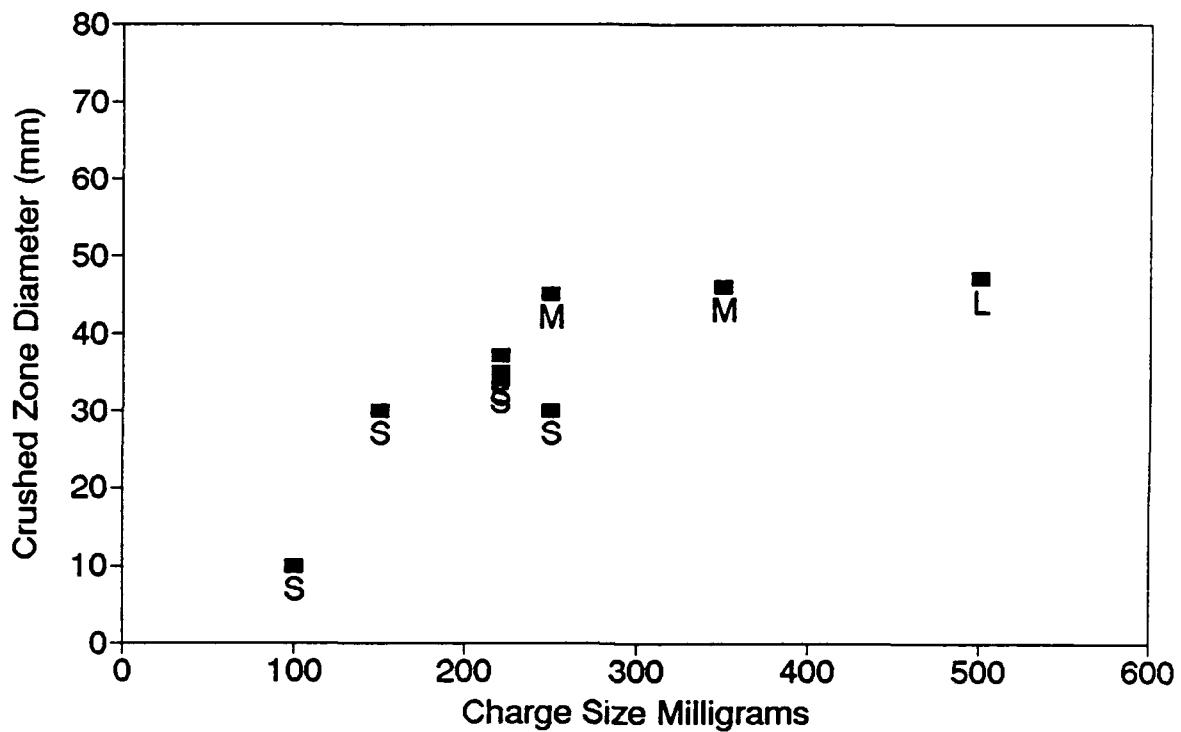


Figure 3.9b. Crushed Zone Diameter as a Function of Charge Size - Homolite 100.

PMMA Crushed Zone Volume As a function of Charge Size

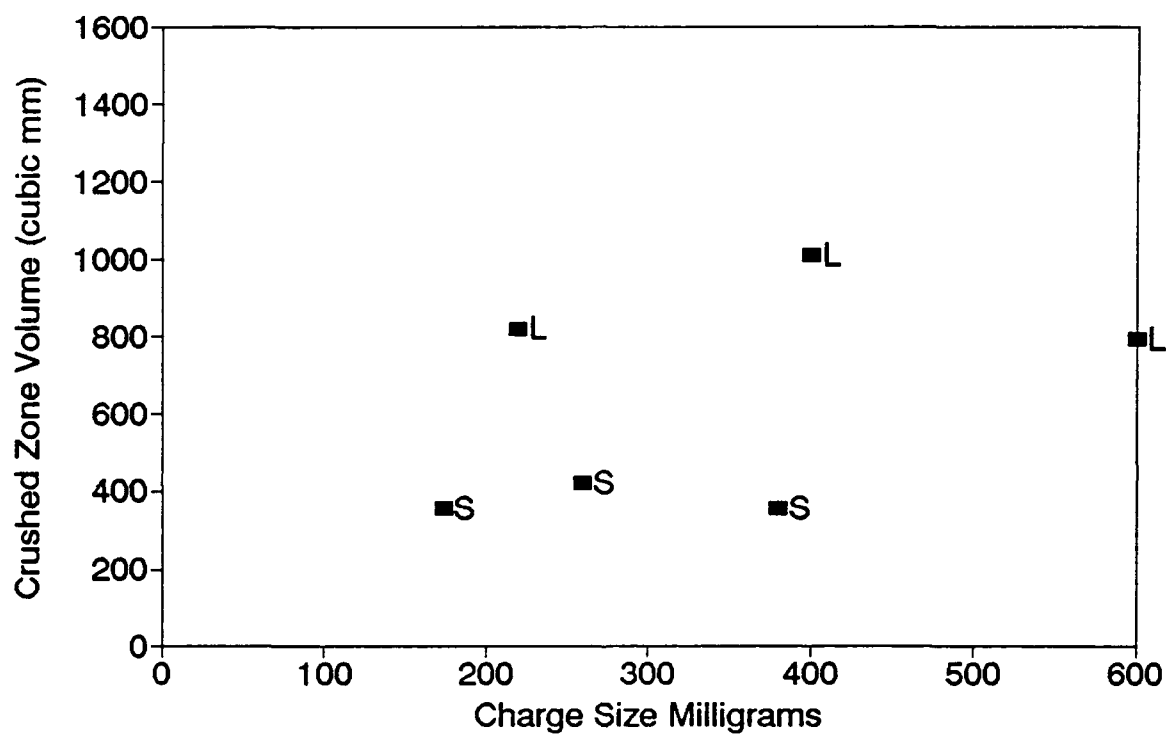


Figure 3.9c. Crushed Zone Volume as a Function of Charge Size - PMMA.

Homolite Crushed Zone Volume As a function of Charge Size

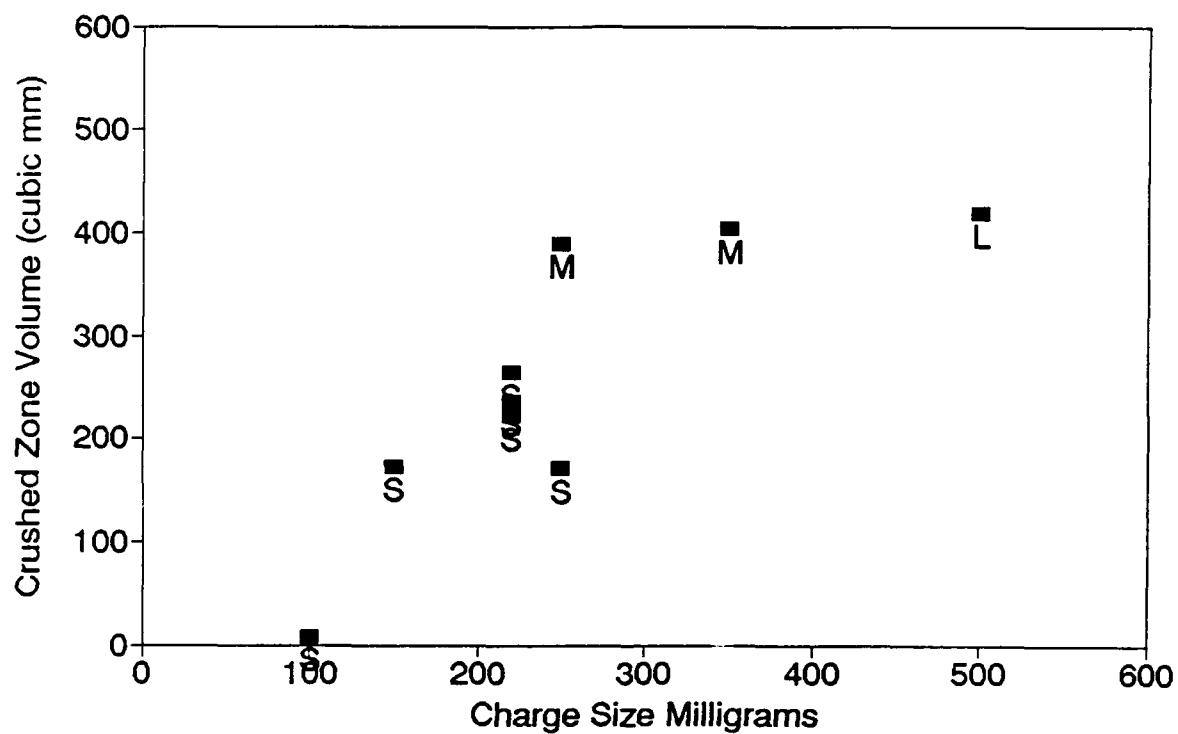


Figure 3.9d. Crushed Zone Volume as a Function of Charge Size - Homolite 100.

Ratio of Crushed Zone Diameter to Borehole Diameter vs. Charge Size

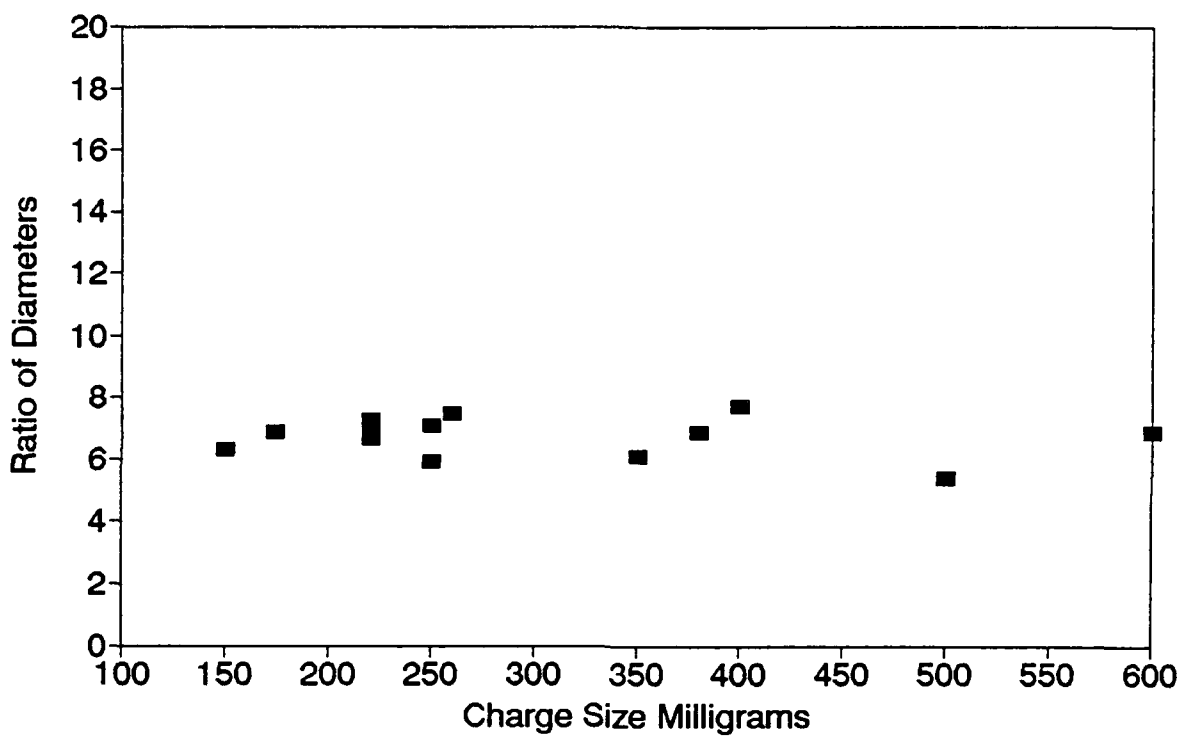


Figure 3.9e. Ratio of Crushed Zone Diameter to Borehole Diameter as a Function of Charge Size - PMMA and Homolite.

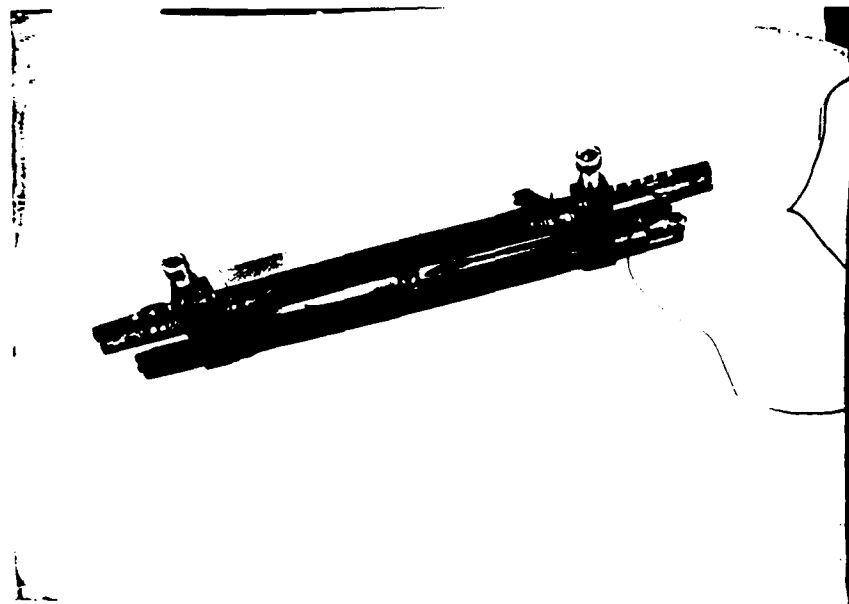
(3.6)

the PMMA models and Figure 3.9d shows the same information for the Homolite models. In the range of charges between 150 and 600 mg there appears to be no effect on either crushed zone diameter or crushed zone volume. The size of the diameter and the volume is different for the different sized boreholes but above 150 mg the diameter or the volume doesn't appear to increase. Figure 3.9e shows the ratio of the crushed zone diameter to the borehole diameter for all the models tested and this ratio appears to be fairly constant with respect to charge size. There is some scatter in the data but the trend is quite clear - as the charge size is increased by a factor of four from 150 mg to 600 mg there is very little increase in crushed zone extent or crushed zone volume.

These two results taken together present somewhat of a puzzle. As the charge size increases greatly (up to a 300 % increase) the crushed zone increases only slightly and the stress level only increases by a small factor (10 % to 33 %). The increase in energy must go into one or more of several possible ends - such as increased crush zone size, increased stress levels, additional air blast, etc.. The tests conducted lead to the conclusion that at least for the two dimensional model configuration investigated that the stress level is increased only slightly and since the crushed zone does not increase that the excess energy must go into the energy vented at the borehole in the way of smoke, noise, and air blast. In any event it is evident that only slight increases in stress levels traveling out into the medium are possible once a certain level is attained. From Figure 3.8 it appears that this level is reached at a very low charge size - well below the minimum 200 mg charge used for the test series conducted.

Looking again at Figure 3.6 in which 380 mg of PETN were used in a 5 mm diameter borehole it is evident that a significant level of loading was reached. As is evident from the figure, this loading resulted in a radial compressive stress of nearly 140 Mpa and a tangential compressive stress of about 34.5 Mpa in the leading edge (22.3 microseconds after detonation). Also evident from the figure is the lack of a significant tensile tail. As will be discussed later the tensile tail in the outgoing P-wave pulse is consumed by the initiation of radial cracks (and the tangential tensile tail is absorbed in the crushed zone).

A second series of tests were conducted to investigate the wave reflection from the free surface as well as the fracture formation in the vicinity of the borehole. These tests were also two dimensional and used Homolite 100 - a photoelastic material with about 10 times the photoelastic sensitivity to stress as PMMA. In these tests it was desired to view the isoclinics as well as the isochromatics - as well as the fracture formation process. The isochromatic fringes are lines along which the maximum shearing stress is a constant - and these are the fringes discussed earlier. Isoclinic fringes give the directions of the maximum principal stresses. We were interested in the isoclinics to determine if the



SMOKE GUIDING TUBE DEVICE

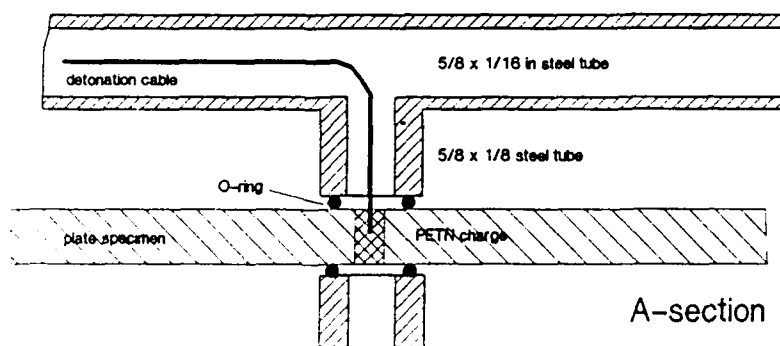
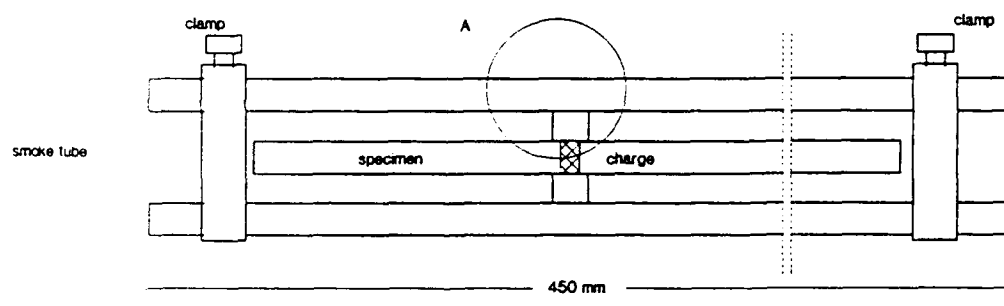


Figure 3.10. Photograph and Drawing of the Smoke Deflection Device used to Make Fracture Patterns Visible in the Borehole Vicinity.



Figure 3.11a. Frames from Three Separate Tests Showing Spall Initiation and Beginning of Branching of Radial Cracks.

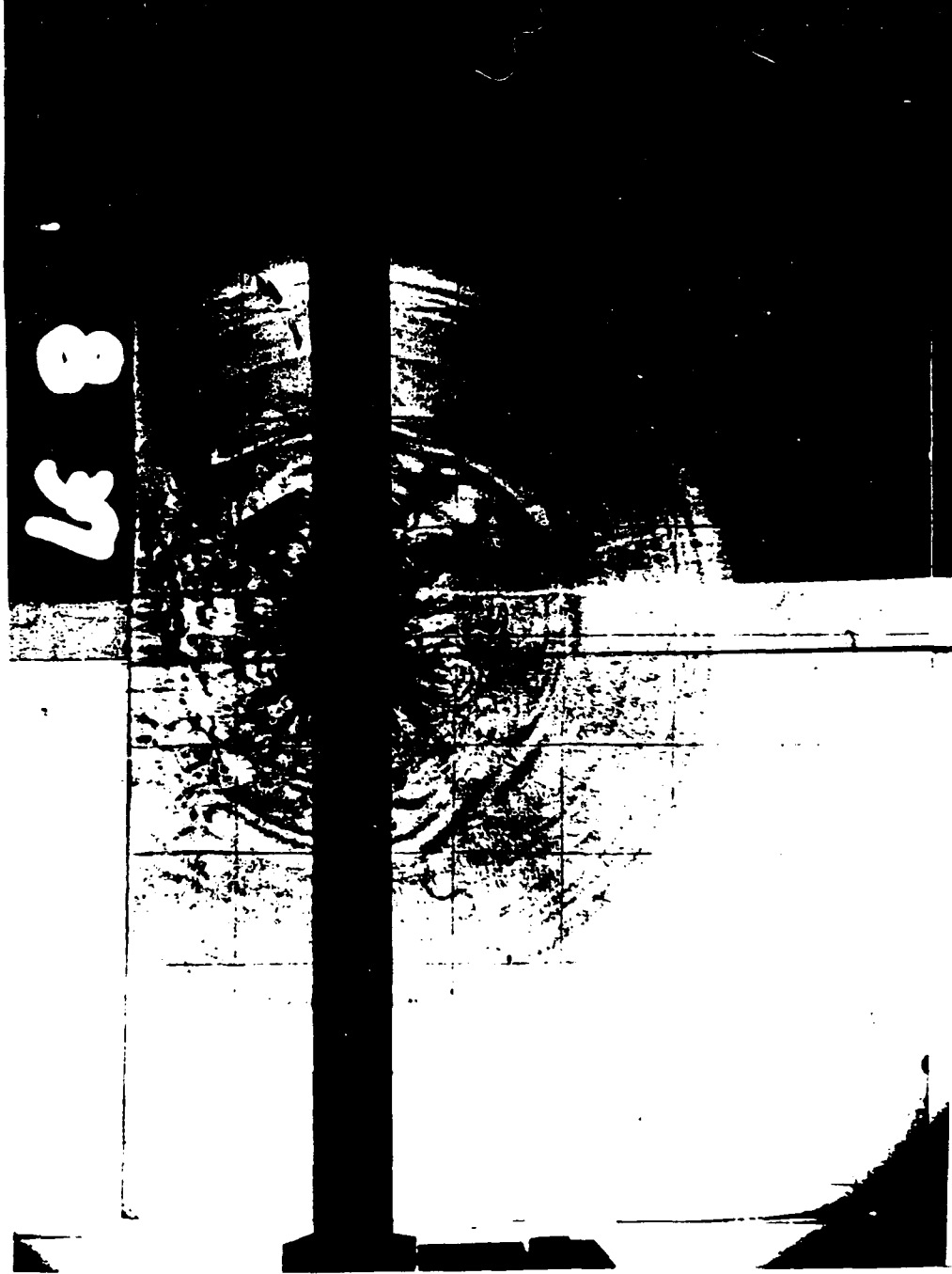


Figure 3.11a. Frames from Three Separate Tests Showing Spall Initiation and Beginning of Branching of Radial Cracks.

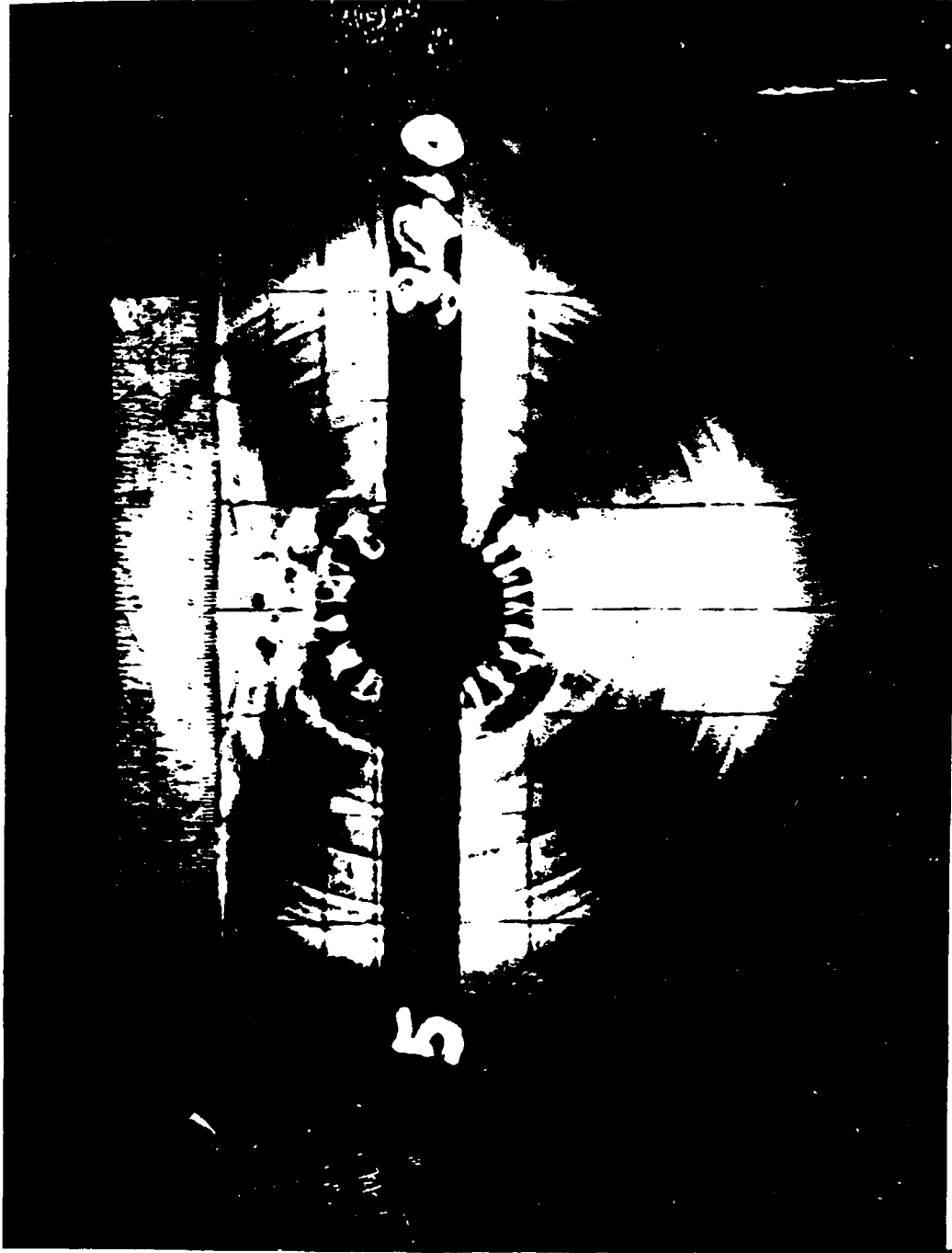


Figure 3.11a. Frames from Three Seperate Tests Showing Spall Initiation and Beginning of Branching of Radial Cracks.

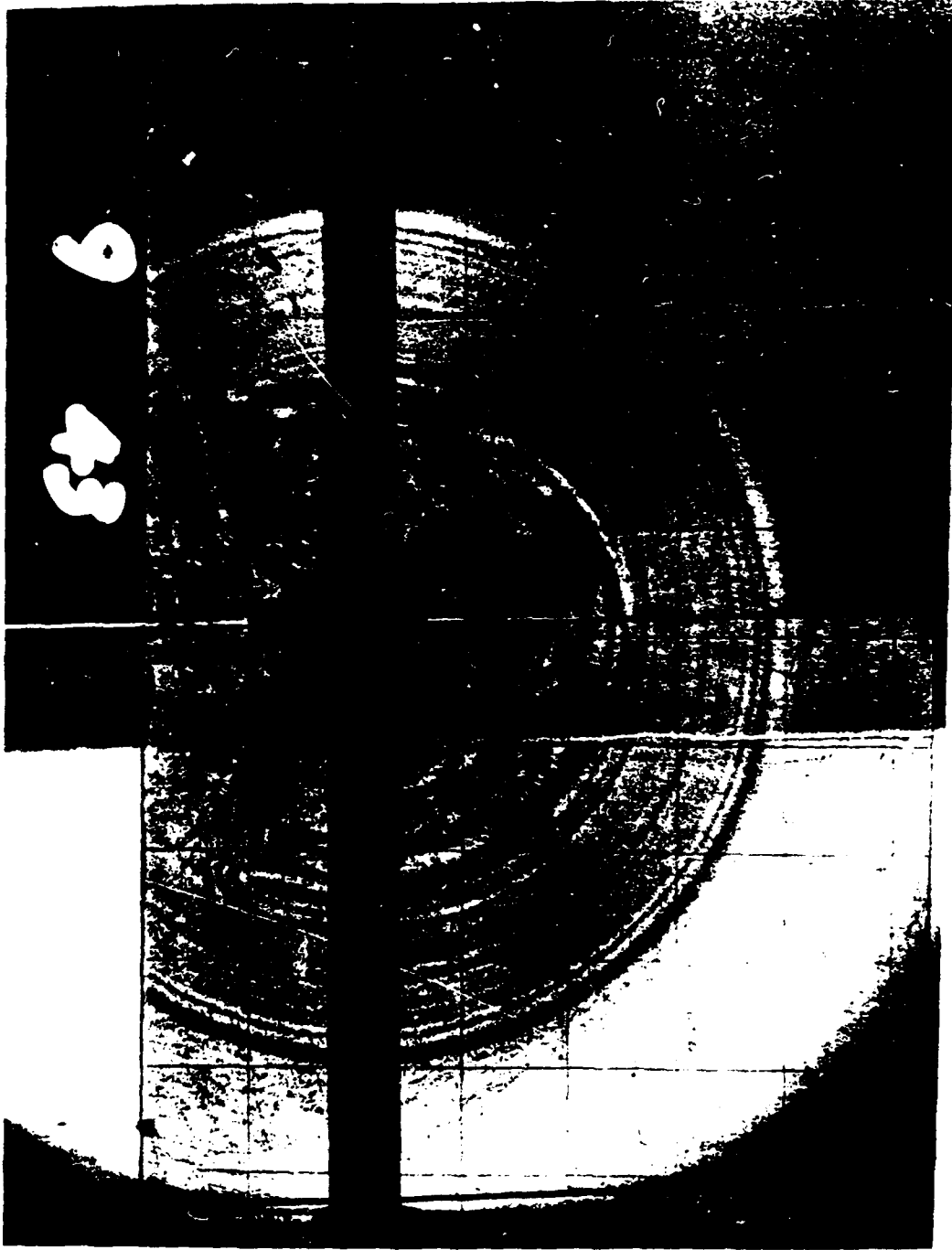


Figure 3.11b. Frames from Three Separate Tests Showing Multiple Spall Pattern and Beginning of Circumferential Cracking.

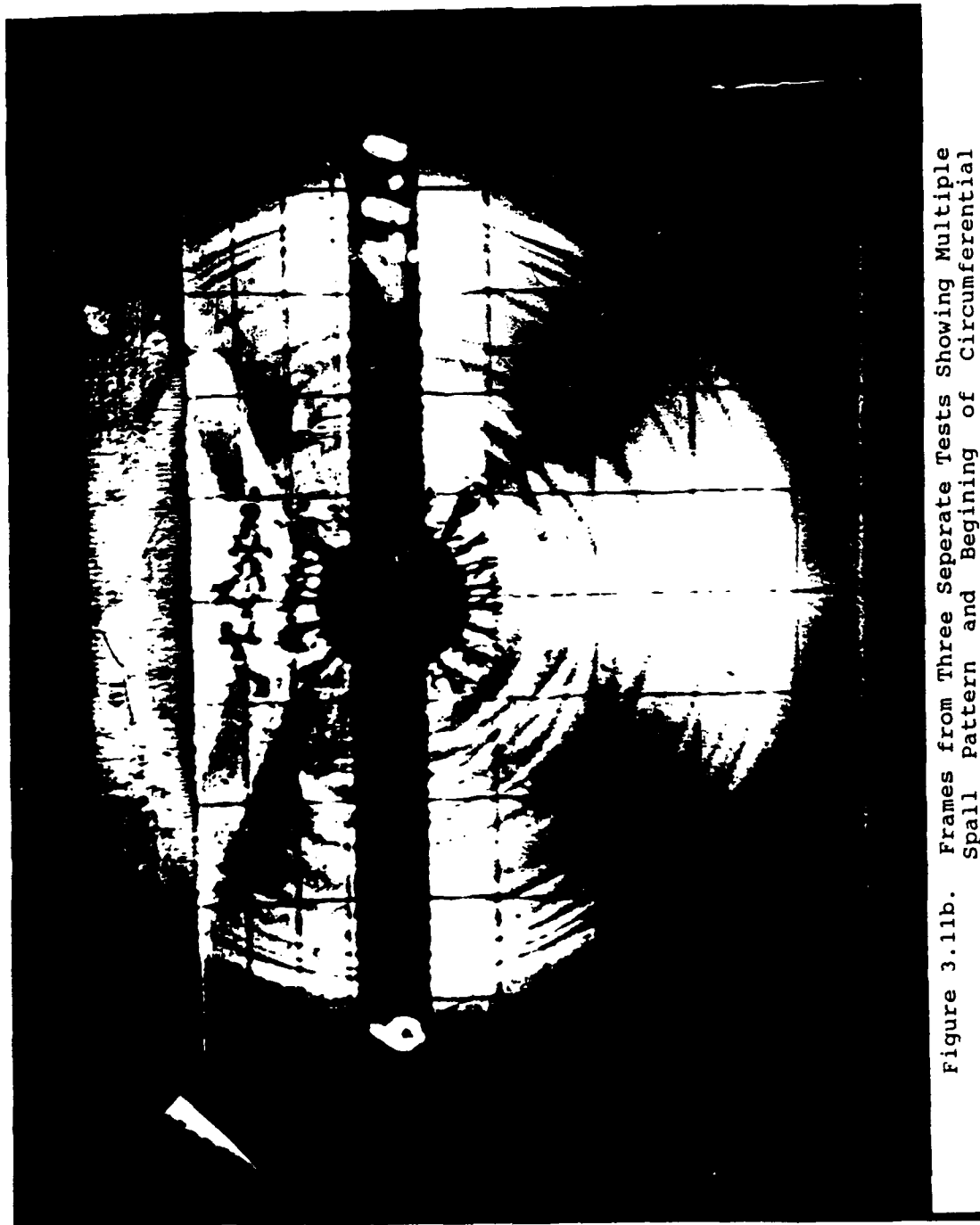


Figure 3.11b. Frames from Three Separate Tests Showing Multiple Spall Pattern and Beginning of Circumferential Cracking.



Figure 3.11b. Frames from Three Separate Tests Showing Multiple Spall Pattern and Beginning of Circumferential Cracking.



Figure 3.11c. Frames from Three Seperate Tests Showing Late Time Spall Development and Circumferential Crack Completion.



Figure 3.11c. Frames from Three Separate Tests Showing Late Time Spall Development and Circumferential Crack Completion.



Figure 3.11c. Frames from Three Separate Tests Showing Late Time Spall Development and Circumferential Crack Completion.

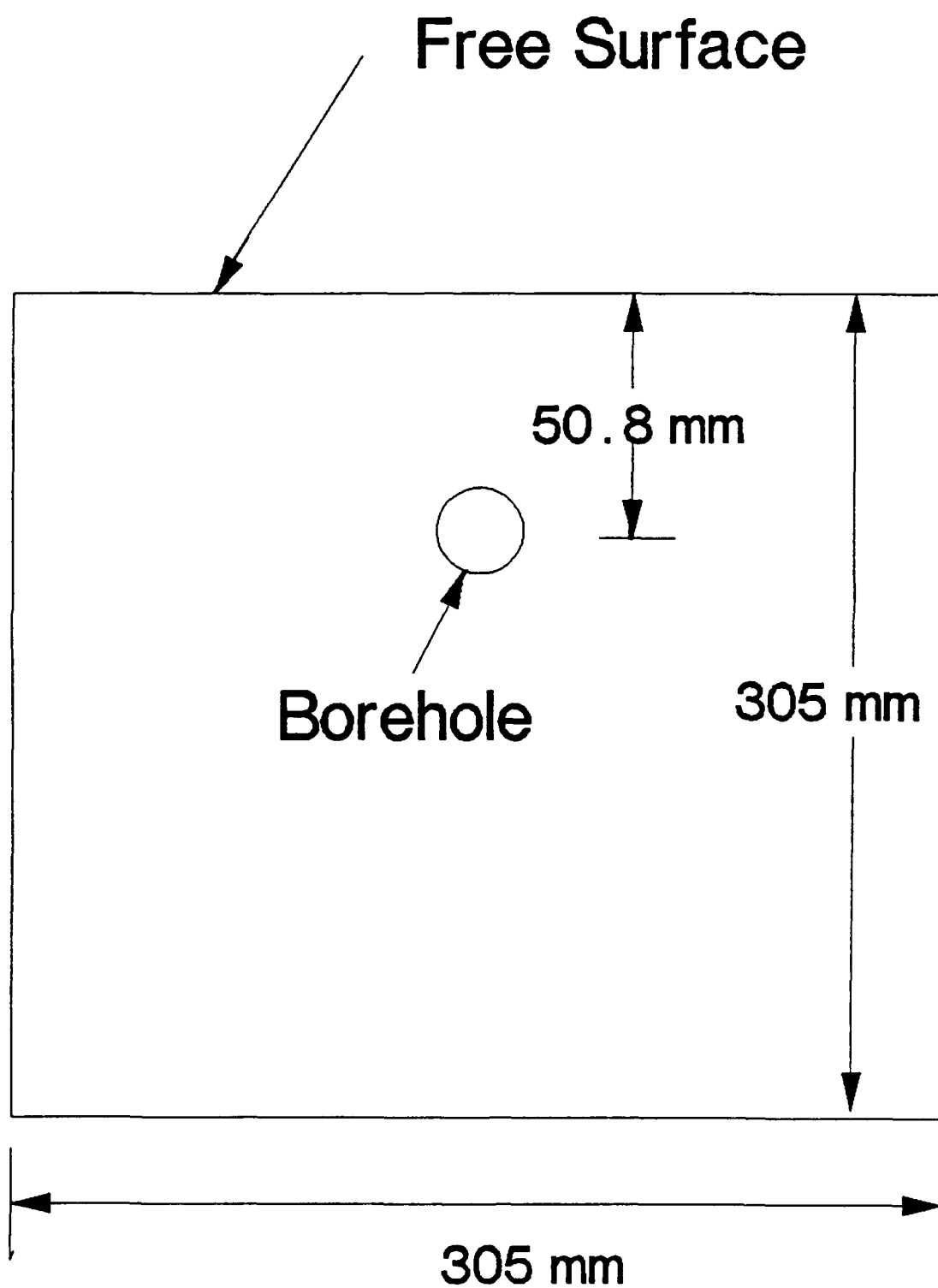


Figure 3.12. Geometry of the Models Used in Test Series.

(3.7)

crater formation angle was connected with the direction of the dynamic isoclinics. Porter [3.4] in work conducted for his doctoral dissertation showed with quasi static testing that the crater geometry was in good agreement with the static isoclinics created by pressure loading of the borehole. We were interested in seeing if this was true in the dynamic case.

In these tests the charge was placed 50 mm from the free surface and a special "tee shaped" tube was used on both sides of the two dimensional model to conduct the smoke and debris created by the explosive away from the fracture site. In this way the high speed camera could be used to maximum advantage to view the fracture formation process. Figure 3.10 shows a photograph and a detailed drawing of the device used. Figure 3.11 shows a series of photographs taken with the high speed camera from several different tests. These were taken between 31 and 51 microseconds after detonation of the explosive. The geometry of the test series is given in Figure 3.12. The size of charge used ranged from 100 mg to 250 mg with the smaller charge being used in a single test which utilized a model of 3.2 mm thickness whereas all of the other tests used models which were 6.4 mm in thickness. In all cases the borehole was located 50 mm from the nearest free surface as shown in Figure 3.12.

The photographs presented in Figure 3.11 are intended to show how the fracture and fragmentation occurs in a cratering situation. The speed of the outgoing P-wave in this material (Homolite 100) is 2460 m/s and as can be seen from the first frame presented the P-wave has travelled 75 mm from the explosive site in 31 microseconds. At this time many radial fractures have formed and have propagated to a distance of about 25 mm from the borehole. This propagation has occurred at an average velocity of about 737 m/s or about 30 % of the P-wave speed. These radial cracks were formed as a result of the tensile stresses which occur in the trailing portion of the outgoing P-wave. As these radial cracks are formed the amplitude of the tensile stress is decreased greatly. The first three photographs shown in Figure 3.11 were taken from three different tests in the time frame between 31 and 34 microseconds after detonation of the explosive. At this time the wave has reached the free boundary and has reflected back into the model a distance of about 25 mm. The fracture patterns in all three tests are very similar - about 24 radial cracks have initiated and are travelling away from the borehole very rapidly. There is a tremendous amount of energy driving these cracks and they are attempting to branch to effectively use up the excessive energy that is available since they cannot travel any faster than they are already moving [3.5]. Upon reaching the free face the bi-axial compression in the leading edge of the wave is converted into bi-axial tension and this tensile wave travels back into the model towards the borehole. The conversion of the compressive stress to the tensile stress occurs such that very near the free surface

(3.8)

there is a shadow zone [3.6] in which the value of the tensile stress is less than the tensile strength of the material - so no fracturing occurs. Outside of this shadow zone, however, the tensile stress in the inward travelling wave exceeds the tensile strength of the material the model is made of and fracturing occurs. This spall type of fracturing is very evident in the photographs shown in Figure 3.11. It is especially clear in the two photographs presented as Figures

3.11b and 3.11c taken at 34 microseconds after detonation where the fracture initiations can be clearly seen along the front of the reflected wave front (about 13 mm away from the free surface). In Figures 3.11b and Figure 3.11c the horizontal grid markings shown are 12.7 mm apart above the borehole and 25.4 mm apart below the borehole. Note that there are multiple initiation sites all along the reflected wave front - especially evident in Figure 3.11b. As the tensile stresses in the forward edge of the inward travelling P-wave initiate fractures the amplitude of the tensile stresses decreases since energy is used for the initiation process. If the amplitude upon reflection was sufficiently high, enough energy remains after the first fracture initiation to initiate other fractures as the wave continues to propagate inward. This is called multiple spalling. Multiple spalling is evident in Figures 3.11d through 3.11f where many lines of spall are visible. A close examination of Figure 3.11d for example shows five lines of initiation sites by multiple spalling. Note the multiple spalling evident in Figures 3.11e and 3.11f as well.

Also shown in Figures 3.11e and 3.11f are the creation of circumferential cracks as the front of the PP wave travels over the outward propagating radial cracks. The stress state in the PP-wave has the effect of turning the radial cracks into a circumferential direction and causing multiple branching to occur. This was noted in our earlier series of tests [3.7] and we called it "barrier branching" since the PP wave front acts momentarily as a barrier to the radial crack propagation. After the PP wave passes by, the cracks once again turn and propagate in the radial direction.

Figures 3.11g through Figure 3.11i give a good picture of what the fracture pattern looks like right after most of the initial wave action has passed. Note that at the time in question - namely about 50 microseconds after detonation - the area very near the free surface is fairly well fractured from the multiple spalling. The material there has very little strength. Although the original direction of initiation was parallel to the PP wave front, the state of stress in the front is bi-axial tension and fractures have formed and grown both parallel to the wave front and perpendicular to the wave front. On the side of the borehole towards the free face radial cracks have propagated about half the distance to the free face (or about 25 mm). On this side of the borehole the radial cracks have all been connected together with the circumferential cracking that was formed as a result of the barrier branching. As can be seen from Figure 3.11g and Figure 3.11i the

(3.9)

material contained in the 90 degree sector just between the free surface and the borehole is fairly well fragmented - even at this very short time after detonation. (The black x grid on those two frames divides the models into four equal segments of 90 degrees each.) In the area outside of this one 90 degree segment only radial fractures exist - not a combination of radial, circumferential, and spall fractures.

One of the biggest puzzles about the mechanism of crater blasting has been the evidence that has shown that the crater appears to travel from the borehole outward towards the free surface as opposed to traveling from the free surface inward [3.8]. If the main mechanism was that of spalling or of multiple spalling the fracture surface should show a propagation that would be from the free surface inward. In previous cratering experiments the evidence is quite clear that the final fracture surface for the crater is created by fractures that start at the borehole and propagate outward towards the surface. Results from this current test series clears up the previous misunderstanding in this regard. The process of crater formation is felt to be as follows. The spalling and multiple spalling occurs as indicated in the high speed frames presented in Figure 3.11, The radial cracking and the circumferential cracking which occurs between the borehole and free face further weakens the material in the 90 degree sector immediately above the borehole. This sector is very weak when compared to the material in the other three sectors. As time progresses the residual gas pressure acts on the material surrounding the borehole and begins to move the material in the directions of greatest weakness. This direction is in the 90 degree sector identified earlier and the radial cracks which define that sector are filled with gas pressure and grow to the free surface as the material in the sector is thrown from the borehole. When the final fracture surface is viewed after the blast is concluded the features on the surface are the outlines of the radial cracks which form the outline of the crater and these did grow from the borehole outward. The mechanism of the formation of the crater is, however, heavily dependent on the spall, multiple spall, and the radial/circumferential crack network which is formed by the PP wave passing back over the extending radial cracks. Once these mechanisms occur and the material between the borehole and the free surface is very much weakened, then the gas pressure fills the fractures that are connected to the borehole and the pressure then lifts and throws the material out of the crater. The radial cracks that form the outline of the crater therefore do grow from the borehole to the free surface. Figure 3.13 was taken relatively late in the dynamic event. The two photographs shown in that figure were taken at 230 and 237 microseconds after detonation. In these figures movement of the fragments near the free face is evident. The top surface is no longer straight due to movement of the pieces above the spall fracture described earlier. A close

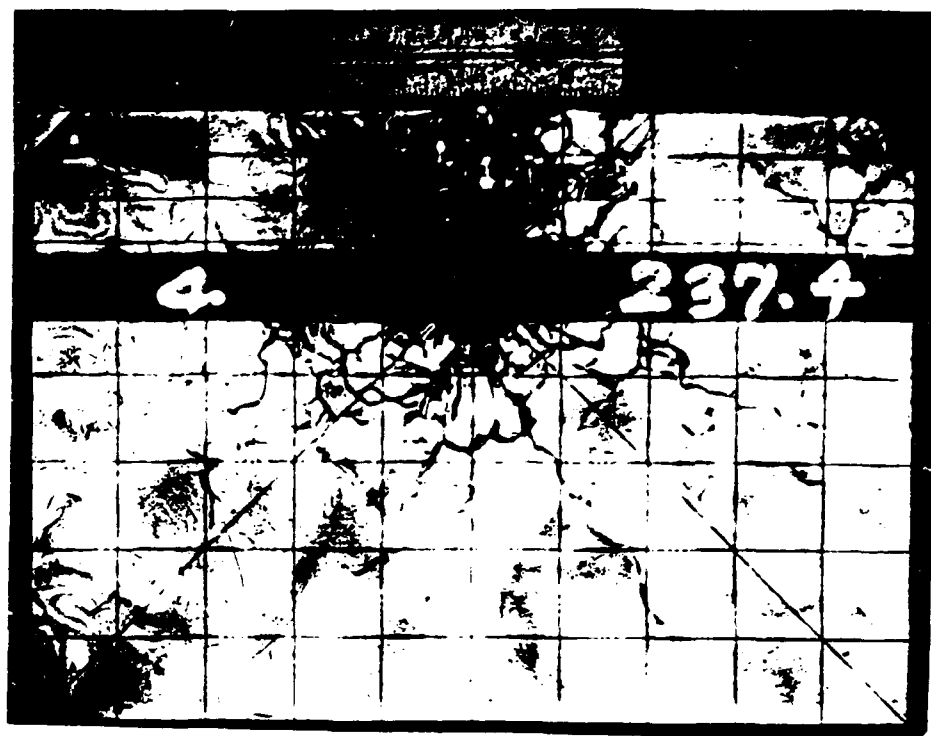
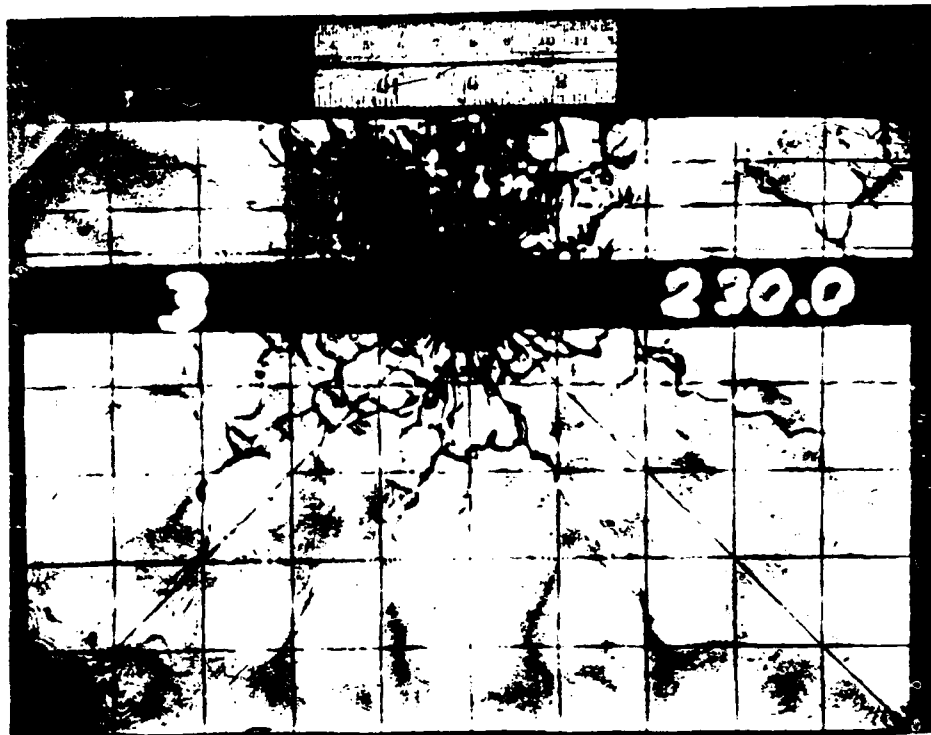


Figure 3.13. Photographs taken very Late in the Dynamic Event Showing the Radial Fractures that Define the Final Crater Propagating Towards the Free Surface.

(3.10)

look at the figures also shows radial cracks just outside of the 90 degree sector which contains most of the crater that are still propagating towards the free face. These are the radial cracks that are felt to define the final crater.

The next Chapter presents a numerical exercise that was conducted to strengthen the mechanism being proposed as a result of the above described tests.

REFERENCES:

3.1 "Photoelastic Investigation of Explosive Induced Fragmentation on Multiply Flawed Models", D.B. Barker, W.L. Fourney, and D.C. Holloway, Proceedings of 1979 SESA Spring Meeting, San Francisco, Calif., May 1979.

3.2 "The Roles of Stress Waves and Discontinuities in Rock Fragmentation", S.R. Winzer and A. W. Ritter, Proceedings 21st US Symposium on Rock Mechanics, Rolla, Mo., 1979.

3.3 "Stress Wave Propagation in a Half Plane Due to a Transient Point Load", J.W. Dally and W.F. Riley, Developments in Theoretical and Applied Mechanics, Vol. 8, 1966.

3.4 "A Role of the Borehole Pressure in Blasting: The Formation of Cracks", D.D. Porter, PhD Thesis, University of Minnesota, Minneapolis, 1979.

3.5 "On the Determination of the σ -K Relationship for Birefringent Polymers", G.R. Irwin, et.al., Experimental Mechanics, Vol. 19, No. 4, 1979.

3.6 "Photoelastic Investigation of Fragmentation Mechanisms, Part II - Flaw Initiated Network", D.B. Barker and W.L. Fourney, National Science Foundation Report, August 1978.

3.7 "Photoelastic Investigation of Fragmentation Mechanisms, Part I - Borehole Crack Network", D.B. Barker, W.L. Fourney, and J.W. Dally, National Science Foundation Report, March 1978.

3.8 "Model Study of Crater Blasting", W.L. Fourney, R.D. Dick, and K.R.Y. Simha, Rock Mechanics and Rock Engineering 21, pp. 183-2005, 1988.

CHAPTER IV. COMPUTATIONAL INVESTIGATION.

In an effort to verify the correctness of the mechanism of fragmentation proposed in the preceding section, it was decided to perform finite element calculations.

The proposed mechanism was based primarily on results obtained from the dynamic photoelastic tests. These were conducted in two-dimensional models. We desired to compare these results to the results of tests conducted in three dimensional models in materials that were more rock like in behavior.

A two-dimensional finite element computation was conducted to predict the velocity (magnitude and direction) of selected points within a model which could be compared to velocity results obtained from instrumented concrete models. The best results for comparison were obtained in cylindrical models made from high pozzolan concrete. These tests were described in Chapter II. The models possessed high strength and low porosity and reacted to the explosive loading in a fashion that simulated as close as possible an actual rock structure. The fact that it was a cement, however, permitted the insertion of various forms of instrumentation into the final models.

Of particular interest are the results obtained from four tests (ROC-7 through ROC-10). Of the four models, two were constructed with velocity gage loops designed to measure vertical velocities and two were constructed with loops designed to measure radial particle velocities. In order to form a complete test matrix, two experiments were conducted with spherical charges of one gram of PETN with each type of velocity gage and two were conducted with cylindrical charges comprising a one gram charge (PETN) in a 6 to 1 cylindrical aspect ratio. With the low porosity, low compaction, high strength and rock like fracturing of the rock stimulant, the four samples covering the two charge geometries and two velocity gage configurations provide a good database for predicting quantitatively rock motion.

Figure 4.1 shows the geometry of the model used for the four tests and the placement of the gages. The model was cylindrical in shape with a diameter of 254 mm and a height of 208 mm. The center of the charge was 57.1 millimeters from the upper (closest) free face. The locations of the six velocity gages used in each test are given in the figure which shows only the upper right hand quarter of the model. Tests ROC-9 (vertical velocity) and ROC-10 (radial velocity) employed the spherical charge and are the ones that will be used to compare to the computational results. All six gages were successfully recorded in all tests except for ROC-9 where gages 1 and 4 were lost due to amplifier malfunction. The results from gages similarly located in the model which used a cylindrical charge will be used for comparison purposes for these two gages.

(4.2)

Typical results obtained from the gages are shown in Figure 4.2. In this figure results are given for radial velocity from the two gages nearest the charge for both the cylindrical charge (ROC-7) and the spherical charge (ROC-10). As shown in the figure the initial velocity is outward and some rebound occurs at about 30 microseconds which results in a short period of inward velocity. The figure also points out that there are slightly higher radial velocities in the case of a cylindrical charge than for a spherical one. Typical results for vertical velocities are shown in Figure 4.3. The results shown are for the gage closest to the free surface and above the charge (gage 3) and the gage just below that gage (gage 2). As was the case for the radial velocities the vertical velocities for the cylindrical charge are also slightly larger than the vertical velocities from the spherical charge. At later times (greater than 30 microseconds) the initial upward velocity from the cylindrical charge reverses and there is a rebounding effect. For the spherical charge the vertical velocities do not reverse but remain positive (upward) during the recording time. Notice that the velocities recorded by gage 3 which is very close to the free surface are both larger at latter times than those recorded by gage 2 - for both the spherical and cylindrical charges - as would be expected. It can also be observed from these figures that the results obtained for the cylindrical charges were not greatly different from the results obtained from the spherical charges.

The velocity data recorded was integrated over time to produce displacements in the radial and the vertical directions and these displacements are shown in Figures 4.4 (Cylindrical Charge) and 4.5 (Spherical Charge). In Figures 4.4 and 4.5 the vertical and radial components have been plotted together to yield particle trajectories. The trajectories given for gages 1 and 4 in Figure 4.5 are really the trajectories for the radial displacement of a spherical charge and a vertical displacement for a cylindrical charge (the vertical displacements for those two gages for a spherical charge were lost as indicated earlier). Once again a comparison of these two figures shows the similarity between the results for the cylindrical charge and the spherical charge at these early times after detonation (100 microseconds).

In order to determine if the fragmentation mechanism proposed in the previous section is valid it was assumed that the two dimensional models tested using dynamic photoelasticity were related to the three dimensional tests described above in the following fashion. The two-dimensional plane stress models tested photoelastically were assumed to have been taken from the three dimensional tests as shown in Figure 4.6. As shown in that figure the two dimensional model represent a section taken from the three dimensional model through the borehole.

The fragmentation pattern that existed at 50 microseconds in the high speed photoelastic models was taken as the starting

AFOSROCK - VELOCITY GAGE DATA
ROC-7 (CYLINDRICAL) VS ROC-10 (SPHERICAL)

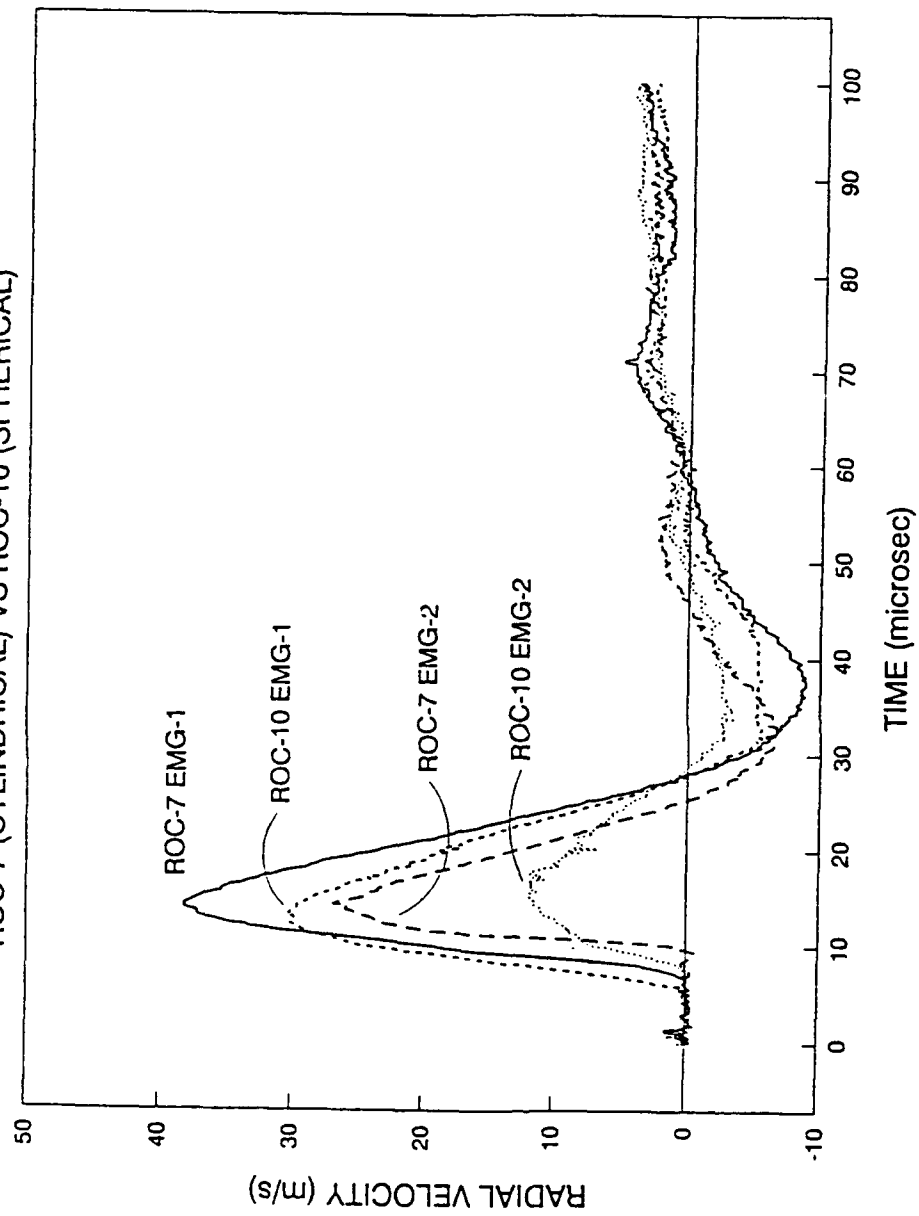


Figure 4.2. Radial Velocities from Concrete Models with Spherical and Cylindrical Charges.

AFOSROCK - VELOCITY GAGE DATA ROC-8 (CYLINDRICAL) VS ROC-9 (SPHERICAL)

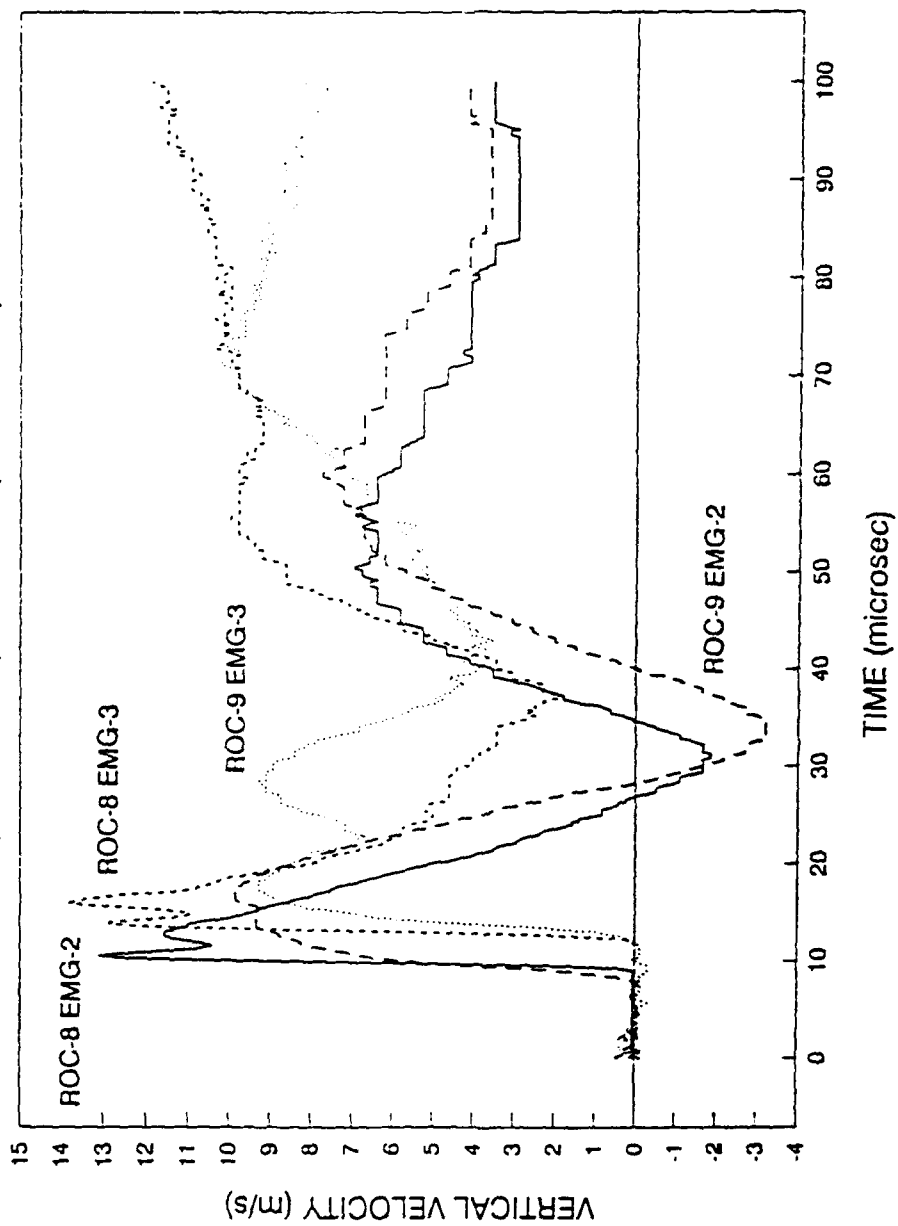


Figure 4.3. Vertical Velocities from Concrete Models with Spherical and Cylindrical Charges.

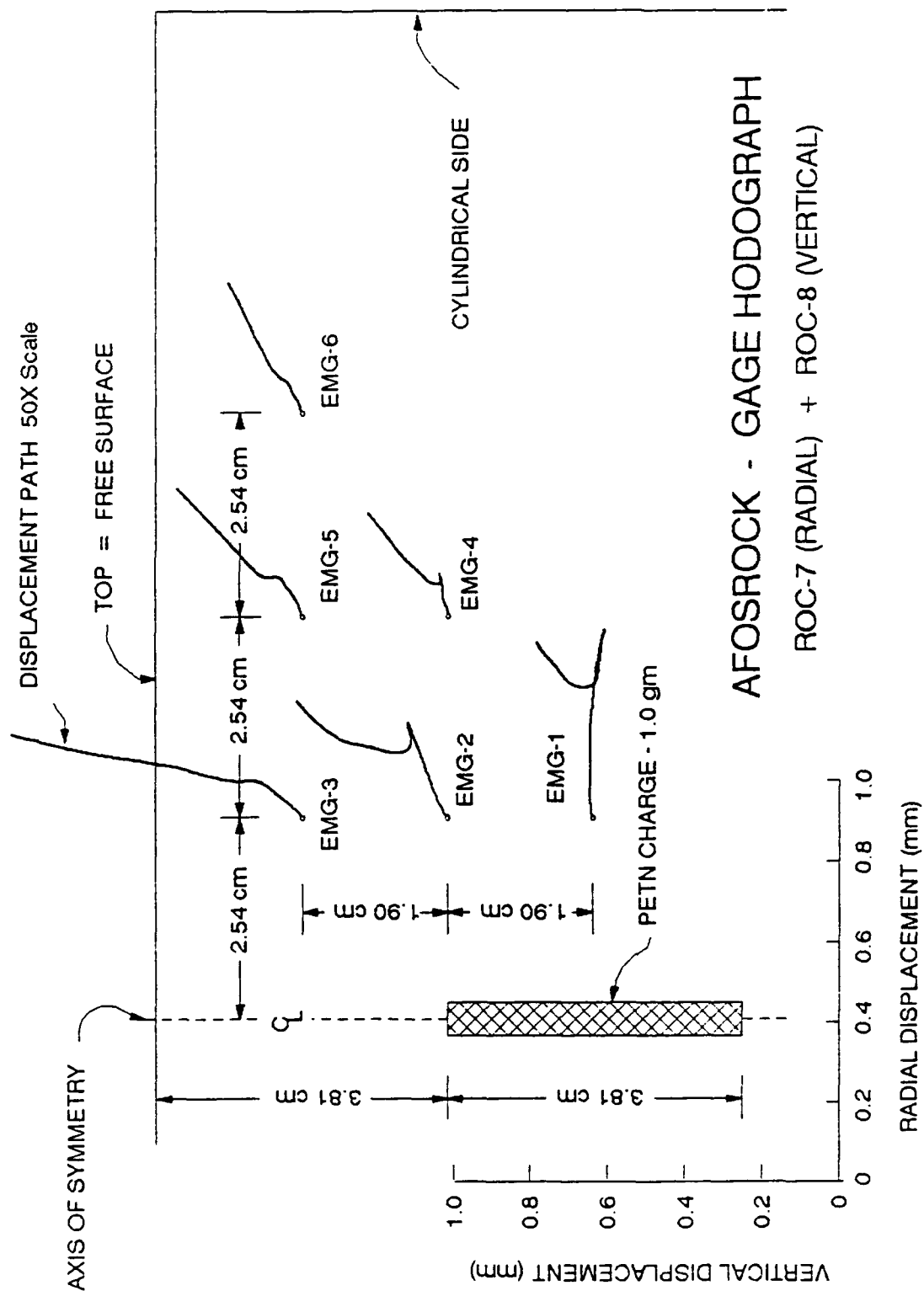


Figure 4.4. Particle Motion Trajectories with Cylindrical Charge.

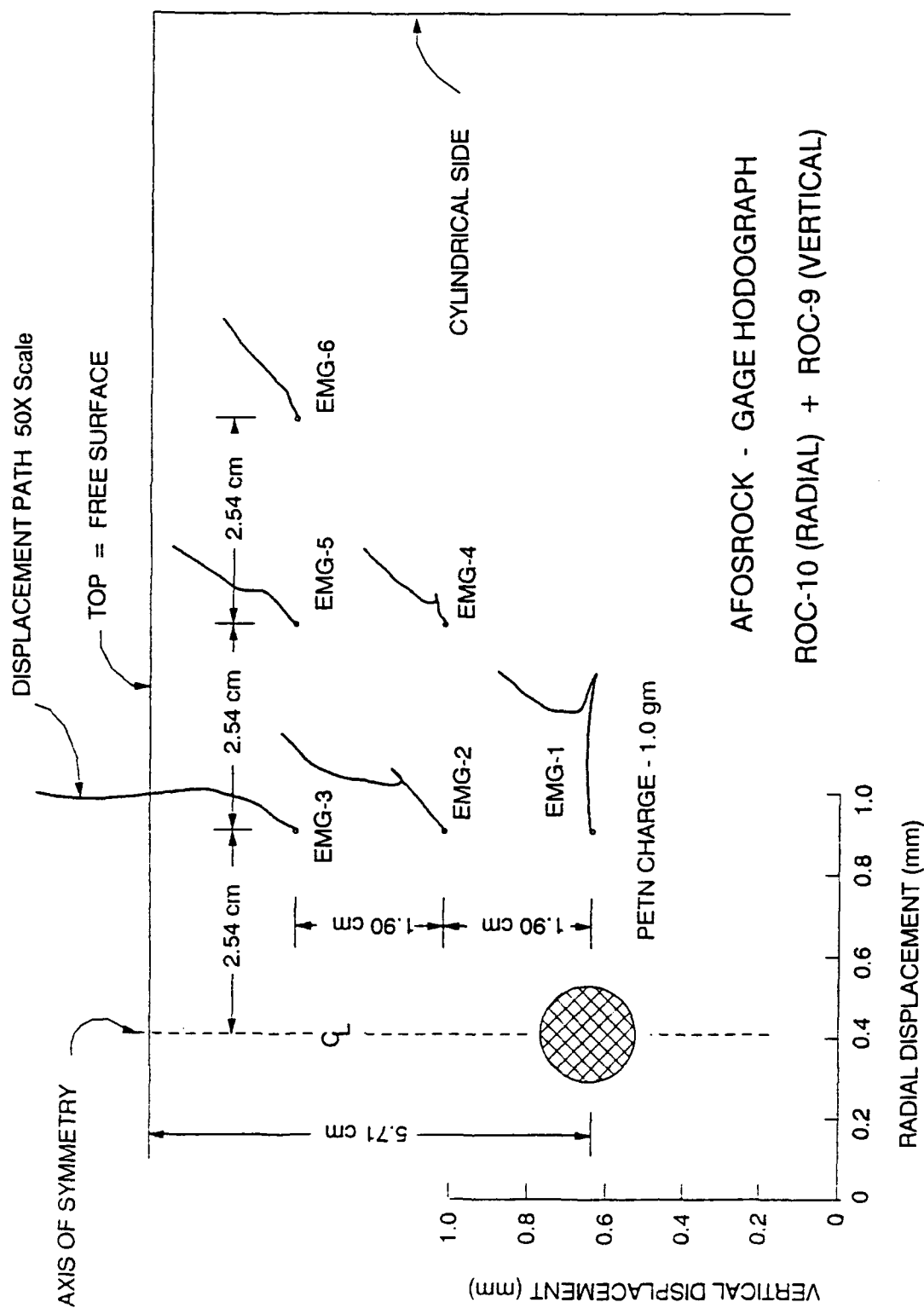


Figure 4.5. Particle Motion Trajectories with Spherical Charge.

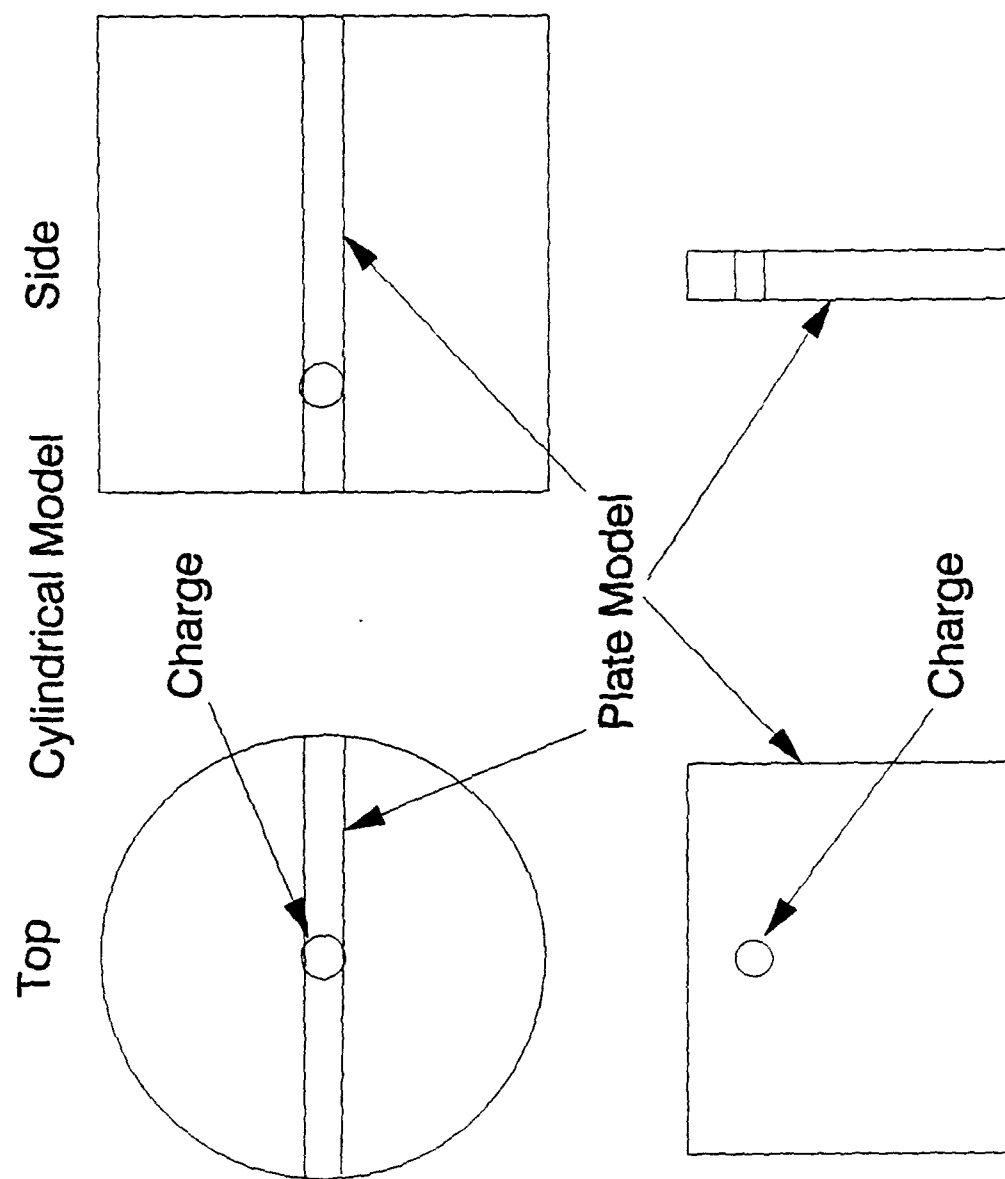


Figure 4.6. Visualization of How Two Dimensional Models were Taken from Three Dimensional Models.

(4.3)

geometry for a static finite element analysis. This fractured and fragmented model was loaded with a static pressure of 1600 psi. The magnitude of the pressure was determined from an examination of pressure versus time determined in similar three dimensional testing configurations which had no stemming and were free to vent to the atmosphere. One such curve is shown in Figure 4.7. The model which was used to determine the pressure time curve shown was unstemmed and was fragmented during the test and therefore vented both through the borehole and through resulting fractures. The pressure value chosen is therefore felt to be representative of what would have been found if pressure in the borehole of the photoelastic tests had been measured.

Figure 4.8 shows the finite element grid used to represent the model. Figure 4.8 a) shows half of the assumed symmetric model. The solution obtained is a plane stress solution with a plate size of 254 mm by 7 177 mm by 6.4 mm thick. MARC 4, a commercial finite element program was used to obtain a solution. Figure 4.8 b) presents an enlarged view of the borehole/free surface area of the model. The curved boundary at the top of the figure represents the boundary of the spalled region as observed in the photoelastic tests. It is assumed therefore that the material between the spall front and the original straight free surface is incapable of carrying any load. The height of this non load carrying area is 10 mm in the finite element computation. It is also assumed that 16 radial cracks have propagated to a distance of 17 mm from the borehole center at the time that the pressure is applied.

In addition, for the seven cracks around the top of the borehole it is assumed that circumferential cracking has occurred. The initial geometry for the borehole area is perhaps better understood by viewing Figure 4.8 c) which shows an enlargement of the borehole region. Note that there is no circumferential cracking assumed for the radial cracks located around the bottom of the borehole. An even larger view of the borehole region is shown in Figure 4.8 d). In the finite element computation the 1600 psi pressure was assumed to act on all crack surfaces - radial and circumferential. The material properties used in the finite element computation were those of Homolite 100. In particular, a modulus of 500,000 psi and a poisson's ratio of 0.2 were used with a borehole diameter of 5 mm to calculate displacements at the six locations where the velocity gages were placed in Tests ROC-7 through ROC-10.

In summary, a finite element computation was carried out. The analysis was a static one and acted on a geometry which corresponded to the fragmentation pattern that was seen in the dynamic tests at a time period corresponding to a time when the strongest wave activity was finished. It was felt that if good

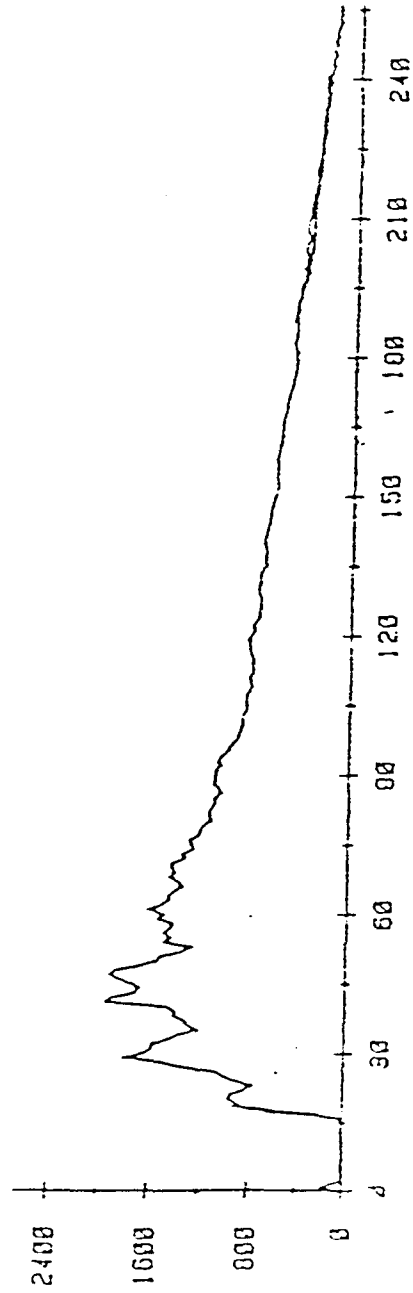


Figure 4.7. Pressure Profile from Model Tests which was used in Computational Effort.

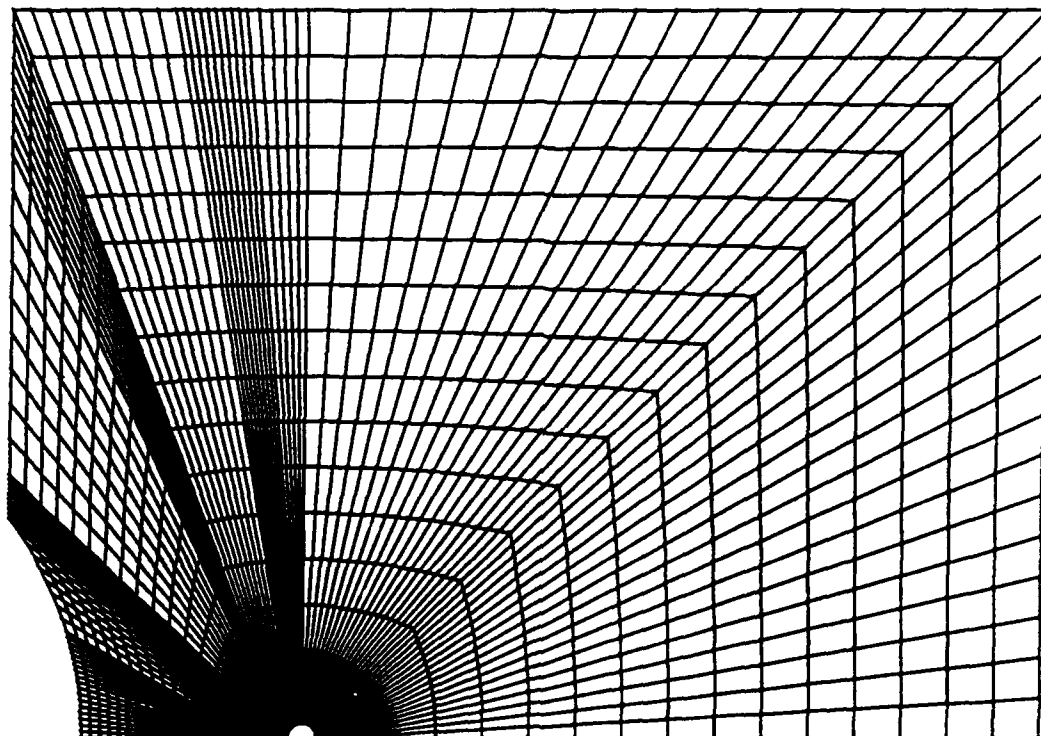


Figure 4.8a. Finite Element Grid used in Computation - only half of model is shown.

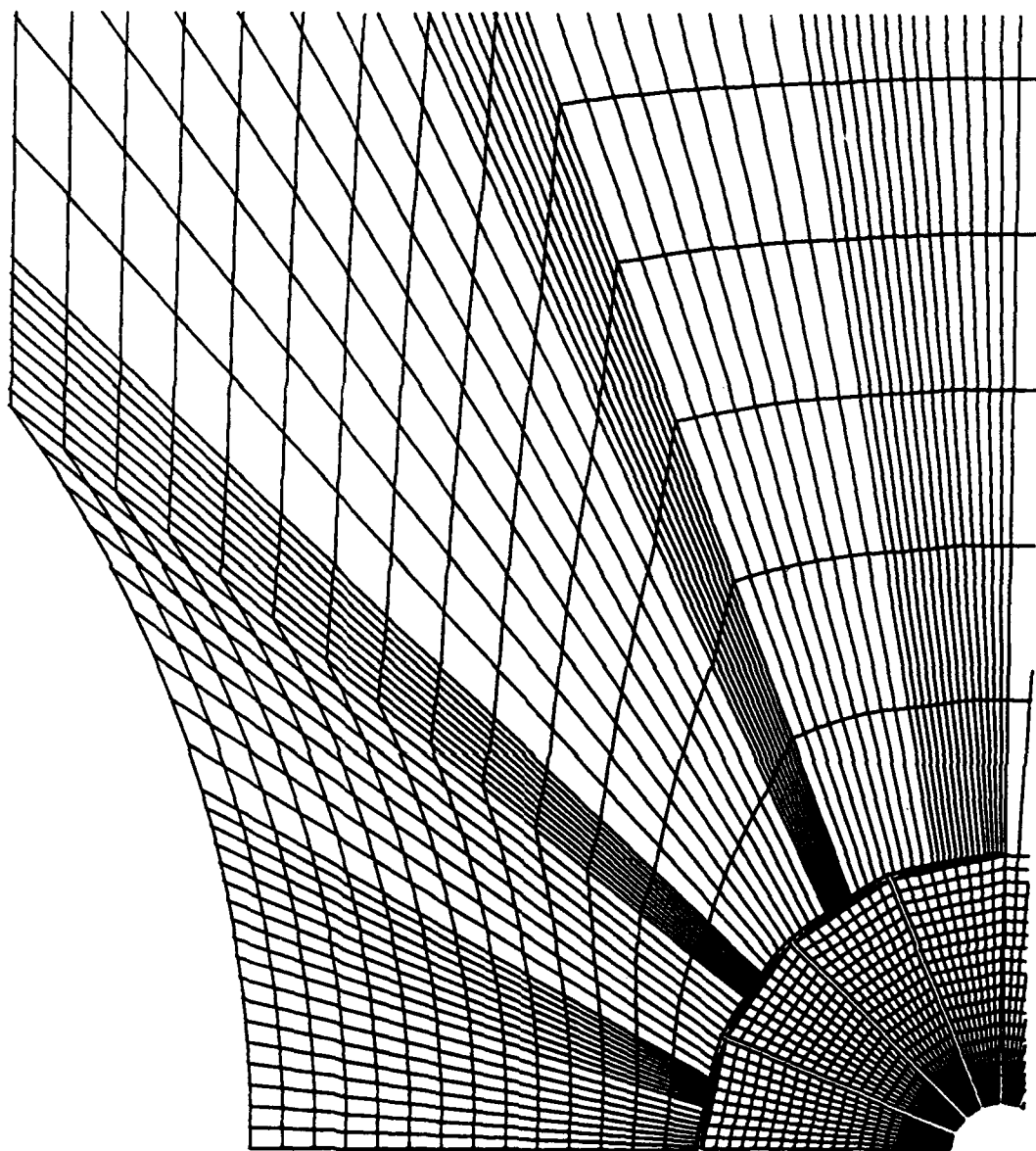


Figure 4.8b. Finite Element Grid Enlargement showing upper quarter of model.

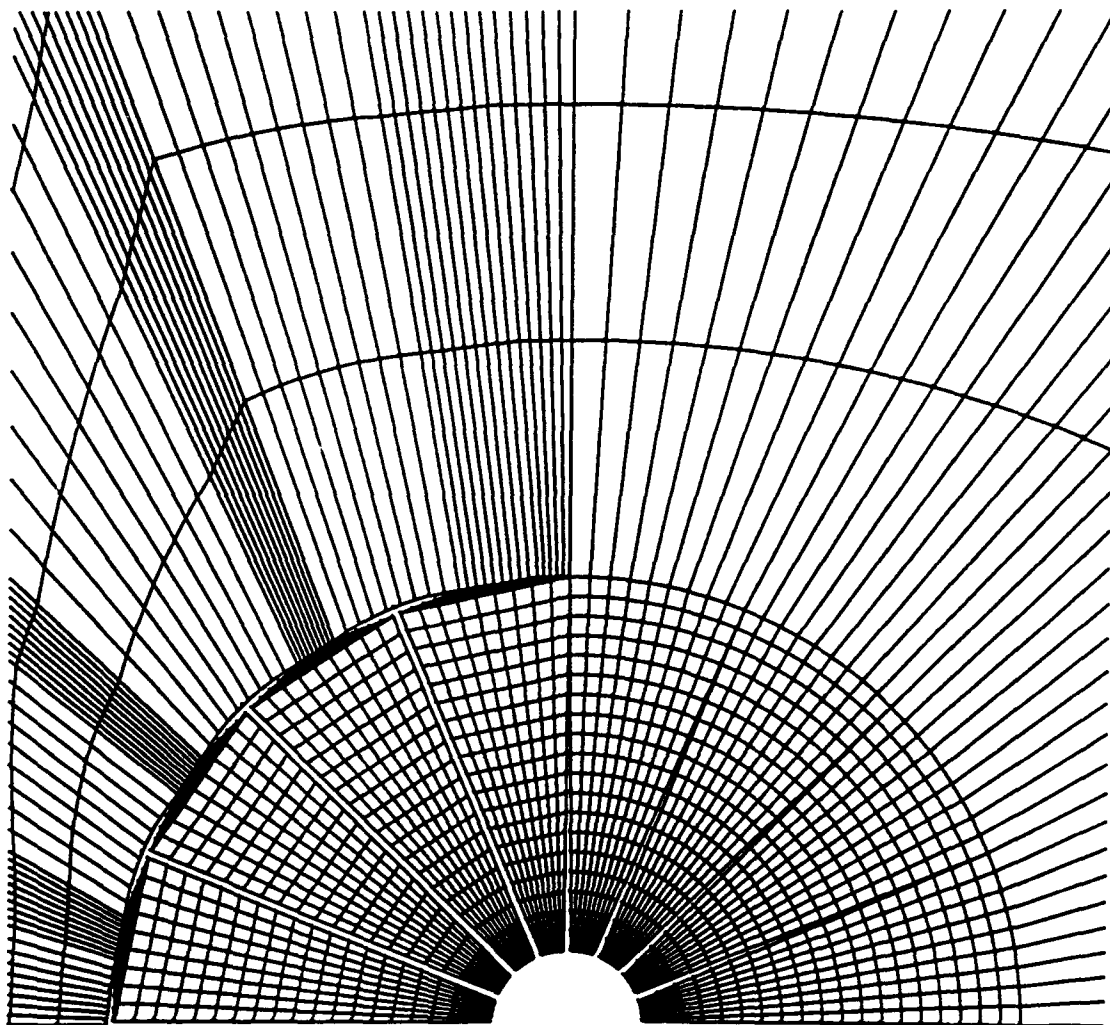


Figure 4.8c. Finite Element Grid in Vicinity of Borehole.

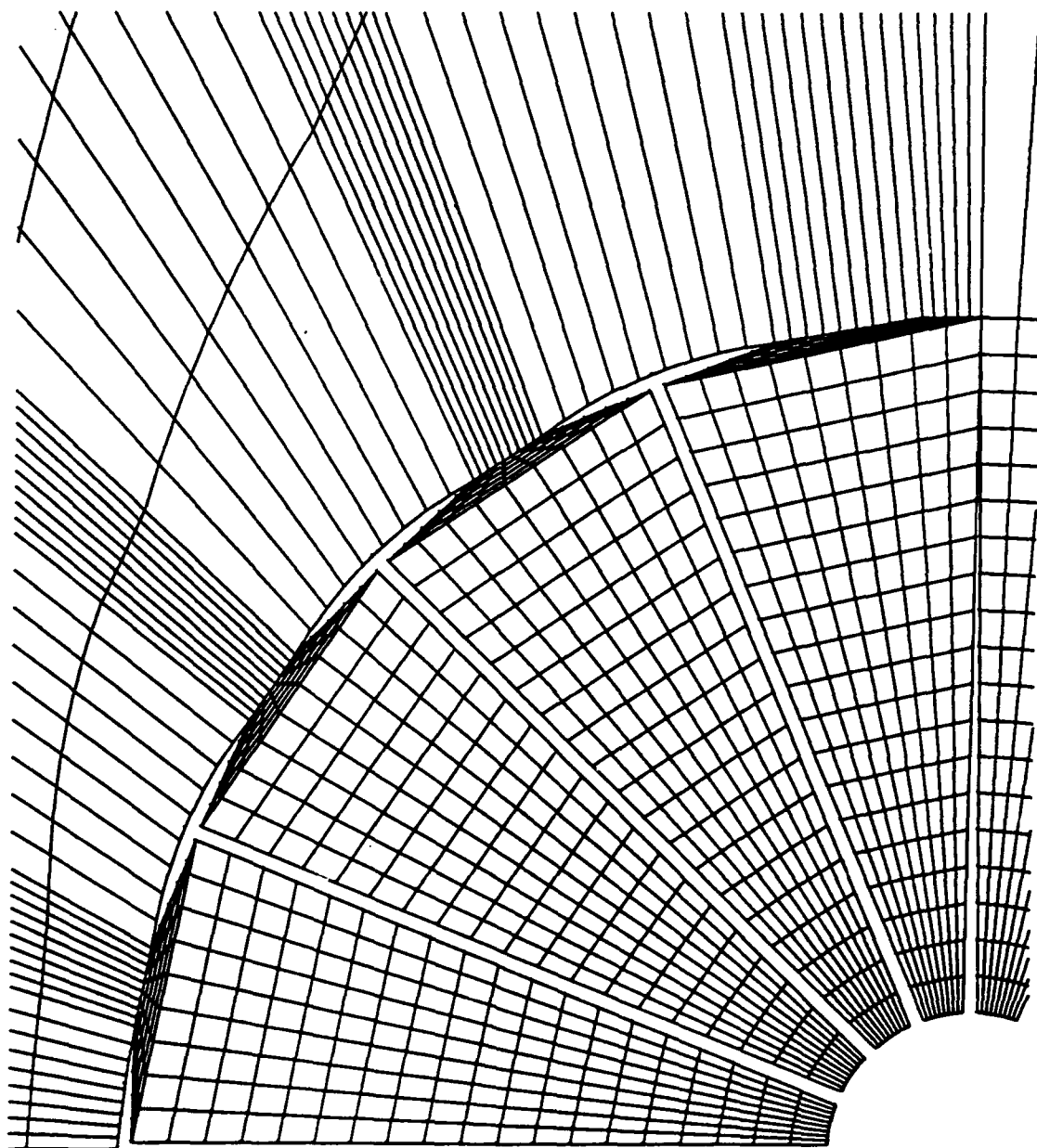


Figure 4.8d. Finite Element Grid showing details of Radial and Circumferential Cracking.

(4.4)

correlation could be shown between these finite element computations and the results of the testing in the three-dimensional cement models that it would add credibility to the proposed mechanism of fragmentation.

A comparison of the results obtained from the finite element computations and the measurements made in the "super" cement - both with a spherical charge - are shown in Figure 4.9. The lines represent the results obtained from integration of the velocity gage data and shows the displacements over the first 100 microseconds after detonation of the charge. The arrow represents the vector displacement obtained from the finite element computation for the static pressure loading of the fragmented model with 16 radial cracks and short circumferential cracks at the tips of the radial cracks around the top of the borehole. Since the material properties used in the finite element computations were for Homolite and the tests were conducted in cement some modification had to be made to reflect these differences in properties. In order to correct for this, the magnitude of the displacement computed for gage 3 was set equal to the magnitude of displacement measured in the cement at 100 microseconds.

As can be seen from Figures 4.9 a) through 4.9 f), the agreement is good - especially at early times for gages 2, 3, 4, and 5. The finite element result agrees very well with the displacement measured at gage 1 at later times and the agreement is not very good with gage 6 - at any time. Looking at the overall trend the measured velocity at gage 3 (the gage above the charge and nearest the free surface) has a much higher vertical component of displacement than predicted by the computation (and the fragmentation mechanism). For all of the other gage locations the finite element prediction is quite good except for gage 6 (the gage farthest from the borehole and closest to the free surface). For that location the measured displacement also has much more of a vertical component than the finite element prediction.

In Figure 4.10 are results obtained from the finite element computation for a slightly different initial fractured geometry. In this finite element computation 16 radial cracks were assumed to exist and no circumferential cracks were assumed to be present. As can be seen from the figure the results from this finite element computation are different from the case with the circumferential and radial cracks. At all gage locations the agreement is better (both with regard to direction and magnitude) for the case with the circumferential cracks. A total of seven different finite element cases were run. The seven different cases are listed below.

- Case 11 - 12 Radial Cracks
- Case 12 - 16 Radial Cracks
- Case 13 - 8 Radial and 8 Small Circumferential Cracks

DISPLACEMENTS AT GAGE LOCATION 1

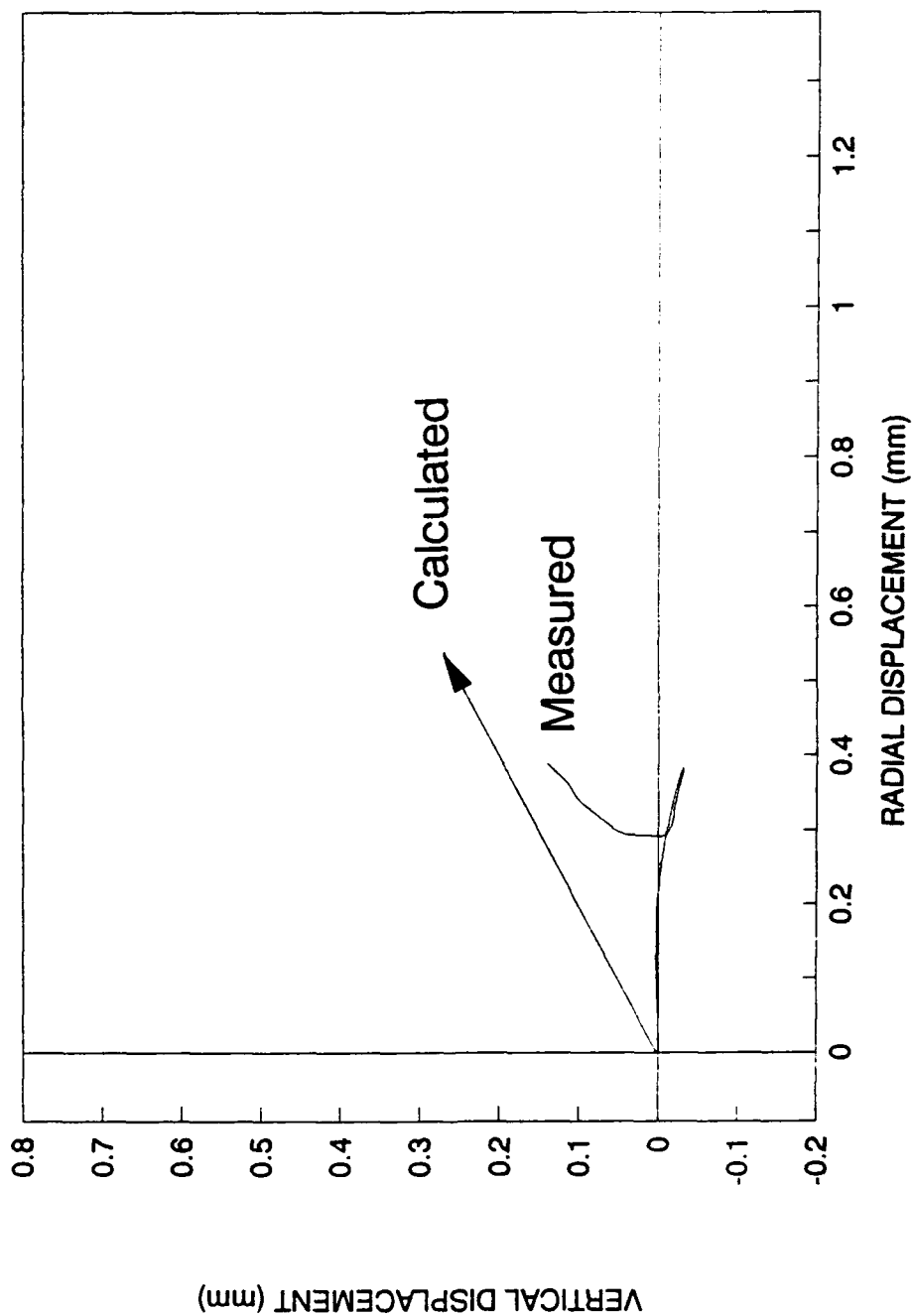


Figure 4.9. Comparison of Computational Displacements with Experimental values.
a) Gage Location EMG-1.

DISPLACEMENTS AT GAGE LOCATION 2

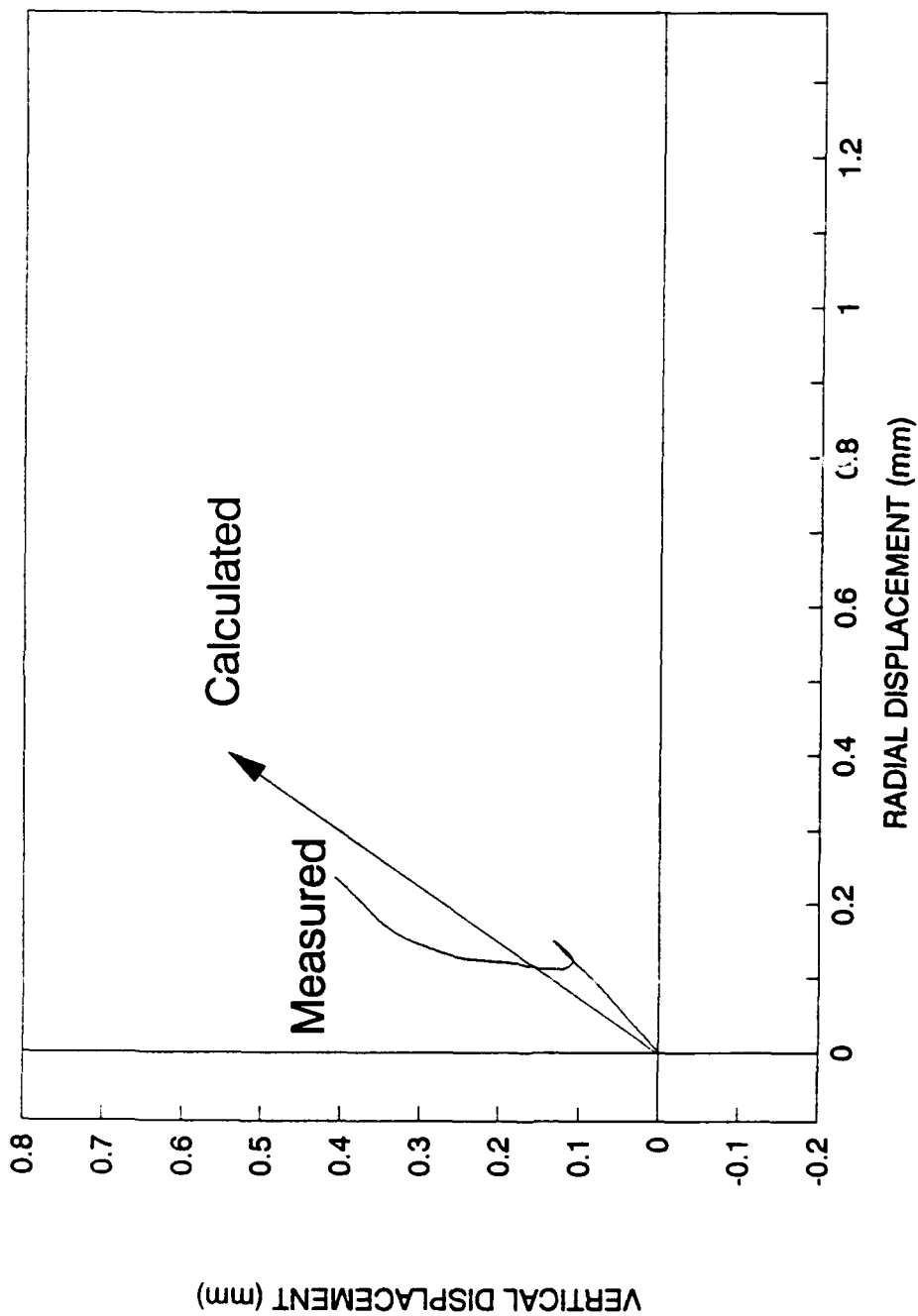


Figure 4.9. Comparison of Computational Displacements with Experimental Values.
b) Gage Location EMG-2.

DISPLACEMENTS AT GAGE LOCATION 3

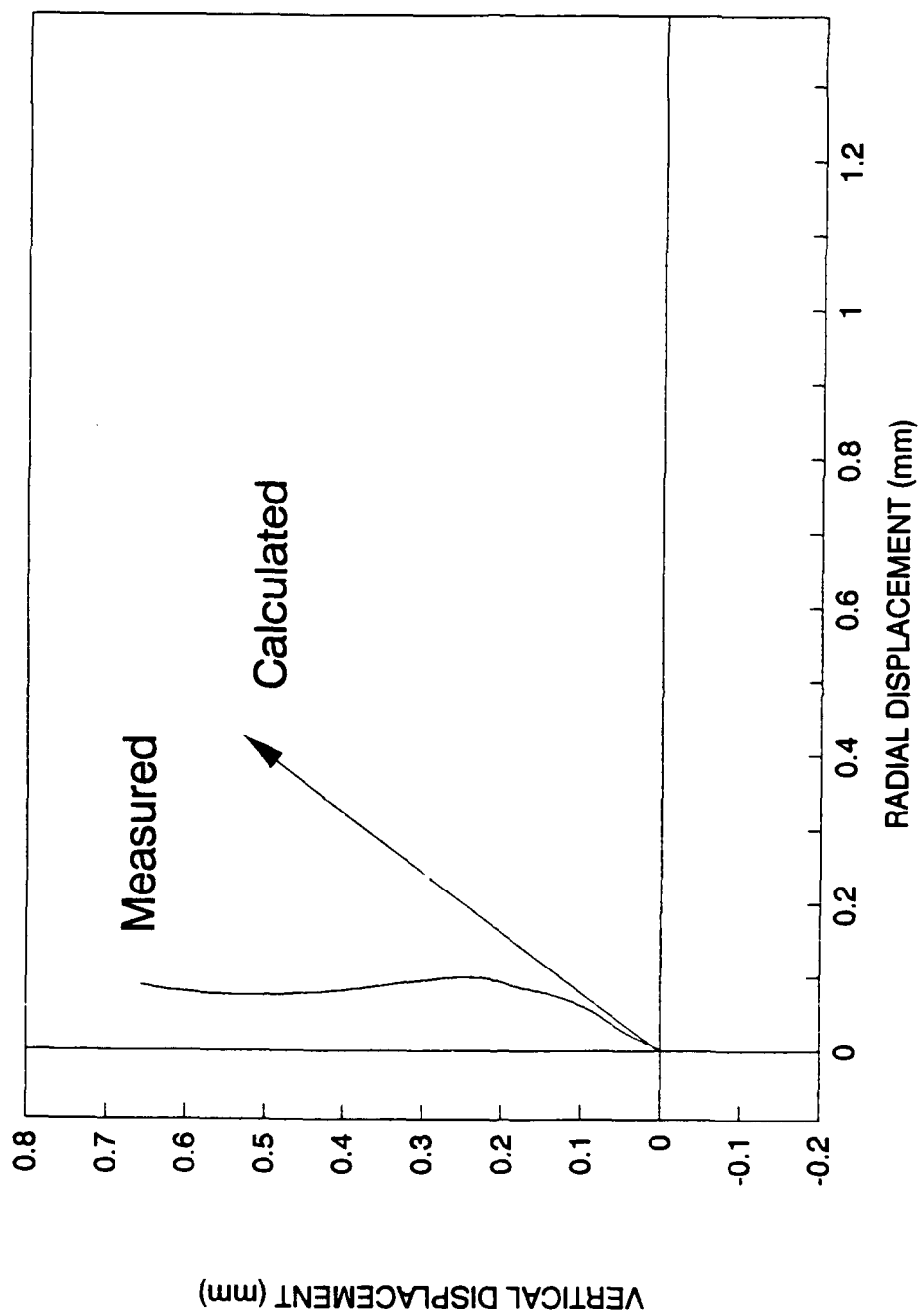


Figure 4.9. Comparison of Computational Displacements with Experimental Values.
c) Gage Location EMG-3.

DISPLACEMENTS AT GAGE LOCATION 4

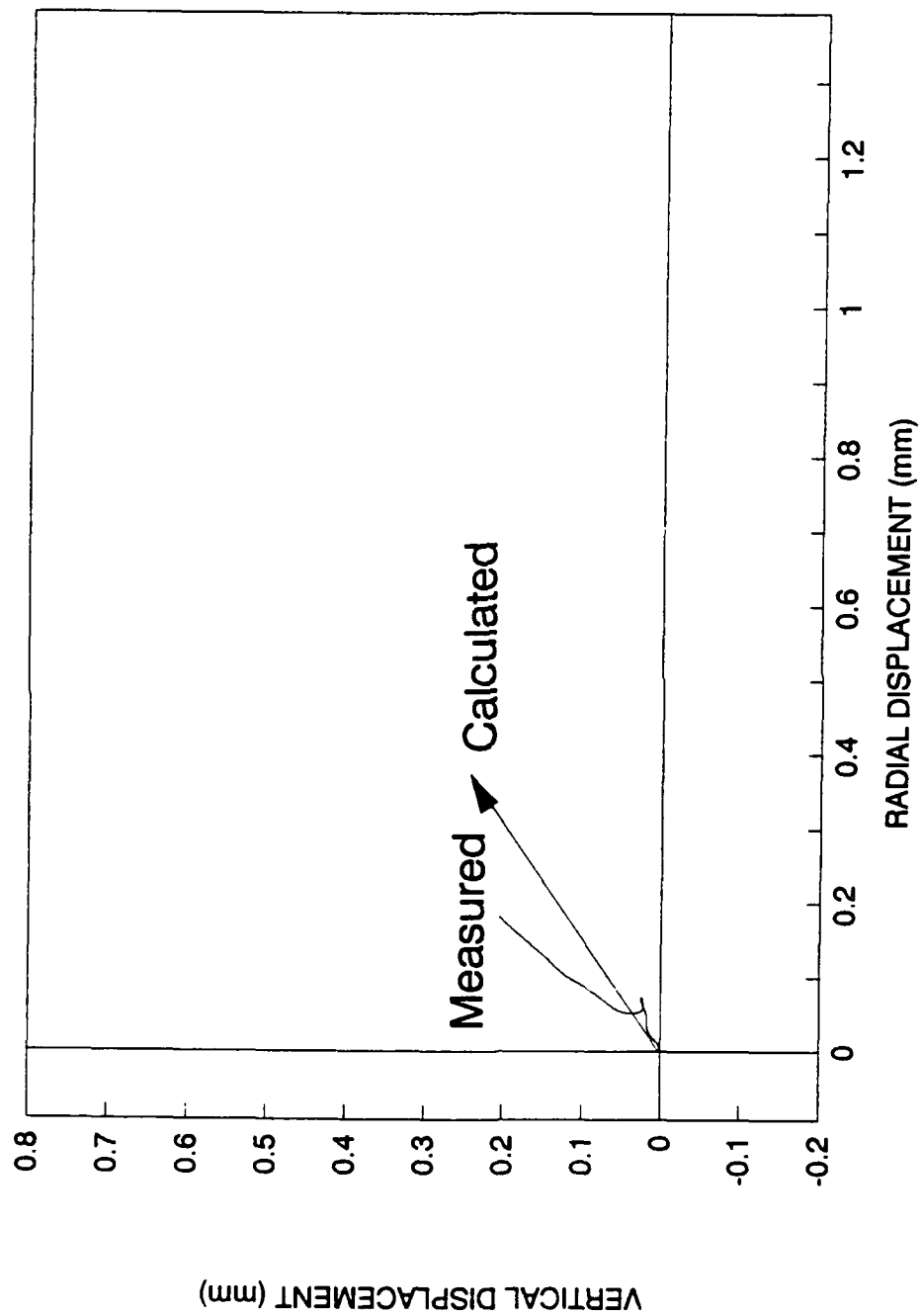


Figure 4.9. Comparison of Computational Displacements with Experimental Values.
d) Gage Location EMG-4

DISPLACEMENTS AT GAGE LOCATION 5

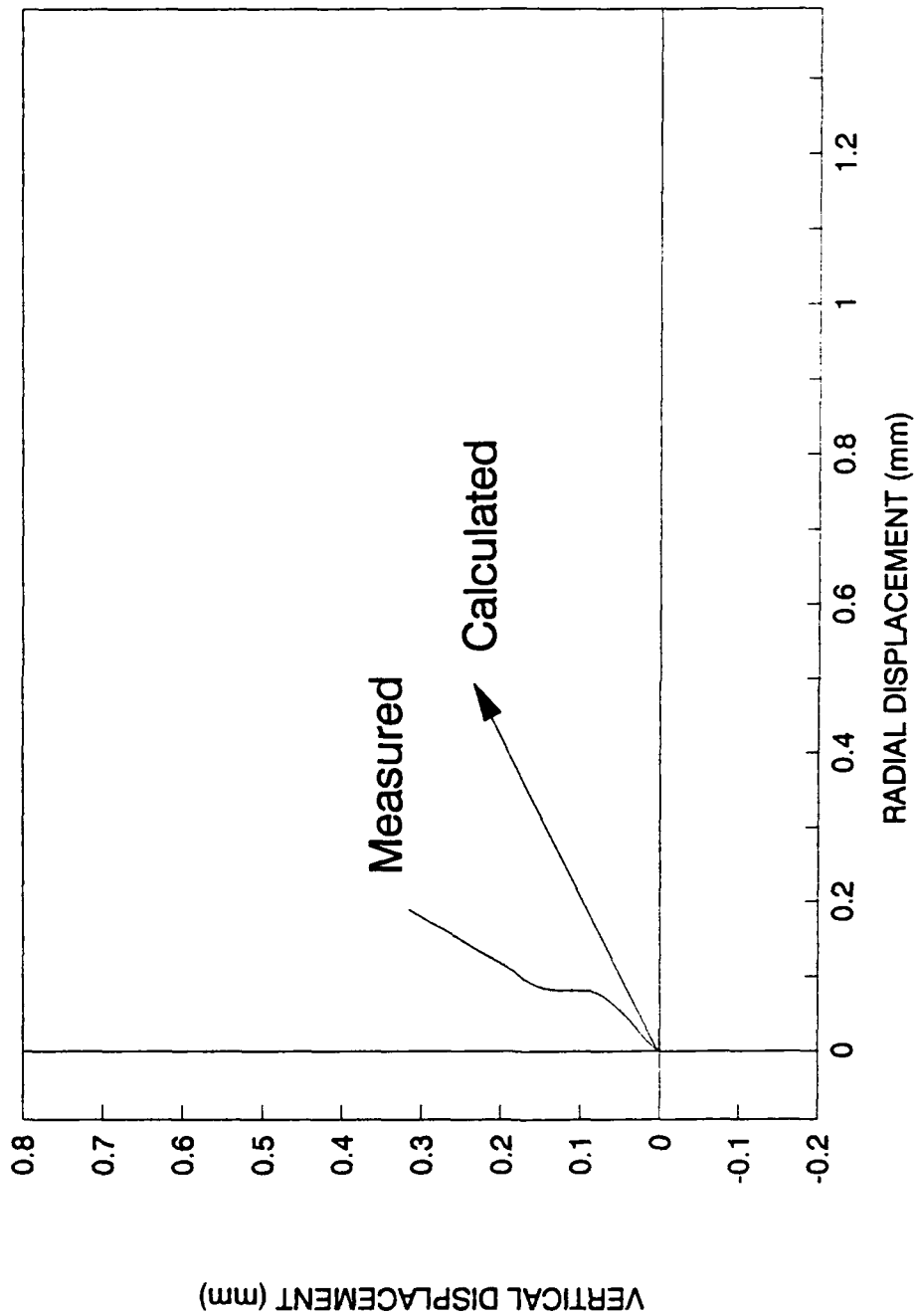


Figure 4.9. Comparison of Computational Displacements with Experimental Values.
e) Gage Location EMG-5.

DISPLACEMENTS AT GAGE LOCATION 6

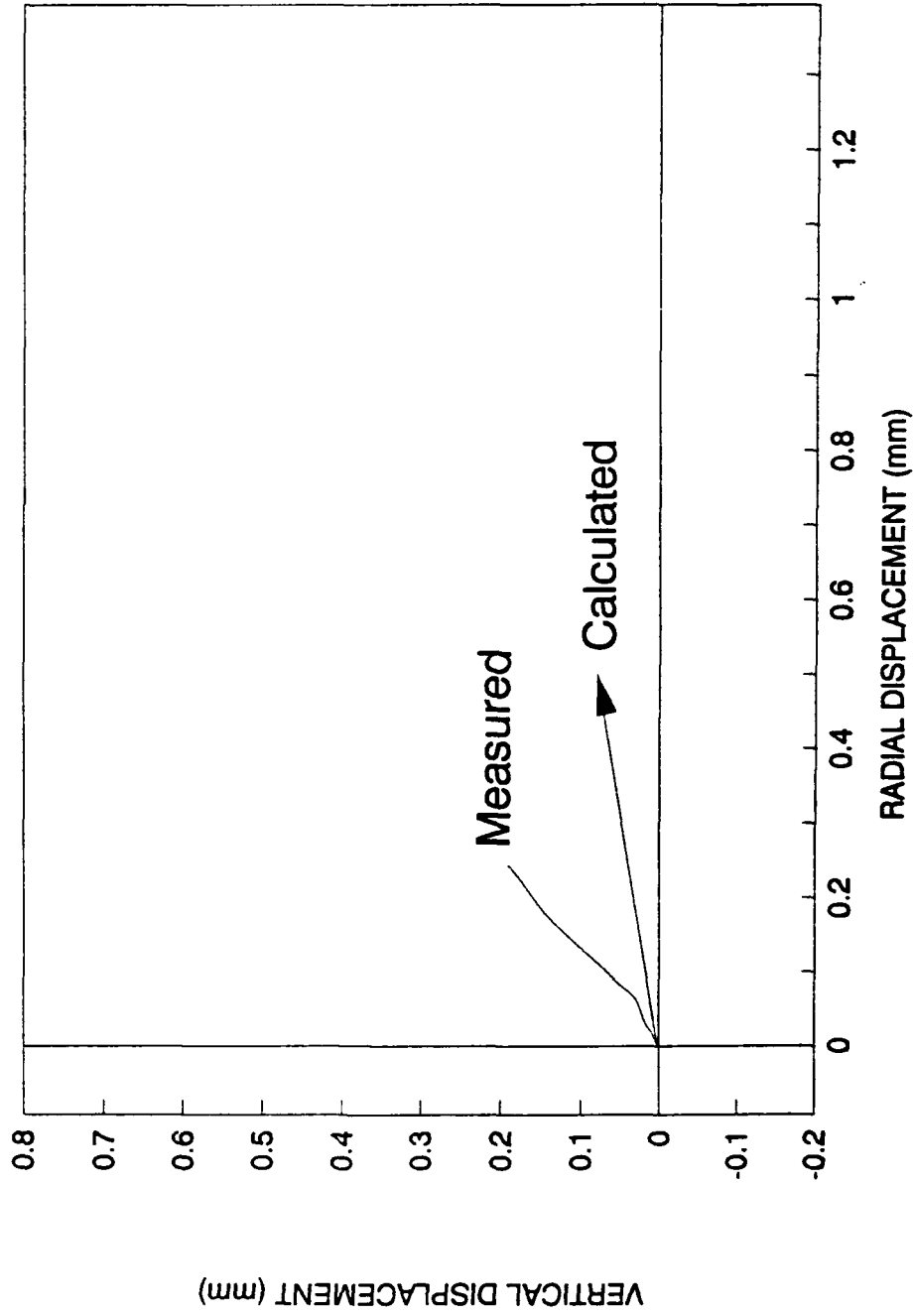


Figure 4.9. Comparison of Computational Displacements with Experimental Values.
f) Gage Location EMG-6.

DISPLACEMENTS AT GAGE LOCATION 2

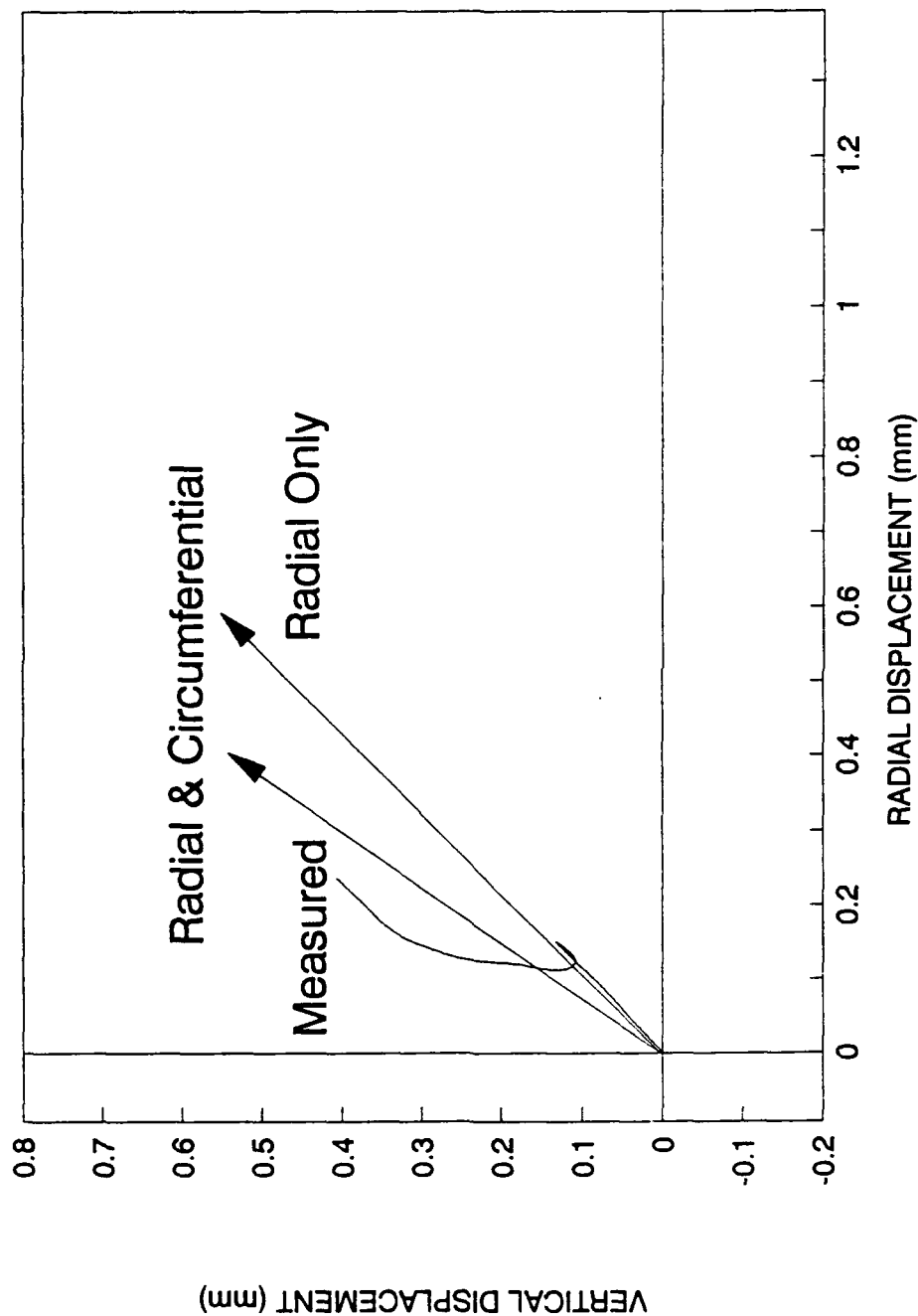


Figure 4.10. Comparison of Experimental Results with Computational Cases 11 and 60.
a) Gage Location 2.

DISPLACEMENTS AT GAGE LOCATION 3

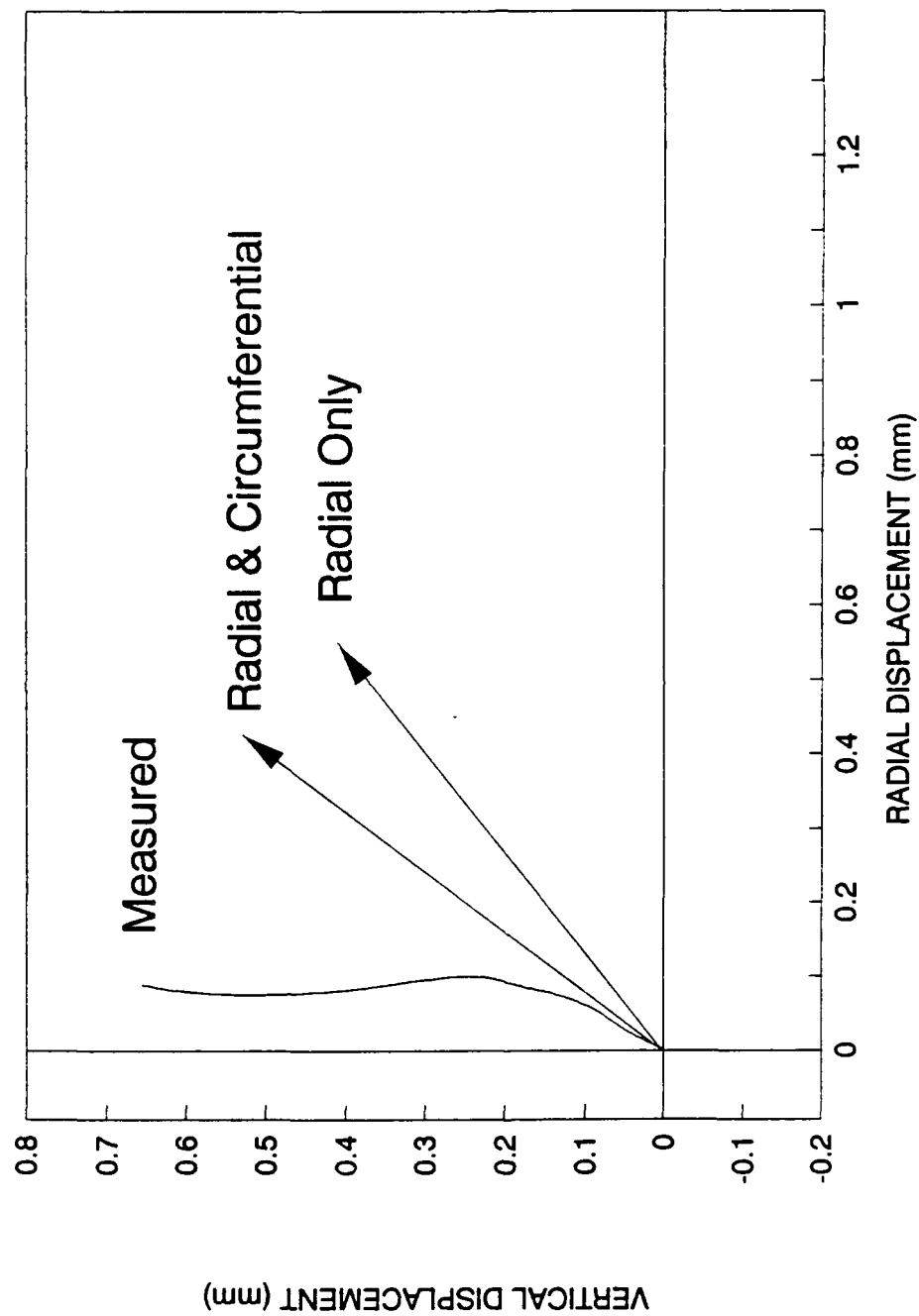


Figure 4.10. Comparison of Experimental Results with Computational Cases 11 and 60.
b) Gage Location 3.

DISPLACEMENTS AT GAGE LOCATION 4

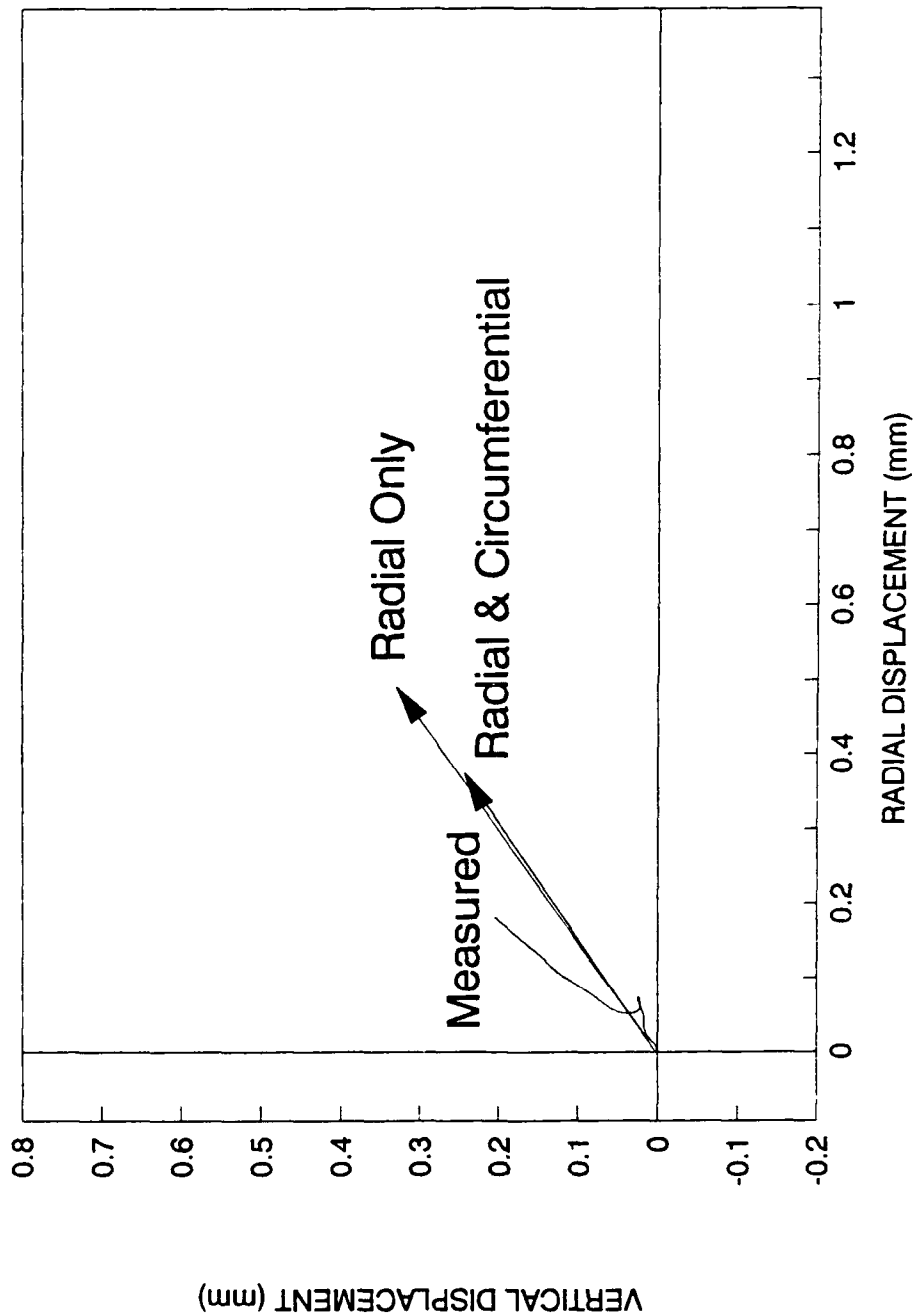


Figure 4.10. Comparison of Experimental Results with Computational Cases 11 and 60.
c) Gage Location 4.

DISPLACEMENTS AT GAGE LOCATION 5

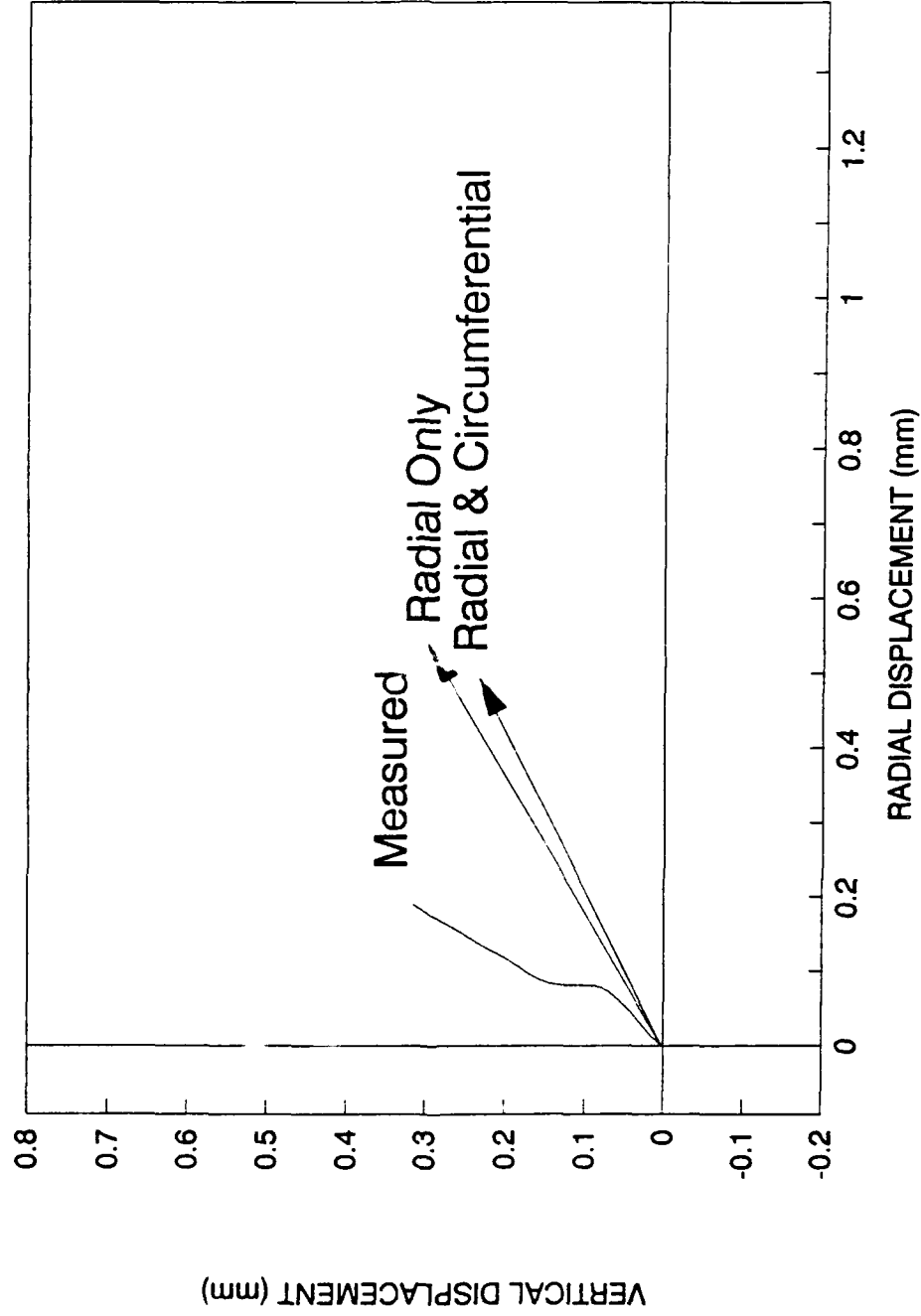


Figure 4.10. Comparison of Experimental Results with Computational Cases 11 and 60.
d) Gage Location 5.

DISPLACEMENTS AT GAGE LOCATION 6

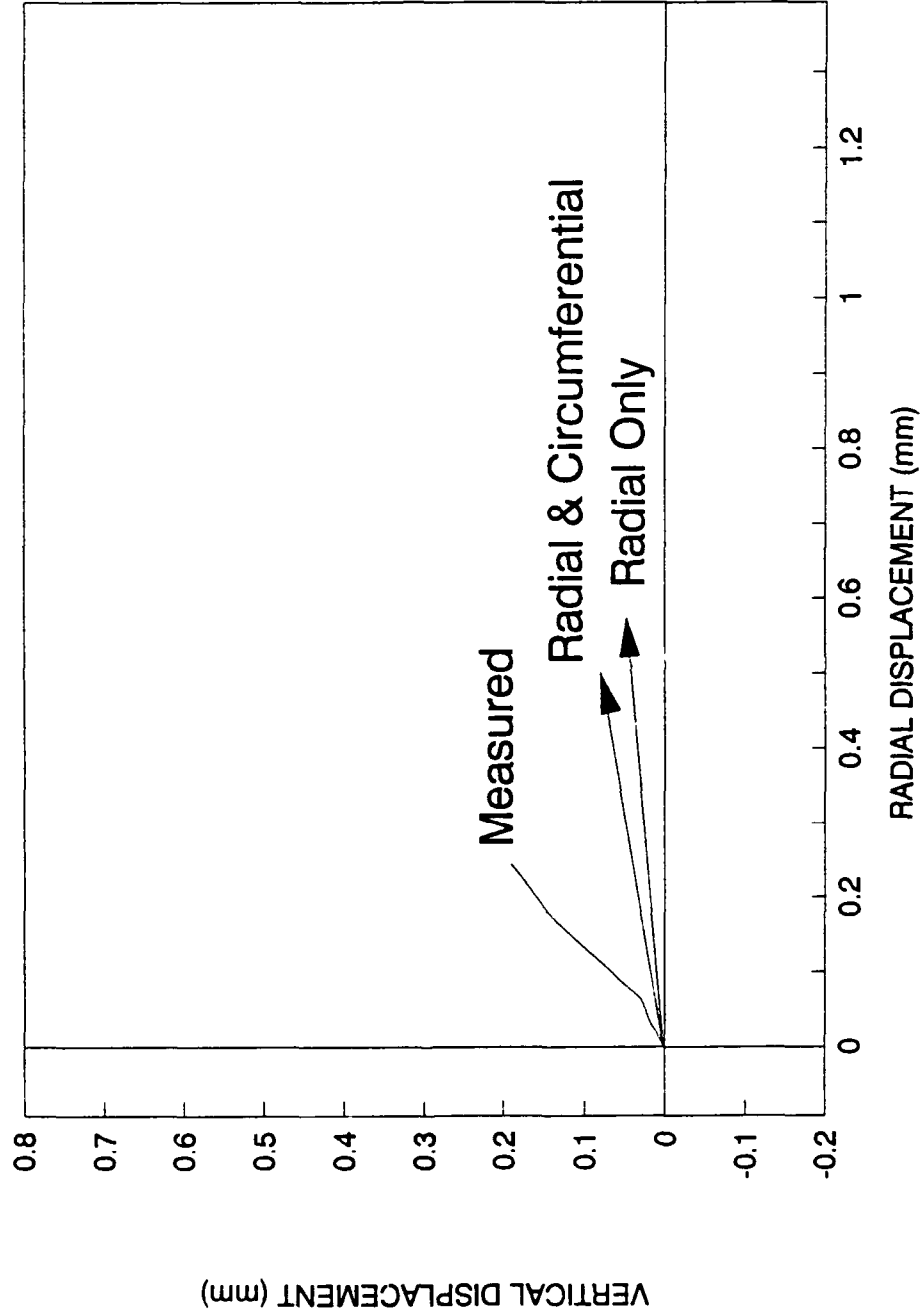


Figure 4.10. Comparison of Experimental Results with Computational Cases 11 and 60.
e) Gage Location 6.

(4.5)

Case 37 - Same as Case 13 but Smaller Poisson's Ratio
Case 38 - 8 Radial and 3 Small Circumferential Cracks
Case 39 - 8 Radial and 3 Large Circumferential Cracks
Case 60 - 16 Radial and 7 Circumferential Cracks.

Figures 4.11 and 4.12 show how the results of all of the computational runs in comparison to the experimental results. Figure 4.11 shows the average difference in orientation angle (degrees) for the seven different cases. The best results were obtained in orientation from Cases 13 and 37 which had radial cracking and circumferential cracking all the way around the borehole. The best results were obtained in amplitude agreement also for Cases 13 and 37.

Figure 4.13 shows the experimental results compared to Cases 60 and 37. In Case 60 a Circumferential Crack was not present on either of the horizontal cracks from the borehole but only on all of the cracks above this position. It is obvious that the case with circumferential cracking both above and below the borehole gives a better comparison to experimental results than does the case where circumferential cracks exist above the borehole - that is on the side towards the free surface. The smoke deflecting device blocked our view of the two horizontal cracks in the photoelastic tests so we cannot be sure if they should be included or not.

Overall the agreement in either of the two cases presented (Case 60 or Case 39) is taken to be good collaboration of the fragmentation mechanisms being proposed. It therefore appears that the wave action is quite important in crater blasting. The contribution of the very first mechanism proposed in the early 1960's (spalling) is quite important and when coupled with the combination of radial cracking and circumferential barrier branching appears to establish the preconditioned rock geometry which when acted upon by residual, long time, gas pressurization describes very well the fracturing which occurs in crater blasting. This mechanism, even though fracturing does begin at the free face and works its way back towards the charge, is defined by radial (conical) cracks which originate at the borehole and propagate to the free face.

It is felt therefore that the mechanism identified by the dynamic photoelastic testing is quite valid in crater blasting situations.

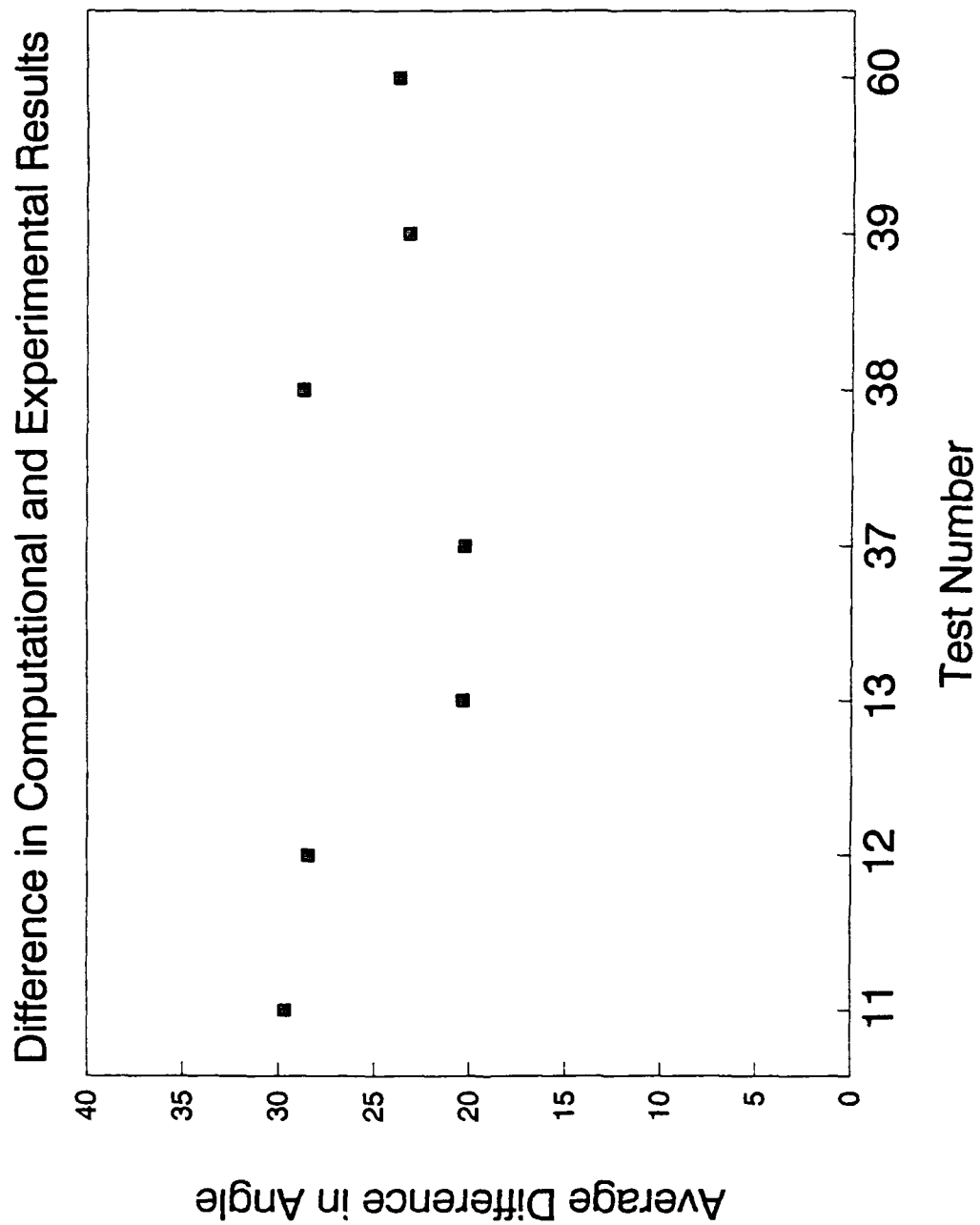


Figure 4.11. Comparison of All Computational Results with Experimental Results. Orientation of Displacement Vector.

Difference in Computational and Experimental Results

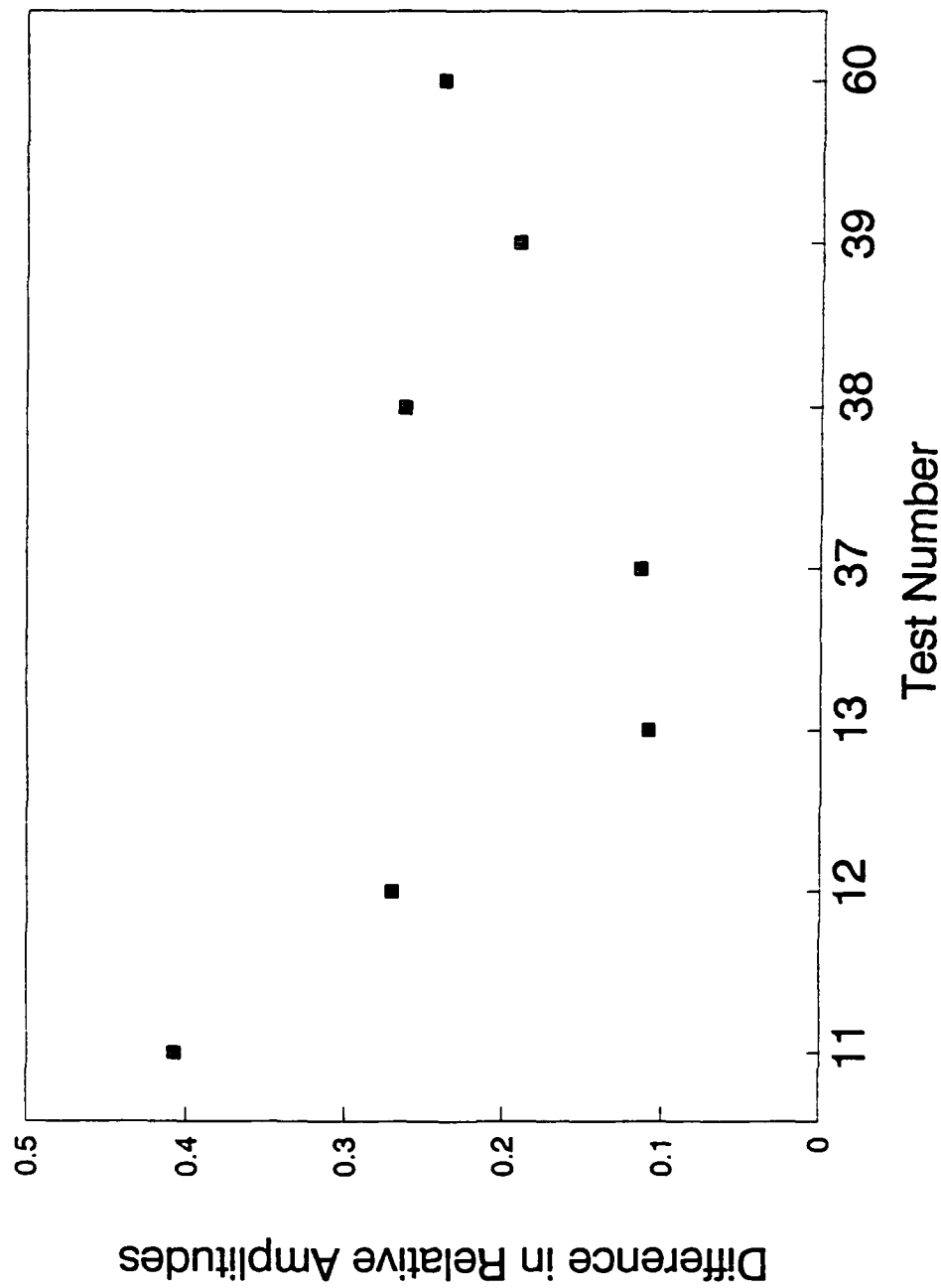


Figure 4.12. Comparison of All Computation Results with Experimental Results. Amplitude of Displacement Vector.

DISPLACEMENTS AT GAGE LOCATION 1

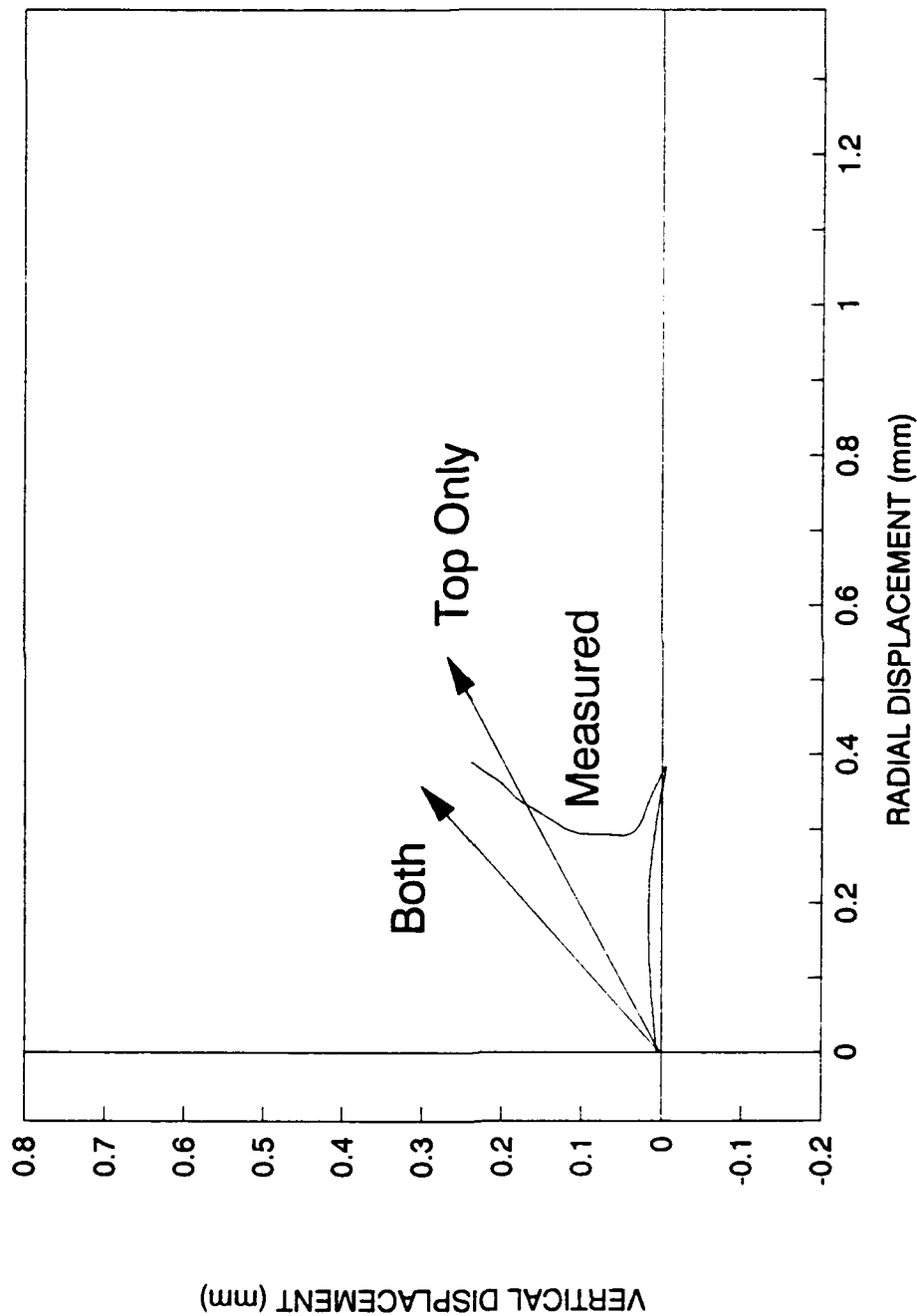


Figure 4.13. Comparison of Experimental Results with Two Computational Results - one with Circumferential Cracks both Above and Below Borehole and one with Circumferential Cracks only Above Borehole. a) Gage 1 Location.

DISPLACEMENTS AT GAGE LOCATION 2

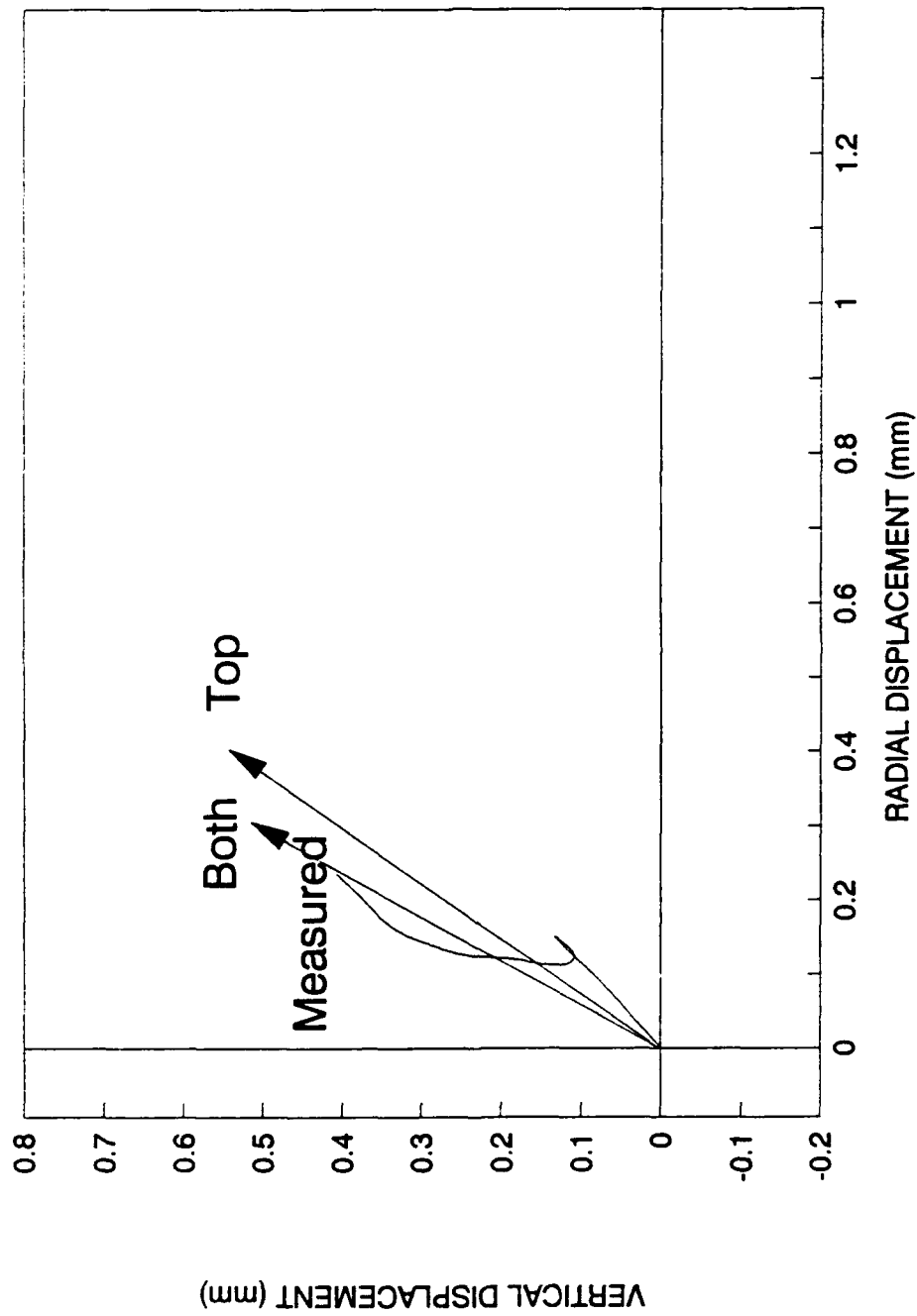


Figure 4.13. Comparison of Experimental Results with Two Computational Results. b) Gage 2 Location.

DISPLACEMENTS AT GAGE LOCATION 3

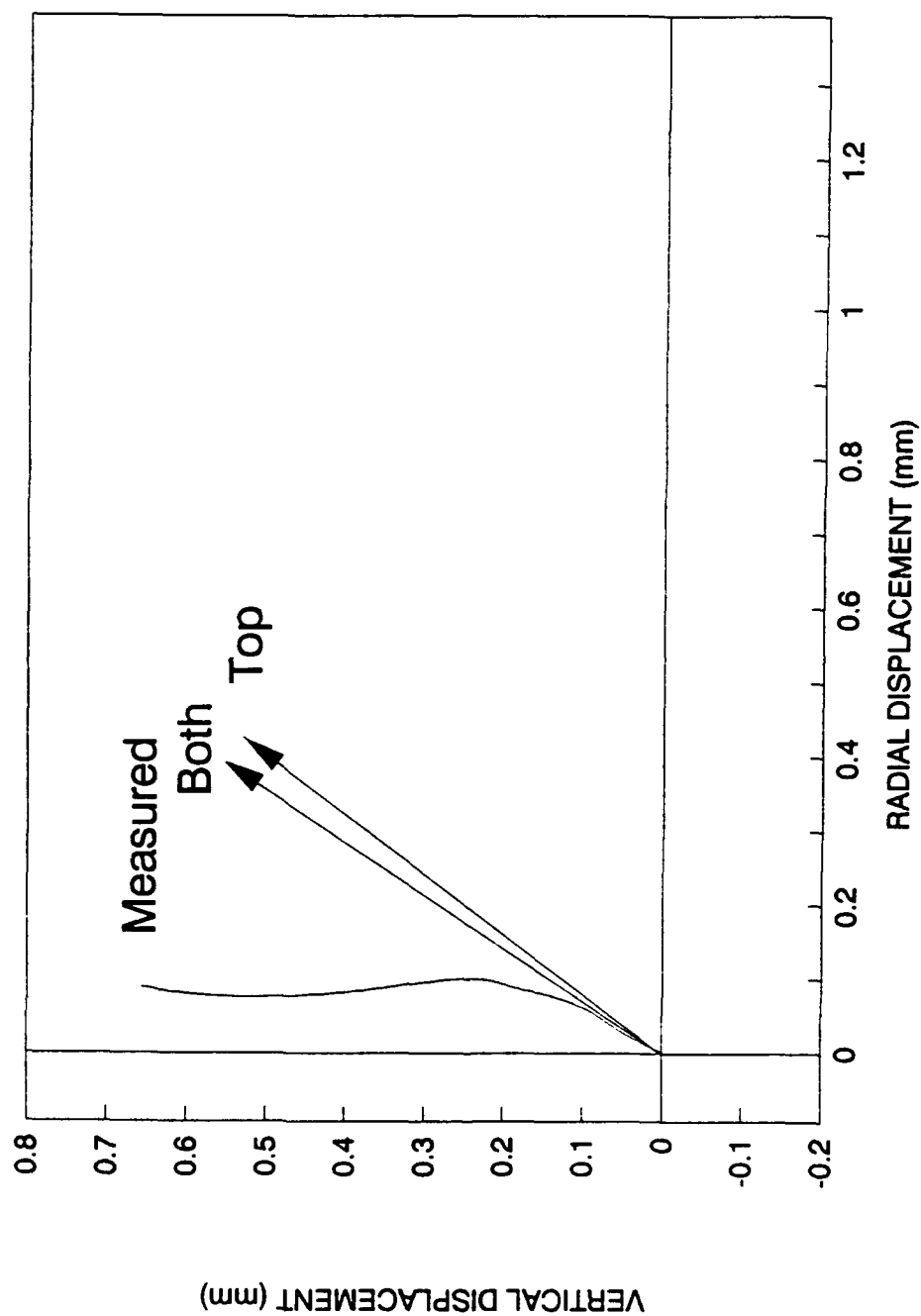


Figure 4.13. Comparison of Experimental Results with Two Computational Results. c) Gage 3 Location.

DISPLACEMENTS AT GAGE LOCATION 4

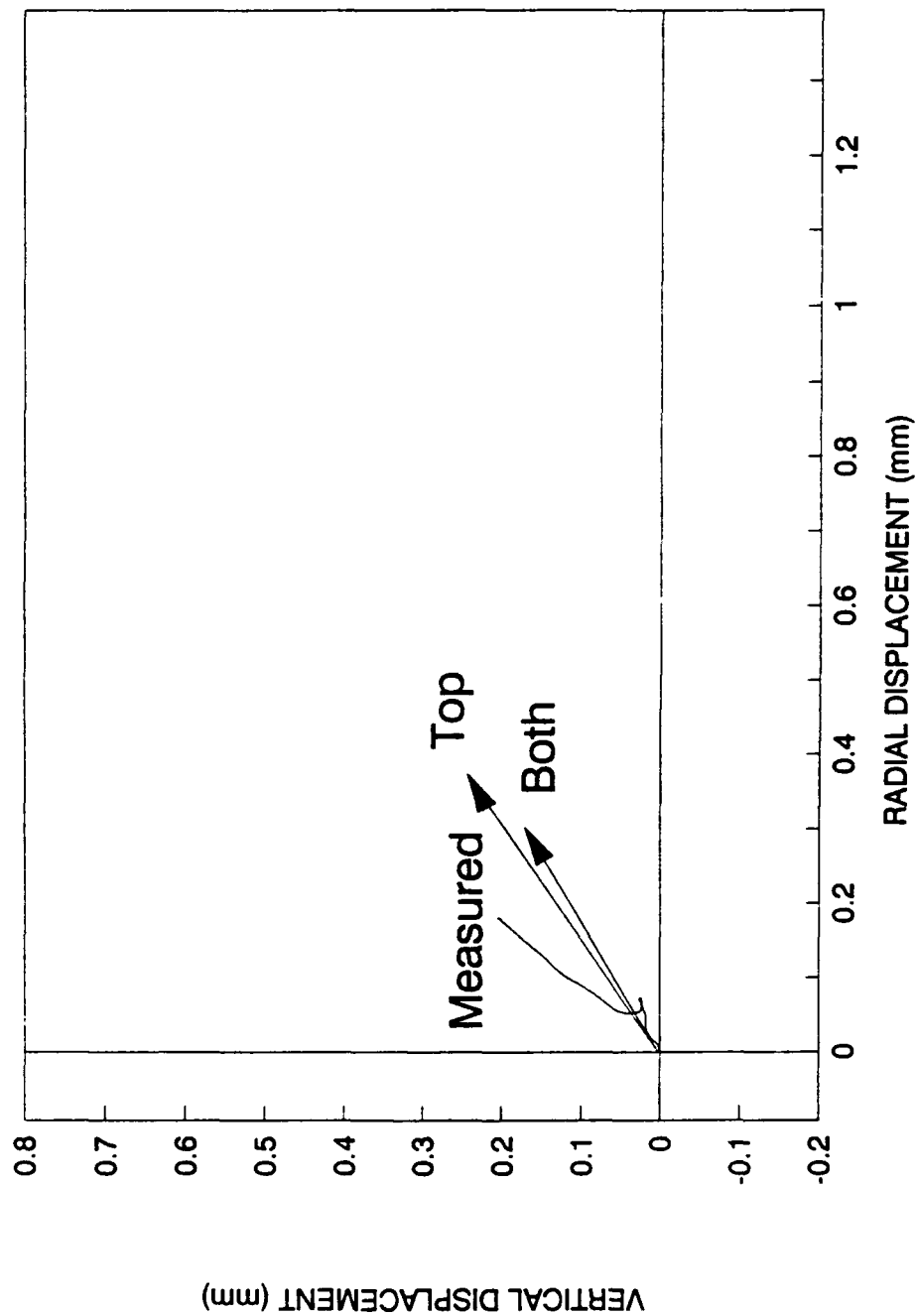


Figure 4.13. Comparison of Experimental Results with Two Computational Results. d) Gage 4 Location.

DISPLACEMENTS AT GAGE LOCATION 5

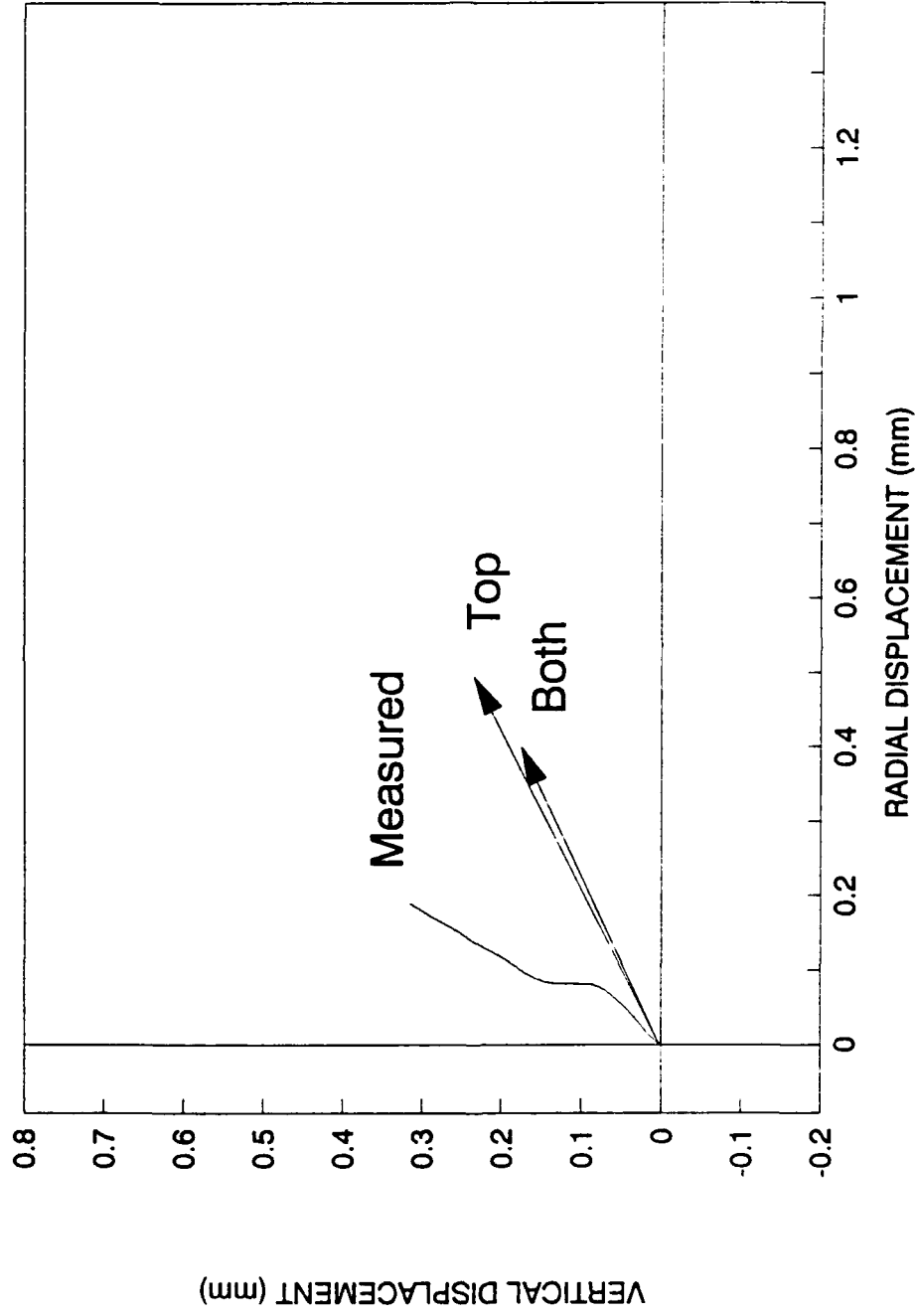


Figure 4.13. Comparison of Experimental Results with Two Computational Results. e) Gage 5 Location.

DISPLACEMENTS AT GAGE LOCATION 6

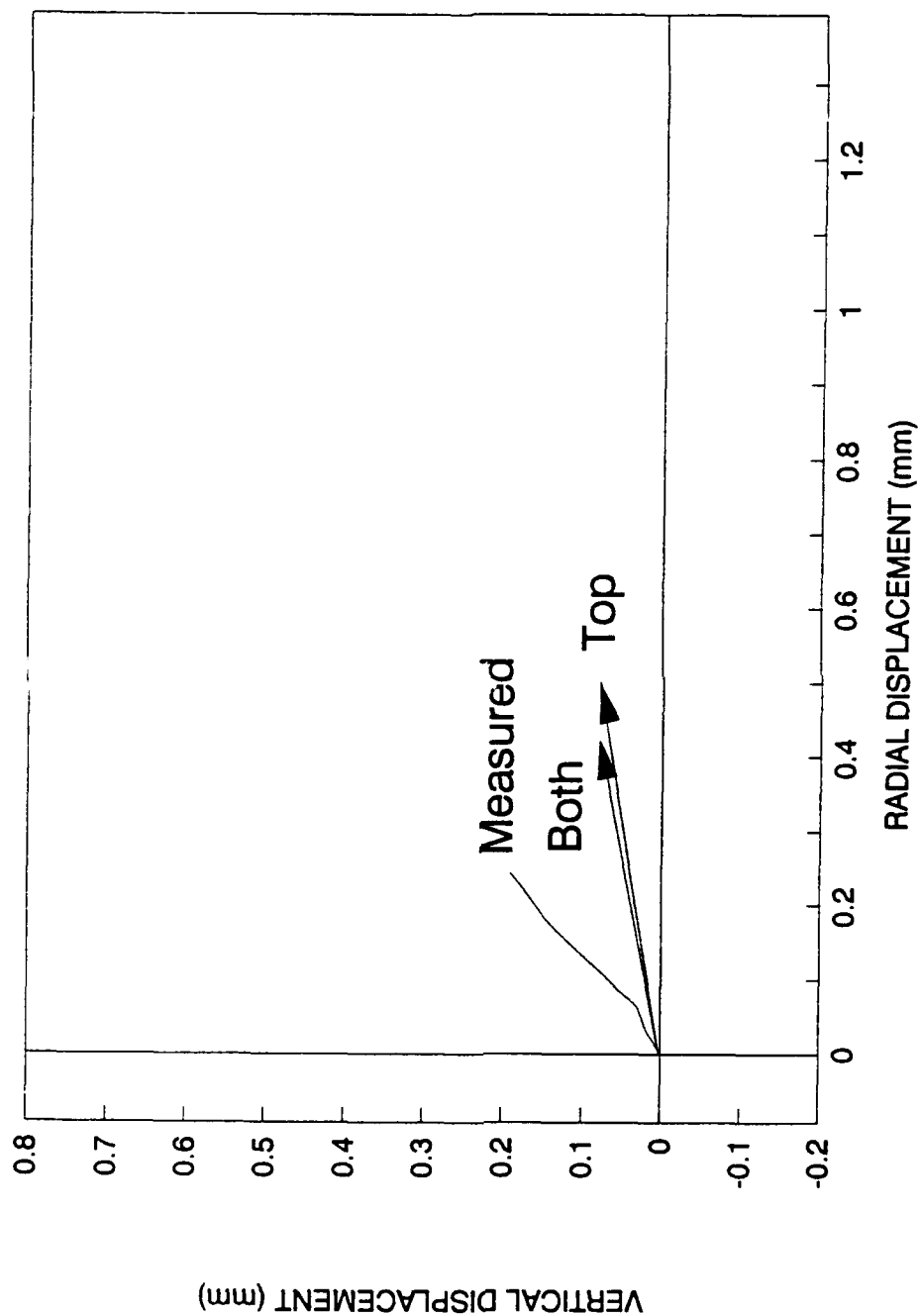


Figure 4.13. Comparison of Experimental Results with Two Computational Results. f) Gage 6 Location.

CHAPTER V. OPTIMIZING CRATER VOLUME.

This chapter describes a series of model tests conducted to investigate possible techniques that could be used to increase the volume of material removed in a crater blasting operation. In a tunnel round the first round to detonate - the opening cut - is a cratering round which needs to create free face nearly parallel to the remaining boreholes. If the resulting crater is larger then more free face will be created and the tunnel round will be more effective.

From the fragmentation mechanism that has been described in Chapter 3 it is clear that the final outline of the crater is defined by fractures that begin at the borehole wall and propagate to the free surface. This final crater outline of course depends greatly on proper preconditioning (fracturing) of the rock between the charge and the free surface by spalling fractures and by radial and circumferential cracking that is caused by the stress wave action in the rock mass.

Model tests were conducted in two different materials - plexiglas and Rockite. The plexiglas material could only be obtained in thicknesses up to 102 mm which proved to be unacceptable for certain depths of burials desired. In those situations greater thicknesses were obtained by "bonding" together two or more pieces of the thinner material. The Rockite material is similar to hydrostone (a fast setting gypsum product) but appears to behave a little less plastically in the vicinity of the borehole as far as compaction by the explosive is concerned. Plexiglas has a density of 1.2 gm/cm^3 , a tensile strength of 62 MPa, and a modulus of 2.3 GPa. Rockite has a density of 1.7 gm/cm^3 , a compressive strength of 53.8 MPa, and a modulus of 2.4 GPa.

In the first series of tests plexiglas was used. The model geometry for eight of the ten tests in this series is shown in Figure 5.1. The models were 152 mm by 152 mm by 102 mm thick. A 6.35 mm diameter borehole was drilled in the center of the block - normally to a depth of 38 mm. A sharp circumferential groove 1.5 mm deep with an included angle of 30 degrees was cut into the borehole. The location of the groove (as measured from the bottom of the charge) was changed from test to test. The charge length was held constant at 19 mm. Ten tests were conducted - eight had charges of 600 mg of PETN and were tightly coupled to the borehole wall and two had charges of 500 mg and were decoupled from the borehole wall. In the decoupled test the charge diameter was 5.8 mm which gave a decoupling ratio of 0.9. Two of the ten tests were conducted in plexiglas blocks that were bigger. These larger thicknesses were obtained by using chloroform to dissolve the

Table 5.1. Grooved model test results.

Test	DOB (mm)	Charge (g)	Charge (mm)	Crater Depth (mm)	Crater Radius (mm)	Crater Volume (mm ³)	Groove Above Bottom (mm)
CG-1PC	28.58	0.6	19.05	15.88	30	20000	0
CG-5PC	28.58	0.6	19.05	20	49	50000	6.35
CG-2PC	28.58	0.6	19.05	25.4	37.5	195000	12.7
CG-6PC	28.58	0.6	19.05	19.05	55.6	80000	12.7
CG-9PC	28.58	0.6	19.05	25.4	40.1	39000	12.7
CG-10PC	28.58	0.6	19.05	20	35	34000	12.7
CG-4PC	28.58	0.6	19.05	19.05	40.9	32000	19.1
CG-3PC	28.58	0.6	19.05	18	38.8	31000	25.4
DECOUPLED TESTS							
CG-7PC	28.58	0.5	19.05	25.4	23	14000	12.7
CG-8PC	28.58	0.5	19.05	25.4	44.25	70000	12.7
ROCKITE TESTS							
RK-1C	57.15	0.95	38.1	35	67	155000	
RK-2S	57.15	1	9.5	47	51	460000	

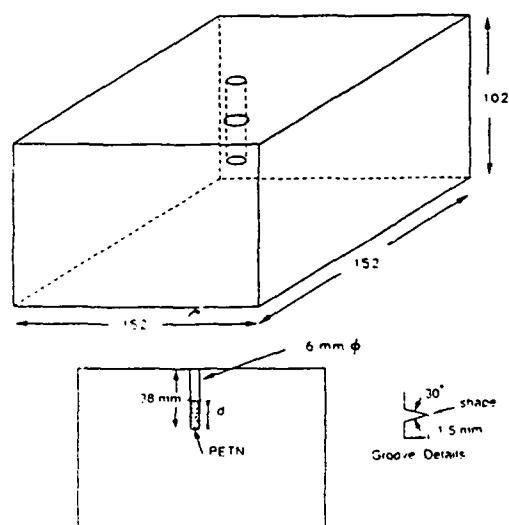


Figure 5.1. Geometry of Plexiglass Models Used in Test Series.

(5.2)

surfaces of two of the thinner pieces of plexiglas which were then placed together to form the thicker models. These larger models helped diminish the problem of strong wave reflection which occurred in the smaller block - both from the sides as well as the bottom of the model. In one of the decoupled tests the borehole was drilled 12.7 mm deeper than was the case in the other nine tests and an air pocket was left under the charge.

Table 5.1 gives a summary of the results obtained in this series of tests. The groove location was varied from being at the bottom of the charge to a location that was 25.4 mm above the bottom of the charge. The grooves 19.1 mm and 25.4 mm above the charge bottom gave no noticeable enhancement to the volume of material removed. In these two tests the normal crater was formed which was located just below the top of the charge. This would place the groove within the normal crater. As can be observed from Table 5.1 these two tests (CG-3PC and CG-4PC) removed 31,000 and 32,000 mm³ of material. These two tests were taken as the control test - i.e. with no grooves the amount of plexiglas that is normally removed would be about 30,000 mm³. Actually the average of the amount of material removed in all of the tests where the normal crater was felt to be formed was slightly higher (34,333 cubic millimeters). The crater volumes were determined by measuring the amount of sand required to fill the craters formed by the explosive detonation.

When the groove was located at the bottom of the charge fractures were initiated but turned downward towards the bottom of the model instead of turning towards the top and improving the resulting crater. In fact, the amount of material removed in CG-1PC which had the groove at the bottom of the charge was only 20,000 mm³ - the smallest amount of material removed in any of the tightly coupled tests. Figure 5.2 shows two photographs of the model CG-1PC. Notice that the crater formed on the top surface is quite small starting just at the top of the charge. The second photograph shows the same model viewed from below. As can be seen from the pictures the fractures from the borehole bottom reached the lower surface of the model on about half of the potential crater lip but without the preconditioning from the stress waves a complete crater did not form. For the model used for this test the bottom surface of the model was located 25 mm farther from the charge bottom than was the top surface and the preconditioning which occurred below the charge was much less than occurred on the top side of the charge due to the larger distance before reflection of the compressive wave could occur. Hence the spalling contribution was less as was the presence of circumferential cracking. None-the-less the fractures initiated at the charge bottom did manage to reach the bottom surface but no crater was formed on that side.



Figure 5.2. Postmortem Photographs of Model Used in Test CG-1PC.
 a) Top View of Model showing Normal (Unenhanced) Crater.
 b) Bottom View of Model Showing Fractures from the Groove that ran to the bottom.

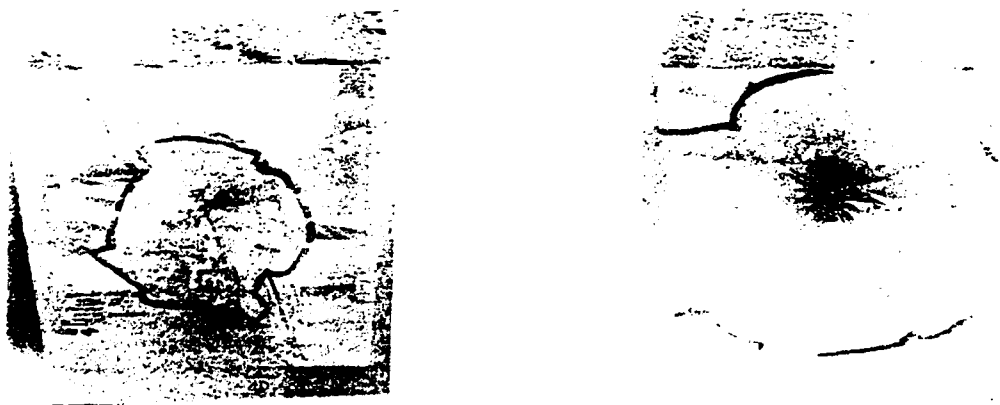


Figure 5.3. Comparison of Enhanced Crater and Normal Crater.
 a) Normal Crater - Test CG-4PC.
 b) Enhanced Crater - Test CG-2PC.

(5.3)

In testing by Young, et. al. [5.1] with small charge drill and blast techniques the fractures initiating at the bottom of very shallow boreholes were found to first travel away from the top (free) surface and then turn and travel upward toward the free surface. In the case of test CG-1PC the fractures traveled downward and never reversed direction - probably due to the closeness of the bottom and side free faces.

In the second test conducted the groove was moved upward from the charge bottom to a location that was 12.7 mm above the bottom of the charge. In this case the crater volume removed was 195,000 mm³ of material (Test CG-2PC). This resulted in a nicely formed, nicely fragmented crater. The outline of the very large (6 times larger than the "normal" crater) crater was formed by fractures which initiated at the groove and travel toward the top surface. Figure 5.3 is a photograph showing the crater formed in this test in comparison with the crater formed in Test CG-4PC where the groove was too high to assist the cratering process.

Additional tests were conducted with the groove located at 12.7 mm from the borehole bottom (or at a location two thirds of the length of the charge). Both in Test CG-10PC and Test CG-9PC (both of which had the groove located at the same location as in CG-2PC) the fractures initiated nicely but ran to and intersected the sides of the 152 mm by 152 mm models. The grooves therefore did not take part in the crater formation and the volumes reported in Table 5.1 are for the "normal" crater that would have occurred with no groove present. The amount of material removed in these two tests therefore were close to the "control test" - 34,000 and 39,000 mm³.

Because of the difficulties with the use of small models the final two tests were conducted in larger blocks of plexiglas. These models were 304 mm by 304 mm by 204 mm thick and were formed as described above by "bonding" two 102 mm thick blocks together to form a block twice as thick as the smaller blocks. This larger block was used to run two tests, one on each side of the thicker block.

In test CG-6PC the groove was once again located at a position two thirds of the length of the charge or 12.7 mm above the borehole bottom. In this case the fractures initiated from the groove and traveled upwards. Along one quarter of the crater lip the fractures reached the upper surface and formed a quarter pie shaped segment of the larger (enhanced) crater. Within the other three quarters of the crater the fractures that initiated at the groove arrested just short of the upper surface and the smaller (or normal) crater was formed. The formation of this "hybrid" crater is possible since the radial fractures form first and outline the pie shaped segments. The cone (crater outline) fractures initiate later at the borehole and travel towards the surface to finish the

(5.4)

crater formation. In one quarter of the crater the larger pie shaped segments formed by the radial cracks and the cone fracture resulted in the larger crater. Along the other three quarters of the crater the larger crater did not completely form due to an insufficient amount of gas pressure (and perhaps less severe wave reflections from the sides of the model) and only the normal sized crater formed. The amount of material removed in this test $80,000 \text{ mm}^3$ agrees well with the previously obtained results. That is $0.25 \times 195,000$ plus $0.75 \times 31,500$ equals $72,325 \text{ mm}^3$ compared to the $80,000 \text{ mm}^3$ removed. Figure 5.4 shows this hybrid crater.

The final coupled test conducted was CG-5PC which was also conducted in the larger block and had the groove located 6.35 mm from the bottom of the borehole or one third of the distance along the charge. In this test good fractures formed at the groove but the energy available from the explosive was insufficient to drive the fracture far enough to intersect the surface. The crater formed was not aided by the groove and the amount of material removed was only $50,000 \text{ mm}^3$. This was higher than most of the other normal craters but did not approach the good cratering achieved when the groove aided the cratering.

Two final tests were conducted with decoupled charges located in small blocks and resulted in good fracture initiation at the groove. Both had the groove located 12.7 mm above the charge bottom and in one case - Test CG-8PC - the borehole was drilled an additional 12.7 mm below the bottom of the charge. In these two tests the amount of charge used was reduced from 600 mg to 500 mg. In Test CG-7PC the fractures arrested before reaching the upper surface and the resulting crater was quite small, being only $14,000 \text{ mm}^3$. There appeared to be an insufficient amount of gas pressure to drive the fractures to the surface and those fractures did not assist crater formation. In the second decoupled test which was in every way identical to the one just described (with the exception of an air pocket below the charge) about one half of the crater was enhanced by the groove while the other half was not. The amount of material removed in this hybrid crater was $70,000 \text{ mm}^3$. This would indicate that if the enhancement by the groove had been totally successful the crater from the decoupled charge would have been about $126,000 \text{ mm}^3$ (or about 9 times larger than the "normal" crater). That is $0.5 \times 14,000 + 0.5 \times 126,000$ equals $70,000 \text{ mm}^3$. The air pocket was left below the charge to give volume in which the gas pressure could accumulate rather than venting quickly from the borehole. It is premature to think that the difference in results between these two decoupled tests was highly dependent on the presence of the air pocket.

Two additional tests were conducted in rockite models. Neither of these tests utilized grooved boreholes. One of these tests used a cylindrical charge of 950 mg of PETN and the other a 1000 mg charge in spherical geometry. The depth of burial of both charges was the same (57.2 mm) and the two models were identical in



Figure 5.4. Photograph of Hybrid Crater from Test CG-6PC.

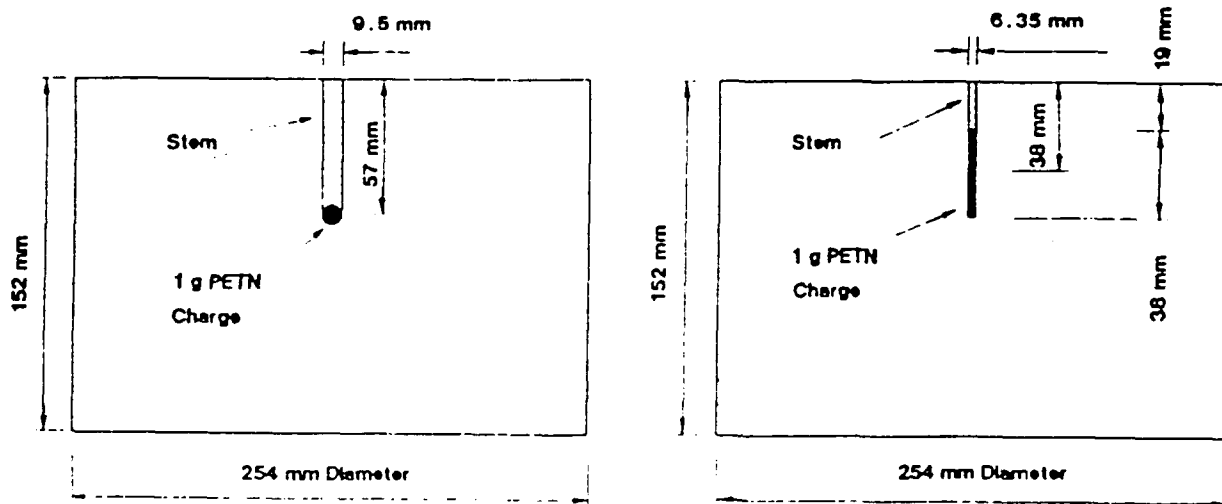


Figure 5.5. Geometry of Rockite Models.
a) Spherical Charge Model.
b) Cylindrical Charge Model.

every other respect. The models were 254 mm in diameter and 152 mm thick. Figure 5.5 shows the geometry of the models used. The diameter of the spherical charge was 9.5 mm. The cylindrical charge was 38.1 mm long and was located in a borehole that was 6.4 mm in diameter, that is, it had a length-to-diameter ratio of six. The amount of material removed by the spherical charge was 460,000 mm³ while the amount removed by the cylindrical charge was only 155,000 mm³. That is the same amount of explosive in spherical form resulted in a crater nearly three times as large in the Rockite material as did the cylindrical charge. A number of tests in addition to those described here have been conducted in the three materials - plexiglas, epoxy, and Rockite. In all cases spherical charges have resulted in craters that are much larger than those produced by the same size charges in cylindrical geometry. The ratio of three found in the Rockite material is characteristic for the other materials as well. In this case even though the depth of burial is the same and the mass center of the two charges is the same it is felt that the spherical charge concentrates more of the explosive energy at a deeper depth and results in the fractures that outline the final crater initiating at a deeper depths and hence producing a much larger crater.

The results of the tests described in this chapter support strongly the mechanism of fracture and fragmentation being proposed for the cratering situation. It has been shown that much larger craters can be formed if the crater can be caused to initiate at locations farther from the free surface. The technique of using a circumferential groove in the borehole at the location where crater initiation is desired have been found to be successful in the model materials used in this investigation. It appears that the most advantageous location for the groove is to thirds of the way along the cylindrical charge from the bottom. The fractures initiated at this location are successfully driven to the top surface and increase the volume of material removed by factors of as much as six. In addition, even though larger boreholes may be required it appears that the size of craters formed can be increased by a factor of about three using spherical charges in place of the normal practice of using cylindrical charges. It also appears possible to increase the cratering efficiency in situation where the use of decoupled charges might be desired - such as in locations where vibration suppression might be required.

The tests conducted are of course only model tests of a very small scale and additional investigations need to be conducted at a larger scale and in more realistic materials.

REFERENCES:

5.1 "Small Charge Cone-Fracture for Rapid Excavation", C.Y. Young, R.D. Dick, and W.L. Fourney, 3rd International Symposium on Fragmentation by Blasting, Brisbane, Australia, August 1990.

CHAPTER VI. EFFECTS OF JOINTS

A. Introduction.

Since spall has been shown to be important in the fragmentation mechanism for cratering it was felt necessary to understand the effects that joints and bedding planes might have on fragmentation resulting from an explosive detonation.

In a geologic medium it is rare to find rock formations which are not jointed and bedded. The strength properties of these interfaces vary greatly from strong calcite filled joints to mud filled joints which possess no tensile strength. The thickness of these interfaces also vary from very tight joints to ones that are quite open.

If the concern with regard to the joints is the amount of stress (or energy) that can be transmitted across the joint then there are several mechanisms by which energy can be passed over the interface. Since work (or energy) is obtained by multiplying force times displacement in the direction of the force it is important to know how effectively an interface will permit forces and displacements to pass. In the case of the research program being described it was felt that it would be best to concentrate on making measurements of the effectiveness of the joint in transmitting (or reflecting) velocity. This was done for two reasons. First, in tests conducted very early in the program it was found when strain gages were used to record the strain level at any point in a polymeric material that the gage itself served as a flaw and as an initiation site for fractures. The subsequent growth of these fractures occurred such that the gage was decoupled from the material - at least on one side. This meant that the readings obtained from the strain gages were only valid up to the time that the gages were decoupled from the model material. The time at which this separation occurred is not precisely known since it is dependent upon the gage geometry, gage orientation, and the stress state in the stress wave. All that was known was that at some time after the strain signal reached the gage the output from the gage ceased to have meaning. Although some valid information can be obtained from strain gages the results must be viewed with some speculation and analysis of the data done with care. Velocity gages on the other hand proved to be much more reliable since the profile of the gage itself (a small diameter wire) seemed to provide no opportunity for fracture initiation.

The second reason for measuring particle velocities is that both stresses and deformations can be found from properly obtained velocity data. The stress in the model can be obtained from a knowledge of both the particle velocity and the shock velocity at any given point. The shock velocity can be obtained from the arrival times of the velocity data and a knowledge of gage

(6.2)

location. The particle velocity is obtained from the gage output and even the displacement can be obtained by integration of the velocity gage signal. Our experience has shown that the velocity records are quite well behaved from the standpoint of signal noise and amplifier drift so that reliable integrations can be obtained to yield valid displacement information.

Both two and three dimensional tests were conducted to investigate the behavior of a material interface when subjected to a stress pulse from an explosive detonation. We were primarily interested in determining how much of the signal was transmitted and how much was reflected when the interface was encountered. All interfaces were between two materials that were the same. In the two dimensional tests Homolite 100 and Plexiglas were used and the velocity gages were placed in surface grooves routed into the model. In the three dimensional tests Hydrocal and Hydrostone were used. Both are quick setting gypsum cements. Only one model test used Hydrostone - all others used Hydrocal.

B. Description of two dimensional tests.

Eight tests were conducted - six in sheets of Homolite 100 and two in plexiglass. In the first six tests the sheets of material were 254 mm x 381 mm by 12.7 mm thick. The models were made by routing one edge of a 254 mm x 254 mm sheet and joining a second sheet that was 254 mm x 127 mm which also had the common boundary routed smooth. Various materials were used to form the interface between the two sheets. Four of the six models used rubber cement as the bonding agent, one used a double sided tape manufactured by 3M, and the last model was made with grease as the material between the two sheets. The model geometry is shown in Figure 6.1 and shows the location of the velocity gages used. In all of the first six tests, three velocity gages were used. The basic measurement made was the velocity just before the interface (gage G1) and the velocity just after the interface (gage G2). Gage G3 was located below the borehole an equal distance from the borehole as G1 was above the borehole. G3 was used to determine the symmetry (or lack of symmetry) of the stress wave produced by the detonation of the explosive and to determine if significant reflection was occurring back into the model as a result of the presence of the interface.

In earlier testing with Homolite 100, it had been determined that the decrease in fringe order with propagation distance from the charge was represented well by a power function of order 0.805, that is the fringe order N as a function of distance from the charge r is given by:

$$N = A / r^{0.805} \quad (1)$$

[illegible]

JOINT: RUBBER CEMENT GLUE

Figure 6.1. Geometry of Models used In Two Dimensional Joint Tests which Used Homolite 100 as the Model Material.

(6.3)

A is a constant for any given test that depends upon the explosive strength (size) and r is given in millimeters. Other investigators who have conducted explosive tests in polymeric materials have found a similar law to be valid with an exponent of 1 [6.1,6.2]. For the purpose of evaluating dispersion of the velocity wave with distance we will assume that the velocity can be determined from the stress (which is directly related to the fringe order). The relationship between stress and velocity is a square root function and therefore we will assume that the velocity as a function of distance from the charge will be given by:

$$v = C / r^{.40} \quad (2)$$

Table 6.1 lists the pertinent parameters for the first six tests and also gives the peak velocity recorded at the gages. A charge of 200 mg of PETN was used in all tests and all but the first test (PJ1) had a borehole diameter of 5 mm (PJ1 had a slightly larger borehole of 6.35 mm). Also given in Table 6.1 is the ratio of the peak velocity read on gage G1 (just before the interface) to the peak velocity read on gage G3. If the stress wave coming from the explosive is completely symmetric and if there is not significant reflection of particle motion back into the model then this ratio should be one. Tests 2, 3, 4, and 6 are reasonably symmetric with this ratio ranging between .984 to 1.27, however both tests 1 and 5 show quite a bit of unsymmetrical behavior with this ratio being 1.52 for the Test 1 and 1.42 for Test 5.

Figure 6.2 shows the results obtained from test PJ2. With the arrangement used in this test the radial velocity is being recorded which is the velocity that is in a normal direction to the interface. In Figure 6.2 it is clear that the gage just before the interface recorded a velocity of just under 2.5 m/s while the gage an equal distance away (G3) but not near the interface recorded a velocity of about 2.25 m/s. The stress wave arrived at both gages at about the same time but the velocity rise time is slightly higher for G1 than for G3. A comparison of the results for gages G1 and G2 show that the velocity signal is delayed (by 1.8 microseconds) by the rubber cement interface and 87.4% of the velocity in the outgoing wave is transmitted through the interface.

Figure 6.3 shows the results obtained from one of the tests which did not exhibit good symmetry - Test PJ1. In this case the velocity recorded at gage G3 was 1.9 m/sec while the velocity recorded just before the interface at gage G1 was about 2.9 m/sec.. The ratio of the velocity recorded before the interface to that recorded after the interface was 1.52 or a transmission of only 80% of the velocity by the rubber cement joint and again a delay (2.9 microseconds) as the wave passes the interface. For the four tests

Table 6.1

Test	Borehole Dia.	Gage Location (from jt)	G1 m/s	G1/G2	G1/G3	Delay (Microsec)
PJ1	6.35 mm	3.2 mm	2.92	1.52	1.52	2.9
PJ2	5.08 mm	3.2 mm	2.43	1.29	1.08	2.5
PJ3	5.08 mm	2.4 mm	2.63	1.51	0.98	1.8
PJ4	5.08 mm	1.6 mm	2.51	1.31	1.20	1.5
PJ5	5.08 mm	1.6 mm	3.68	2.18	1.42	3.0
PJ6	5.08 mm	1.6 mm	2.73	2.24	1.27	2.5
PJ7	5.08 mm	1.6 mm	2.27	1.15	G1/G4 1.02	1.3
PJ8	5.08 mm	1.6 mm	2.19	1.11	0.98	1.5
	G3	"G3"				
PJ1	1.9	2.41				
PJ2	2.25	2.22				
PJ3	2.68	2.18				
PJ4	2.09	2.22				
PJ5	2.59	2.68				
PJ6	2.15	1.98				
PJ7	2.23	2.12				
PJ8	2.23	2.08				

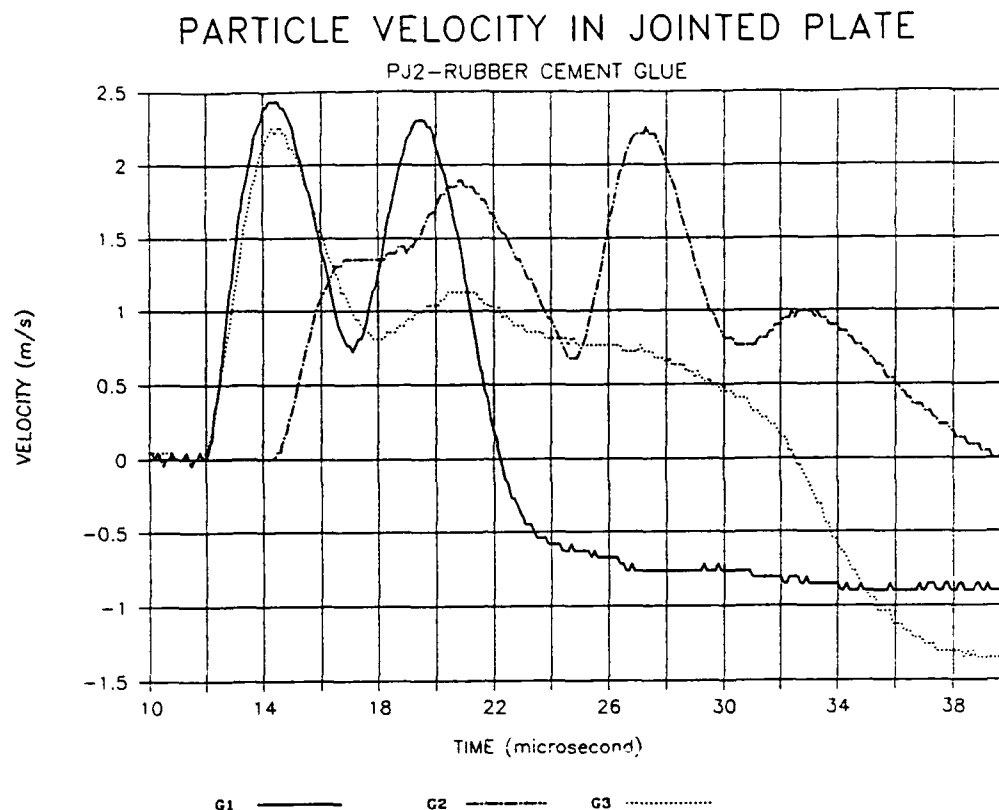


Figure 6.2. Particle Velocity Results Obtained in Test PJ2 which Used Rubber Cement as Bonding Agent.

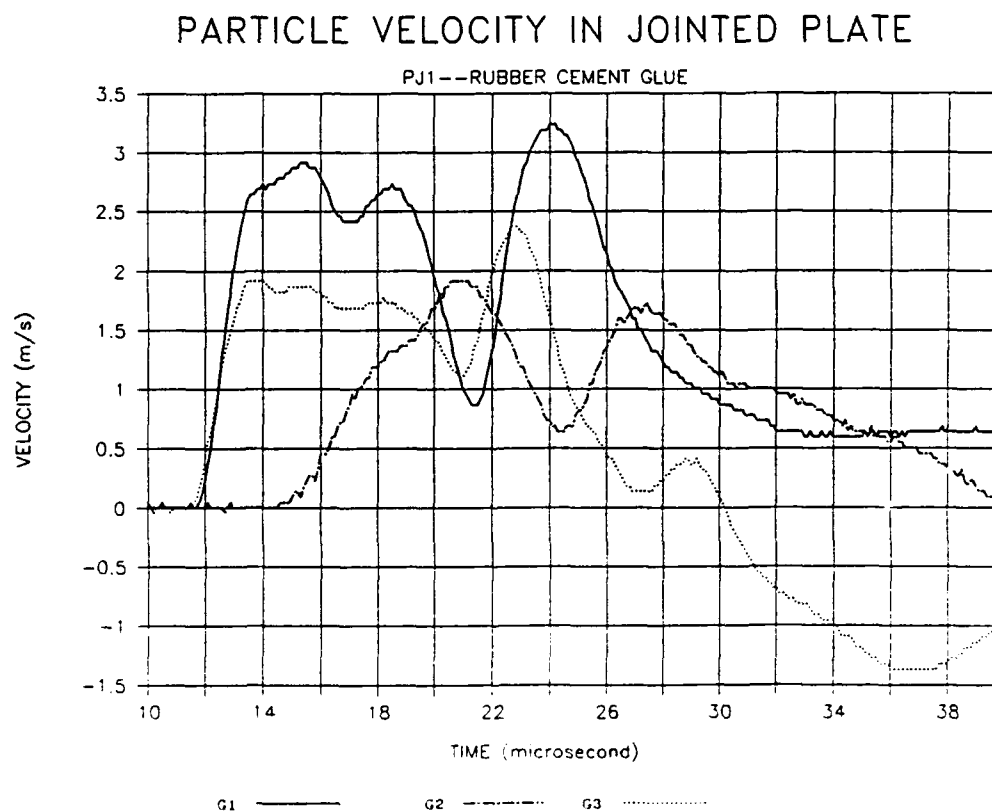


Figure 6.3. Particle Velocity Results Obtained in Test PJ1. This Test Also Used Rubber Cement to Bond the Model Parts Together.

(6.4)

conducted in models which had joints constructed with the rubber cement the percentage of velocity transmitted were found to be 80, 87.4, 79.86, and 86.5 percent. The time delay for the four tests were 2.9, 2.5, 1.8, and 1.5 microseconds.

For the test which used the double sided tape only 63.1% of the velocity was transmitted with a time delay 3 microseconds. For the grease interface only 61.6 % of the velocity was transmitted with a time delay of only 2.5 microseconds. Figure 6.4 presents the results obtained for the model with the grease interface. Gage G1 just before the interface recorded a velocity of 2.7 m/s while gage G3 measured only 2.1 m/s and showed a later arrival time for the leading edge of the wave than did G1. Across the interface the velocity was measured to be only 1.25 m/s.

The last two tests in this series used models that were somewhat smaller than those used for the first six tests. It was desired to determine the effect that a free boundary would have on the velocity measurement. The model was reduced in size therefore to result in gage G3 being located the same distance from the borehole as the gage just before the interface but G3 was located very near a free boundary. A fourth gage (G4) was used to check on the symmetry of the explosive wave. Figure 6.5 shows the geometry of the model and as shown G1, G2, and G4 were all located the same distance from the borehole but G1 was located just before the interface, G3 just before a free surface, and G4 was located near neither an interface nor a free surface. The overall model size was 230 mm x 152 mm x 9.5 mm thick. The material used for these two tests was plexiglas instead of Homolite 100. The material used to form the interface was a glue from a hot glue gun and PJ7 had an interface thickness of 0.127 mm (5 mils) while PJ8 had a 0.254 mm (10 mils) layer of hot glue. Other pertinent parameters for the two tests are given in Table 6.1. As seen from the table the explosive charge in both tests was very symmetrical with the ratio of the readings obtained at G1 compared to those obtained at G4 being 1.02 and 0.98. Figure 6.6 shows the results for the model with the 0.127 mm (5 mil) layer. The velocities measured at G1 and G4 are nearly identical with a peak velocity measurement of about 2.2 m/s. Gage G3, located near the free surface, recorded a velocity of 4 m/s showing the reinforcement of the velocity by the wave reflection from the free boundary. After passing the interface the velocity drops from 2.2 m/s to 1.9 m/s. The transmission for the 0.127 mm (5 mil) layer was 93 % and that for the 0.254 mm (10 mil) layer was 94.7 percent showing that the increased layer thickness had no great effect. The time delay imposed by the hot glue was 1.3 microseconds for the 0.127 mm (5 mil) layer and 1.5 microseconds for the 0.254 mm (10 mil) layer - once again showing no noticeable effect from the increased thickness of the layer.

The values reported for the percentage velocity transmitted need some explanation. By looking at the results from PJ7 and PJ8

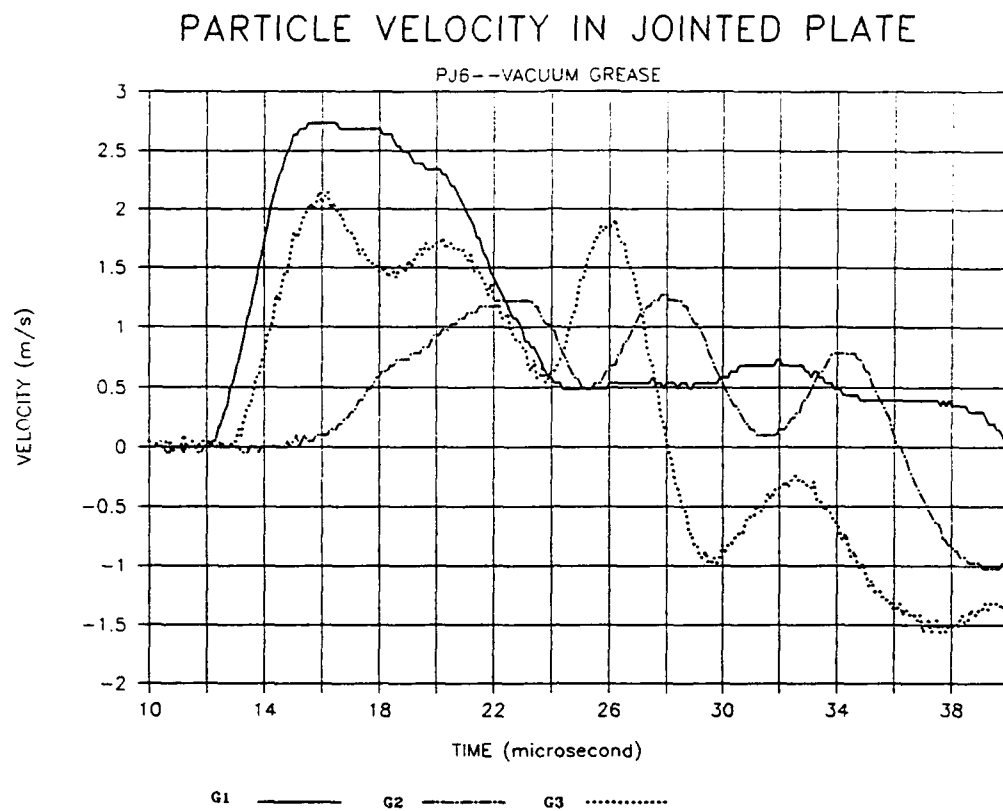


Figure 6.4. Results From Test PJ6 which had Grease Between the Two Model Halves.

Technical drawing of a rectangular plate with dimensions and labels. The plate has a total width of 230 mm and a total height of 76.2 mm. The drawing shows a central vertical dashed line and a horizontal dashed line. The distance from the left edge to the central vertical line is 115 mm (230 mm / 2). The distance from the bottom edge to the horizontal dashed line is 36.5 mm. The distance from the central vertical line to the right edge is 115 mm. The distance from the horizontal dashed line to the top edge is 39.8 mm (76.2 mm - 36.5 mm). The labels G1, G2, G3, and G4 are positioned near the center of the plate. G1 is at the intersection of the dashed lines. G2 is above G1. G3 is below G1. G4 is to the right of G1. The drawing also shows a small circle at the intersection of the dashed lines.

THICKNESS: 9.5mm

CHARGE: PETN 200 mg

GAGE LENGTH:12.7 mm

G1 AND G2 ARE 1/16" FROM JOINT

G3 IS 1/6" FROM FREE SIDE

JOINT:HOTGUN GLUE (5 mil. THICK)

Figure 6.5. Geometry of Models Used in Tests PJ7 and PJ8 which were made of PMMA.

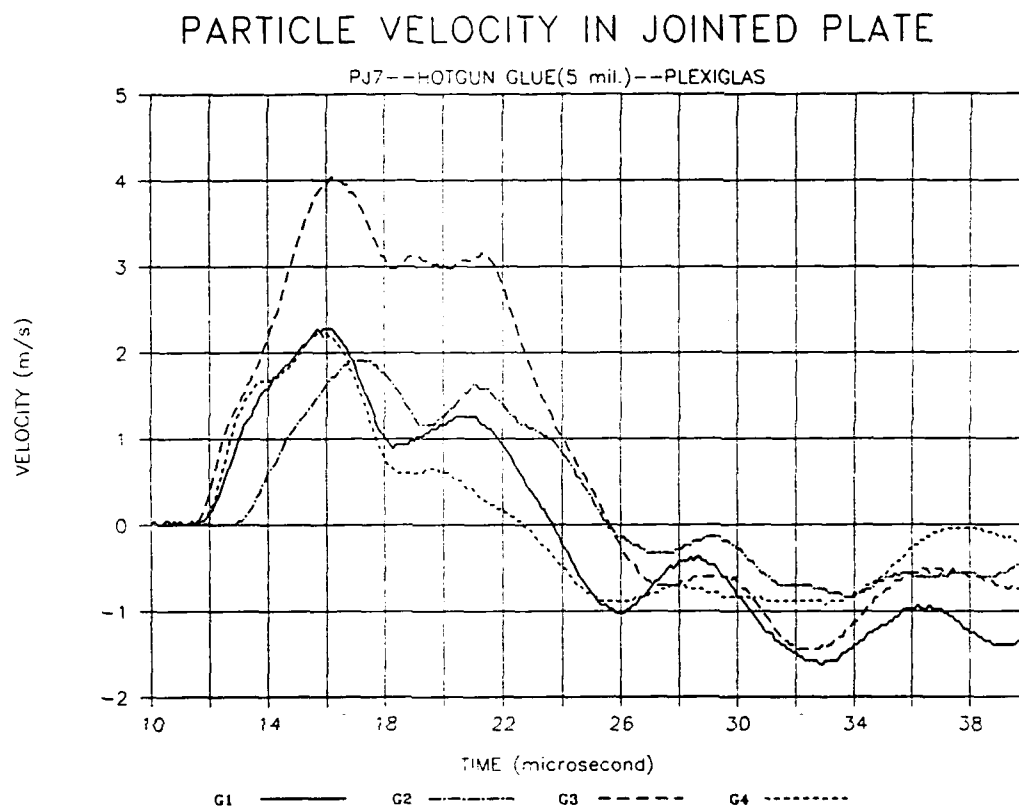


Figure 6.6. Particle Velocities Recorded in Test PJ7 which had Model Halves Bonded Together with Hot Glue.

(6.5)

it is clear when 100 percent reflection occurs (as at a free surface) that velocities measured near the free boundary are nearly twice as large as velocities measured in the free field (4 m/s compared to 2.2 m/s). Since in all cases there was a reduction in the velocity measured on the far side of the interface compared to that measured on the near side some reflection is occurring at each of interfaces. Some of the velocity difference measured across the interface is due to hysteresis losses and some is due to reflection at the boundary. The loss due to hysteresis is assumed to be very small. Whatever is reflected back into the main part of the model helps to boost the reading just before the interface so that the value recorded there is an inflated figure. The actual amount of velocity transmitted is therefore calculated by taking the signal just before the interface to be made up of two terms - the actual velocity plus the amount of reflected velocity.

Listed in Table 6.1 are a comparison of the reading from the free field gage - G3 and the corrected reading on gage G2 (under "G3") when the reflection from the interface is taken into account as described above. The agreement is good except for tests PJ1 and PJ4 where in both cases the corrected reading does not agree well with the free field velocity reading. At this time this disagreement would have to be attributed to an unsymmetrical loading on the borehole. In the case of PJ1 the free field horizontal velocity (to the side of the borehole) is less than the vertical velocity and in the case of PJ3 the horizontal velocity was larger than the vertical velocity. Both of these tests (PJ1 and PJ4) indicated a transmission of around 80%, while the other two tests with rubber cement (PJ2 and PJ3) indicated a transmission nearer to 87%. It is felt that in view of the disagreement of the horizontal and vertical velocities that the transmission of 87% is the more correct figure.

C. Three dimensional tests.

A number of tests were conducted in three dimensional models made of entirely of Hydrocal or entirely of Hydrostone to investigate the velocity propagation across artificial interfaces. These models were cast in the form of cubes and had dimensions that were 305 mm³ or 457 mm³. The two different materials used in constructing the models are similar in that they are fast setting gypsum cements. Both have similar densities (0.055 lbs/cubic inches) and poisson's ratios (0.38) but hydrocal sets up less quickly and has a modulus of elasticity about twice that of hydrostone (3.15 GPa vs. 1.79 GPa). Both are felt to behave similar to rock except in the immediate vicinity of the charge where the high porosity in both materials result in excessive compaction compared to rock.

Figure 6.11 shows a typical model geometry. As shown for this 305 mm cube an interface was placed at the top and velocity gages were poured in place as the model was cast. In the model shown

(6.6)

gages were located just before the interface (G2) and just after the interface (G1). In this model gages were also located 25.4 mm above the borehole (G3) and an equal distance below the borehole (G5) and just before the free surface at the bottom of the model (G9). The distance from the charge to gage G9 was equal to the distance from the borehole to gage G2 - the gage just before the interface.

The tests conducted were intended to investigate several different aspects of the presence of interfaces and their effects upon particle velocities. Tests were conducted with models containing both rough and smooth interfaces. The rough interfaces were created by replicating a natural surface found in a granite joint while the smooth interfaces were formed by replicating the surface of a formica countertop. The magnetic coils and gage locations were arranged to permit measurements to be made of the transmission of normal velocities across interfaces as well as transmission of tangential velocities and velocities which contained both normal and tangential components.

Tests were also conducted to permit an investigation of velocities transmitted across smooth interfaces which had a known separation. This known separation was achieved by pouring the two parts of the model with a smooth boundary and then using various grit sizes of sand between the two surfaces to achieve the desired separation.

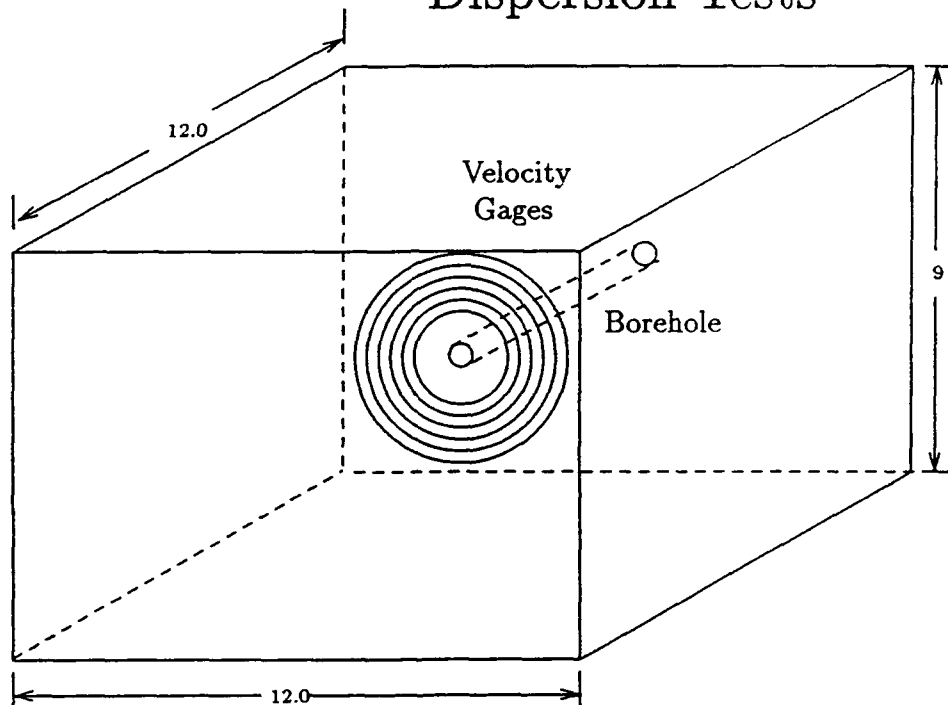
D. Material dispersion.

Figure 6.7 shows the location of pick up loops used to measure the loss in velocity magnitude as a function of distance from the charge in the Hydrocal material. In this case the loops shown were located on the same plane as the explosive source and the magnetic field was arranged to measure radial velocity. The model size for this particular test was 305 mm x 305 mm by 229 mm high. Figure 6.8 shows the response of the six gages and indicates a peak radial velocity of 21.7 m/s at 25.4 mm from the charge with a decrease in velocity to 2.15 m/s measured at 57.2 mm from the charge. This data was fitted by both a power law and an exponential decay law in order to see which would best fit the data. Figure 6.9 shows a comparison of the experimental data with the two approximate fits and indicates that the power law best describes the decay with distance. As indicated in the figure only two data points were used to find the approximate curves - a radius of 25.4 mm and a radius of 50.8 mm. The function found to fit the data (the power law) is:

$$v = 6.885 \times 10^5 / r^{3.2} \quad (3)$$

This compares to an exponent of 0.40 for the polymeric materials used in the two dimensional tests and reflects the high porosity of the gypsum material as discussed above. In Figure 6.10 the

Tests 35 and 36 Model Geometry Dispersion Tests



Velocity Gages had radii of 1.0, 1.25, 1.5, 1.75, 2.0, 2.25 inches moving radially out from the charge.

Charge was located in center of model 4.25 inches from the bottom face.

All dimensions are in inches.

Figure 6.7. Layout of Velocity Gages Used to Determine Dispersion in Three Dimensional Models.

Height above
Bottom Surface
of Model in
inches

Test 36, Dispersion Test 2

12 inches \times 12 inches \times 9 inches (height)

Velocity gage radii are in inches

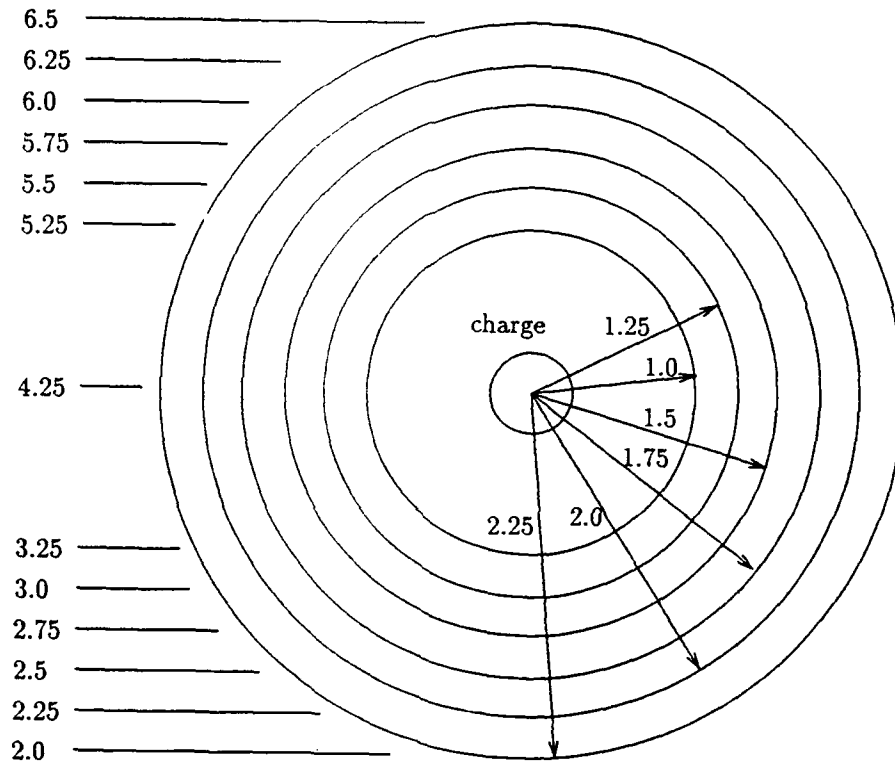


Figure 6.7. Layout of Velocity Gages Used to Determine Dispersion in Three Dimensional Models.

Test 36, Dispersion Test 2

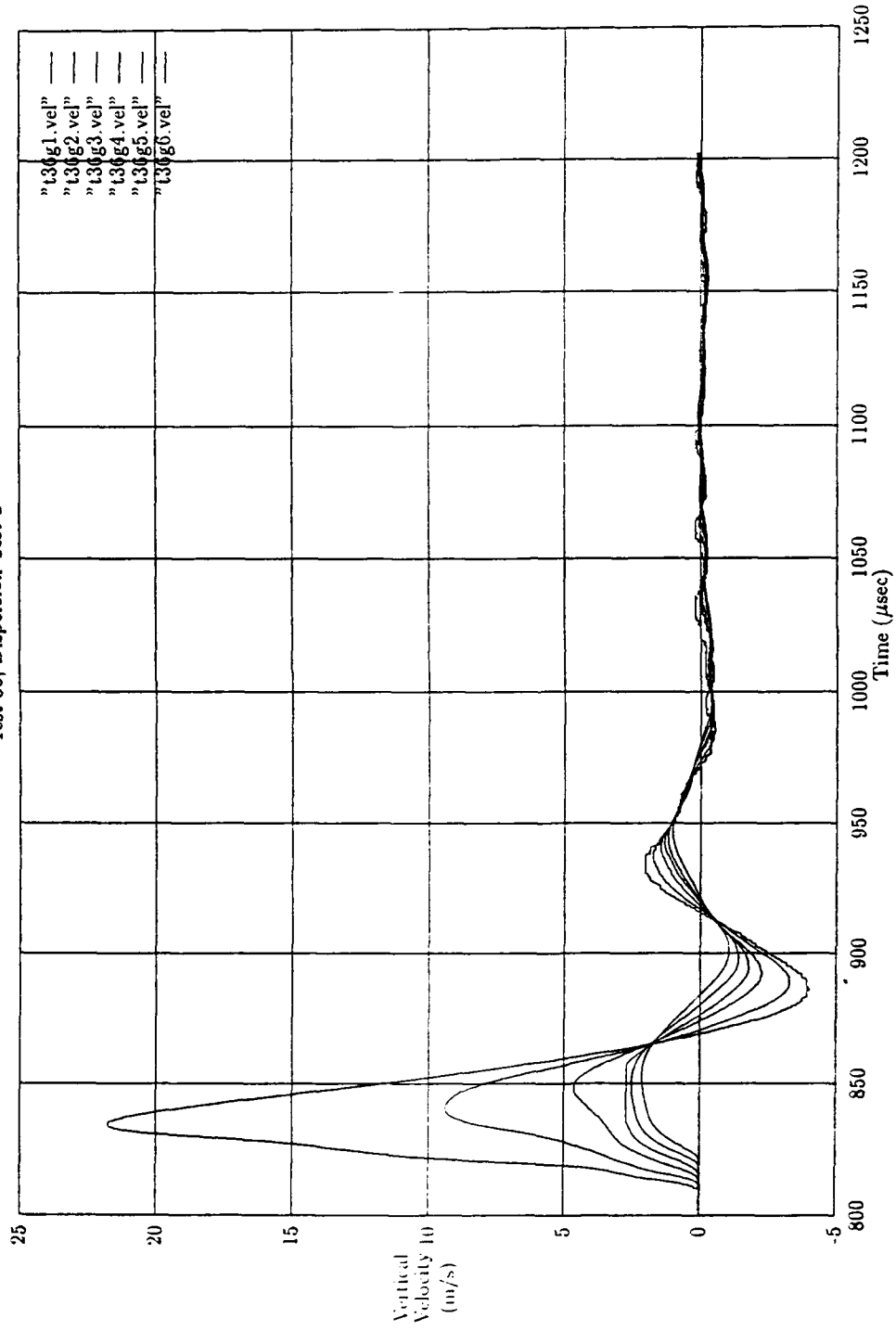


Figure 6.8. Velocities Measured as a Function of Distance From Charge in Dispersion Test.

Velocity as a Function of Radius

Comparisons with Experimental

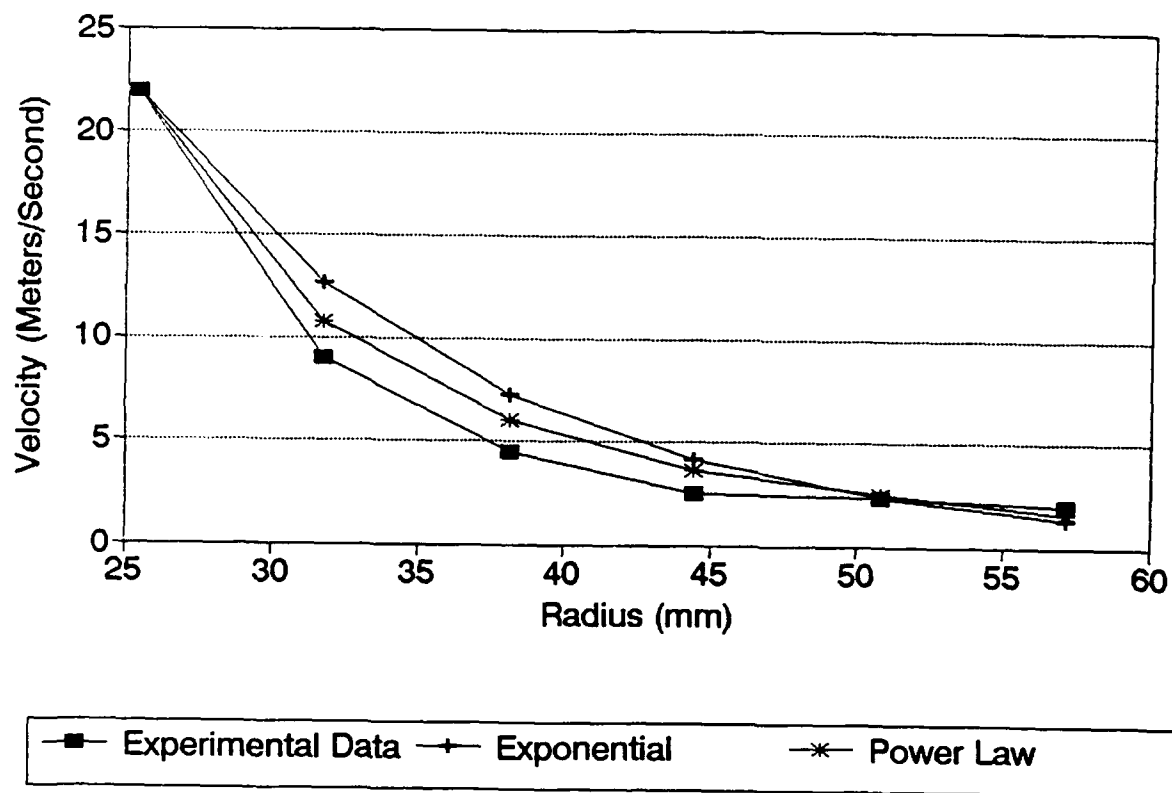


Figure 6.9. Comparison of Velocities Measured Experimentally With an Exponential Decay Law and a Power Law Decay.

Velocity as a Function of Radius

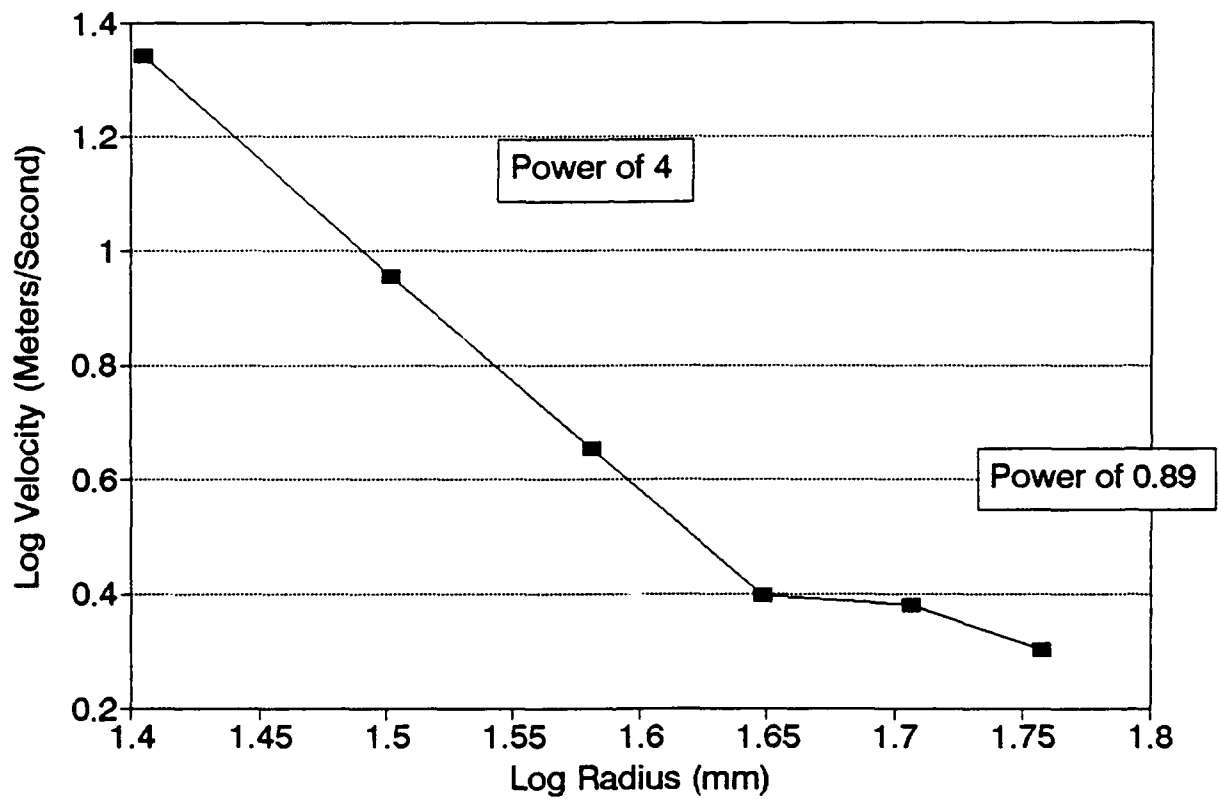


Figure 6.10. Log-Log Plot of Velocity versus Distance From Charge Showing Decrease in Decay Rate at Distances Greater Than 38 mm.

(6.7)

velocity - distance results are plotted on Log Log paper and shows that a better fit would be obtained by using two different power laws. Close to the borehole (out to 45 mm) an exponent of 4.0 would be appropriate while at further distances an exponent of 0.89 would be better to use. This indicates that most of the loss (due to material dispersion) occurs within the first 45 mm. After that the loss is quite small and can be ignored unless large propagation distances are involved.

E. Results from three dimensional tests.

Figure 6.11 shows the location of the velocity gages for Test 18. This model was Hydrocal and the interface was replicated from a slab of granite. The surface used for replicating the interface is shown in Figure 6.12. The roughness of the surface was documented by a profilometer. A PETN charge of 500 mg was used in all of the three dimensional tests. The velocities measured in this test were the velocity component normal to the interface (or vertical). Figure 6.13 shows the velocities recorded at the five of the six velocity gages - no record was obtained for gage G5. At gage G3 (Figure 6.13a) - the closest gage to the borehole - a velocity of 2.3 m/s was obtained. Figure 6.13b compares the readings obtained at gages G9 (just before the free surface) and gage G2 (just before the interface). As can be seen from the comparison the free surface caused an increase in amplitude (1.75 m/s vs 1.1 m/s) and a broadening of the waveform. In Figure 6.13c the velocity recorded just before the interface (G2) and the velocity recorded just after the interface (G1) are compared. The decrease in signal across the interface was not great - only about 10 % of the signal or a transmission of 90%. Figure 6.14 summarized the amplitudes of velocity recorded in the two tests (18 and 19) which measured vertical velocities). In test 19 only two valid velocities were recorded. Note that these two gages (G5 and G6) were not located directly above the borehole and the velocities amplitudes shown are the vertical components of the radial velocity caused by the explosive charge.

Figure 6.15 gives a summary of the results obtained in three tests (27, 28, and 29) which measured vertical velocities transmitted across a smooth interface. Recall that this interface was made by replicating a formica counter top in the model material. In the case of tests 27 and 28 the material was Hydrocal and in test 29 Hydrostone was used. Once again these are vertical velocities and for gages 1, 2, 5, and 6 are a measure of the vertical component of a radial stress wave. The values obtained for test 29 are smaller than those obtained from the other two tests and might be the result of the change in material from Hydrocal to Hydrostone.

Figure 6.16 shows results from tests (20 and 23) which measured the transmission of horizontal velocities across a rough

Test 18 Model Geometry

All dimensions are in inches

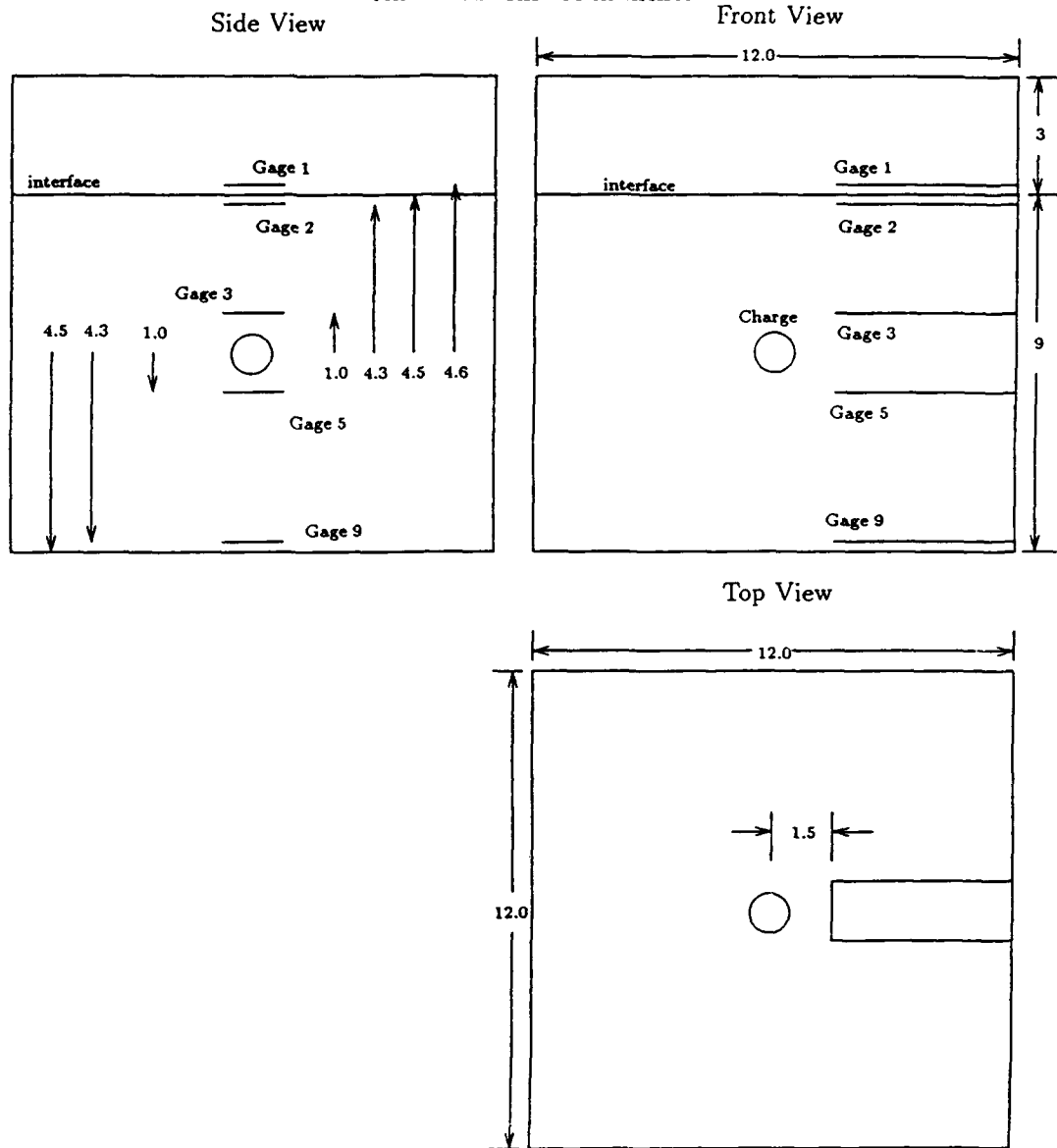


Figure 6.11. Geometry of Three Dimensional Models - Test 18.

Tests 19 and 20 Model Geometry

All dimensions are in inches

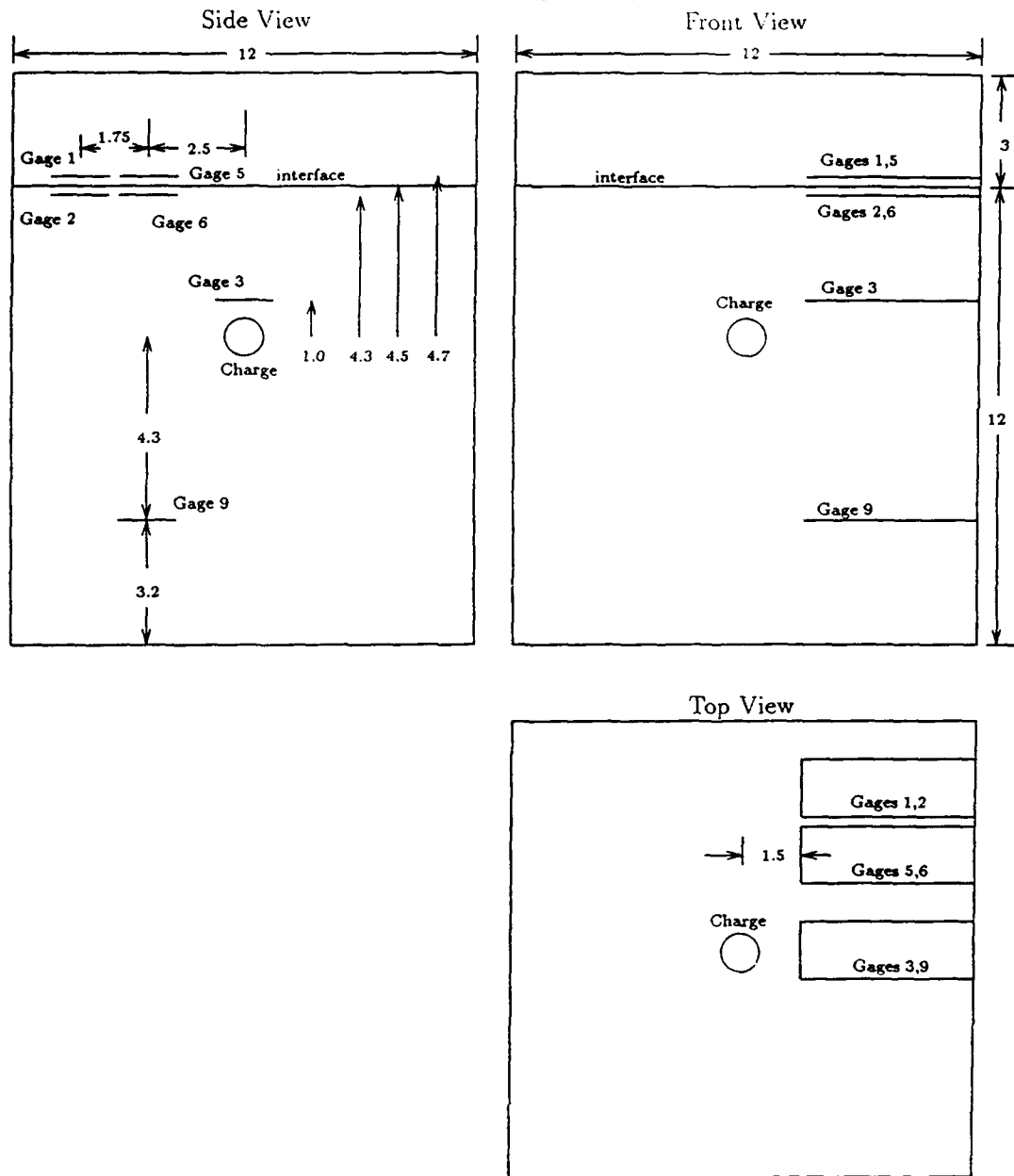


Figure 6.11. Geometry of Three Dimensional Models
Tests 19 and 20.

Test 23 Model Geometry

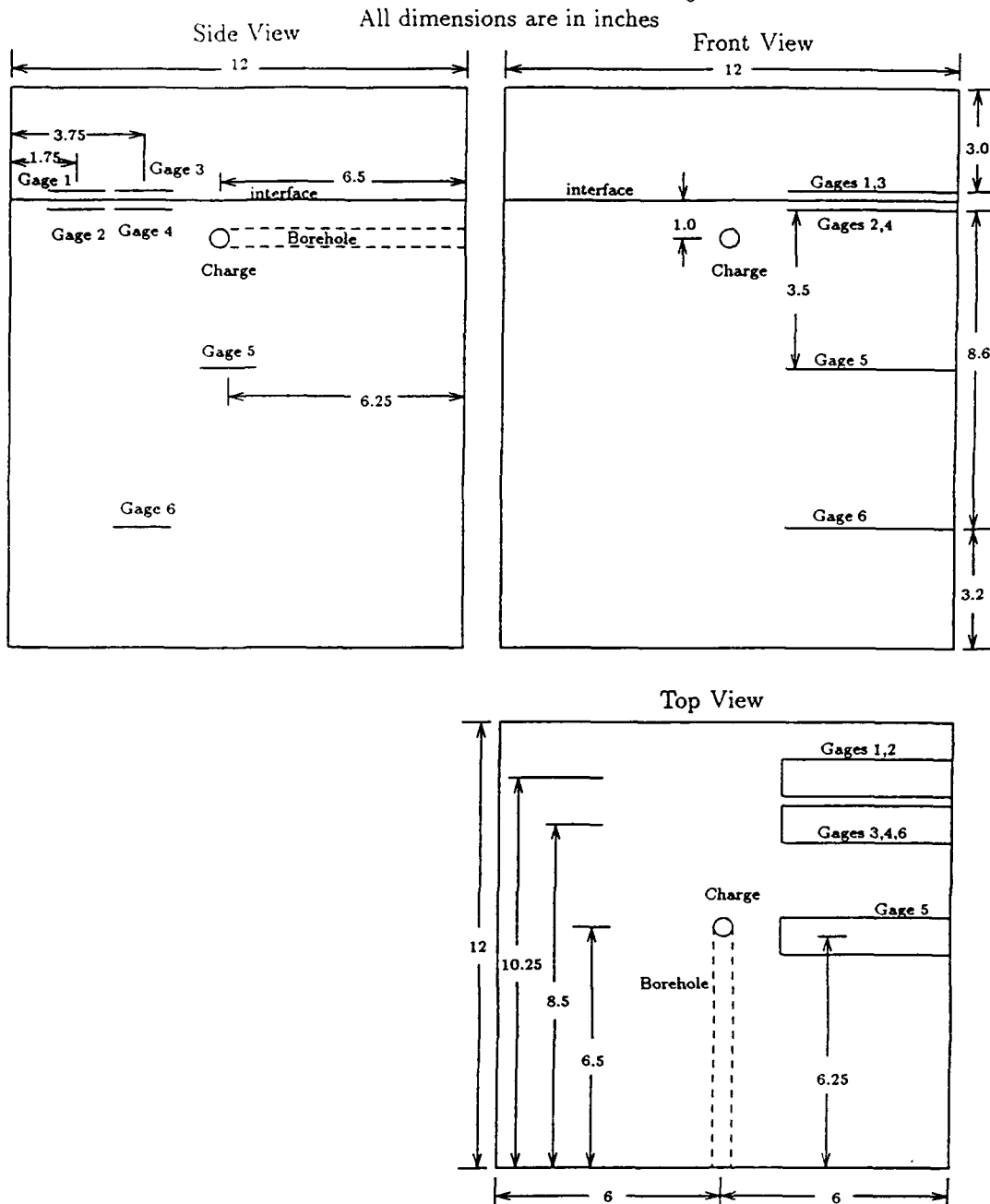


Figure 6.11. Geometry of Three Dimensional Models - Test 23.

Tests 27, 28, and 29 Model Geometries

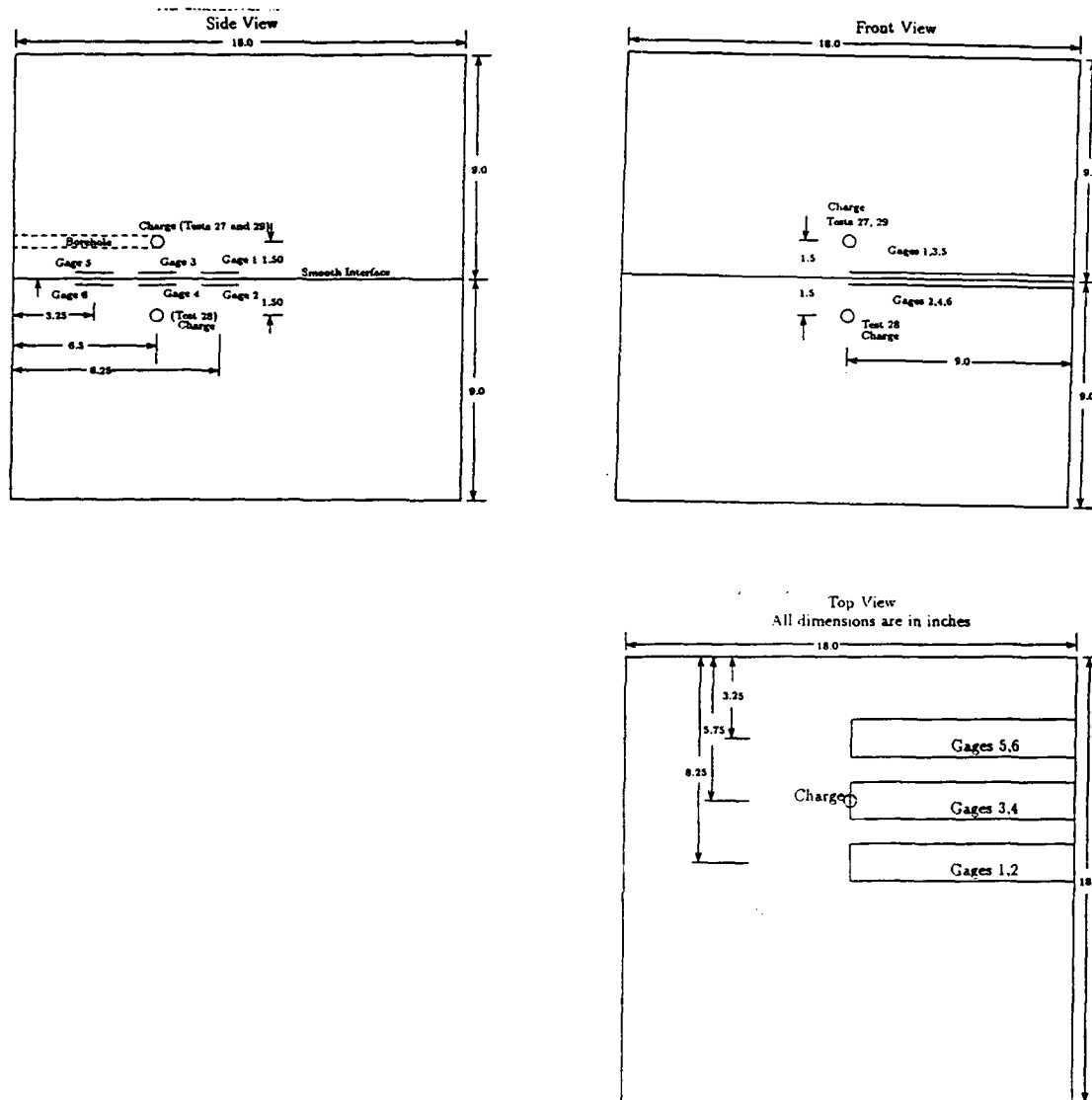


Figure 6.11. Geometry of Three Dimensional Models Tests 27, 28, and 29.

Tests 30-34 (Air Gap) Model Configuration

All dimensions are in inches

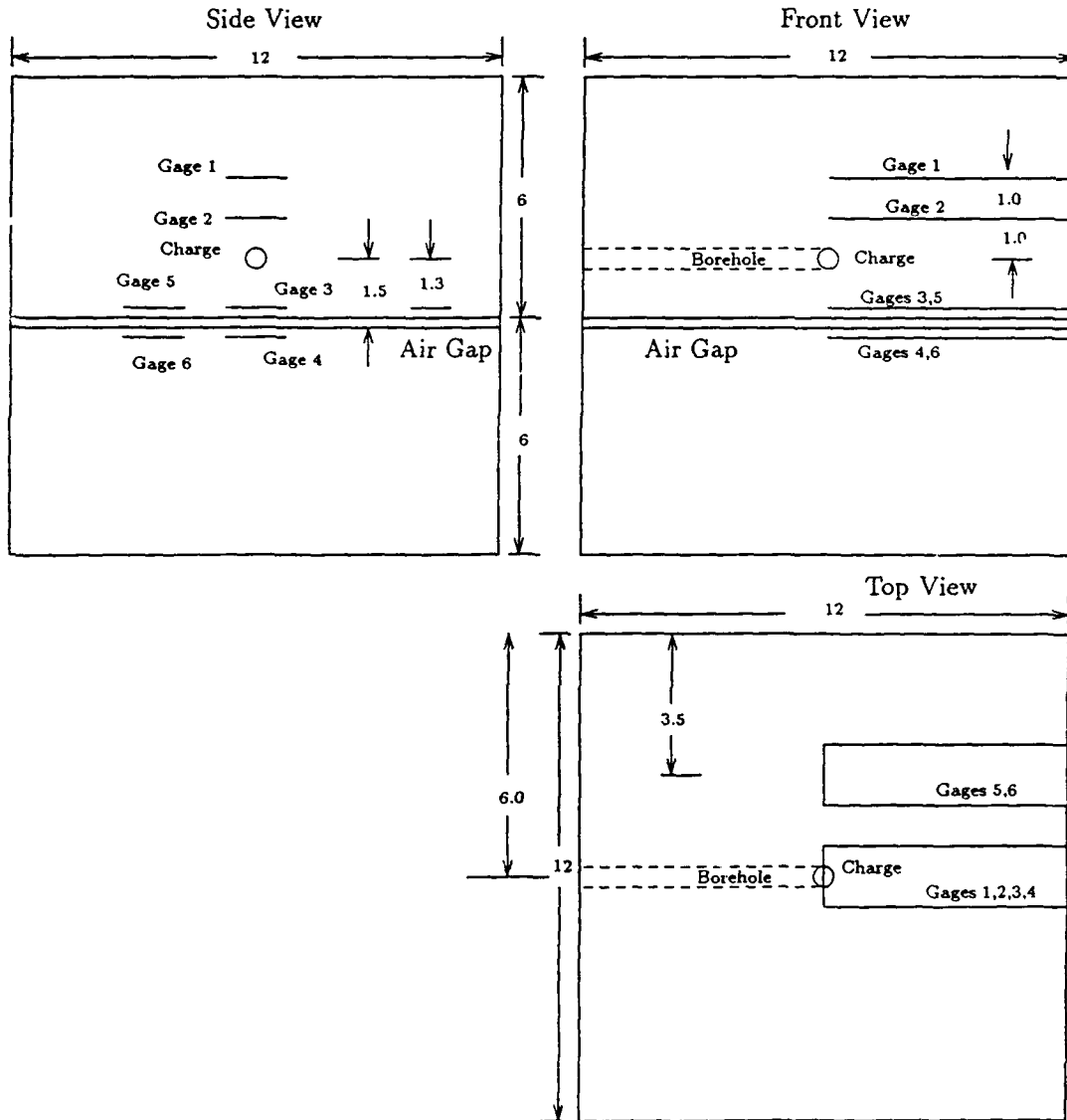
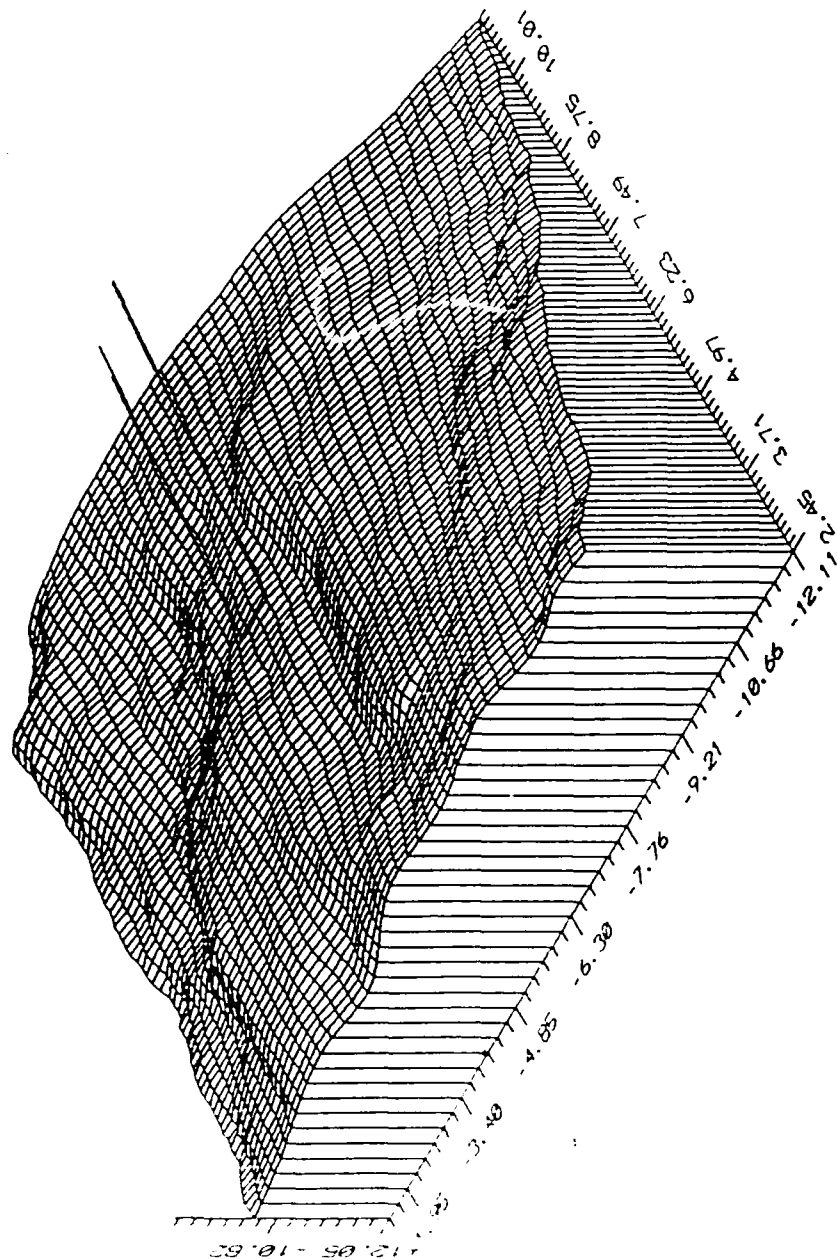


Figure 6.11. Geometry of Three Dimensional Models
Tests 32, 33, and 35.

Figure 6.12. Representation of Rough Surface Used in Interface Tests.



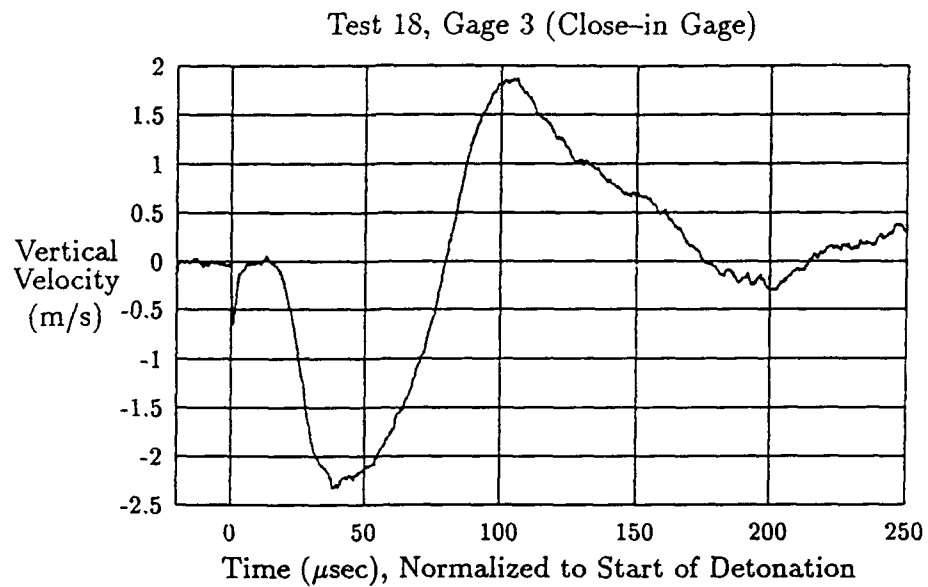


Figure 6.13. Velocities Recorded in Test 18.
a) Close in Gage (G3).

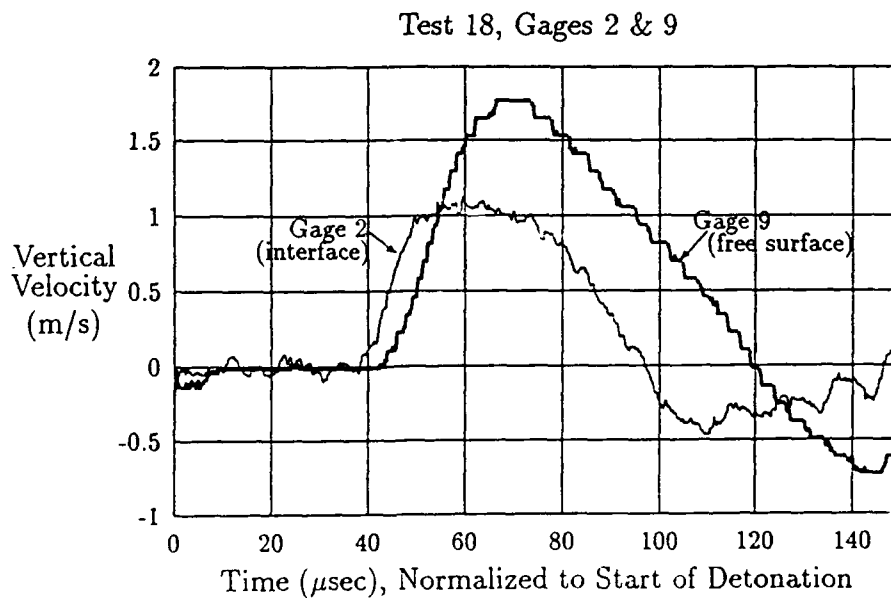


Figure 6.13. Velocities Recorded in Test 18 - b) Gage Just Before Interface (G2) and Just Before Free Face (G9).

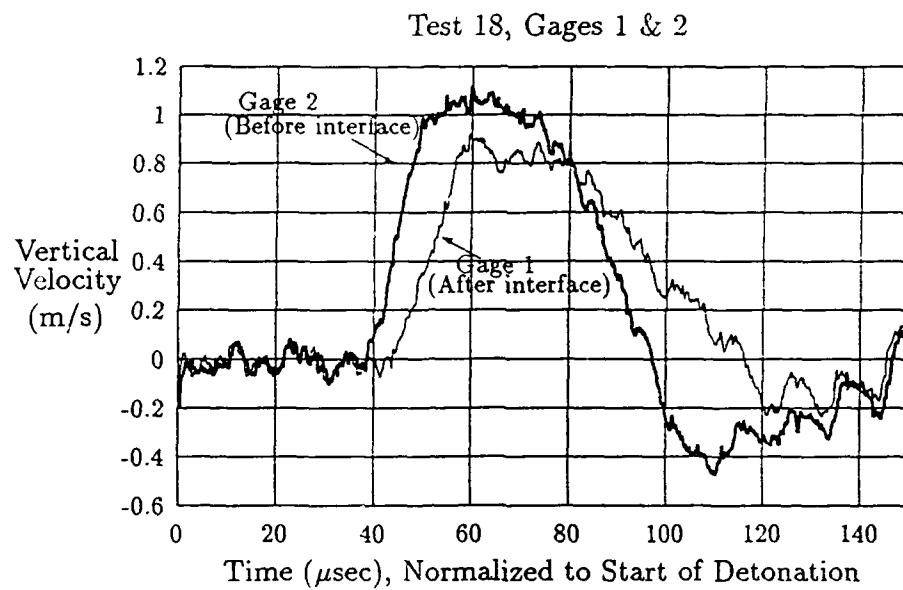


Figure 6.13. Velocities Recorded in Test 18 - c) Gage Just Before Interface (G2) and Just After Interface (G1).

Results for Test 18 - Vertical Velocity

Rough Interface

Interface	G1 = 0.9 m/s
	G2 = 1/1 m/s
Borehole	G3 = 2.3 m/s
	G5 No Data
	G9 = 1.75 m/s

Figure 6.14. Summary of Results Obtained From Vertical Velocity Measurements With Rough Interface. a) Test 18 Results.

Results for Test 19 - Vertical Velocity

Rough Interface

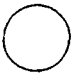
Interface	G5 = 0.5 m/s G6 = 0.59 m/s
Borehole	
G1,G2,G9,G3 No Data	

Figure 6.14. Summary of Results Obtained From Vertical Velocity Measurements With Rough Interface. b) Test 19 Results.

Results for Test 27 - Vertical Velocity Smooth Interface

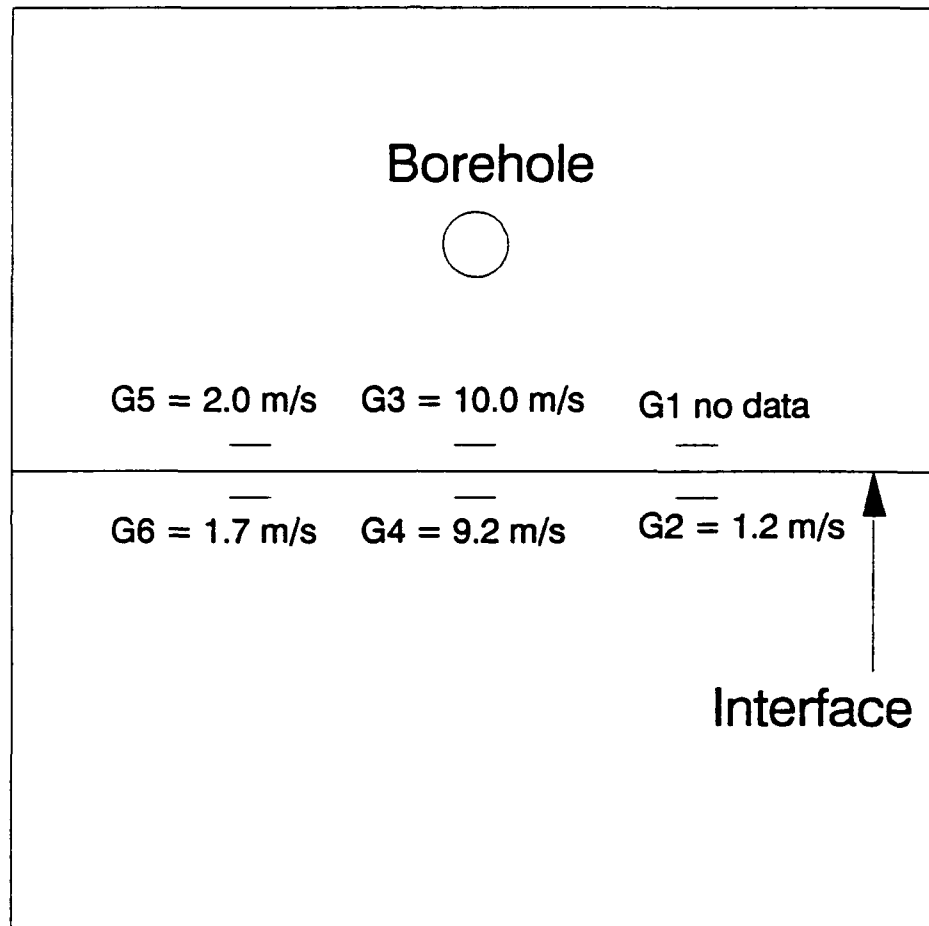


Figure 6.15. Summary of Results Obtained From Vertical Velocity Measurements With Smooth Interface. Test 27 Results.

Results for Test 28 - Vertical Velocity

Smooth Interface

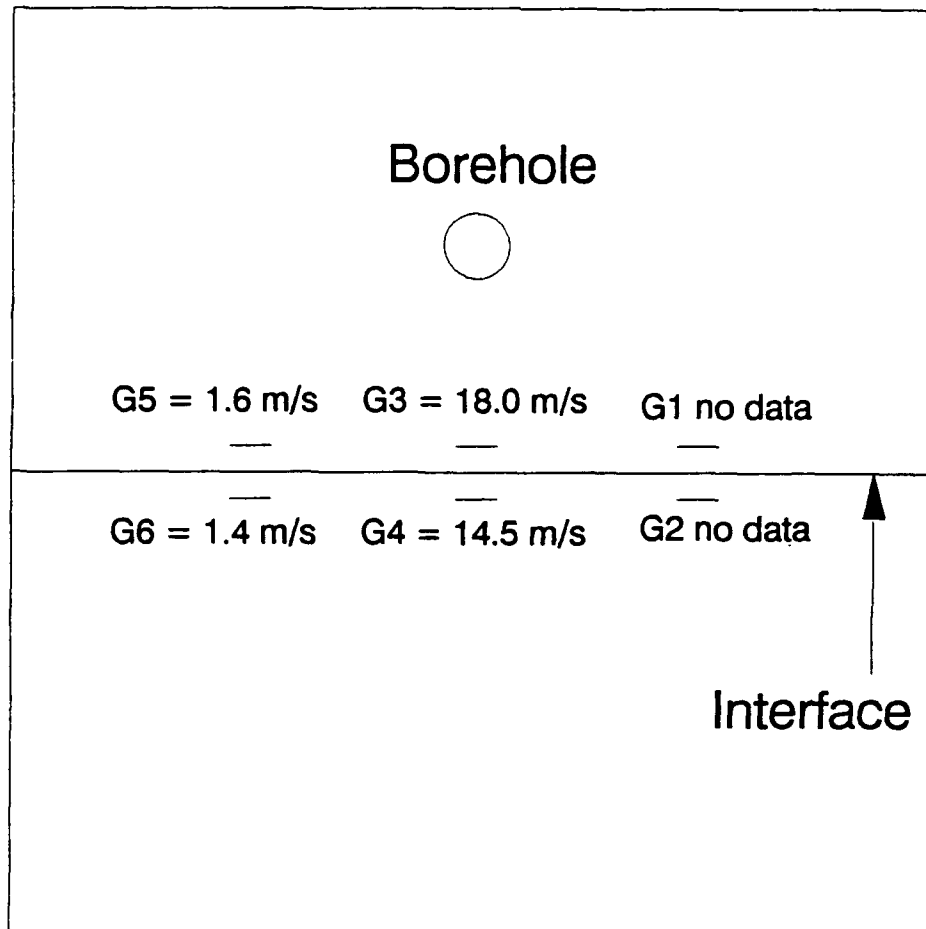


Figure 6.15. Summary of Results Obtained From Vertical Velocity Measurements With Smooth Interface. Test 28 Results.

Results for Test 29 - Vertical Velocity

Smooth Interface

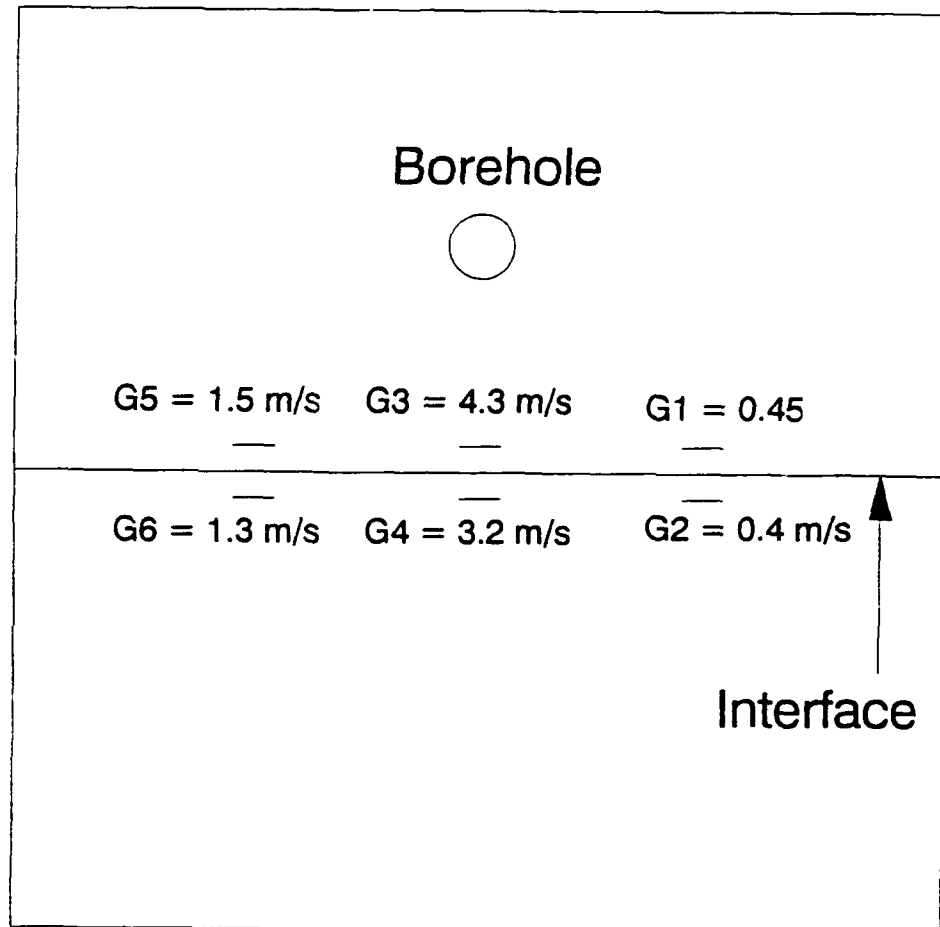


Figure 6.15. Summary of Results Obtained From Vertical Velocity Measurements With Smooth Interface. Test 29 Results.

Results for Test 20 - Horizontal Velocity

Rough Interface


G1=0.58 m/s G5=0.68 m/s	Interface
G2=0.60 m/s G6=0.78 m/s	
G3=2.7 m/s	
	Borehole
G9 No Data	

Figure 6.16. Summary of Results Obtained From Horizontal Velocity Measurements With Rough Interface. a) Test 20 Results.

Results for Test 23 - Horizontal Velocity

Rough Interface

G1=0.13 m/s	G3=0.55 m/s	Interface
G2=0.15 m/s	G4=0.53 m/s	○ Borehole
G6 No Data		

Figure 6.16. Summary of Results Obtained From Horizontal Velocity Measurements With Rough Interface. b) Test 23 Results.

interface. Once again the figure reported represents the horizontal component of a radial stress wave.

Figure 6.17 presents the results obtained in transmission of velocity normal to a smooth interface with a fixed separation distance between the joint faces as obtained from three tests (33-2.05 mm separation, 32-2.29 mm separation, and 34-3.825 mm separation). As can be seen from this figure a gap of only 2 mm is quite effective in preventing transmission of normal velocities across an interface. Not only do the readings from gage G4 indicate very little transmission but the relative high readings (compared to G2) indicated significant reflection from the interface back into the model. Gage 3 is 38.7 mm from the charge while gage G2 is 25.4 mm away. According to the dispersion curve determined earlier the readings at G3 should be only 20% of the value recorded at G2 - assuming that the exponent 4 is used in the power law since the distance is within 44 mm. The readings just before the interface are however somewhat greater than those at G2 indicating meaningful reflections are occurring. As seen from Figure 6.18 the waveform is also broadened significantly at G3 compared at G2.

F. Discussion.

Table 6.2 presents a summary of the results obtained in the tests conducted to determine the ability of joints to transmit or reflect velocity. Results are shown for both the two and three dimensional tests conducted in the polymeric and fast setting gypsum materials. The average transmission for the four tests conducted in Homolite with rubber cement as the bonding agent (PJ1, PJ2, PJ3, and PJ4) was 83.4 percent of the normal velocity. The test which used double sided tape was able to transmit only 63 % of the velocity normal to the interface across. The weakest joint was the one which used grease between the two halves of the model and it transmitted only 61.6%. The two models which used a hot glue gun to form the two halves of the model transmitted 94% of the normal velocity across the interface. It was felt that the rubber cement used in the first four model to bond the two halves together did not dry properly in the center areas of the interface and this would tend to be borne out by the relatively low transmission values compared to the results obtained with the hot glue gun. The results from the grease filled joint seem to indicate that this is not a very effect way to form a momentum trap as is often used when wave reflection back into the model are not desired.

The results from the three dimensional models which used no bonding agent but merely relied upon self weight to hold the two surfaces together indicate that quite efficient transmission was obtained. For the models which were used to determine the transmission of velocity normal to the interface the transmission percentages were quite high - around 82 % for the rough surfaces and 85 % for the smooth interface models.

Table 6.2

Test	Type of test	Velocity Direction	% Transmission		
PJ1	2D Homolite RC	Normal	80		
PJ2	2D Homolite RC	Normal	87.4		
PJ3	2D Homolite RC	Normal	79.8		
PJ4	2D Homolite RC	Normal	86.5		
PJ5	2D Homolite Tape	Normal	63.1		
PJ6	2D Homolite Grease	Normal	61.6		
PJ7	2D PMMA Glue 5 mil	Normal	93		
PJ8	2D PMMA Glue 10 Mil	Normal	94.7		
18	3D Rough Hydrocal	Normal	81.8		
19	3D Rough Hydrocal	Normal	84.7		
27	3D Smooth Hydrocal	Normal	92	85	
28	3D Smooth Hydrocal	Normal	80.6	87.5	
29	3D Smooth Hydrostone	Normal	74.4	88.9	86.6
20	3D Rough Hydrocal	Horizontal	87.2	97	
23	3D Rough Hydrocal	Horizontal	86.7	104	
33	3D Smooth Hydrocal 2.05 mm Gap	Vertical	6.8		
32	3D Smooth Hydrocal 2.29 mm Gap	Vertical	7.3		
34	3D Smooth Hydrocal 3.82 mm Gap	Vertical	6		

RC indicates Rubber Cement

Results for Test 32 - Vertical Velocity

Air Gap = 2.29 mm

G1=2 m/s G2=22 m/s		○ Borehole Interface
G5=6.7 m/s	G3=25 m/s	
G6 No Data	G4= 1.2 m/s	

Figure 6.17. Summary of Results Obtained From Vertical Velocity Measurements Across Interfaces With Known Separations. Test 32 Results.

Results for Test 33 - Vertical Velocity

Air Gap = 2.05 mm

<p>G1=2 m/s</p> <p>G2=25 m/s</p> <p>○ Borehole</p>	
G5=1.3 m/s	G3=33 m/s Interface
G6 No Data	G4= 1.5 m/s

Figure 6.17. Summary of Results Obtained From Vertical Velocity Measurements Across Interfaces With Known Separations. Test 33 Results.

Results for Test 34 - Vertical Velocity

Air Gap = 3.825 mm

<div> <div>G1 No Data</div> <div>G2 No Data</div> <div>○ Borehole</div> </div>	
G5=1.4 m/s	G3=25 m/s Interface
G6 No Data	G4= 1.0 m/s

Figure 6.17. Summary of Results Obtained From Vertical Velocity Measurements Across Interfaces With Known Separations. Test 34 Results.

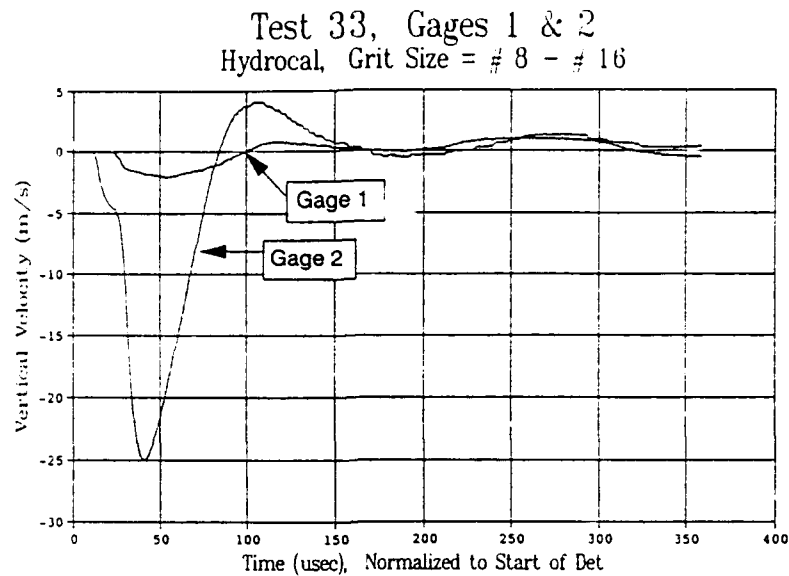


Figure 6.18. Velocities Measured in Test 33 with Interface Gap of 2.05mm. a) Results From Gages 1 and 2 showing Decay of Signal over 25.4 mm Range.

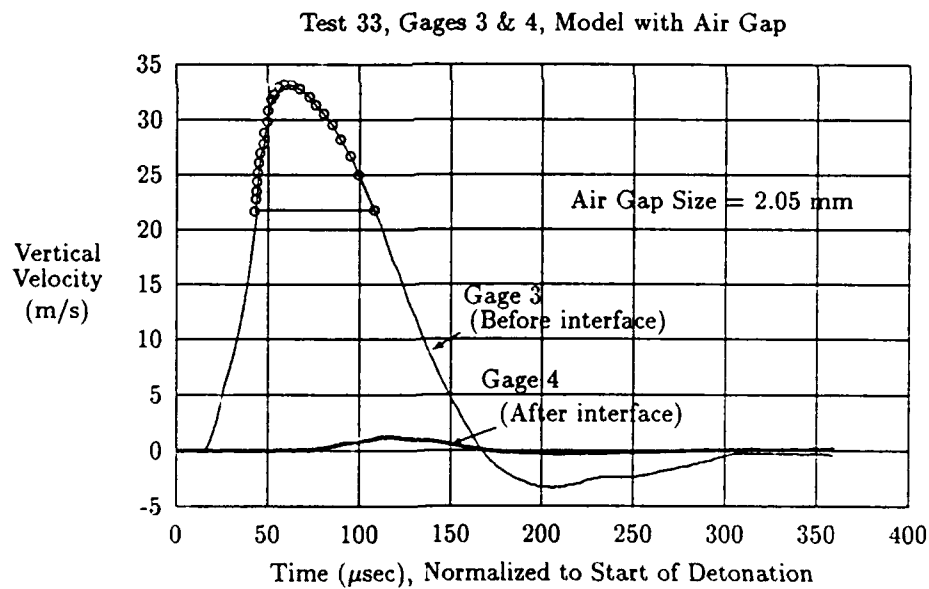


Figure 6.18. Velocities Measured in Test 33 with Interface Gap of 2.05 mm. b) Results From Gages 3 and 4 showing Decrease in Velocity Across Interface.

(6.9)

The transmission of horizontal velocities for the rough interface models was found to be even higher - around 94 %. The fact that one of the gage pairs resulted in a transmission percentage greater than 100 % is nothing more than scatter or inaccuracy of the readings from the velocity gages.

The last three tests which used an air gap of known dimensions between the two parts of the model resulted in very little transmission of normal velocities across the open interface. A gap of as little as 2 mm resulted in less than 10% of the velocity being transmitted across the interface and resulted in large reflections back into the model. This indicates that open (or mud filled) interfaces even though they may be quite small might affect greatly the amount of fragmentation and fracturing in the vicinity of the borehole. These open interfaces could quite easily increase spall very near the borehole and show results quite different than those expected in the absence of such interfaces.

The effects of such joints is very important and should be studied in more detail in future investigations.

REFERENCES:

- 6.1. "Recording Dynamic Fringe Patterns with a Cranz-Schardin Camera", W.F. Riley, and J.W. Dally, Experimental Mechanics, 9(8), 27N-33N (1969).
- 6.2. "Close-field Optical Analysis of an Explosive-loading Function", J.B. Ligon and W.F. Riley, Experimental Mechanics, 184-189, May 1974.

CHAPTER 7. SUMMARY.

A. Measurements and Observations.

The measurement of strain and particle velocity in transparent materials from dynamic loading produced believable values. The measurement of stress produced inconsistent values, mainly due to breakage of the electrical connection shortly after passage of the stress wave. The strain gages and mica flaws embedded in the transparent models acted as crack initiation sites. These cracks initiated approximately 20 microseconds after passage of the P-wave so that the signal after that time was disregarded. Cracks initiated at these sites arrested after traveling about 5 mm.

In rock-like materials, the method for measuring radial and vertical particle velocities proved very reliable and provided consistent results. Spherical and cylindrical charge shapes with the same weight and at the same depth of burial produced nearly identical particle velocities (radial and vertical). However, the spherical charge created a crater volume much larger than that created by the cylindrical charge.

There is not a clear correlation between fracture and fragmentation and the field measurements (strain, etc.).

Joints control the crater shape and size. Also the presence of boundaries influence to an extent the size and shape of the crater. The shape of the model has only a minor effect on the fracture and fragmentation results.

Post-test observations suggest the crater is formed in stages, that is, a crater within a crater within a crater is formed with larger diameters as time increases.

B. Fracture and Fragmentation Mechanisms.

An important mechanism is the formation of multiple spall surfaces resulting from reflections of the P-wave from the free surface and from subsequent spall layers. The radial and the circumferential cracks occurring between the charge and the free surface weakens the material as the material fragments. The high pressure explosive gases act on the fragments and causes the fragments to move in the direction of the weakened material. Eventually these fragments fly away revealing the crater fracture surface.

Therefore, the fracture and fragmentation mechanism is a two stage process. The first stage is very much dependent on the formation of spall, multiple spall surfaces, and the radial and circumferential crack network as the P- and PP-waves propagate back over the advancing fractures. The second stage of the process is the infiltration of the weakened and fragmented volume with the residual high pressure explosive gas.

(7.2)

Previous evidence indicated that the crater appeared to begin at the borehole and travel outward to the free surface. The mechanism proposed as a result of this research suggests the crater begins near the free surface and proceeds inward. However, the very first cracks to form at the borehole are the radial cracks generated by the outwardly propagating shock wave. These cracks develop into a network of many cracks that define the crush zone. A few of these radial cracks propagate beyond this zone towards the free surface and outline the final crater.

C. Finite Element Calculations.

The finite element analysis, though only a static calculation, of a geometry corresponding to a fragmentation pattern at a specific time showed agreement with the experiments conducted in three dimensional models made from cement and support the proposed fragmentation mechanism. There was good agreement between measured displacements and the computed displacements. The analysis included both radial and circumferential fractures in the finite element geometry as observed in the photoelastic tests.

The spall resulting from the stress wave, combined with the propagating radial and circumferential fractures (and crack branching) condition or weaken the rock for removal by the high pressure gases.

D. Optimization of Crater Volume.

Crater volumes in plexiglass were enhanced by grooving the borehole. By locating a groove 2/3 the up the borehole from the bottom the crater was encouraged to initiate further from the free surface than without a groove. Fractures were found to initiate from this groove location and proceed upward. Volumes removed were increased by a factor of two to three using this scheme.

E. Effects of Joints.

As stated earlier joints are very effective in defining the fragmentation and the extent of cratering. Results from two and three dimensional tests in polymeric and gypsum models with several types of joint material indicate a significant reduction in transmission of energy across the interface. A 2-mm wide sand grain gap (mostly air) virtually reduced the transmission to zero. The magnitude of the reduction appears to depend on the impedance (density times the P-wave speed) or material properties of the joint material and the thickness. There is evidence from the tests that a rough interface surface attenuates the wave amplitude 5 to 10 % more than a smooth surface. The transmissions in the normal direction and the horizontal direction are nearly equal for a given joint material.

Joints must be included when attempting to calculate or to

(7.3)

predict the result from a blasting event. Even a small gap can reflect significant energy back towards the borehole.

F. Students Supported.

Three students were supported by this research contract over the last three years. Two have received their MS Degree in Mechanical Engineering and the third student plans to use these research results as his PhD dissertation topic. The students supported were as follows.

1. Sanyi Zheng, MS Degree in Mechanical Engineering December 1991. Thesis title "An Experimental Study of Dynamic Strain and Displacement in Crater Blasting Using The Moire Method."

2. David Fordyce, MS Degree in Mechanical Engineering May 1992. Thesis title "Stress Wave Propagation Across Smooth and Rough Interfaces".

3. X. J. Wang, PhD program in Mechanical Engineering. Dissertation subject is a theoretical and experimental investigation of joints and interfaces and their effects on stress wave propagation.

G. Papers and Presentations from This Research.

1. Dick, R.D., W.L. Fournery, X.J. Wang, C. Young, and S. Zheng, 1990, "Mechanisms of Fracture and Fragmentation by Explosive Loading," Proceedings International Conference on Micromechanics of Failure of Quasi-Brittle Materials, June 6-8, Albuquerque, NM Elsevier Applied Science Publishers.

2. Wang, X.J., W.L. Fournery, and R.D. Dick, 1990, "Model Studies of Optimized Crater Blasting," Proceedings Third International Symposium on Rock Fragmentation by Blasting, Brisbane, Australia, August 26-31.

APPENDIX A.

APPENDIX

TEST LIST

CRATOR TEST IN POLYMER MODELS

ID	DATE	SPECIMEN	CHARGE	MEASUREMENTS
CT-1		6x6x(4+1)", PLEXIGLAS	0.5g.PETN,SPH. STM.	6 RADIAL & TANGENTIAL STRAIN
CT-2		"	0.5g.PETN,SPH,UNSTM.	4 RADIAL & TAN., STRAIN
CT-3		"	0.25g.PETN,SPH,STM.	"
CT-4		"	0.25g.PETN,SPH,UNSTM.	"
CT-5		"	0.25g.PETN,SPH,STM.	"
CT-6		10x10x(4+2)". PLEXIGLAS	0.5g.PETN,SPH,STM.	4 STRN., ACC., PHOTO.
CT-7	02/21/89	"	"	"
CT-8		6x6x5", EPOXY	0.35g.PETN,SPH,STM.	4 STRN., ACC., PHOTO.
CT-9		10x10x6", EPOXY	"	5 STRN., ACC., PHOTO.
CT-10	08/20/89	"	0.35g., PETN,SPH., STM.	2 STRSS, 2 VELOCITY
CT-11	09/02/89	"	"	5 STRN., 2 STRESS
CT-12	08/20/90	"	"	4 STRN., 2 STRESS
CT-13		10x5", CYLINDRICAL, EPOXY	"	7 STRN., 2 STRESS, ACC.,
CT-14		10x10x6", EPOXY	"	3 VELOCITY
CT-15		"	"	WAVE SPEED
				STRAIN, STRESS, PHOTO.

CRATOR TEST WITH CIRCUMFERENTIALLY GROVED BOREHOLE

ID	DATE	SPECIMEN	CHARGE	MEASUREMENTS
CG-1	12/14/89	6x6x4" PLEXIGLAS	0.6g.PETN, CYL.	CRATER VOLUME
CG-2	12/15/89	6x6x4" PLEXIGLAS	0.6g.PETN, CYL.	CRATER VOLUME
CG-3	12/19/89	6x6x4" PLEXIGLAS	0.6g.PETN, CYL.	CRATER VOLUME
CG-4	01/04/90	6x6x4" PLEXIGLAS	0.6g.PETN, CYL.	CRATER VOLUME
CG-5	01/15/90	6x6x4" PLEXIGLAS	0.6g.PETN, CYL.	CRATER VOLUME

CRATER VOLUME
CRATER VOLUME

0.6g. PETN, CYL.
0.5g. PETN, CYL., DEC.

CRATOR TEST WITH CIRCUMFERENTIALLY GROVED BOREHOLE

MEASUREMENTS
CRATER VOLUME
CRATER VOLUME
CRATER VOLUME

CHARGE
0.5g. PETN, CYL., DEC.
0.6g. PETN, CYL.
0.6g. PETN, CYL.

ID	DATE	SPECIMEN
CG-8	02/04/90	6x6x4" PLEXIGLAS
CG-9	02/11/90	6x6x4" PLEXIGLAS
CG-10	02/11/90	6x6x4" PLEXIGLAS

CRATOR TEST IN CONCRETE MODELS

MEASUREMENTS
RADIAL VELOCITY
VERTICAL VELOCITY
VERTICAL VELOCITY

CHARGE
1.0g. PETN, CYL., STM.
1.0g. PETN, SPH., STM.

ID	DATE	SPECIMEN
RT-1		10x6", CYL., ROCKITE
RT-2		"
RT-3		10x6", CYL., CONCRETE
RT-4		"
RT-5		"
RT-6		"

"
" RADIAL VELOCITY
RADIAL VELOCITY
VERTICAL VELOCITY
VERTICAL VELOCITY
RADIAL VELOCITY
VERTICAL V. & STRESS
VERTICAL V. & STRESS
"

1.0g. PETN, CYL., STM.
1.0g. PETN, CYL., STM.
1.0g. PETN, SPH., STM.
1.0g. PETN, SPH., STM.
"
"
"

RT-7	05/31/90	10x6", CYL., H.S. CNCRT.
RT-8	05/31/90	10x6", CYL., H.S. CNCRT.
RT-9	06/01/90	"
RT-10	06/01/90	"
RT-11	06/13/90	"
RT-12	10/15/91	"
RT-13	10/15/91	12x12x10", H.S. CONCRETE

JOINT TEST IN POLYMER MODELS

MEASUREMENTS
STRAIN, INV. & WIPER JNT.
STRAIN, LINEN & PAPER JNT.
STRAIN, GREASE & RUBBER
CEMENT JNT.

CHARGE
0.35g. PETN, SPH.
0.35g. PETN, SPH.
0.5g. PETN, SPH.

ID	DATE	SPECIMEN
JNT-1	03/19/90	10x10x6", EPOXY
JNT-2	03/21/90	10x10x6", EPOXY
JNT-3	03/22/90	10x10x6", EPOXY

JOINTED PLATE TEST

MEASUREMENTS

CHARGE

ID	DATE	SPECIMEN
----	------	----------

PJ-1 03/22/91 0.5" HOMAITE
 PJ-2 03/23/91 0.5" HOMAITE
JOINTED PLATE TEST

0.2g. PETN
 0.2g. PETN
 PARTICLE VELOCITY
 PARTICLE VELOCITY

ID DATE SPECIMEN
 PJ-3 03/23/91 0.5" HOMAITE
 PJ-4 03/23/91 0.5" HOMAITE
 PJ-5 04/08/91 0.5" HOMAITE
 PJ-6 04/08/91 0.5" HOMAITE
 PJ-7 06/11/91 0.5" HOMAITE
 PJ-8 06/11/91 0.5" HOMAITE

CHARGE
 0.2g. PETN
 0.2g. PETN
 0.2g. PETN
 0.2g. PETN
 0.2g. PETN
 0.2g. PETN
 0.2g. PETN
MEASUREMENTS
 PARTICLE VELOCITY
 PARTICLE VELOCITY
 PARTICLE VELOCITY
 PARTICLE VELOCITY
 PARTICLE VELOCITY
 PARTICLE VELOCITY
 PARTICLE VELOCITY

JOINT TEST IN HYDROSTONE MODELS

ID DATE SPECIMEN
 HS-10 05/26/91 12" CUBE
 HS-11 05/26/91 12" CUBE
 HS-12 05/26/91 12" CUBE
 HS-13 06/08/91 12" CUBE
 HS-14 06/08/91 12" CUBE
 HS-15 06/08/91 12" CUBE
 HS-16 06/25/91 12" CUBE
 HS-17 06/25/91 12" CUBE
 HS-18 07/19/91 12" CUBE, HYDROCAL
 HS-19 07/26/91 12x12x15", HYDROCAL
 HS-20 07/26/91 12x12x15", HYDROCAL
 HS-21 08/03/91 12x12x10", HYDROCAL
 HS-22 07/26/91 12x12x10", HYDROCAL
 HS-23 08/11/91 12x12x12", HYDROCAL
 HS-24 10/08/91 18" CUBE
 HS-25 10/11/91 18" CUBE, HYDROCAL
 HS-26 10/11/91 18" CUBE, HYDROCAL

CHARGE
 1.0g. PETN, SPH.
 1.0g. PETN, SPH.
 1.0g. PETN, SPH.
 1.0g. PETN, SPH.
 1.0g. PETN, SPH.
 1.0g. PETN, SPH.
 1.0g. PETN
 1.0g. PETN
 1.0g. PETN
 1.0g. PETN
 1.0g. PETN
 1.0g. PETN
 1.0g. PETN
 1.0g. PETN
 1.0g. PETN, SPH
 1.0g. PETN, SPH.
 1.0g. PETN, SPH.
MEASUREMENTS
 VERTICAL VEL. PLASTIC FILM
 & SMOOTH JNT.
 "
 VERTICAL VELOCITY,
 SMOOTH JNT.
 VERTICAL VELOCITY, SMOOTH
 & GREASE JNT.
 VERTICAL VELOCITY, SMOOTH
 & PLASTIC FILM JNT.
 VERTICAL VELOCITY, SMOOTH
 & PLASTIC FILM & DOWEL
 VERTICAL VELOCITY, ROUGH
 VERTICAL VELOCITY, ROUGH
 VERTICAL VELOCITY, ROUGH
 VERTICAL VELOCITY, ROUGH
 SHEAR VELOCITY, ROUGH
 SHEAR VELOCITY, ROUGH
 SHEAR VELOCITY, ROUGH
 SHEAR VELOCITY, ROUGH
 VERT. VEL., SMOOTH & DOWEL
 VERT. VEL., SMOOTH & DOWEL
 VERT. VEL., SMOOTH & DOWEL

HS-25 10/11/91 18" CUBE, HYDROCAL
HS-25 10/11/91 18" CUBE, HYDROCAL

1.0g. PETN, SPH.
1.0g. PETN, SPH.

VERT. VEL., SMOOTH & DOWEL
VERT. VEL., SMOOTH & DOWEL

2-D PHOTOELASTIC TEST

ID	DATE	SPECIMEN	CHARGE	MEASUREMENTS
CZ-1	05/15/90	12x12x1/4" HOMALITE	0.25g. PETN 0.25" DIA.	CRASHED ZONE, RATIO 7.087
CZ-2	05/15/90	12x12x1/4" HOMALITE	0.35g. PETN 19/64" DIA.	CRASHED ZONE, RATIO 4.906
CZ-1	05/15/90	12x12x1/4" HOMALITE	0.5g. PETN 11/32" DIA.	CRASHED ZONE, RATIO 4.696
IC-1	01/08/91	8x5x0.25" HOMALITE	0.15g. PETN 3/16" DIA.	ISOCLINIC FRG. & CRATER
IC-2	01/20/91	10x7x0.25" HOMALITE	0.25g. PETN 0.2" DIA.	ISOCLINIC FRG. & CRATER

2-D PHOTOELASTIC TEST

ID	DATE	SPECIMEN	CHARGE	MEASUREMENTS
IC-3	02/04/91	10x7x0.125" HOMALITE	0.1g. PETN 0.2" DIA.	ISOCLINIC FRG. & CRATER
IC-4	02/12/91	10x7x0.25" HOMALITE	0.22g. PETN 0.2" DIA.	ISOCLINIC FRG. & CRATER
IC-5	01/18/91	10x7x0.25" HOMALITE	0.22g. PETN 0.2" DIA.	ISOCLINIC FRG. & CRATER
IC-6	01/22/91	10x7x0.25" HOMALITE	0.22g. PETN 0.2" DIA.	ISOCLINIC FRG. & CRATER
IS-1	03/17/91	12x12x3/8", PLEXIGLAS	0.22g. PETN, 0.3" DIA.	ISOCROMATIC FRG. & CRASH ZONE, RATIO 6.87
IS-2	04/03/91	12x12x3/8", PLEXIGLAS	0.38g. PETN, 0.2" DIA.	ISOCH. FRG., CRATER & CRASH ZONE, RATIO 6.89
IS-3	07/23/91	12x12x3/8", PLEXIGLAS	0.26g. PETN, 0.2" DIA.	ISOCH. FRG., CRATER & CRASH ZONE, RATIO 7.5
IS-4	07/23/91	12x12x3/8", PLEXIGLAS	0.6g. PETN, 0.3" DIA.	ISOCH. FRG., CRATER & CRASH ZONE, RATIO 6.88
IS-5	07/29/91	12x12x3/8", PLEXIGLAS	0.174g. PETN, 0.2" DIA.	ISOCH. FRG., CRATER & CRASH ZONE, RATIO 6.88
IS-6	07/29/91	12x12x3/8", PLEXIGLAS	0.4g. PETN, 0.3" DIA.	ISOCH. FRG., CRATER & CRASH ZONE, RATIO 7.74
SV-1	11/05/89	10x10x2" EPOXY	0.35g. PETN SPH.	STRAIN GAGE VERIFICATION, - 4 RADIAL STRAIN GAGES

SV-2 11/10/89 10x10x2" EPOXY 0.35g.PETN SPH.

STRAIN GAGE VERIFICATION, -
4 TANGENTIAL STRAIN GAGES

FREE SURFACE MOTION TEST--IN-PLANE DISPLACEMENT

ID	DATE	SPECIMEN	CHARGE	MEASUREMENTS
MT-1	08/11/90	6x6x1" PLEXIGLAS	0.3g.PETN	1000L./IN. MOIRE FRG. IN-PLANE DISPLACEMENTS
MT-2	08/14/90	6x6x1/4" HOMALITE	0.2g.PETN	1000L./IN. MOIRE FRG. IN-PLANE DISPLACEMENTS
MT-3	08/11/90	6x6x4" PLEXIGLAS	0.35g.PETN	1000L./IN. MOIRE FRG. IN-PLANE DISPLACEMENTS
MT-4	08/31/90	6x6x4" PLEXIGLAS	0.35g.PETN	1000L./IN. MOIRE FRG. IN-PLANE DISPLACEMENTS
MT-5	08/31/90	6x6x4" HOMALITE	0.35g.PETN	1000L./IN. MOIRE FRG. IN-PLANE DISPLACEMENTS

FREE SURFACE MOTION TEST--OFF-PLANE DISPLACEMENT

ID	DATE	SPECIMEN	CHARGE	MEASUREMENTS
WD-1	10/19/90	6x6x4" PLEXIGLAS	0.3g.PETN	OPTONIC SENSOR
WD-2	10/22/90	6x6x4" PLEXIGLAS	0.3g.PETN	OPTONIC SENSOR
WD-3	11/12/90	6x6x4" NYLON	0.3g.PETN	OPTONIC SENSOR
WD-4	03/12/90	6x6x4" HOMALITE	0.3g.PETN	OPTONIC SENSOR

FREE SURFACE MOTION TEST--PARTICLE VELOCITY

ID	DATE	SPECIMEN	CHARGE	MEASUREMENTS
FS-1	10/19/90	6x6x4" PLEXIGLAS	0.3g.PETN SPH.	NORMAL VEL., EMV GAGE
FS-2	10/22/90	6x6x4" PLEXIGLAS	0.3g.PETN SPH.	NORMAL VEL., EMV GAGE
FS-3	11/12/90	6x6x4" NYLON	0.3g.PETN SPH.	NORMAL VEL., EMV GAGE
FS-4	01/02/90	6x6x4" PLEXIGLAS	0.3g.PETN SPH.	NOR. & TAN.VEL., EMV GAGE
FS-5	01/14/91	6x6x4" PLEXIGLAS	0.3g.PETN SPH.	NOR. & TAN.VEL., EMV GAGE
FS-6	01/28/91	6x6x4" PLEXIGLAS	0.3g.PETN SPH.	NOR. & TAN.VEL., EMV GAGE
FS-7	01/31/91	6x6x4" PLEXIGLAS	0.3g.PETN SPH.	NOR. & TAN.VEL., EMV GAGE
FS-8	02/19/91	6x6x4" PLEXIGLAS	0.3g.PETN SPH.	NOR. & TAN.VEL., EMV GAGE